Three-Dimensional Turbulence Characteristics of the Bottom Boundary Layer of the Coastal Ocean

by

Edward C. C. Steele

A thesis submitted to the University of Plymouth

in partial fulfilment of the degree of

Doctor of Philosophy

School of Marine Science and Engineering

Faculty of Science and Engineering

2015

Copyright Statement

Signed ....

Edward C. C. Steele

Date ....

Abstract

Three-Dimensional Turbulence Characteristics of the Bottom Boundary Layer of the Coastal Ocean

Edward C. C. Steele

The form and dynamics of ocean turbulence are critical to all marine processes; biological, chemical and physical. The three-dimensional turbulence characteristics of the bottom boundary layer of the coastal ocean are examined using a series of 29,991 instantaneous velocity distributions. These data, recorded by a submersible 3D-PTV system at an elevation of 0.64 m above the seabed, represent conditions typical of moderate tidal flows in the coastal ocean.

A complexity associated with submersible 3D-PTV in the coastal ocean is that gaps and noise affect the accuracy of the data collected. To accommodate this, a new Physics-Enabled Flow Restoration Algorithm has been tested for the restoration of gappy and noisy velocity measurements where a standard PTV or PIV laboratory set-up (e.g. concentration / size of the particles tracked) is not possible and the boundary and initial conditions are not known *a priori*. This is able to restore the physical structure of the flow from gappy and noisy data, in accordance with its hydrodynamical basis. In addition to the restoration of the velocity flow field, PEFRA also estimates the maximum possible deviation of the output from the true flow.

3D-PTV measurements show coherent structures, with the hairpin-like vortices highlighted in laboratory measurements and numerical modelling, were frequently present within the logarithmic layer. These exhibit a modal alignment of 8^o from the mean flow and a modal elevation of 27^o from the seabed, with a mean period of occurrence of 4.3 sec. These appear to straddle sections of zero-mean along-stream velocity, consistent with an interpretation as packets. From these measurements, it is clear that data collected through both laboratory and numerical experiments are directly applicable to geophysical scales – a finding that will enable the fine-scale details of particle transport and pollutant dispersion to be studied in future. Conditional sampling of the Reynolds shear stress (without using Taylor's hypothesis) reveals that these coherent structures are responsible for the vertical exchange of momentum and, as such, are the key areas where energy is extracted from the mean flow and into turbulence.

The present study offers the first assessment of the magnitude of the errors associated with assuming isotropy on shear-based sensors of the TKE dissipation rate and its consequential effect on the Kolmogorov microscale using 3D-PTV data from the bottom boundary layer of the coastal ocean. The results indicate a high degree of spatial variability associated with the flow conditions. The averaged data supports the validity of measurements obtained by horizontal and vertical profilers, however along-stream velocity derivatives underestimate the TKE dissipation rate by more than 40% – a factor of two higher than for the equivalent cross-stream and vertical estimates. This has important implications for the deployment of these sensors and the subsequent interpretation of higher-order statistics.

Finally, the data have been processed to test four popular sub-grid scale (SGS) stress models and SGS dissipation rate estimates for Large-Eddy Simulations using these in situ experimental data. When the correlation and SGS model coefficients are assessed, the nonlinear model represents the best stress models to use for the present data, consistent with the substantial anisotropy and inhomogeneity associated with these flows.

The detailed measurement and analysis of coherent structures in the coastal ocean undertaken therefore supports the development of numerical models and assists with the understanding of all marine processes.

Contents

List of Figures

List of Tables

Acknowledgements

The very essence of research in a scientific field effectively represents a body of work which extends far beyond the boundaries of one's chosen field of study. So too, a huge team of academics, colleagues and friends have assisted my quest for answers and understanding in support of my endeavours. I would therefore like to thank the many people who have provided this assistance.

For his professional expertise and encouragement throughout my studies at the University of Plymouth, I am indebted to Dr Alex Nimmo-Smith, who first introduced me to the mysteries of turbulence, particle imaging, and the important role that MATLAB would play in my life as a new undergraduate. He has been generous with his extensive knowledge and direction in providing research data, for which I am immeasurably grateful.

My gratitude extends to my other supervisors, Dr Phil Hosegood and Dr Vasily Vlasenko, whose humour and mathematical genius delight in equal measure – also to Dr Nataliya Stashchuk – all of whom have provided valuable guidance throughout the duration of this work. Similarly, I am grateful to Dr Andrey Vlasenko at the University of Hamburg, Germany, for his time and patience, teaching me to enjoy maths, and for his invaluable contribution to the development of the new Physics Enabled Flow Restoration Algorithm.

Funding for the Studentship was supplied by the School of Marine Science and Engineering (University of Plymouth), with conference attendance supported by University of Plymouth Marine Institute and PlyMSEF. I am most grateful for their financial support.

During my studies, I have been fortunate to further my collaborations with The Scottish Association for Marine Science. In addition to my thanks to all at SAMS, I would like to thank Professor Mark Inall for his recognition in awarding me the Neil MacDougall Research Bursary, and for sharing his incredible experience of velocity microstructure measurements of ocean turbulence during our Arctic research expedition which ensued from this. My debt of thanks rests also with the late Dr Tim Boyd, who as a truly inspirational physical oceanographer and scientist, tragically killed in January 2013, taught me to continually extend the conversation beyond the science.

A vote of thanks is due to the next generation of particle imaging researchers, Dr Emlyn Davies, Dr George Graham and Dr Jaimie Cross whose individual conversations have inspired many ideas that have been incorporated in this work, as well as their longstanding association as both students and friends. Likewise, I am grateful to my fellow TurboPIGs (Turbulence & Particle Imaging Group) and the PhD students within my office: Ellie, Emma, Emma, Emlyn, Jaimie, and Sam, who have provided both valuable discussion and distraction.

Finally, I have drawn shamelessly on the help of my parents, brother, family and friends, including Liz and Francis Woodward, who have all dispensed time and wisdom, and cake; and especially, and most gratefully in this respect, to Ellie.

Author's Declaration

At no time during the registration for the degree of Doctor of Philosophy has the author been registered for any other University award without prior agreement of the Graduate Committee.

This study was financed with the aid of a Studentship from the School of Marine Science and Engineering (University of Plymouth), with conference attendance supported by University of Plymouth Marine Institute and PlyMSEF.

Journal papers

- A. Vlasenko, **E. C. C. Steele**, and W. A. M. Nimmo-Smith (2015) A physics-enabled flow restoration algorithm for sparse PIV and PTV measurements, *Measurement Science & Technology*, 26, 065301 (23pp).

Note that only material contributed by the author is included within the body of the thesis.

Conference papers

- **E. C. C. Steele**, W. A. M. Nimmo-Smith, A. Vlasenko, V. Vlasenko, and P. Hosegood (2013) Examination of turbulence structures in the bottom boundary layer of the ocean by submersible 3D-PTV. 10th International Symposium on Particle Image Velocimetry (PIV2013) July 2013, Delft, The Netherlands.

- **E. C. C. Steele**, T. Boyd, M. Inall, E. Dumont and C. Griffiths (2012)

Cooling of the West Spitsbergen Current: AUV-based turbulence measurements west of Svalbard, Autonomous Underwater Vehicles (AUV2012), October 2012, Southampton, UK.

Conference abstracts

- **E. C. C. Steele**, T. Boyd, M. Inall, E. Dumont and C. Griffiths (2012) Cooling of the West Spitsbergen Current: AUV-based turbulence measurements west of Svalbard, Challenger Society Conference, September 2012, Norwich, UK.

- **E. C. C. Steele**, W. A. M. Nimmo-Smith, A. Vlasenko, V. Vlasenko, and P. Hosegood (2012) 3D Turbulence structures in the Bottom Boundary Layer of the Coastal Ocean. Challenger Society Conference, September 2012, Norwich, UK.

Courses

- Fluid Dynamics of Sustainability and the Environment, Ecole Polytechnique, Lozere, France. 9 September 2013 – 20 September 2013. Directors: Caroline Muller (Ecole Polytechnique), Paul Linden (Cambridge University) and Alexandre Stegner (Ecole Polytechnique).

The word count of this thesis is: 37,957.

Data processing and visualisation: MATLAB®.

Typesetting: LaTeX, 12 pt, Computer Modern, 1.75 line spacing.

Signed ....

Edward C. C. Steele

Date ....

Chapter 1

Overview

The rotational, eddying and dynamic motions implied by the term turbulence are the dominant state of fluid movement on Earth. As such, turbulence is effective in the transferral of heat and momentum in the sea, as well as dispersing, stressing and straining both particles and living matter in the water column, while diluting and stirring its chemical constituents (Thorpe, 2004). Turbulence in shelf-seas has a strong influence on the large-scale distribution of biological production (Tett et al., 1993) and suspended sediments (Jago and Jones, 1998). Tidally-generated turbulence limits the areas of thermal stratification (Simpson and Hunter, 1974), which in turn affects the shelf-sea "pumping" of carbon dioxide and is an important process for the global carbon cycles (Thomas et al., 2004). Modelling work has also shown that small changes in the vertical distribution of the stress associated with turbulence can have a strong effect on the patterns of circulation at much larger scales (Lentz, 1995). In tidal flows, turbulence is generated near the seabed (Heathershaw, 1974). However, while its one-dimensional characteristics have been well-studied, little is known of its three-dimesional structure and subsequent development throughout the water column. On reaching the surface of well-mixed waters, bottom-generated “boils” – areas of local upwelling and associated eddies – have a marked impact on the dispersion of pollution and contributes to the replacement of surface waters from depth (Nimmo-Smith et al., 1999, Thorpe et al., 2008). A detailed understanding of turbulence is therefore critical to explaining all marine processes (physical, biological and chemical) and for the development of models that allow us to plan the sustainable exploitation of the marine system, for example marine renewable energy, fishing and pollution policies.

Numerical models of marine processes are usually unable to resolve all but the largest scales of motion and so rely on the parameterisation of subgrid-scale processes, to which these are very sensitive. Good parameterisation is only possible with knowledge of the structure of the turbulence but, away from the surface, this is notoriously difficult to measure. Traditionally, micro-structure profilers and Acoustic Doppler instrumentation have been used to measure turbulence parameters that might reveal vertical patchiness, but these cannot show the detailed vortex structure (size, intensity, attitude and alignment). Recently, however, three-dimensional optical flow visualisation methods using four high frame-rate, high resolution digital cameras have been developed, yielding unique insight into the full vortex structures in ocean flows (Nimmo-Smith, 2008). The cameras track suspended particles, advected by the mean flow and turbulent eddies within a 15L sample volume, allowing the corresponding velocity field to be quantified. The time-resolved three-dimensional velocity flow field can then be used to test assumptions inherent in traditional instrumentation, as well as turbulence models by temporal and / or spatial filtering.

Therefore, the aim of the present thesis is to study the small-scale three-dimensional turbulence characteristics of the bottom boundary layer of the coastal ocean, with the purpose of aiding the interpretation of other experimental and numerical modelling data sets.

The thesis takes the following format: Chapter 2 presents a summary of the literature available on turbulent boundary layers and coherent structures, as well as existing measurements and numerical modelling of these both in laboratory / idealised flows and in the sea. Chapter 3 presents the instrumentation used, together with a novel physics-based processing method developed for highly sparse optical flow visualisation data. Here, the characteristics of the data sets that will be examined in this thesis are also summarised. Chapter 4 presents visualisations of the instantaneous 3D form of turbulence in the bottom boundary layer of a tidal flow. These data offer a unique insight into the spatial characteristics of the dynamical phenomena that are responsible for the statistical properties of ocean flows. This is extended in Chapter 5 where the dissipation characteristics of turbulence structures are compared to 1D, 2D and 3D estimates to quantify the response of more traditional instruments to varying vortex structures. The data are used to test common turbulence parameterisations for numerical models in Chapter 6. Chapter 7 presents the conclusions of the thesis and discusses possible directions for further work.

Chapter 2

Scientific background

2.1 Boundary Layer Turbulence

The tendency of fluid elements to adhere to a material surface, the so-called no-slip condition, is essential for the comprehension of wall-bounded flows (Klewicki, 2010), where the mean speed decreases from an uninhibited value away from the boundary to zero at the bed. While it is apparent that wall-bounded flow in the ocean (the subject of this thesis) is more complicated than an idealised case, an introduction to the turbulence characteristics of a primitive boundary layer offers a suitable starting point for the discussion. Most importantly, it allows the coordinate system, scaling frameworks and two-layer flow structure necessary to understanding these wall-bounded flows to be identified.

2.1.1 Boundary layer structure

Figure 2.1A illustrates an idealised boundary layer, showing the three-dimensional (orthogonal) coordinate system that is used for the present study. Here, the X-axis is aligned (along-stream) with the direction of the mean flow, the Y-axis to perpendicular to this in the cross-stream dimension and the Z-axis is perpendicular to this in the wall normal dimension. Here, The associated velocity components are labelled U (also termed U_1), (V also termed U_2) and W (also termed U_3), respectively, with boundary layer thickness (δ) determined statistically as the height where the $\overline{U}(x, \delta)$ is 99% of the free-stream velocity, U_∞ (Pope, 2000). Flow within the interior of this near wall layer is represented by the turbulent Reynolds number $Re_x = \frac{U_\infty X}{\upsilon}$ (where υ is the kinematic viscosity and X is an along-stream position) that acts to locally moderate the boundary layer thickness, as well as to exert a shear stress on the bed, often expressed as the friction velocity, U_*:

$$U_* = \sqrt{\frac{\tau_v}{\rho}} \tag{2.1}$$

where, ρ is the density, and τ_v is the viscous stress at $z = 0$ (defining μ as the dynamic viscosity):

$$\tau_v = \mu \frac{\partial U_1}{\partial X_3} \tag{2.2}$$

The stress arising from turbulence-associated velocity components (later labelled u'_1, u'_2, and u'_3, respectively) is expressed as the Reynolds stress, τ_r:

$$\tau = -\rho \overline{u'_1 u'_3} \tag{2.3}$$

Defining the viscous stress and the Reynolds shear stress it is therefore possible to determine a total stress at an elevation as the sum of these two formulas:

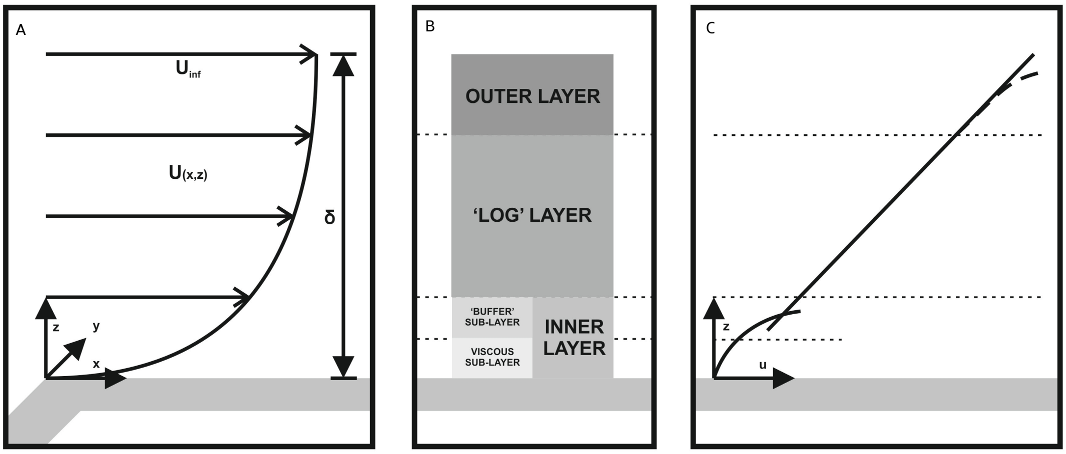

Figure (2.1). An illustration of the structure of the boundary layer where (A) the coordinate system and time averaged axial velocity profile is seen relative to (B) the two overlapping inner and outer wall layers. (C) An illustration of the log law of the wall responsible for these divisions, presented with u^+ on the X-axis and $log(z^+)$ on the Y-axis. Note that in ocean boundary layer flows, an inflection point typically occurs immediately below the log layer.

$$\tau_t = -\rho\overline{u_1'u_3'} + \mu\frac{\partial U_1}{\partial U_3} \tag{2.4}$$

In accordance with mean velocity and stress profiles, the boundary layer is usually divided into two overlapping layers (the inner-wall layer and the outer-wall layer) where different processes occur (Panton, 2001). This area of overlap is referred to as the log layer due to its local velocity characteristics.

Figure 2.1B illustrates this boundary layer structure. A viscosity difference between the inner layer and the outer layer necessitates two different scales be considered. The inner length scale arises from the interaction with the wall and the associated shear force it imparts. It is expressed using the friction velocity, U_* and the kinematic viscosity, v, in non-dimensional wall units:

$$x^+ = \frac{U_* x}{v} \tag{2.5}$$

$$y^+ = \frac{U_* y}{v} \tag{2.6}$$

$$z^+ = \frac{U_* z}{v} \tag{2.7}$$

The inner length scales therefore represent the smallest turbulent motions (Panton, 2001). The outer length scale, however, represents the dynamics of large-scale fluid flows and are represented by the wall-normal eddy scales, uninhibited by viscosity. This is therefore expressed using a boundary layer thickness, δ, i.e.

$$Z = \frac{z}{\delta} \tag{2.8}$$

Having addressed the inner/outer layer scaling issue, we will proceed to elaborate on boundary layer structure.

Following Pope (2000), after Coles (1956), it is possible to represent the dependence of the mean along-stream velocity on the distance from the wall ($0 \rightarrow \delta$) as the sum of two functions; the law-of-the-wall (dependant on $\frac{v}{u_*}$), $f_w(z^+)$, and the law-of-the-wake, $W(Z)$ (dependant on $\frac{z}{\delta}$):

$$U^+ = \frac{\overline{U}}{U_*} = f_w(z^+) + W(Z) \tag{2.9}$$

Figure 2.1C illustrates this general profile, where the inner layer is typically $z^+ < 100$. The inner layer, in fact, consists of two sublayers – the viscous sublayer and the buffer sublayer – as well as part of the log layer. Here, the law-of-the-wake, $W(Z)$, is negligible and the law-of-the-wall, f_w, will represent the velocity (Panton, 2001). The viscous sublayer is that immediately overlying the bed is ($z^+ < 5$). In this area, the viscous stresses exceed the Reynolds stresses ($\mu\frac{\partial U}{\partial Z} \gg -\rho\overline{u'w'}$) and the law-of-the-wall is $f_w(z^+) \approx z^+$ (Pope, 2000, Dennis, 2009). This is, in turn, succeeded by the buffer sublayer ($5 < z^+ < 30$ or 50) that offers transition to the log layer beyond. The log-law profile (Pope, 2000, Panton, 2001) is representative of the mean along-stream velocity at a height of between $z^+ > 30$ or 50 and $Z \ll 1$:

$$U^+ = \frac{\overline{U}}{U_*} = f_w(z^+ \rightarrow \infty) = \frac{1}{\kappa}\ln(z^+) + B \tag{2.10}$$

where, κ is the von Karman's constant $= 0.41$ and B is a positive coefficient (dependant on the Reynolds number).

In the log layer, the Reynolds shear stress exceeds the viscous stress ($-\rho\overline{u'w'} \gg \mu\frac{\partial U}{\partial Z}$) and the flow populated with an abundance of eddies. This is in contrast to the viscous sublayer, for example, where such turbulence is suppressed by near-wall viscosity. As is implied by Equation 2.10, the extent of the log layer is proportional to its Reynolds number, Re. Somewhere in the outer layer, however, the mean velocity profile departs from the log law (Pope, 2000). This defect at, say, $Z > 0.2$, is often expressed using Cole's law-of-the-wake, $W(Z)$ Coles (1956). At the extent of the outer layer, δ, the mean along-stream velocity profile evaluates to:

$$U^+ = \frac{\overline{U}}{U_*} = f_w(z_\delta^+) + W(Z_\delta) = \frac{1}{\kappa}\ln(z_\delta^+) + B + \frac{2\Pi}{\kappa} \tag{2.11}$$

where Π is the flow dependent wake parameter, with all other coefficients defined in Equation 2.10.

2.1.2 Energetics of turbulence

Turbulence consumes energy by transferral through a series of successively smaller scales, until it is converted into heat by molecular processes. Within the context of these energetics, the Turbulent Kinetic Energy is defined as:

$$E_T = \frac{1}{2}q^2 = \frac{1}{2}(u_1^2 + u_2^2 + u_3^2) \tag{2.12}$$

where subscript indices are the velocity components aligned with the X, Y and Z-axis, respectively. E_T is a scalar property, produced and dissipated through the fluid motion, which is subject to change by advection and diffusion. When conditions are horizontally uniform, $w = 0$. The evolution of E_T is:

$$\frac{\partial E_T}{\delta t} = \underbrace{\frac{\partial(u_3' E_T')}{\partial z}}_{\text{diffusion}} - \underbrace{\frac{1}{\rho_0}\left(\tau_1 \frac{\partial U_1}{\partial z} + \tau_2 \frac{\partial U_2}{\partial z}\right)}_{\text{production}} - \underbrace{\frac{g\rho' u_3'}{\rho_0}}_{\text{mixing}} - \underbrace{\epsilon}_{\text{dissipation}} \tag{2.13}$$

in which the elements of diffusion, production (via the the Reynolds shear stress, τ), mixing and dissipation are all represented.

Boundary layer turbulence comprises a continuum of wavenumber scales represented by an energy spectrum. Most energy is associated with large scale motion (i.e. lower wavenumber than where dissipation occurs), however this rapidly decreases with increasing wavenumber (decreasing eddy size) and more rapidly still at scales where molecular processes dominate (Thorpe, 2004). In high Reynolds number flows, assuming isotropy and homogeneity, there exists a range of wavenumber scales ($k = 2\pi/(\text{eddy size})$), where the energy spectrum has the form:

$$E(k) = \alpha\epsilon^{2/3}k^{-5/3} \tag{2.14}$$

where $\alpha = 1.5$ is a constant and ϵ is the TKE dissipation rate that represents the loss of energy through viscosity to heat, i.e.:

$$\epsilon = (\nu/2)\langle S_{ij}S_{ij}\rangle \tag{2.15}$$

where, in turn, $S_{ij} = (\partial u_i/\partial x_j + \partial u_j/\partial x_i)$ and $i = 1, 2, 3$.

The spatial (η) and velocity (U_ν) scales where viscosity becomes important are expressed by their Kolmogorov microscale and are used to parameterise the smallest vortices within the velocity flow field, i.e.:

$$\eta = \left(\frac{\nu^3}{\epsilon}\right)^{1/4} \tag{2.16}$$

and

$$U_\nu = (\nu\epsilon)^{1/4} \tag{2.17}$$

In the present study, the TKE dissipation rate (ϵ) and the Kolmogorov microscale (η) are used in Chapter 5 and Chapter 6.

2.2 Coherent structures

Turbulence appears complex, multi-scaled and seemingly random in nature. In an attempt to understand these flows, it is common to deconstruct the dynamics into persistent motions, called eddies or coherent structures. This approach is often represented in the evolution equation for the Turbulence Kinetic Energy. While not explicitly accounted for, these expressions imply an inherent organisation through the correlation of the velocity components that constitutes the Reynolds stress τ. If boundary layer turbulence was random, and no coherent structures present, then τ must equal zero (Robinson, 1991). Clearly, this is not the case and this τ is necessary to close the equations representing the production and dissipation balance of turbulence in the boundary. However, while it is apparent that such coherent structures are (likely to be) present and, indeed, are significant to all fluid flows, there is currently no firm agreement with the community on a universally accepted definition. Therefore, the general criteria offered by Robinson (1991) have been adopted for the present thesis:

> A coherent motion is defined as a three-dimensional region of the flow over which at least one fundamental variable (e.g. velocity components, density, etc.) exhibits a correlation with itself or with another variable over a range of space and / or time that is significantly larger than the smallest local scales of the flow.

This is also consistent with the numerical representation in evolution equation for the Turbulence Kinetic Energy, as only spatially-coherent structures that remain persistent over long time periods will contribute to the time-averaged statistics of the flow. In addition, the definition used permits opportunity to further classify these motions. The specific characteristics of streaks, bursts, sweeps, hairpin vortices and other large-scale events are outlined below.

2.2.1 Streaks, bursts & sweeps

The inherent organisation of motions associated with boundary layer flows causes the development of near-wall 'streaks' (traces of the interaction of the overlying eddies with the wall layer fluid; Kline et al. 1967, Smith et al. 1991). These flows therefore constitute areas of low axial momentum, occurring at a height of between $5 < z^+$ and $z^+ < 45$ or 50, characteristic of their inner layer origin. Typically, low-speed streaks are about $x^+ = 1000$ in the along-stream dimension by $y^+ = 80$ or 100 in the cross-stream dimension, with a separation between them of approximately $x^+ = 100$ (Smith and Metzler, 1983). While usually quiescent, these streaks are critical for the interaction between the inner and outer layer of the flow. Such interactions mainly occur in the form of bursts and sweeps. Bursts occur when low-momentum fluid (such as a streak) lifts and oscillates, prior to ejection away from the wall (Kline et al., 1967). This is subsequently followed by fast in-rushes of water towards the wall, known sweeps. As these dynamic motions promote the transferral of momentum, bursts and sweeps can be defined in terms of the velocity fluctuations that contribute to the Reynolds stress, τ, via quadrant analysis. A burst (or ejection) consisting of the outward ($u_3' > 0$)

movement of low speed fluid ($u_1' < 0$) is therefore considered a Quadrant 2 event, while a sweep consisting of the inward ($u_3' < 0$) movement of high-speed fluid ($u_1' > 0$) is considered a Quadrant 4 event. As both Quadrant 2 and Quadrant 4 events contribute to a positive (i.e. $u_1'u_3' < 0$) Reynolds shear stress, bursts and sweeps are deemed jointly responsible for the turbulence production in wall-bounded flows. However, their two respective areas of influence, and therefore contribution to the Reynolds shear stress in the boundary layer, are, in fact, different (Corino and Brodkey, 1969, Grass et al., 1991). Given that ejections originate at elevations between $5 \leq z^+ \leq 15$ and break-up at elevations between $7 \leq z^+ \leq 30$, while the in-rushes are more prominent at $z^+ < 15$, it follows that the area of influence of bursts is more extensive than that of sweeps occurring near the wall. The frequency of this burst-sweep sequence is between $\sim 350s$ and $\sim 550s$, with events typically of the order of $\sim 10\,\mathrm{s}$ in duration. The cyclical nature of such a sequence implies that these processes are self-sustaining, modified by the characteristics of the overlying dynamical motions, e.g. horseshoe and hairpin vortices.

2.2.2 Horseshoe and hairpin vortices

Horseshoe and hairpin vortices dominate the outer layer of wall-bounded flows (e.g. Adrian et al. 2000b). Here, the characteristics of these motions are reviewed through the conceptual models formed from many past laboratory and numerical experiments. The earliest of these models, proposed by Theodorsden (1952), is illustrated in Figure 2.2. These coherent structures are called horseshoe vortices because of their typical form, consisting of a cross-stream vortex filament, lifted by an upward motion to form a head, attached to two trailing legs. As the head is furthest from the wall, it experiences a higher mean flow velocity and so is carried downstream faster than the legs (Adrian, 2007). The difference in advection rate causes the legs to stretch, concentrating vorticity and resulting in subsequent lifting. A complimentary contribution, conveying the growth of structures in the boundary layer, was the attached eddy hypothesis proposed by Townsend (1956). While seemingly different to horseshoe vortices, the two wall attached cone vortices (Figure 2.3) that extend into the log layer in the latter model are reminiscent of the two trailing quasi-streamwise legs conjectured by Theodorsden (1952). Therefore, it may be suggested that horseshoe vortices and attached eddies (or headless horseshoes as these are occasionally known) are synonymous with one another. These vortices are squeezed at high Reynolds flow, where they resemble that of a hairpin. Therefore, the terms horseshoe and hairpin vortices are, similarly, interchangeable.

Initially, the significance of horseshoe and hairpin vortices were deemed inferior to that of streaks. Using smoke visualisation, however, Bandyopadhyay (1980) and Head and Bandyopadhyay (1981) established that hairpin vortices, with a mean angle to the wall of approximately 45°, are, in fact, a major constituent of boundary layer turbulence. These measurements were supported by a model where the cross-stream dimension of hairpin legs is typically $y^+ = 10 - 100$ and the structures extend from the wall in a regular, increasing, sequence. Similarly, in data presented by Smith (1984), the successive formation of in-line hairpin vortices in water flows occur. To attempt to explain these dynamics, Perry and Chong (1982) proposed various mechanisms of boundary layer turbulence

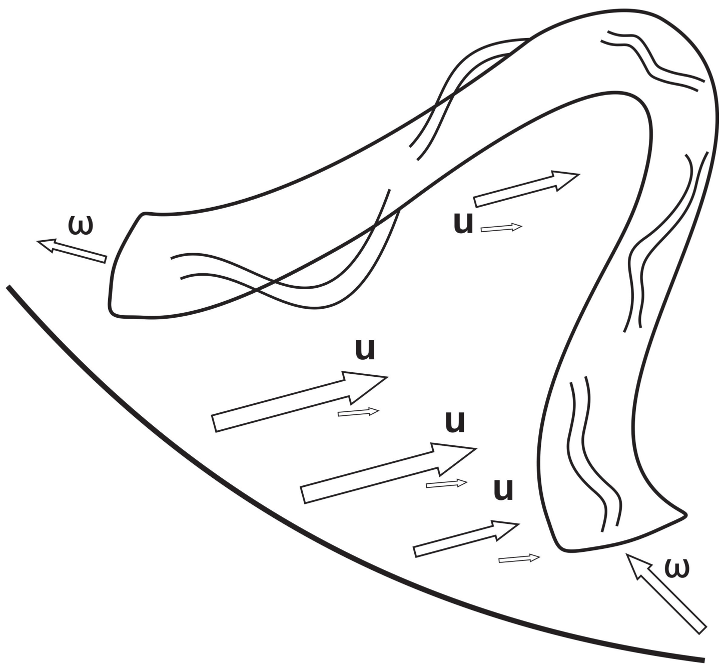

Figure (2.2). A conceptual model of Theodorsden's Horshoe vortex (modified from Panton 2001).

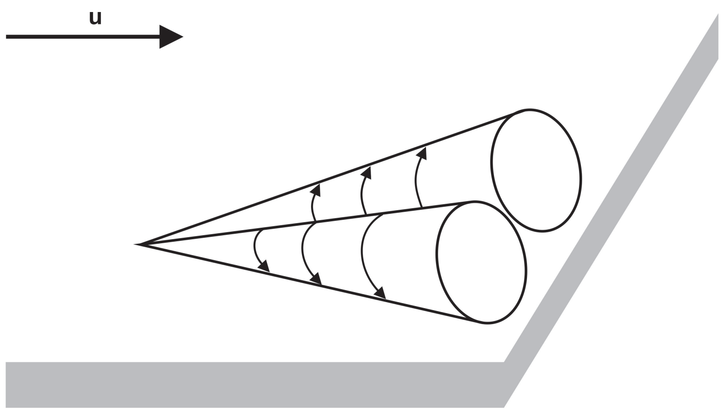

Figure (2.3). A conceptual model of Townsend's attached eddy hypothesis (modified from Panton 2001).

involving Λ-type horseshoe and hairpin vortices. Here, individual structures (of a hierarchy of scales, randomly scattered within the domain) were essential to explaining the previously published near-wall dynamics. This is consistent with the appreciable quantity of horseshoe and hairpin vortices that were modelled by Moin and Kim (1982) and Moin and Kim (1985). These three-dimensional, time-dependent Large-Eddy Simulations also provided a means of eddy generation, via the deformation or roll-up of sheets of transverse vorticity. Moin and Kim (1982) and Moin and Kim (1985) highlighted the need for the three-dimensional approach, as the vortices were not necessarily confined to a two-dimensional plane. From an examination of low Reynolds number Direct Numerical Simulation data Robinson (1989) came to a similar conclusion, where a hierarchy of scales were also seen to exist, with it reported that quasi-streamwise vortices exist in the inner layer, quasi-streamwise vortices and arches exist in the log layer, while arches and hairpin vortices exist in the outer layer of wall-bounded flow. An arch is defined by Robinson (1989) as a horseshoe head with no attached legs, whose occurrence was more common than complete hairpin vortices. On the occasion that complete hairpin vortices were identified, these were predominantly one-sided, with an appearance similar to a “walking cane” rather than symmetrical (but also seen to exist in succession). The advent of LES and DNS modelling (Moin and Kim, 1982, 1985, Kim and Moin, 1986, Robinson, 1989) was critical for the development of our understanding of the three-dimensional nature of boundary layer turbulence (Adrian, 2007). Most importantly these simulations confirmed the two-dimensional data collected in the early experiments were, indeed, coherent structures and these are the key sites where energy is extracted from the mean flow and into turbulence. These findings were consolidated by Smith et al. (1991), who presented a detailed model describing the fluid dynamics of the near-wall region, where the horseshoe and hairpin vortices were essential to explaining both the generation of new vortices and their growth to larger scales, further from the boundary.

As evidenced above, the succession of horseshoe and hairpin vortices in a regular, increasing sequence is well-reported (e.g. Smith et al. 1991, Haidari and Smith 1994, Singer and Joslin 1994). It is suggested that such vortices occur in groups or packets with a typical velocity difference of less than $\sim 7\%$ (Adrian et al., 2000b, Adrian, 2007). Zhou et al. (1996, 1999) considered the processes responsible for the genesis of these hairpin packets following a Quadrant 2 event, with it seen that the subsequent development of the initial hairpin vortex causes two new heads to form: one upstream and one downstream from the original. The upstream eddy is formed from vortex roll-up, associated with the interaction of the low-momentum fluid pumped between the legs and the high-momentum flows above (Adrian, 2007). These flows generate an arch that will join with the legs and the sequence is repeated. In addition, hairpin vortices lift adjacent quasi-streamwise vortices that appear as protrusions on the downstream edge of the head, that then become extruded into legs to form an arch, as above. The characteristics of these two new hairpin vortices are, however, different. The result of the former mechanism is consistent with the Attached Eddy Hypothesis, while the latter mechanism produces vortices that are detached from the wall. Zhou et al. (1996, 1999), and later authors, collectively refer to these processes as 'autogeneration' (Figure 2.4). The effects of 'noise' on the autogeneration of

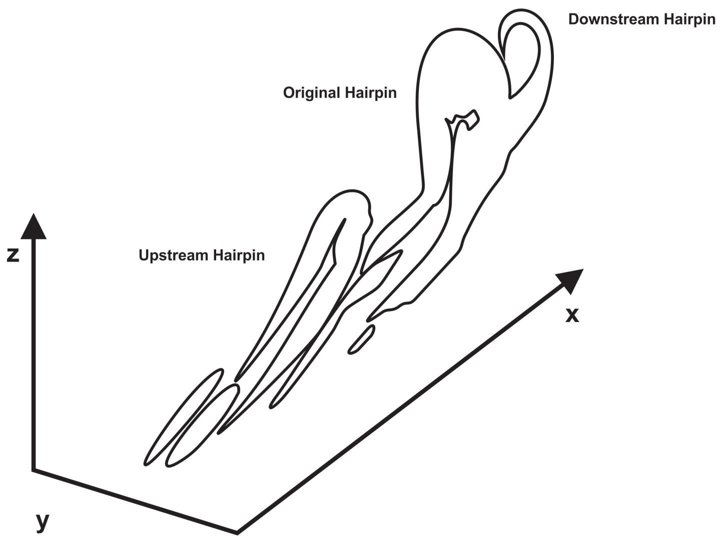

Figure (2.4). An illustration of the sequence of vortices associated with the processes of autogeneration (based on model by Zhou et al. (1996, 1999).

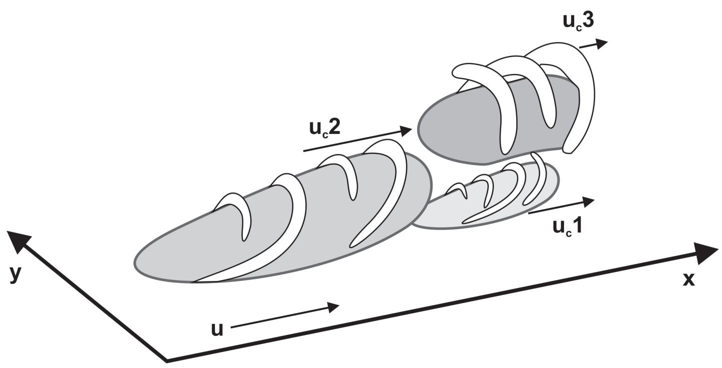

Figure (2.5). A conceptual model of the hierarchy of coherent packets of hairpin vortices travelling with different convection velocities (U_c). It is suggested that convection velocities increase with the age of hairpin packets. These structures may be responsible for the back-flow of low-speed fluid, forming areas of low streamwise momentum as illustrated by the grey patches (adapted from Adrian et al. 2000b).

these packets in fully turbulent flows were further addressed by Adrian and Liu (2002). With the addition of 5% noise, these processes were seen to proceed similarly to that of the clean packet. In both clean and noisy simulations, the development of trains of vortices was dependent on the magnitude of the initial Quadrant 2 event. Specifically, while low intensity ejections can cause an initial horseshoe, high intensity ejections (that account for approximately 5% to 10% of all Quadrant 2 events) are needed to stimulate continuous autogeneration of new upstream and downstream vortices. These conclusions were supported by the two-dimensional flow visualisation measurements of, for example, Adrian et al. (2000b).

The characteristics of boundary layer turbulence and its associated processes were unified in the seminal models by Adrian et al. (2000b) and Adrian (2007). Here, the concepts of packets of hairpin vortices and the mechanism of autogeneration allow the velocity flow field to be defined as the summation of the complex, multi-scaled contributions arising from a hierarchy of vortex groups, each containing eddies of different size (Figure 2.5). Adrian et al. (2000b) and Adrian (2007) therefore suggest the passage of such packets of hairpin vortices (and their inherent zones of uniform momentum) help explain the origin of bursts, sweeps and streaks. The conjecture is that this mechanism promotes the vertical exchange between wall-bounded layers. Similarly, recent quasi-instantaneous three-dimensional flow visualisation results (Figure 2.6) obtained from an engineering water tunnel (Dennis and Nickels, 2011a,b) offer support to models consisting of packets of hairpin vortices although, as uncertainty about the specific manner of the vortex interactions (e.g. Chernyshenko and Baig 2005) and the dynamics

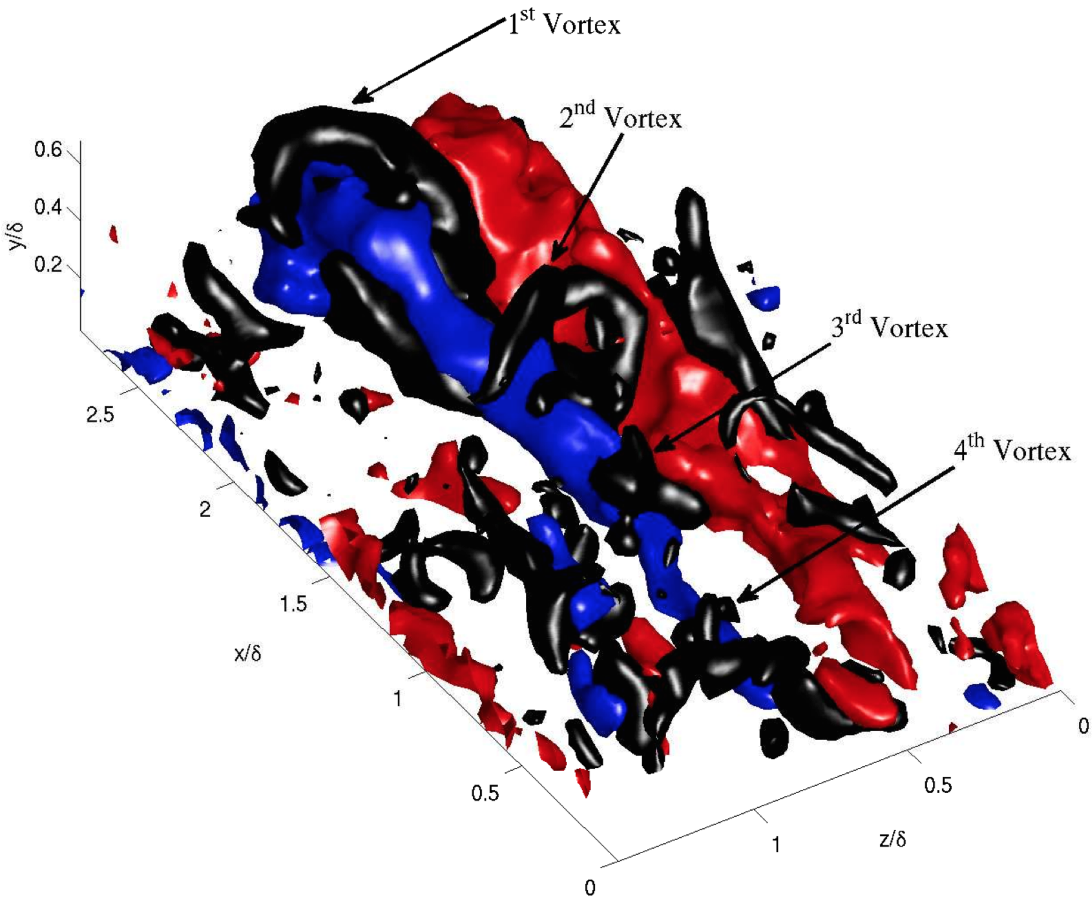

Figure (2.6). Visualisation of vortices with high and low momentum structures (adapted from Dennis 2009). The vortices (black) isosurface appear draped across low momentum structures (blue) more so than high speed structures (red).

at high Reynolds flow persists within a minority of the community, the authors accept that other researchers may wish to interpret the results using a different paradigm.

This review of the form of the coherent structures in wall-bounded flow is based on flat-plate, zero pressure gradient flow visualisation experiments in the laboratory, together with equivalent numerical simulations at low Reynolds number. It is apparent, therefore, that simulations of coherent packets of hairpin vortices do not prove their occurrence, while two-dimensional and quasi-instantaneous three-dimensional flow visualisation methods rely on an assumption of Taylor's Hypothesis (Adrian, 2007). While it is encouraging that the results collected by Dennis and Nickels (2011a) and Dennis and Nickels (2011b) support these seemingly robust models, the caveat on their interpretation serves as a reminder that further observations, particularly in more realistic, natural flows, are essential to understanding these dynamics. Similarly, in such conditions, it is important that individual vortices are recorded without the assumptions of Taylor's Hypothesis. As this thesis aims to offer qualitative and quantitative insight into small-scale turbulence in the ocean, the additional complexity in terms of the boundary layer structure will be highlighted prior to addressing the characteristics of these flows.

2.3 Turbulence in the Sea

In situ measurements of marine bottom boundary layers collected in shallow seas bear some resemblance to their laboratory equivalents, but also exhibit some differences (Hackett et al., 2011). Like the flat-plate conditions detailed earlier, a similar profile of turbulence parameters may be extracted in accordance with the same general (layered) scaling and structure. Such profiles must, however, be modified to account for the effects of surface irregularities, bottom roughness and tidal flows. In addition, in areas where the depth of water is less than $0.16gt_w^2$ (where $g = 9.81$ and t_w is the wave period; Burchard et al. 2008), surface motions penetrate to the bed forming a wave boundary layer. This wave boundary layer is known to be thinner, yet much more turbulent, than its tidal equivalent and the non-linear interactivity between the two serves to further complicate these dynamics.

Under quasi-steady conditions, in tidal flows, a classic velocity profile (consistent with the law of the wall) will form over a plain, solid bed (Burchard et al., 2008). This is supported by measurements by Caldwell and Chriss (1979) that demonstrate that flow speed decreases linearly within the viscous sub-layer, from a value of $\sim 8\,\mathrm{cm\,s^{-1}}$ at 0.6 cm above the water-sediment interface to a value of $\sim 0\,\mathrm{cm\,s^{-1}}$ at the boundary (Thorpe, 2004, 2007). Similarly, above the viscous and the buffer sublayer, the characteristics are consistent with that of the atmospheric boundary layers (Lueck and Lu, 1997, Lien and Sanford, 2000). This velocity profile is well-fitted by a logarithmic expression, adjusted for the inclusion of the roughness length to account for the possible irregularities of the boundary (Caldwell and Chriss, 1979, Thorpe, 2004, 2007):

$$U(z) = (\frac{U_*}{\kappa}) \ln(\frac{z}{z_0}) \tag{2.18}$$

where, κ is the von Karman's constant $= 0.41$ and z_0 is the 'roughness length' (i.e. where $U(z) \to 0$).

Usually, this is felt as form drag, i.e. the stress imposed by such irregularities (Chriss and Caldwell, 1982). Form drag causes a significant difference from conditions typically expected over horizontally homogeneous surfaces, such as the development of multiple log layers (Chriss and Caldwell, 1982). This is consistent with measurements by Sanford and Lien (1999) in the wake of cross-stream orientated ripples with typical heights of 0.3 m and wavelengths of 16 m, where two distinct 'log' layers were seen between 0 m to 3 m and 5 m to 12 m, respectively. Friction velocities in the upper log layer are higher than friction velocities in the lower log layer. Accordingly, total stress in the upper layer is also higher (by a factor of three) than total stress in the lower layer, associated with the effects of form drag (Sanford and Lien, 1999). A similar two-layered structure is also seen in profiles of the Reynolds shear stress, although this is not as identifiable as the velocity equivalent. In these measurements, it is suggested the height of the transition between the upper log layer and the lower log layer 3 m to 5 m will decrease in areas of smoother bottom roughness, as reported by Chriss and Caldwell (1982). In addition, mobile sediment suspended into the water column from the bed can cause density stratification that will attenuate the turbulence in the boundary layer and generate down-slope turbidity currents, further affecting these flows (Burchard et al., 2008, Conley and Inman, 1994).

Other differences are associated with the acceleration and deceleration of tidal flows. Specifically, when the water column is accelerated ($\frac{dU}{dx} > 0$) from $U = 0$ near the wall, the total stress propagates upward, albeit with a height-dependent phase delay after the bed shear stress (Burchard et al., 2008). This is in agreement with the patterns of variability of turbulent energy production and dissipation rates that also propagate upwards (Rippeth et al., 2003). Conversely, when the water column is decelerated ($\frac{dU}{dx} < 0$), an adverse pressure gradient is formed (Pope, 2000). This adverse pressure gradient is seen as an inflection in profiles of turbulence parameters, where it is often associated with high flow instabilities and high turbulence intensities. Similar effects occur where wave and current boundary layers co-exist and subsequently interact. Such conditions have an appearance equivalent to the effects of increased bed roughness, corresponding to increased friction and modified velocity profiles (Burchard et al., 2008). Accordingly, the bed shear stress of a combined wave and current boundary layer is higher than that of an individual layer. This is consistent with measurements by Hackett et al. (2011) at an unstable interface between wave and current boundary layers. Hackett et al. (2011) established that the presence of waves increases the characteristic roughness above that expected by a factor of three, shifting the position of peak turbulence production, dissipation and Reynolds shear stress higher in the water column. The instability at the inflection point (i.e. below the log layer) is synonymous with the occurrence of a large number of small-scale eddies that, in turn, increases the Turbulence Kinetic Energy dissipation at the transition between the inner layer and the outer layer (Figure 2.1) (Hackett et al., 2011). Note, however, that such small-scale eddies are persistent throughout the boundary layer.

The first in situ measurements of the Reynolds shear stress associated with coherent structures were made by Bowden and Fairbairn (1956), using a mechanical current meter. This instrument was able to determine both a wall-normal and an along-stream velocity component, the correlation of which is equal to the Reynolds shear stress, τ. Similar sampling, conducted by Heathershaw (1974) assessed the $\overline{u_1'u_3'}$ trace associated with the near wall sequence of bursts over a range of depths, flow conditions and sediment types. These events were seen to occur in situ with typical timescales of the order of 5 s to 10 s separated by periods of between 20 s and 100 s (Heathershaw, 1974). Like the laboratory flow, the amplitudes of Quadrant 2 and Quadrant 4 events both exceeded that of Quadrant 1 and Quadrant 3 interactivity, with bursts associated with local deceleration and sweeps associated with local acceleration (Heathershaw, 1974). While such point measurements continued to validate these early observations of intermittent momentum transport (cf. Gordon 1974), it was not until recently that submersible flow visualisation instrumentation allowed the corresponding eddy structures to be recorded without the assumption inherent in the interpretation of arrays of multiple sensors. Such data (Bertuccioli et al., 1999, Doron et al., 2001, Nimmo-Smith et al., 2002, 2005) present a 2D cross-section of the bottom boundary layer over a seabed consisting of sand ripples with typical heights of 0.1 m and wavelengths of 0.5 m. Deployments under different tidal conditions allowed a range of combinations to be analyzed. As expected, under a weak wave/current climate the flow is characterized by eddies of less than 2 cm diameter, with no large-scale vortices recorded (Nimmo-Smith et al., 2005). As the current velocity increases, the moderately quiescent conditions are punctuated by eddies of 4 cm in diameter, as well as those of scalings up to 10 cm diameter, occurring intermittently. Such large-scale eddies occur singly or in groups – the latter termed 'gusts' by Nimmo-Smith et al. (2005) – with an along-stream extent in excess of 1 m. These gusts have characteristics similar to hairpin packets identified in laboratory flows, although a classification as such is dependent on the inferences. This likeness is continued in the threshold nature of these events, similar to that suggested by Zhou et al. (1996, 1999) and Adrian et al. (2000b), where large gusts occur in high flow conditions yet are unseen during low flow. In comparable in situ 2D-PIV measurements performed by Hackett et al. (2011), the generation and subsequent dynamics of eddies in the boundary layer was also considered, where these are seen to relate to roughness elements in both position of origin and typical scalings. The number of eddies increases as elevation decreases until the inflection point in the velocity profiles. A transition in size of eddies also occurs, from those of more than 7 cm diameter in the log layer to those of less than 2 cm at the inflection point (Hackett et al., 2011). These in situ deployments reveal that turbulence in the sea is anisotropic (Nimmo-Smith et al., 2002, 2005, Luznik et al., 2006), requiring a fully three-dimensional approach to measurements of turbulence. While development of the necessary three-dimensional flow visualisation system has been completed (Nimmo-Smith, 2008), the opportunities that this system offers in understanding the three-dimensional turbulence characteristics of the bottom boundary layer of the coastal ocean are still to be explored.

Compared to laboratory / idealised flows it is not surprising that additional complexities are to be found in the bottom boundary layers in shallow, tidal seas. While variable flow conditions have been treated independently in the laboratory, it is the combined interaction of the waves and currents, together with the complex nature of mobile bed forms that will affect the mixing near the bed (Burchard et al., 2008, Hackett et al., 2011). Due to difficulties associated with data collection in this environment, available literature on the three-dimensional coherent structures in the sea is scarce, and mainly comprises point-measurements. Recent studies by Nimmo-Smith et al. (2002, 2005), Luznik et al. (2006) and Hackett et al. (2011) offer a two-dimensional cross-section of the flow structure in the bottom boundary layer of the coastal ocean, where turbulence characteristics (e.g. gusts) similar to those of laboratory experiments (e.g. hairpin packets) were seen. However, these cannot inform the full three-dimensional velocity flow field necessary to confirm such a likeness, nor can the cross-stream scales necessary for the understanding of lateral dispersion and anisotropy be accurately obtained. In light of the significance of such coherent structures to transport processes, an in situ understanding of 3D turbulence in natural flows is essential for the accurate parameterisation and subsequent validation of numerical models of the marine environment. Therefore, it is this understanding of the three-dimensional turbulence characteristics of the bottom boundary layer of the coastal ocean that the present thesis explores.

Chapter 3

Methods

3.1 Introduction

Ocean flows have traditionally been sampled using a multiplicity of methods spanning a one-, two- or three-dimensional domain in space/time (Chapter 2). However, these miss at least one spatial dimension, requiring assumptions to be made to quantify turbulence statistics. In the present chapter, the specific methods used to address the aim of the thesis, as well as some of the limitations identified earlier, are discussed. To do so, commercially-available Acoustic Döppler sensors (e.g. ADCP and ADV) are used to supplement the inherently four-dimensional data that was collected by a unique submersible three-dimensional time-resolved Particle Tracking Velocimetry (3D-PTV) system that was developed recently (Nimmo-Smith, 2008). 3D-PTV is a robust method for the visualisation of coherent structures, and has been used in the laboratory to study the boundary layer of free-surface flow and the characteristics of grid turbulence (Virant and Dracos, 1997, Ott and Mann, 2000). The method uses multiple synchronous cameras to view a sample volume from different angles, wherein particles are located and tracked in three dimensions, allowing the full velocity flow field to be determined.

Velocity measurements were made in the bottom boundary layer of a tidal flow. All underwater instrumentation were mounted on a rigid frame that allows simple adjustment of their position (Figure 3.1). A vane attached to the frame align it at an angle to the mean flow direction as it is lowered to the sea-bed, to prevent contamination of the sample volume from the wake of the 3D-PTV system. Using the long-term mean over the 20 min time-series, the data were then rotated in processing, such that x_1 is aligned with the along-stream velocity component, $\langle u_1 \rangle$, x_2 is aligned with the cross-stream velocity component, $\langle u_2 \rangle$, and x_3 is aligned (positive upward) with the wall-normal velocity component, $\langle u_3 \rangle$. This is achieved by minimising $\langle u_2 \rangle$ and $\langle u_3 \rangle$. Within this frame of reference, the zero-mean velocity (turbulence) of the flow, u_i', is established using Reynolds' Decomposition, i.e.:

$$u_i' \equiv u_i - \langle u_i \rangle \tag{3.1}$$

where, $\langle u_i \rangle$ is the mean of the velocity component i (discussed in §3.5.3).

The ADCP, ADV and 3D-PTV instrumentation that were used are discussed in connection with their data processing in §3.2, §3.3 and §3.4, and the characteristics of the data sets that will be examined in subsequent chapters are summarised in §3.5.

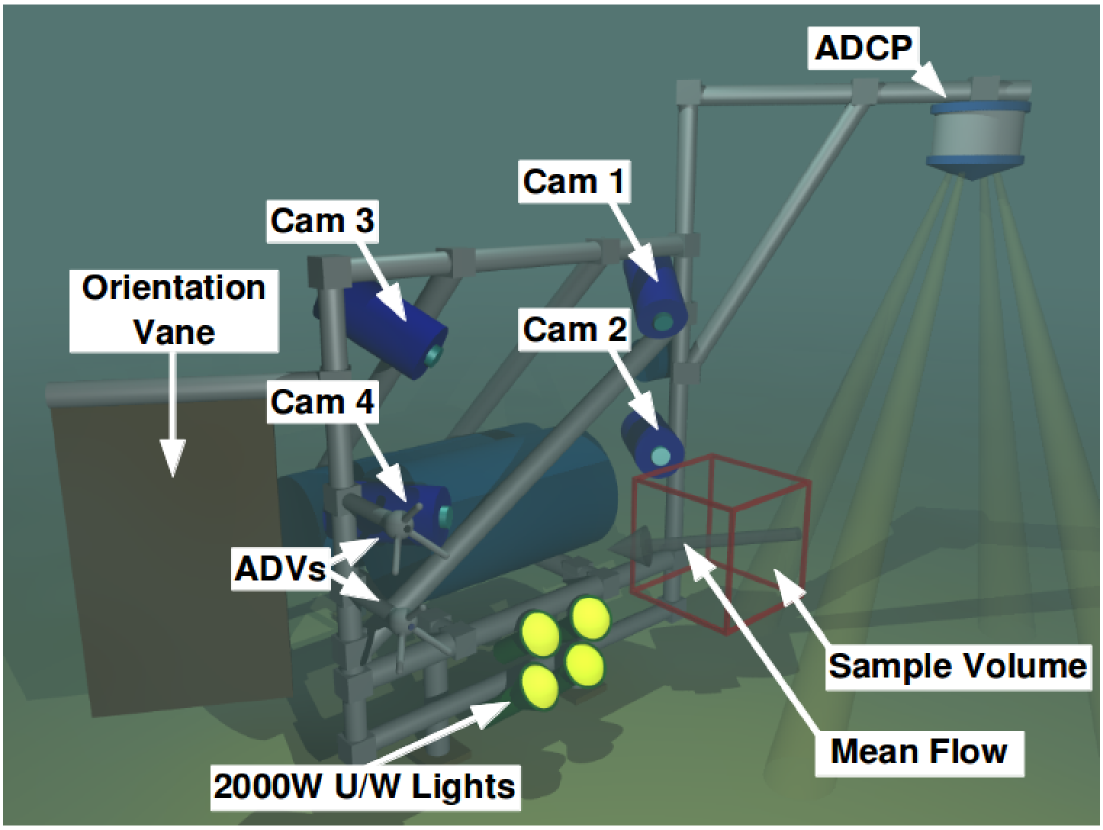

Figure (3.1). Illustration of the submersible 3D-PTV system, ADCP and ADV (after Nimmo-Smith (2007)).

3.2 ADCP

3.2.1 Instrumentation

An ADCP is a three-dimensional, remote-sensing, monostatic system offering velocity measurements at a high sampling rate at multiple points along a single profile of the water column. The system consists of four transducers, set in a convex arrangement inclined 20 ° from vertical, that emit a sound pulse at a fixed frequency and listen to echoes returning from scatterers in the water column. The pulse-coherence and the Döppler frequency shift are used in obtaining the three velocity components. To do so, the along-beam component is recorded along each beam axis and these are then combined to give orthogonal measurements using a transformation matrix.

In the present study, two ADCPs were used in obtaining the background flow conditions. A 600 kHz downward-looking ADCP (operated in Mode 12) was mounted on a pole on the surface support vessel, providing a velocity profile between the sea-bed and the sea-surface, with a vertical bin separation of 0.50 m and a sampling frequency of 2 Hz. A complementary 1200 kHz downward-looking ADCP (operated in Mode 11) was mounted on the underwater frame 0.50 m upstream of the 3D-PTV sample volume, providing a velocity profile between 0.25 m and 1.25 m above the sea-bed, with a vertical bin separation of 0.02 m and a sampling frequency of 2 Hz.

3.2.2 Data processing

The four transducers on an ADCP offers redundancy in the computation of the three-dimensional velocity recorded by the system. This redundancy is utilised internally to establish the data quality. Velocity measurements of insufficient data quality are identified by the manufacturer-supplied ADCP processing software, and these are subsequently eliminated.

3.3 ADV

3.3.1 Instrumentation

An ADV is a three-dimensional, remote-sensing, bistatic system offering velocity measurements at a high sampling rate at single points (i.e. a single 1.49 cm^3 sample volume, 15 cm from the sensors). The system consists of one transmitter and three (separate) receivers that work on the basis of the pulse-coherence and the Döppler frequency shift, similar to an ADCP.

In the present study, one ADV was mounted on the underwater frame adjacent to, but 0.50 m downstream of, the 3D-PTV sample volume. The ADV was used during sampling to monitor the orientation of the system to the mean flow direction in real-time to ensure the underwater instrumentation did not interfere with the flow structures, as well as providing auxiliary velocity measurements and turbulence statistics used in later analysis. Therefore, triggering of the ADV was synchronous with the 3D-PTV system, at a sampling frequency of 25 Hz. To limit the effects of the hardware on velocity measurements, the nominal range of the ADV was set to $100 \pm 1\,\mathrm{cm\,s^{-1}}$ to be able to resolve a maximum vertical velocity of $60\,\mathrm{cm\,s^{-1}}$ and a maximum horizontal velocity of $210\,\mathrm{cm\,s^{-1}}$.

3.3.2 Data processing

ADV measurements represent the joint effects of flow velocity, as ambiguous data generated by air bubbles, Döppler noise, and the flow rate exceeding the nominal range of the system (Volguaris and Trowbridge, 1998). Such ambiguous data are connected with spiking and aliasing, and must be eliminated to prevent the contamination of turbulence statistics.

3.3.2.1 Despiking

Ambiguous data connected with spiking is characterised by a deviation from the local velocity trend that, uncorrected, will bias flow quantities. The difficulty is that this spiking is qualitatively similar to turbulence; a fact that complicates

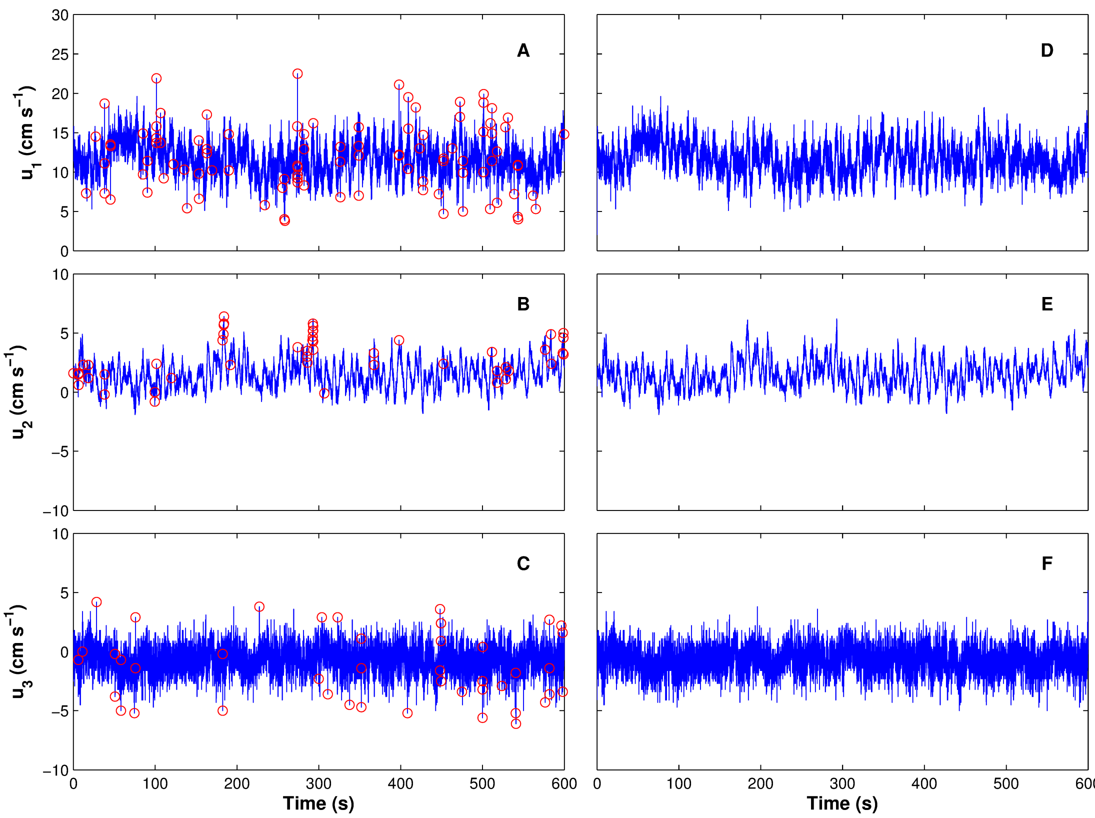

Figure (3.2). (A) ADV velocity time-series with spikes identified. (B) The corresponding clean signal after despiking with the phase space method.

its detection (Figure 3.2). Therefore, several despiking methods have been proposed, from using signal coherence parameters to using low-pass filtering, moving-averaging or acceleration criteria.

Traditionally, manufacturer-recommended data processing methods suggest the ADV phase correlation (COR) and signal-to-noise ratio (SnR) parameters allows the ambiguous data to be identified where the instantaneous velocity measurements of COR < 70 % and SnR < 20 dB. However, Mori et al. (2007) established that such noise occurs randomly across the full velocity range and, contrary to common belief, exhibit no correlation with the COR and SnR data and therefore phase-space methods are preferred.

Used for their accuracy, efficiency and lack of empirical tuning parameters, such phase-space methods were originally developed by Goring and Nikora (2002) and modified in three-dimensions by Wahl (2003). These apply a three-dimensional Poincaré map, where the zero-mean velocity, u_i', is plotted against its derivatives, $\Delta u_i'$ and $\Delta^2 u_i'$. To illustrate this, ADV data in Figure 3.2A are plotted in phase-space in Figure 3.3. The valid data are clustered within an ellipsoid, whose shape and size are determined by the standard deviation of u_i', $\Delta u_i'$ and $\Delta^2 u_i'$, as well as a universal parameter, λ_U, determined by the length of the velocity time-series (Donoho and Johnstone, 1994). Ambiguous data connected with spiking are those points that plot outside the ellipsoid. This separation is exaggerated for the derivatives, as differentiation accentuates the high-frequency components (Graham, 2010). Despiking is completed after an iterative process, where the quantity of valid data in all three velocity components asymptotes. Since the ADV data are recorded along each beam axis and converted into orthogonal co-ordinates, these are not independent such that one affected beam will bias all three velocity components. Therefore, the equivalent data are eliminated in the other velocity components, whether or not they contain identified spiking.

To illustrate the effectiveness of phase-space methods over manufacturer-recommended data processing, ADV data in Figure 3.2 – processed using the COR, SnR and phase-space methods – are presented in Table 3.1. Here, 1.01 % of the velocity time-series consists of spiking identified in phase-space, while all meet the COR criteria and 92.31 % fail to meet the SnR criteria. It is apparent that filtering using the COR and SnR criteria are inadequate at providing reliable despiking and so are avoided.

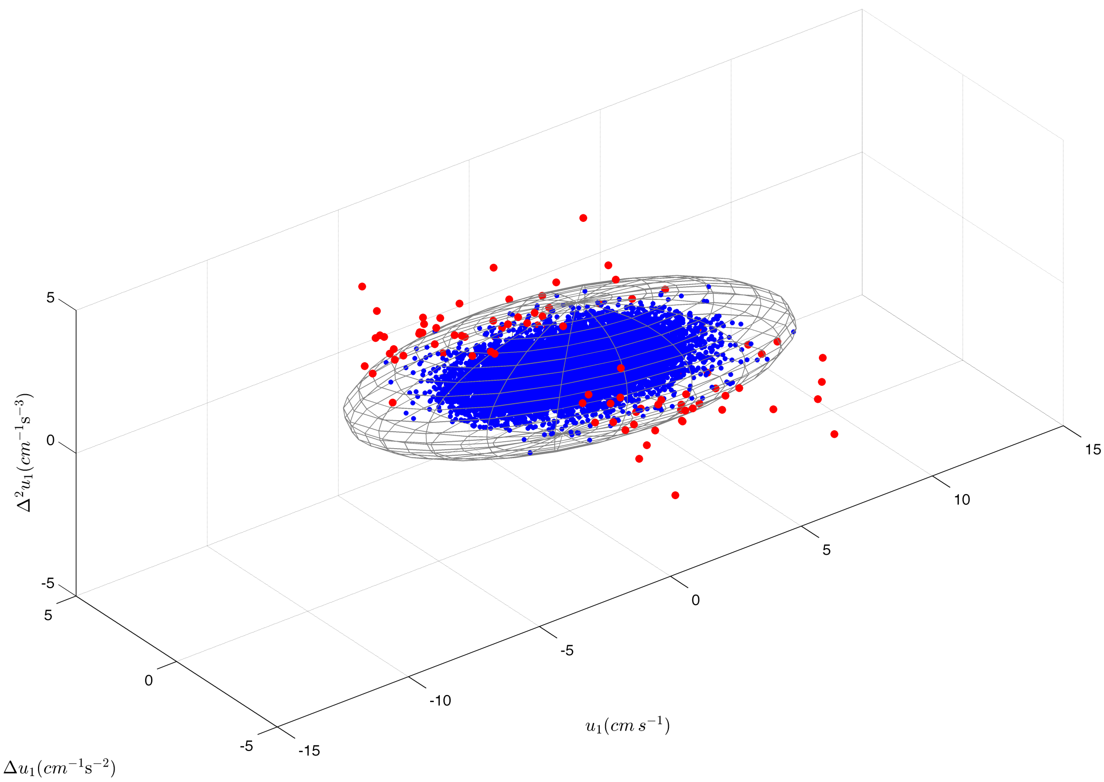

Figure (3.3). Example of phase-space analysis of ADV data for the along-stream velocity component.

	U_1	U_2	U_3	samples
Phase-Space	120	112	71	29999
COR Criteria	0	0	0	29999
SnR Criteria	1930	24159	1602	29999

Table (3.1). Comparison of phase-space spike detection with those identified with reference to quality indicators (Correlation and SnR) less than manufacturers recommended thresholds.

3.3.2.2 Spike replacement

Regardless of how spiking was detected it is essential that data eliminated *is* refilled to preserve the temporal characteristics of the signal, as well as being necessary in using iterative phase-space methods. This replacement is essentially an arbitrary process with several methods available, none with any more validity than any other. What is critical, however, is that spike replacement does not add any additional spiking. Therefore, in the present study, a cubic polynomial interpolation across the affected area (consistent with Mori et al. 2007) is used.

3.3.2.3 Denoising

Similar to spiking, aliasing of Döppler noise will also bias flow quantities. This aliasing is characterised by a folding of the signal from a higher frequency to a lower frequency, and rectified by low-pass filtering the velocity time-series to eliminate any signal components exceeding the Nyquist frequency. As this Döppler noise occurs randomly, is non-biased and Gaussian (Graham, 2010), the aliasing effects are eliminated by low-pass filtering the velocity data using a Gaussian smoothing function (Biron et al., 1995), i.e.:

$$R(t) = (2\pi\sigma^2)\exp\left(\frac{-t^2}{2\sigma^2}\right) \tag{3.2}$$

where, σ is the standard deviation of the normal curve, with a half-power frequency (f_{50}) equalling $f_s/6$:

$$\sigma = \left(\frac{\ln 0.5^{0.5}}{-2\pi^2 f_{50}^2}\right)^{0.5} \tag{3.3}$$

To illustrate the loss of these higher frequency components, the power-spectra of the raw velocity time-series (Figure 3.2) and the results of the Gaussian low-pass filtering are compared in Figure 3.4. The raw velocity data exhibit a noise floor between $5\,\mathrm{m}^{-1}$ to $10\,\mathrm{m}^{-1}$. Filtering removes a significant proportion of the

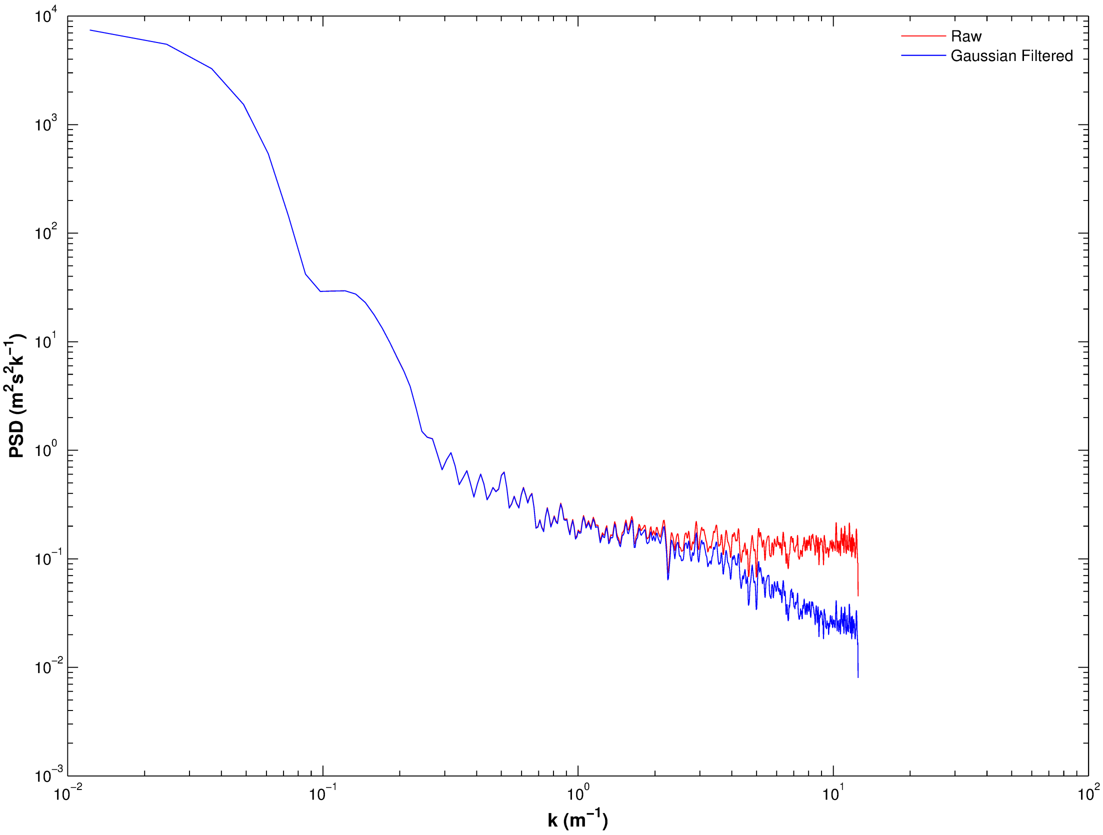

Figure (3.4). Power spectral density (PSD) of the raw (red) and the Gaussian low-pass filtered (blue) ADV time-series.

noise in the raw signal, allowing better visualisation of the characteristic $k^{-5/3}$ slope.

Graham (2010) established the order that despiking and denoising are applied have no impact on the total change these processes impart on the results. Note that while, in the present study, these specific despiking and denoising methods (applied in that order) are used, there is currently no firm agreement on standard ADV data handling protocols within the community (Graham, 2010).

3.4 PTV

3.4.1 Instrumentation

The submersible 3D-PTV system used in the present study was developed by Nimmo-Smith (2008) at the University of Plymouth (Plymouth, UK). The system consists of four 1004×1002 pixel, 30 frame/s, 8 bit digital cameras with 9 mm lenses that view a $20 \times 20 \times 20\,\mathrm{cm}^3$ sample volume. Naturally-occurring suspended particles are used as tracers. An aperture of $f/9$ allows sufficient depth-of-field for the suspended particles to be in-focus within the sample volume, while an exposure of 2.5 ms allows these to be recorded blur-free in a mean flow of up to $20\,\mathrm{cm\,s^{-1}}$ (determined by the specifications of the cameras, the sampling rate and the seeding density of the particles). Illumination of the sample volume is necessary to account for the natural tracers, small aperture and short exposure that are used, and this is yielded by four 500 W underwater lights. Since the submersible 3D-PTV system is deployed in moving water, at an angle to the mean flow, convection generated by these underwater lights is minimal.

Electrical power is supplied from a surface support vessel by a 50 m umbilical cable. The umbilical cable also allows communication by RS422 – as well as an Ethernet connection – to the 3D-PTV master computer, that synchronises triggering of the cameras at a rate of 25 Hz. Data from each of these cameras is transmitted by a 2 m IEEE-1394 Firewire cable to four acquisition computers, each with 2×400 GB of SATA hard disk storage (3.2 TB total). Commercially available mini-ITX computers are used for their convenience, cost and size. The 3D-PTV master and four acquisition computers run a Linux OS, that allows sampling to be administered remotely by special acquisition software. A real-time kernel synchronises the processes, with a maximum jitter of $5\,\mu$s.

All underwater components are mounted such that the light scattering from the suspended particles is maximised, while the illumination of the sea-bed is minimised to increase the signal-to-noise ratio (SnR). The common volumes between the cameras and the lights is also minimised to limit contamination from unfocussed particles, as shown in Figure 3.1.

3.4.2 Calibration

The calibration of the 3D-PTV system is necessary to relate the exposures from the four independent cameras such that the three-dimensional position of the particles is yielded. This is done in situ, just before sampling, using a moving single-point target ($1 \times 3\,\mathrm{mm}\ \varnothing$ Light Emitting Diode, LED) and self-calibration methods (Svoboda et al., 2005). Here, movement of the LED within the 3D-PTV sample volume is recorded by the cameras. After the position of this single-point target is extracted, an iterative process of target pairing, verification, projection, non-linear distortion estimation and re-projection is used for the refinement of the calibration (until re-projection errors of less than 0.35 pixel are attained). Finally, measurements between cameras are used to align the calibration with a physical coordinate system. The scaling and the alignment of the sample volume are verified using a moving two-point target and static three-point target. A sequence of more than 500 tracers, with good coverage of the sample volume, allows high-quality calibration and can also account for the refraction that occurs within images (Nimmo-Smith, 2008).

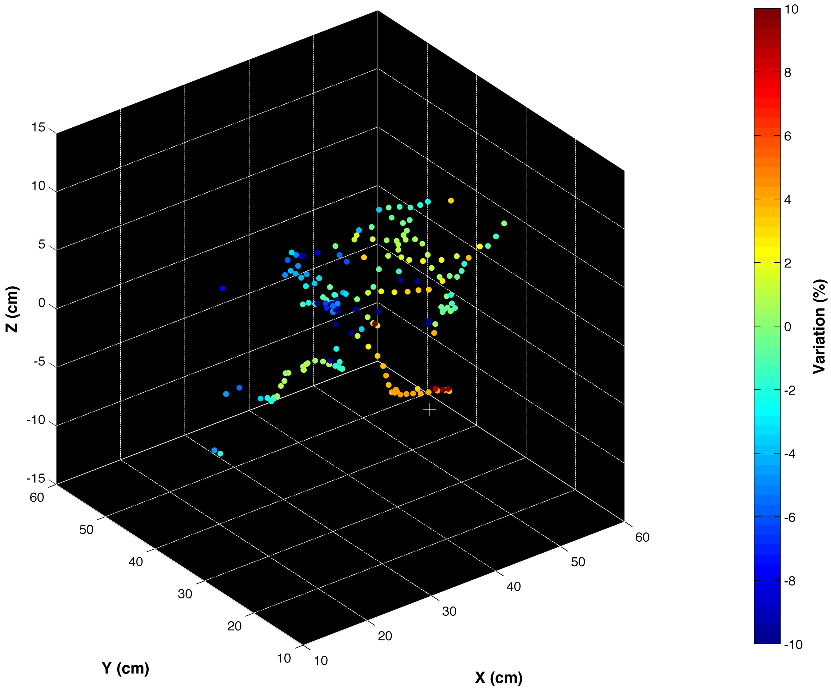

Figure (3.5). Verification of the calibration procedure, showing three-dimensional views of the distribution of scale check-point within the sample volume, shaded by variation.

The calibration of the 3D-PTV system is assessed every time it is deployed. To do so, the movement of a reference target (that consists of $2 \times 3\,\mathrm{mm}$ ⌀ LEDs, with a fixed separation of $50\,\mathrm{mm}$ between them) is recorded by the cameras. The Particle Tracking Velocimetry software (§3.4.3), and the output from the single-point target calibration, are used to extract the three-dimensional coordinates of the reference target and their separation, s, is determined. The pattern of the variation of this separation is presented in Figure 3.5. While the calibration results in an accurate scaling of the reference target (where $53.76\,\%$ of points exhibit $< 2.5\,\%$ variation), $18.50\,\%$ of points exhibit $> 5.0\,\%$ variation from the true separation ($s = 50\,\mathrm{mm}$). These points are randomly scattered within the sample volume and, as such, are resistant to a correction based on the output from the two-point target data.

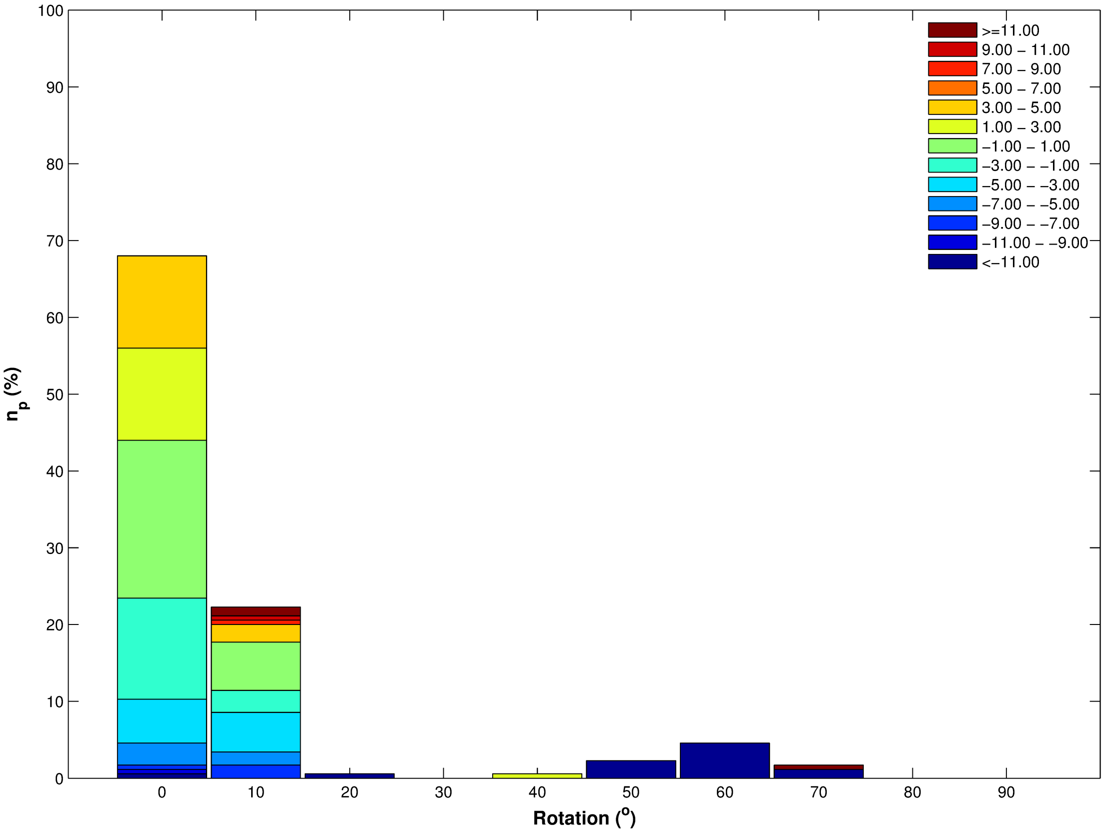

Figure (3.6). Frequency distribution of the orientation of the system to the two LEDs, by angle (from parallel to perpendicular), shaded by the variation.

To reconcile adjacent points exhibiting a different variation from each other, the orientation of the system to the two LEDs must be considered. This is necessary as an LED is not a point light source, meaning that any preferred orientation will impact on the detection of the centroid and, subsequently, on the separation determined. Based on the dimensions of the target and the diameters of the LEDs, such mis-detection can account for up to 6 % variation from the true separation ($s = 50$ mm).

Figure 3.6 presents a frequency distribution of the orientation of the system to the two LEDs, by angle (from parallel to perpendicular), and shaded by the variation, s. Despite the high degree of scatter within the data, it is apparent that this increase of angle is accompanied by an increase of s, as confirmed by an

$r^2 = 0.5631$. Such artefacts have long been a persistent issue in image processing (Davies, 2013), requiring that action must be taken in data processing (§3.4.3) and data post-processing (§3.4.4) to mitigate against these effects.

3.4.3 Data processing

Data processing is completed in three stages using the special "Particle Tracking Velocimetry" software developed by Maas et al. (1993) and Willneff (2003). Here, particles are identified within the exposures from the four cameras by high-pass filtering, segmentation and weighted-centroid methods. In addition, maximum and minimum size criteria are used to limit contamination by noise or large objects. The calibration parameters are then used to relate the exposures from the four independent cameras, such that the three-dimensional positions of the particles are yielded. Finally, tracking of the particles is done in both image- and object-space, running the sequence in both directions so that linkages between adjacent frames are maximised.

The new spatial-temporal tracking algorithm enhances tracking efficiency, permitting higher seed densities and longer trajectories, even in complex turbulence. Redundant tracking data, in both image- and object-space, as well as estimates of the position of the particles, are used to limit any ambiguities. This tracking algorithm is dependent on several parameters. Minimum and maximum velocity criteria are used to define a search area, limited by a permissible acceleration and angle. In cases of ambiguities, the particles with the smallest acceleration are selected. Under optimum laboratory conditions, the 3D-PTV system can track more than 1000 particles concurrently. These are located within the sample volume to within 0.25 mm, limited by the irregularities of the particles and the specifications of the cameras.

While static parameters are adequate with a steady flow, unsteady flow (e.g. from wave motion) causes these to be exceeded, giving poor results. Where the amplitude of the unsteady flow is comparable to (or more than) that of the mean flow, it is essential that dynamic parameters are used. The necessary adjustment of the tracking software to update parameters with a velocity time-series was developed by Nimmo-Smith (2008).

To limit the jitter arising from imaging errors, the position of the particles at each time-step, t, is determined by low-pass filtering the position data, x_i, using a moving cubic spline:

$$x_i(t) = c_{i,0} + c_{i,1}t + c_{i,2}t^2 + c_{i,3}t^3 \tag{3.4}$$

The constants of Equation 3.4 are fitted to 7 points along the trajectories at each time step, from $t-3$ to $t+3$. After filtering, the velocity, u_i is determined by differentiation of Equation 3.4:

$$u_i(t) = c_{i,0} + c_{i,1}t + c_{i,2}t^2 \tag{3.5}$$

The mean of the three velocity components are used to rotate the coordinate system such that x_1 is aligned with the along-stream component of velocity, $\langle \overline{u}_1 \rangle$, x_2 is aligned with the cross-stream component of velocity, $\langle \overline{u}_2 \rangle$, and x_3 is aligned (positive upward) with the vertical component of velocity, $\langle \overline{u}_3 \rangle$.

Figure 3.7 presents an instantaneous sample of 150 particles tracked by the 3D-PTV system. Here, some of the particles are tracked over more than 60

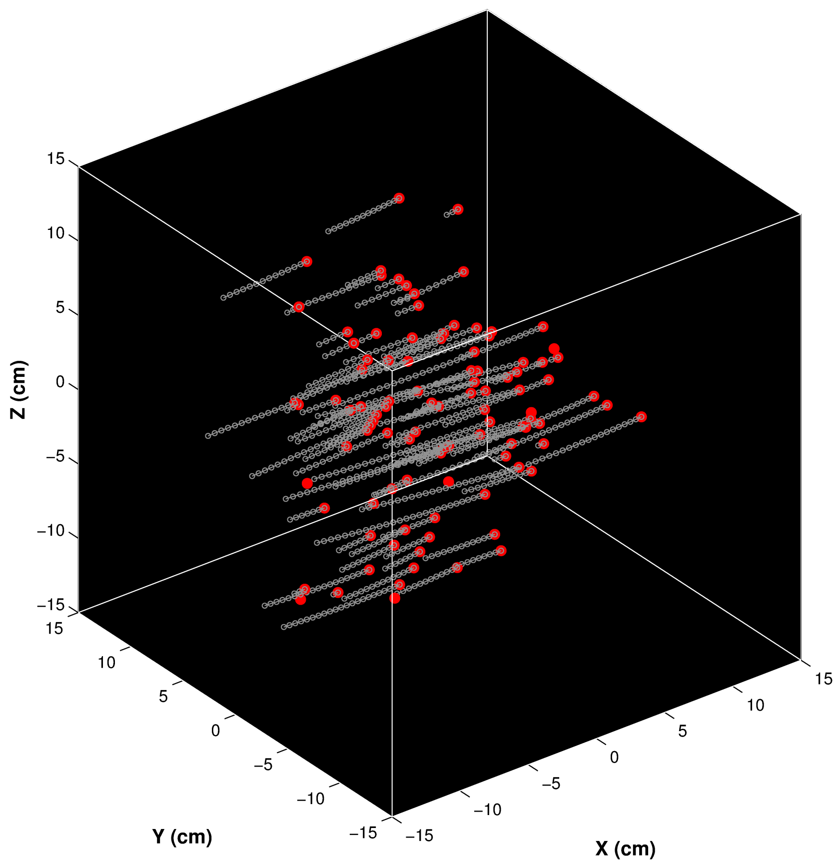

Figure (3.7). Instantaneous three-dimensional distribution of suspended particles as they are tracked by the 3D-PTV system (red dots). The grey tail behind each particle shows its location in the preceding time steps.

frames ($> 2.4\,\mathrm{s}$) as they are carried by the mean tidal flow, weak wave motion and turbulence. Typically, 100 particles survive the low-pass filtering at each time step and are used in obtaining an instantaneous velocity flow field. An example sequence of the three-dimensional instantaneous velocity flow field (of frames up to, and that includes, Figure 3.7) is seen in Figure 3.8. The instantaneous mean velocity, $\langle \overline{u}_i \rangle$, is subtracted from each of these vectors to reveal turbulence structures. This large ($10\,\mathrm{cm}\ \varnothing$) vortex, advected through the sample volume at $10\ \mathrm{cm\,s^{-1}}$, is consistent with the two-dimensional data presented by Nimmo-Smith et al. (2005). Therefore, these visualisations will allow the full three-dimensional

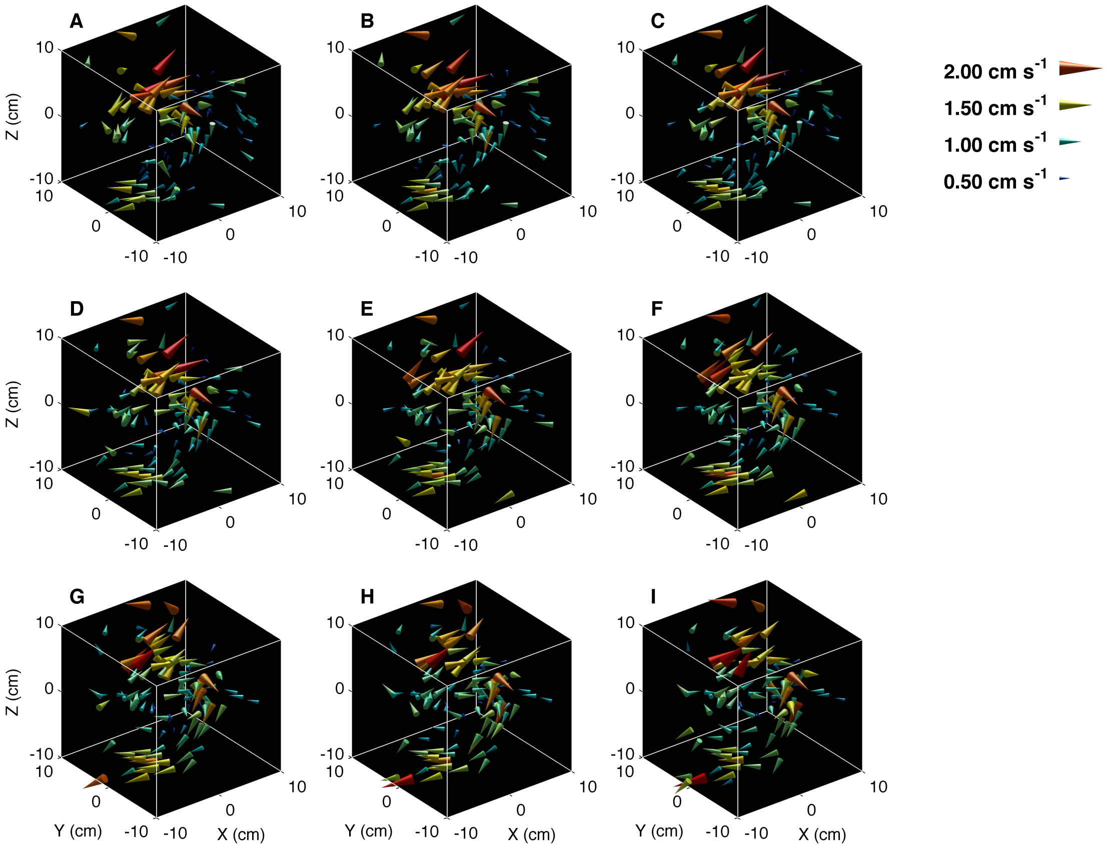

Figure (3.8). Time-sequence of instantaneous distributions of the three-dimensional velocity structure at intervals of 0.04 s. The sample volume mean velocity components have been subtracted from each vector. Vectors are coloured and scaled by the velocity magnitude. The reference vectors in the upper left of the frame are for u=2.0 cm s^{-1}, 1.5 cm s^{-1}, 1.0 cm s^{-1} and 0.5 cm s^{-1}. The mean flow is in the direction of the x-axis.

form of similar coherent structures to be examined.

3.4.4 Data post-processing[1]

The noise and gaps present in experimental measurements typically affects the accuracy of the data collected (Westerweel, 1994, Raffel et al., 2007). The noise arises from errors connected with the characteristics of the particles and their representation in the images (Hart, 2000). A low seeding density complicates these issues, as well as any subsequent analysis (Cenedese and Querzoli, 1997, 2000, Stanislas et al., 2004).

In recent years, several methods have been developed for the denoising and restoration of such data; exploiting the statistical or the physical characteristics of the velocity flow field.

In statistical methods, individual vectors that depart from the ensemble of the recorded velocity flow field are identified and subsequently eliminated. Such data post-processing commonly consists of using global-mean, local-mean or local-median tests or using global histogram operators (Westerweel and Scarano, 2005, Raffel et al., 2007, Duncan et al., 2010). Here, it is assumed that locally-occurring errors are randomly scattered within the sample volume, and that a sufficient quantity of tracers are present for the outliers to be detected. These methods are used for their convenience, computational cost and ease of implementation.

[1]This material is adapted from: A. Vlasenko, E.C.C. Steele and W.A.M. Nimmo-Smith (2015). A physics-enabled flow restoration algorithm for sparse PIV and PTV measurements, *Measurement Science & Technology*, 26, 065301 (23pp). The algorithm was developed by A.V. and was applied to 3D-PTV by E.C.C.S. The text of the paper was jointly authored by A.V. and E.C.C.S and included as Appendix 1.

However, only individual vectors are eliminated and not the noise that exists homogeneously within the sample volume.

Concomitant issues relate to infilling gaps in experimental measurements, and are tackled after statistical denoising. The restoration of 'gappy' data commonly consists of using different types of interpolation, e.g. kriging, nearest neighbour or polynomial interpolation from linear to nth order (cf. Stuer and Blaser 2000). Similarly, methods that employ Proper Orthogonal Decomposition have gained popularity, remaining cost efficient while still being applicable to any type of flow (Venturi and Karniadakis, 2004, Gunes and Rist, 2008). These exhibit good restoration capabilities where the sparsity of these data are 50 %, but the performance decreases as the sparsity of the data approaches 20 %.

In physical methods, hydrodynamical equations, e.g. Navier-Stokes (NSE) or Vorticity Transport Equations (VTE), are used for the restoration of noisy *and* gappy data. Typically, this is achieved by fitting numerical pre-estimates of the (same) velocity flow field to data collected from experimental measurements using Kalman filtering (Suzuki, 2012) or variational methods (Okuno et al., 2000, Suzuki et al., 2009a,b), such that they are similar. Since the velocity data from these schemes are determined from the results of the numerical hydrodynamical model, the results of the restoration are physically-plausible yet are not limited by the occurrence of noise or the sparsity of the data. However, this is only feasible where numerical pre-estimates of the velocity flow field are possible (i.e. where boundary and initial conditions are known *a priori*).

Contrary to methods using numerical pre-estimates, Sciacchitano et al. (2012) suggested deriving boundary conditions directly from experimental measurements, that are then used to infill gappy data in a physically-plausible way. However, this is very sensitive to noise (Sciacchitano et al., 2012).

All these methods are able to be used for the denoising and restoration of experimental measurements within the context of a well-prepared laboratory set-up, where no unsuitable particles are present and tracers with known light scattering characteristics are selected and seeded in the velocity flow field. Tuning laboratory settings (e.g. by optimising the concentration / size of the particles tracked) results in the permissible level of gaps and noise that allows successful restoration using existing methods. Even if gaps and noise cannot be sufficiently reduced, the laboratory set-up offers enough details that numerical pre-estimates are possible, as the boundary conditions or the pattern of the velocity flow field are known *a priori*. However, in several cases, it is not possible for these gaps and noise to be sufficiently reduced nor any pre-estimates to be made. An example of this is seen in PIV and PTV measurements in ocean flows (Nimmo-Smith et al., 2002, 2005, Nimmo-Smith, 2008) where the arrangement of usual experimental conditions using ideal tracers is not possible and naturally-occurring suspended particles are used instead. The uneven shape of these particles, scattered inhomogeneously within the velocity flow field, causes an increase in the occurrence of gaps and noise that, in turn, complicates any later analysis. In addition, as only the part of the ocean advected through the sample volume are recorded, the boundary conditions are unknown and numerical pre-estimates are not feasible. Therefore, restoration of such data with existing methods is debatable; requiring the development of a new Physics-Enabled Flow Restoration Algorithm (PEFRA) for these velocity measurements (Vlasenko, Steele, and Nimmo-Smith, 2015). This is founded on a hydrodynamical basis, as represented by the Vorticity Transport Equation (VTE), however it is independent of specified boundary conditions and the algorithm exhibits a weak sensitivity to noise, as confirmed by tests using both artificial / numerical and in situ experimental data.

PEFRA is from the same pedigree as the Physically-Consistent and Efficient Variational Denoising (PCEVD) algorithm developed by Vlasenko and Schnorr (2010), but with a significant improvement that allows restoration of gappy and noisy data. Both methods conform to a black box philosophy, requiring no specific user-background in fluid dynamics (except in special cases) and may be applied to any velocity time-series, formed from any type of flow and corrupted by any type of noise. However, PCEVD is limited in the sparsity permitted, especially under turbulence. This failing is corrected in PEFRA, and confirmed by the restoration of a velocity flow field with only 10% of data available.

Following data processing (§3.4.3), the experimental measurements are projected from an irregular grid onto a regular grid, where only the nearest neighbour of each of the detected particles are filled by interpolation (and all others set to zero) to minimise noise that arises from gridding. Similarly, if the distance, D, between each of the particles and the nearest grid node exceeds $0.5\sqrt{h_x^2 + h_y^2 + h_z^2}$ (where, h_x, h_y and h_z are the spatial discretization in X, Y and Z, respectively), these grid-points are set to zero also. Note that this algorithm is therefore adaptable to processor speed and memory such that, in theory, at an infinite resolution, all the particles will fall on the grid exactly.

The quality of the subsequent restoration is assessed using the normalized root-mean square error, Δ_n, and the mean angle deviation, θ. Since the in-situ velocity flow field has an arbitrary turbulent pattern and the PIV or PTV instrumentation is directionally independent, it is assumed that the noise has zero-mean and its level in these experimental measurements is at least twice as small as the level of the signal. In these cases, the variation between the root-mean-square difference of the noisy and the true flow is not greater than 12% and may be considered as approximately equal.

Consistent with past in situ 2D-PIV measurements (Nimmo-Smith et al., 2002, 2005), a variety of different conditions were recorded, as characterised by different turbulence strengths ($I = \sqrt{u^2 + v^2 + w^2}$). Here, the restoration of two different conditions – corresponding to the 5th ($I = 0.6065\,\mathrm{cm\,s^{-1}}$) and the 85th ($I = 1.0929\,\mathrm{cm\,s^{-1}}$) percentile of the turbulence strengths during an example 10 min time-series – are discussed. The sparsity of these flows are 2.14 % and 1.95 % while their characteristic lengths are 9 and 8 grid-points, in turn. Therefore, following Vlasenko et al. (2015), the critical sparsity equals 1.09 % where $I = 0.6065\,\mathrm{cm\,s^{-1}}$ and 1.56 % where $I = 1.0929\,\mathrm{cm\,s^{-1}}$. Since the sparsity of these data exceeds the critical sparsity condition, it is expected that a successful restoration is possible.

Three orthogonal cross-sections of these flows are presented in Figure 3.9A to Figure 3.9C and Figure 3.9D to Figure 3.9F. The vectors corresponding to the PEFRA input (red) and the PEFRA output (black) are overlapped to illustrate the adjustment made. The projection of the convex hull of the tracked particles, representing the area where data were recorded, is shaded white. The subsequent restoration of these data culminates in the vorticity iso-surfaces presented in Figure 3.10A and Figure 3.10B. Qualitatively, Figure 3.10A exhibits small velocity gradients typical of a low turbulence level and Figure 3.10B is consistent with that

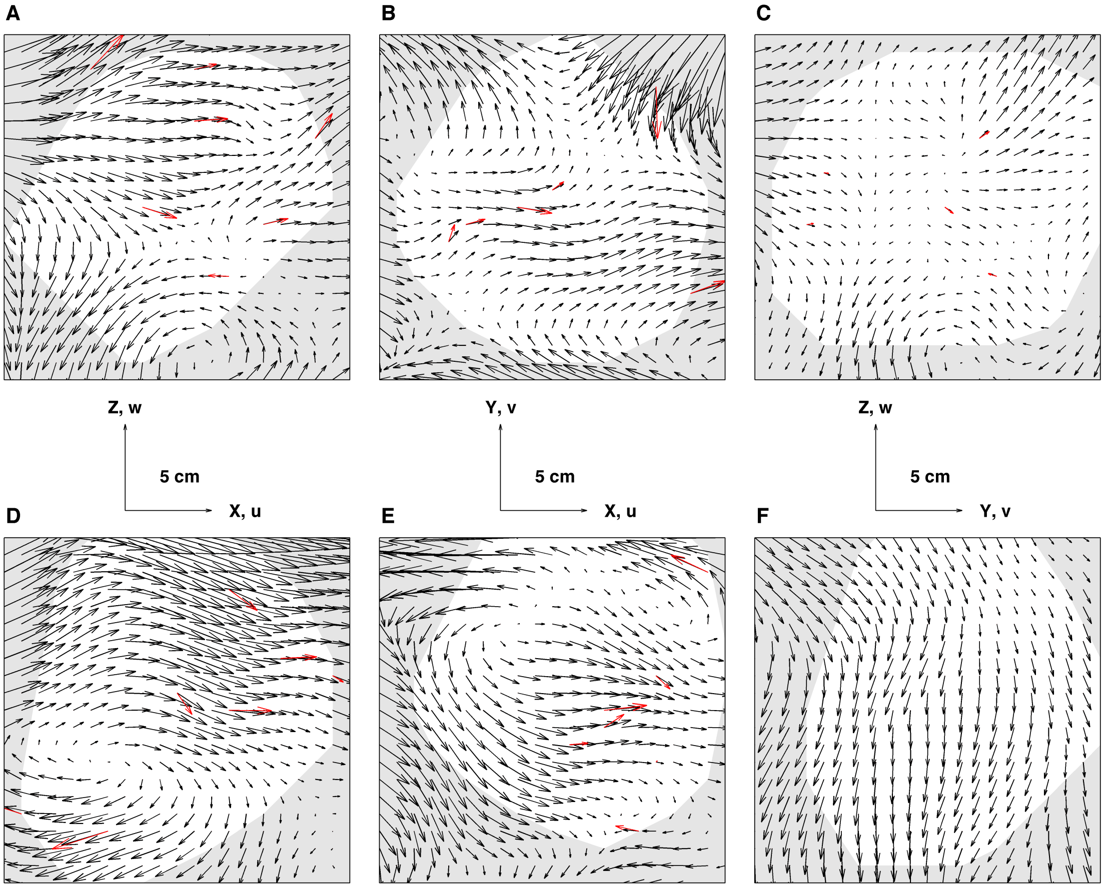

Figure (3.9). Row 1: cross-section of the velocity flow field corresponding to the minimum turbulence intensities recorded. Row 2: cross-section of the velocity flow field corresponding to the maximum turbulence intensities recorded. In each case, the orientation of the slices are indicated by the axes. The 3D-PTV measurements (red) and post-restoration velocity distribution (black) are overlapped. The projection of the convex hull of the tracked particles is shaded white.

expected of a higher turbulence level. While these cannot themselves confirm a correct restoration, the excellent agreement between the PEFRA input and the PEFRA output for the two different conditions, as well as that of the coherent structures and the turbulence level (Adrian, 2007), implies the physics of these flows have been successfully restored. Specific details of the restoration of Figure

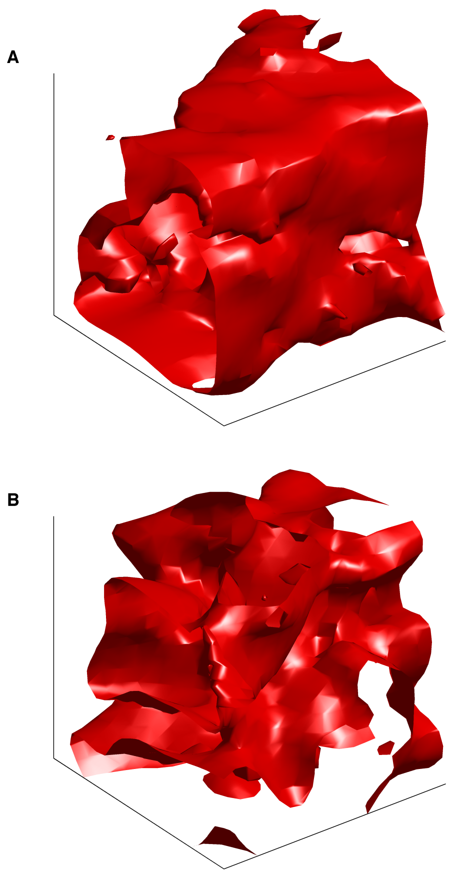

Figure (3.10). Vorticity iso-surfaces of the PEFRA output for the two conditions presented in Figure 3.9.

3.10A and Figure 3.10B are quantified below.

Figure 3.11 presents an instantaneous velocity flow field where $I = 0.6065\,\mathrm{cm\,s^{-1}}$. Here, 79 particles output by the tracking software survived filtering by moving cubic spline (Figure 3.11A). For the grid used ($h_x = h_y = h_z = 1\,\mathrm{cm}$), $D > 0.87\,\mathrm{cm}$ at one of these grid-points (red '+' markers). The interpolation of the velocity components onto the remaining grid-points results in a usable number of seed-points for the new algorithm of 78 (green '+' markers). After the application of PEFRA Δ_n and θ are quantified on a particle-by-particle basis (Figure 3.11B). The corresponding velocity flow field that has been modified by PEFRA is presented in Figure 3.11C, where the instantaneous sample volume mean velocity

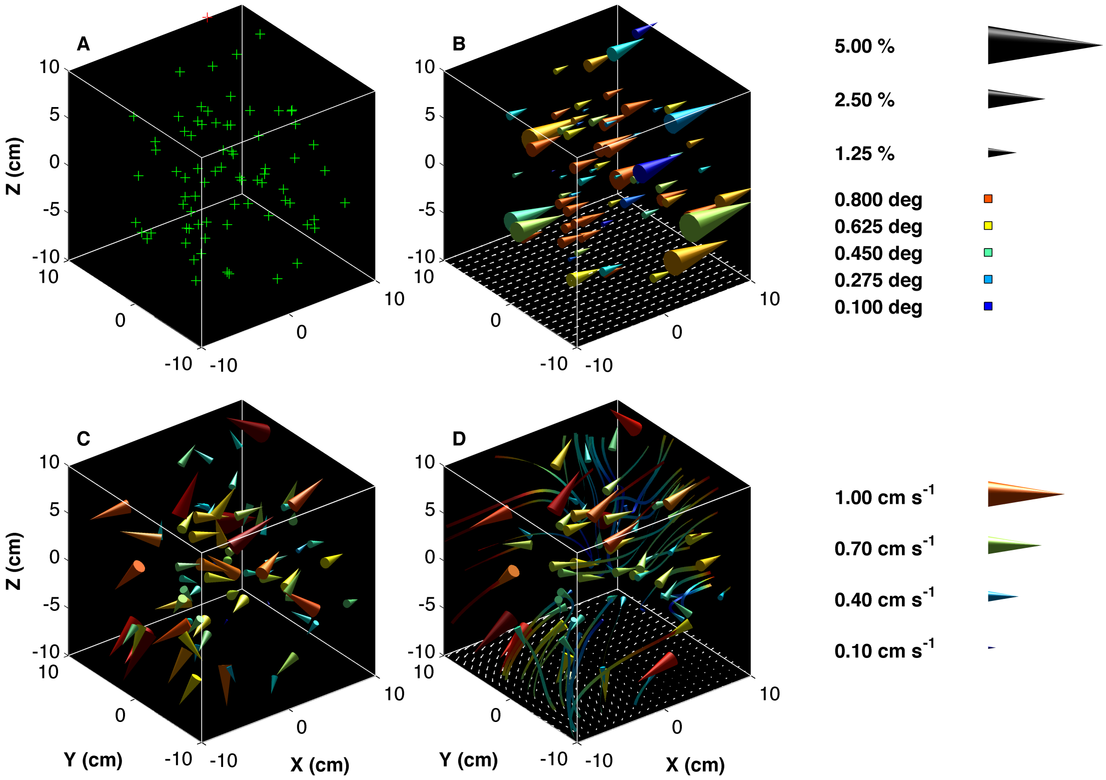

Figure (3.11). An instantaneous velocity flow field with a low turbulence strength: (A) output from the tracking software and gridding process; (B) The Δ_n (vector scale) and θ (vector colour) between the input and output velocity flow field at each of the seed-points; (C) Velocity distribution (coloured and scaled by the velocity magnitude) corrected by PEFRA; (D) Velocity distribution (coloured and scaled by the velocity magnitude) not corrected by PEFRA

.

components have been subtracted from each of the vectors to reveal the three-dimensional turbulence structures. This is similar to the pattern of the velocity flow field presented in Figure 3.11D, where PEFRA was not applied. The cause of this similarity is that the sparsity of the data exceeds the critical sparsity condition by a factor of two and therefore will not affect the quality of the restoration. This, in turn, is aided by the small velocity gradients within the sample volume meaning that both large particles and small particles will follow the streamlines

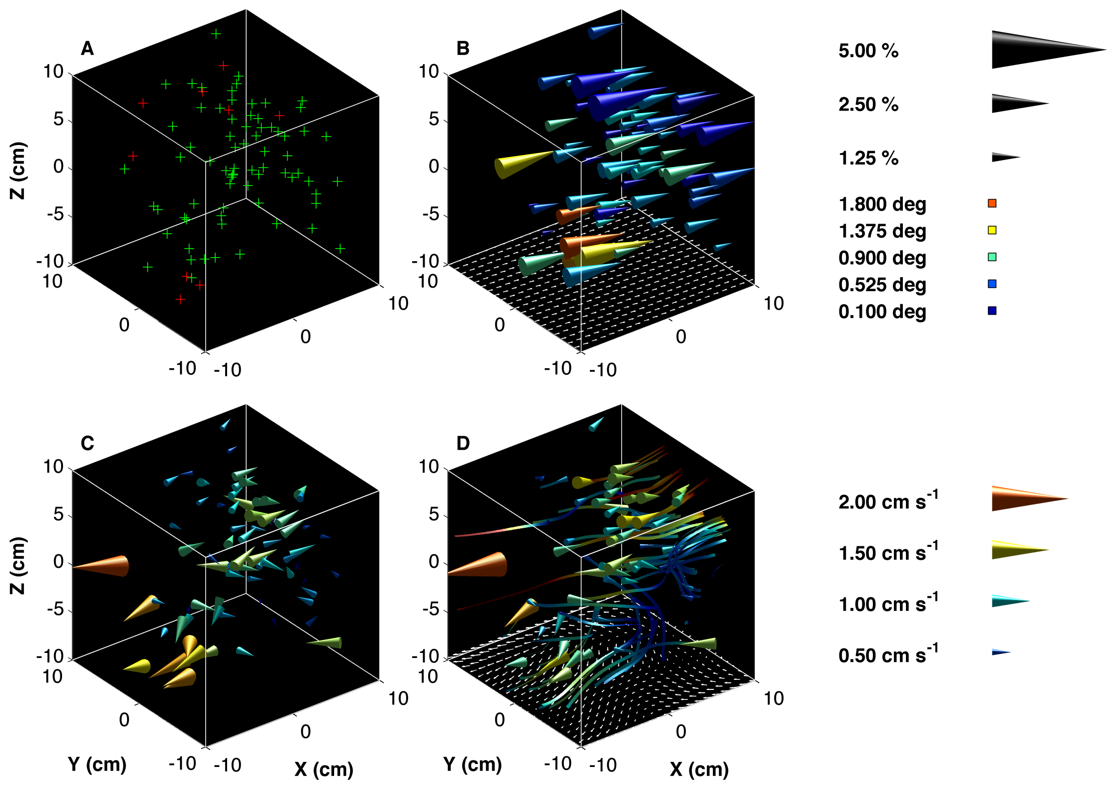

Figure (3.12). An instantaneous velocity flow field with a higher turbulence strength. The visualisation process is as per Figure 3.11.

alike. Consequently, neither particles increase the noise level substantially.

Figure 3.12 presents an instantaneous velocity flow field where $I = 1.0929\,\mathrm{cm\,s^{-1}}$. The format of these panels are the same as for the last figure, with 75 unique seed points used (Figure 3.12A). An increase in Δ_n and θ on a particle-by-particle basis (Figure 3.12B) is visible and more adjustment seen in the velocity flow field that was modified by PEFRA (Figure 3.12C) over that where PEFRA was not applied (Figure 3.12D). The cause of this adjustment is that the sparsity of the data is nearer the critical sparsity condition and therefore a very small part of this modification is likely to be an error (that increases as the sparsity of the data approaches the critical sparsity). This, in turn, is compounded by the large velocity gradients within the sample volume, as large particles cannot react to these as quickly as small particles and are affected by differential shear along their length.

As a verification of the adjustment made by PEFRA, the image containing a record of each of the particles must be examined to establish whether individual tracer characteristics (e.g. bubbles, large or heavy particles) are responsible for these differences. Figure 3.13 presents three sections of the image, viewed from each of the four different camera angles. The particles corresponding to the frame minimum Δ_n (0.6798) and frame minimum θ (0.0461) are highlighted in Figure 3.13A and Figure 3.13B. Although exhibiting the differences in shape expected of natural particles, these appear to be small in size and therefore the lack of adjustment is in agreement with the reasoning that they will not affect the noise level as much as a larger, more irregular particle. Accordingly, the particle corresponding to the frame maximum Δ_n (29.2589) and θ (15.9934) is revealed in Figure 3.13C to be a larger, irregular aggregate typical of a sediment floc. Such particles increase the noise level, and therefore need adjustment by PEFRA. Note that this connection to individual tracer characteristics is appropriate as there are a sufficient number of particles within the sample volume for the algorithm not to fail, while the small distance that separates these from their nearest grid-points (i.e. $D < 0.87\,\text{cm}$) ensures that errors linked with interpolation will also be small.

This approach also provides a secondary method of validation. In 3D-PTV, individual particles are tracked as they are advected through the three-dimensional sample volume. If a time-series of the instantaneous velocity flow field is examined (Figure 3.14A, Figure 3.14B and Figure 3.14C), it may be seen from the stream

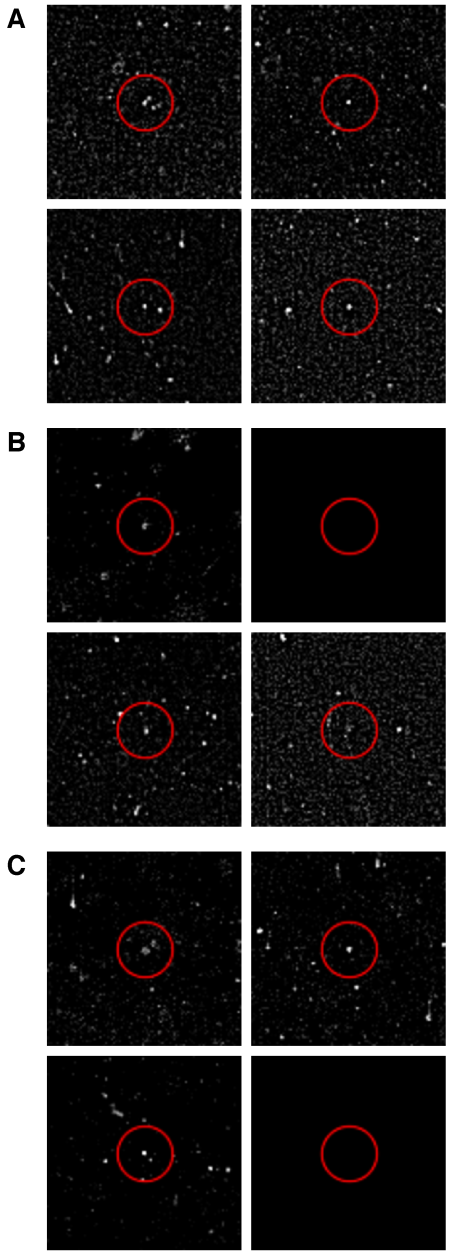

Figure (3.13). Three sections from the 3D-PTV image (A to C), viewed from each of the four different camera angles. The particles nearest the grid-points corresponding to: (A) the frame-minimum Δ_n; (B) the frame-minimum θ; (C) the frame-maximum Δ_n and frame-maximum θ are highlighted.

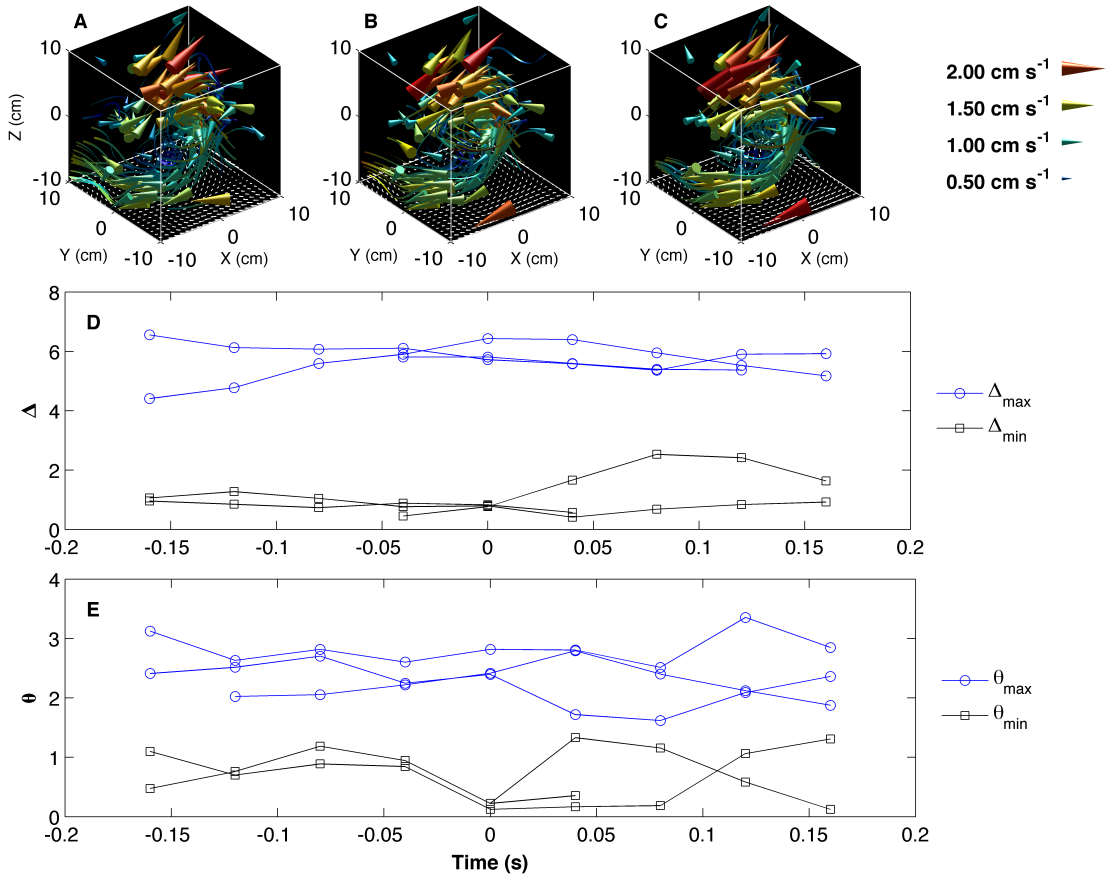

Figure (3.14). (A to C) Time-series of the instantaneous velocity flow field of a three-dimensional coherent structure at intervals of 1/25 s. Visualisation procedures are as in Figure 3.11 and Figure 3.12. (D) Time-series of the adjustment made by PEFRA to 6 particles that represent the 3 maximum and 3 minimum Δ corrections made in (B) over a sequence of 7 frames. (E) Time-series of the adjustment made by PEFRA to 6 particles that represent the 3 maximum and 3 minimum θ corrections made in (B) over a sequence of 7 frames.

.

ribbons that depict the gridded PEFRA output that the same coherent vortical structure is spatially and temporally coherent, and from the cones that depict the gridded particle positions that these progress through the sample volume. If the PEFRA output were incorrect, then there would be no coherence in the structure over the sequence of snapshots. Additionally, for any single particle moving through the sample volume, a similar correction (related to the individual tracer characteristics, as discussed with Figure 3.13) may be expected. Figure 3.14D and Figure 3.14E presents time-series of the correction of a total of 12 different particles associated with the maximum and minimum adjustments that were made in Figure 3.14B to the total difference and angle deviation, respectively, over a sequence of 7 frames. These are seen to be both spatially and temporally invariant, giving confidence that it is the physical characteristics of the particles that causes the errors that are successfully corrected by PEFRA.

To complement the assessment of the instantaneous velocity flow fields presented above, Figure 3.15 shows a time-series of the turbulence strength and total particle count (Figure 3.15A and Figure 3.15B), as well as the corresponding Δ_n and θ quantities (Figure 3.15C and Figure 3.15D). An increase in the sample volume mean turbulence intensities are generally connected to the passage of large coherent motions. This, in turn, is associated with the corresponding increase in Δ_n and θ that arises from tracking difficulties when the flow structures are more complex. In extreme instances of swimming particles not advected through the flow field, however, a single tracer can bias both restoration and turbulence statistics. An example of this is presented in Figure G.19, where one particle is seen to move very differently to that of the pattern of the velocity flow field and

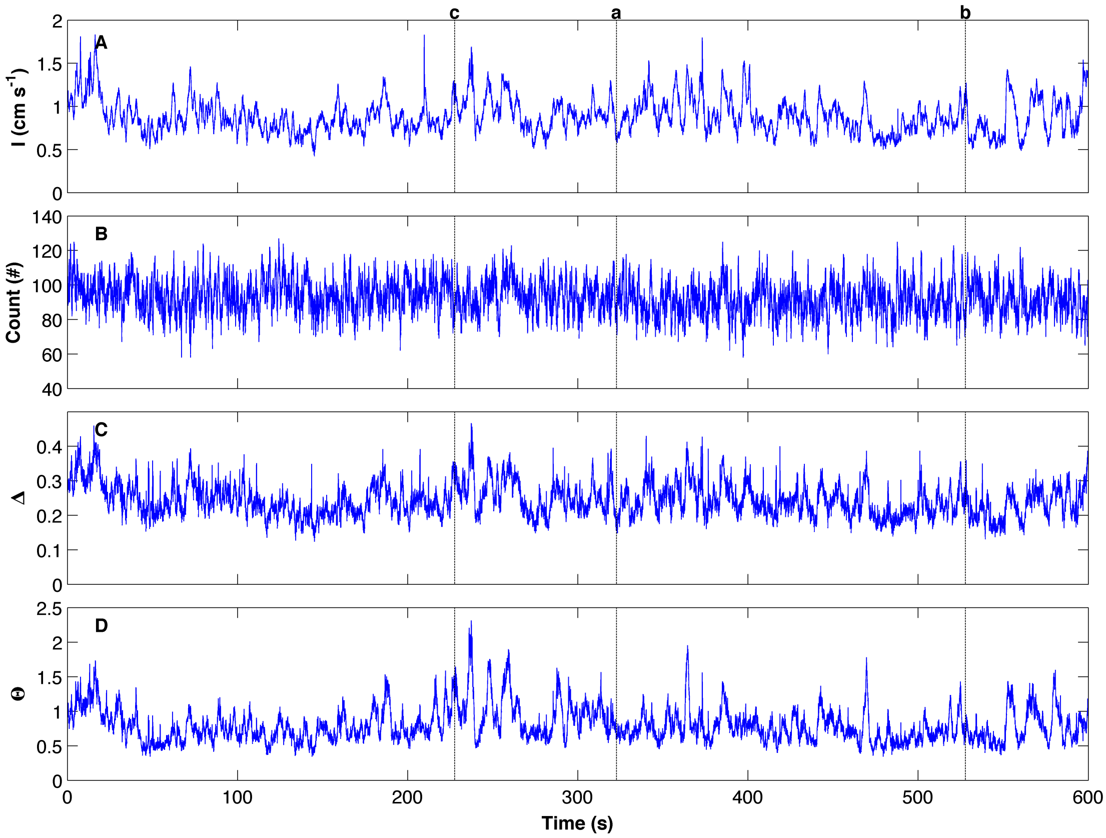

Figure (3.15). Time-series of the sample volume (A) mean turbulence strength, (B) total particle count, (C) frame-averaged Δ_n and (D) frame-averaged θ. The black lines represent where the velocity distributions shown in (a) Figure 3.11, (b) Figure 3.12 and (c) Figure 3.16 occurs in the sequence.

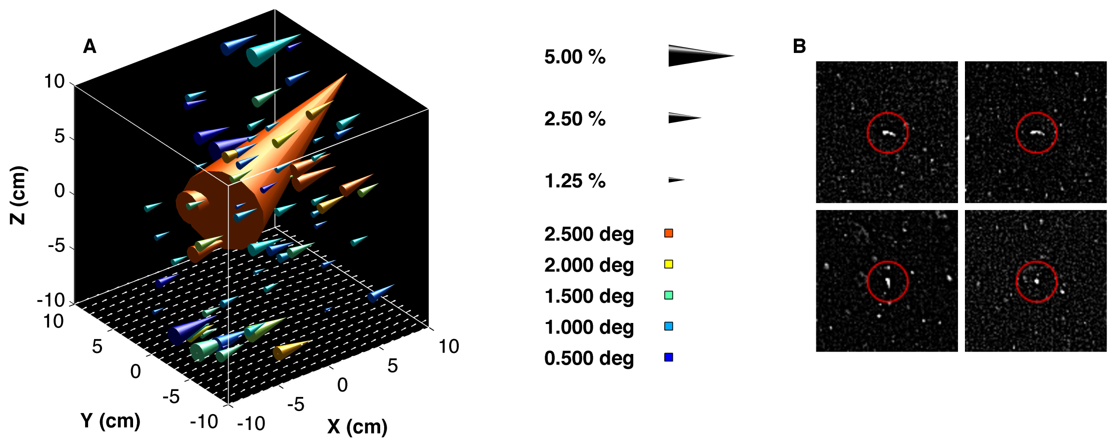

Figure (3.16). (A) The Δ_n and θ between the input and output velocity flow field at each of the seed-points. (B) Section from the 3D-PTV image, viewed from each of the four different camera angles, with the particle responsible for the single large vector in (A) highlighted.

necessitates a large adjustment by PEFRA (Figure 3.16A). The examination of the original image (Figure 3.16B) reveals that this ‘particle’ has a distinct body and tail, is 4.0 mm in length, and swims at a speed of 5.68 $\mathrm{cm\,s^{-1}}$, or 14.2 body lengths per second. These quantities are consistent with laboratory measurements of the swimming speed of fish larvae (Bellwood and Fisher, 2001). This contamination is easily eliminated by removing single outliers using local Δ_n and θ anomalies and reprocessing the affected frame, but the example also confirms that PEFRA correctly identifies erroneous biological particles in situ.

3.4.5 3D-PTV

As an assessment of the data recorded by the 3D-PTV system and its processing, Figure 3.17 compares an example 10 min time-series with the equivalent data recorded by the 1200 kHz ADCP and the ADV. It is seen that a good agreement exists between the mean 3D-PTV velocity measurements (both with and without

PEFRA) and that from the ADCP and the ADV, all exhibiting the same effects of mean tidal flow and small amplitude oscillatory motion from surface gravity waves (Nimmo-Smith, 2008). Any small difference between the instrumentation arises from the separation between, and the size of, the sample volume of each of these systems. An additional, comprehensive, assessment of the submersible 3D-PTV system was reported by Nimmo-Smith (2007), Nimmo-Smith (2008) and Vlasenko et al. (2015). The results confirm the potential of the system for the study of three-dimensional turbulence characteristics of ocean flows in situ.

In contrast to traditional instrumentation, time-resolved submersible 3D-PTV is capable of providing an instantaneous snapshot of the velocity flow field in a $20 \times 20 \times 20\,\mathrm{cm}^3$ sample volume and therefore represents an important tool for the study of coherent structures. However, consistent with any image-based instrumentation, this is associated with a much higher computational cost (both in data collection and processing) than other systems. Similarly, these are limited to flow conditions containing sufficient particles to reveal the turbulence characteristics but not so many as to overload the Particle Tracking Velocimetry software. Tracking of particles is possible in a mean flow of up to $25\,\mathrm{cm\,s^{-1}}$, becoming more difficult as the mean displacement between images exceeds the mean separation of the particles, however this is adequate for the conditions typical within the bottom boundary layer of the coastal ocean (Nimmo-Smith et al., 2002, 2005). As with other methods that use the scattering of light and sound to determine velocity, 3D-PTV assumes that particles act as neutrally-buoyant tracers of the velocity flow field. Individual tracer characteristics (e.g. bubbles, large or heavy particles) will, therefore, bias the results. However, in these cases, the use of

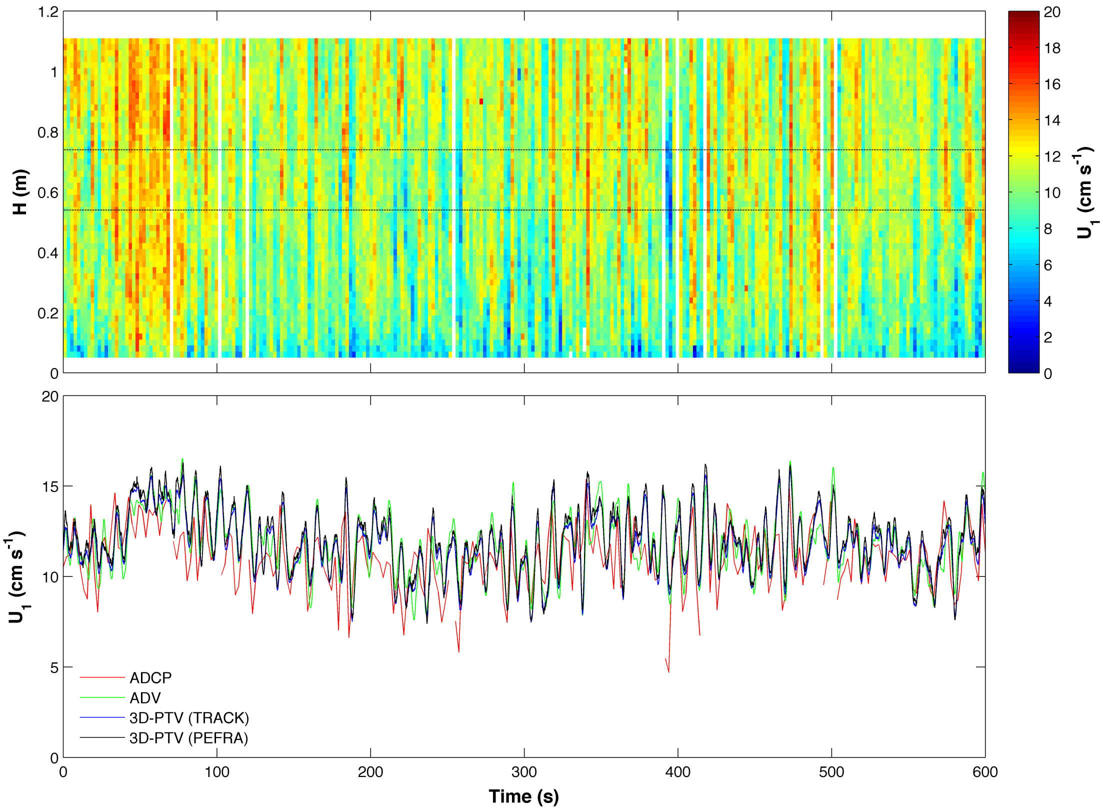

Figure (3.17). Comparison between the 3D-PTV, ADV and ADCP data over a 10 min data series. The velocity (U_1) in the direction of the mean flow is shown. (A) High-resolution ADCP data. The vertical extent of the 3D-PTV sample volume is indicated by the dashed lines. (B) Time series of the 3D-PTV, ADV, ADCP data. The 3D-PTV data are the instantaneous sample volume mean (with and without PEFRA), the ADCP data are averaged over the vertical range bounded by the dashed lines in (A) and the ADV data have been low-pass filtered at 1Hz to account for the differently sized sample volume.

PEFRA allows such anomalies to be detected, and the original camera images of each of the particles checked, when these unexpected results are encountered.

3.5 Data Sets

3.5.1 Time/site

The submersible 3D-PTV system was deployed on the night of 21-22 May 2007, on the East side of Plymouth Sound (Plymouth, UK), at 50°22′17″ N, 04°08′32″ W (Figure 3.18). Here, the sea-bed is flat and consists of mud and sand without notable ripples or bedforms, and the depth of the water decreased from 14.0 m to 10.5 m during the accelerating phase of the ebb-tide (Figure 3.19). Near-surface currents may be of up to $\sim 0.5\,\mathrm{m\,s^{-1}}$ during a spring tide, however this site is sheltered from most surface wave motion by an artificial breakwater. Although in an area of fresh-water influence, the water column was vertically well-mixed with no density stratification (as confirmed by a single Conductivity, Temperature and Depth cast, not presented).

After deployment and calibration, the frame was lowered to near the sea-bed, such that it is able to align with the mean flow direction, before being set down. Data were collected in ten runs, each of 20 minutes (30,000 frames), with the centre of the sample volume at the elevation of 0.64 m above the seabed. One of these runs is presented in this thesis. The mean velocity profile that was recorded by the two ADCPs during the run, is presented in Figure 3.20, with the area viewed by the 3D-PTV system marked by the two dashed lines at $z = 0.54$ m and $z = 0.74$ m. It is seen that these 3D-PTV data were collected within a well-developed logarithmic layer, whose statistics are quantified below.

3.5.2 Statistics

To relate the in-situ data examined in the present thesis to the body of existing work (Chapter 1), several scaling parameters must be quantified.

The boundary layer thickness, δ, is defined as the elevation above the seabed where the mean flow equals 99 % of the free-stream velocity, u_∞. This is determined for the mean ADCP data in Figure 3.20 using:

$$\delta = 0.99 u_{max}. \tag{3.6}$$

where, u_{max} is the maximum horizontal velocity recorded by the 600 kHz ADCP (i.e. 21.8911 cm s^{-1}), assumed be to equal to u_∞ and the flow assumed to be steady over the period of averaging.

This is known to be a poorly conditioned quantity, however, as it is dependant

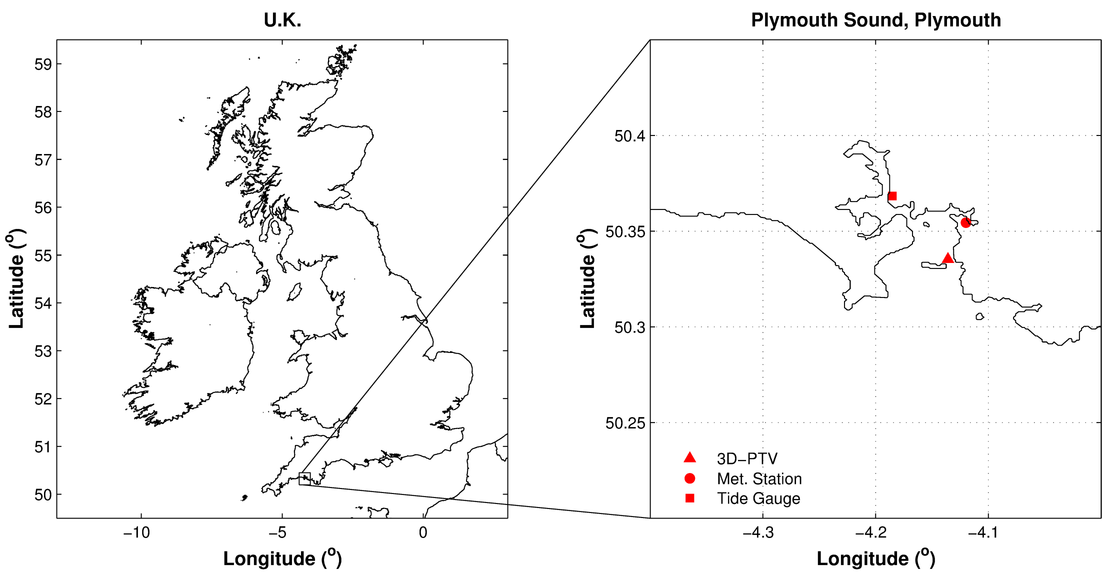

Figure (3.18). Location map showing the position of the 3D-PTV system deployed in Plymouth Sound, Plymouth, UK.

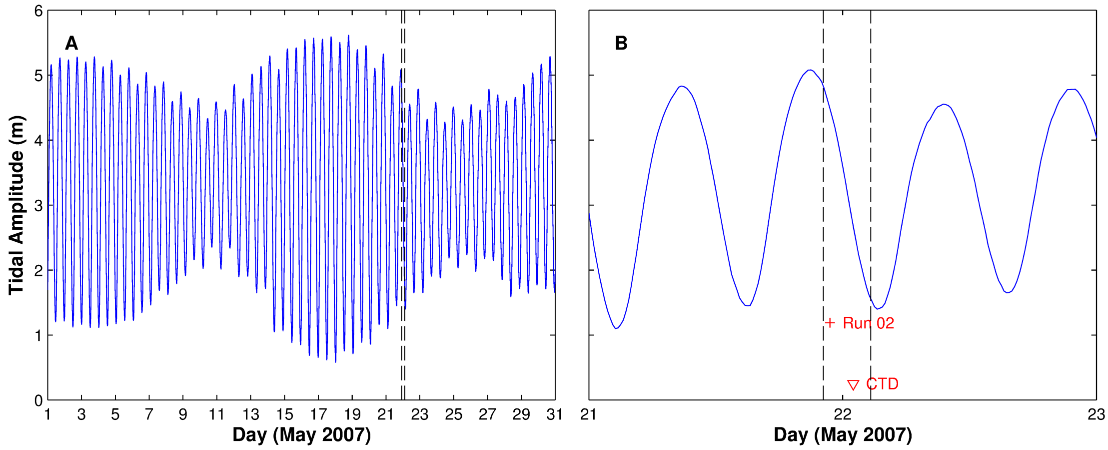

Figure (3.19). Time-series of tidal elevation. Data were collected in ten runs, each of 20 minutes (30,000 frames), with the centre of the sample volume at the elevation of 0.64 m above the seabed. The run used is denoted by the red cross.

on measurements of small velocity differences, meaning that integral parameters (e.g. displacement thickness, δ^*, or momentum thickness, δ^θ) are commonly used (Pope, 2000):

$$\delta^* = \int_0^\infty (1 - \frac{u}{u_\infty})dz \tag{3.7}$$

$$\delta^\theta = \int_0^\infty \frac{u}{u_\infty}(1 - \frac{u}{u_\infty})dz. \tag{3.8}$$

For the mean ADCP data in Figure 3.20, δ=9.4456 m, $\delta^* = 2.0719$ m and δ^θ=1.5655 m (labelled in Figure 3.20A), in turn giving several Reynolds numbers (based on these thicknesses): $Re_\delta \equiv (u_\infty \delta)/\nu = 1.6168 \times 10^6$, $Re_{\delta *} \equiv (u_\infty \delta^*)/\nu = 3.5465 \times 10^5$ and $Re_{\delta *} \equiv (u_\infty \delta^\theta)/\nu = 2.6797 \times 10^5$ (where $\nu = 1.2789 \times 10^6$ m^2 s^{-1} is the kinematic viscosity of seawater at the elevation 0.5 m above the seabed).

Within the boundary layer, the mean velocity profile, $u(z)$, follows the law of the wall:

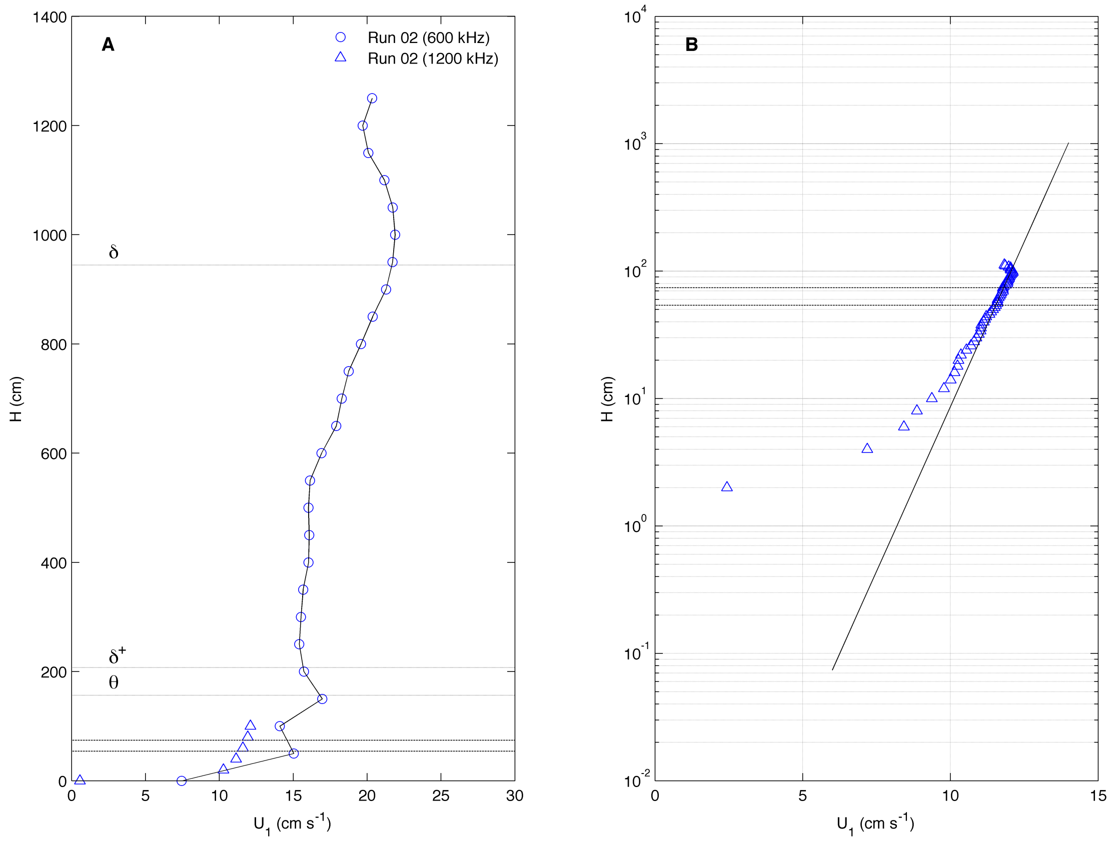

Figure (3.20). (A) Vertical profile of mean horizontal velocity measured by the 600 kHz ADCP (circles) and the 1200 kHz ADCP (triangles). Horizontal dashed lines show relevant boundary thickness parameters. (B) Least-squares fit to the mid-section of the data showing a logarithmic profile.

$$u(z) = \frac{u_*}{k} \ln \frac{z}{z_0} \tag{3.9}$$

where, $k = 0.41$ is the von Kármán constant, z is the distance from the seabed, z_0 is a characteristic roughness (Schlichting, 1960).

Here, the friction velocity ($u_* = \sqrt{\tau_*/\rho}$, where τ_* is the shear stress at the wall and ρ is the density of seawater) is determined by fitting the ADCP data to the logarithmic velocity profile expressed in Equation 3.9. The vertical extent of the data used in obtaining this fit is limited to the logarithmic velocity profile range (between 0.54 m and 0.74 m above the seabed) and results in an $r^2 = 0.99$ (Figure 3.20B). The characteristic roughness, z_0 is, similarly, determined by regression. For the mean ADCP data in Figure 3.20, $u_* = 0.69\,\mathrm{cm\,s^{-1}}$ and $z_0 = 0.07\,\mathrm{cm}$. These, in turn, are used to convert the physical measurements to their dimensionless equivalents (Chapter 1). Note that due to a lack of necessary data sufficiently near the seabed, it is not possible for these estimates of u_* and z_0 to be compared to that from other formulae. However, based on data collected by Kim et al. (2000) and Biron et al. (2004), it is acknowledged that the methods used are the most variable, with a typical error of ±20%.

3.5.3 Mean flow

Throughout the present thesis, a 'mean flow' is defined is several ways, depending on averaging used. For ease of reference, this terminology is consistent with that of Luznik (2006).

A temporal average is labelled $\overline{u_i}$, and defined as:

$$\overline{u}_i(x, y, z) = \frac{1}{N}\sum_{n=1}^{N} u(x, y, z, t_n) \tag{3.10}$$

where N is the number of particles and t_n is a velocity time series.

A spatial average is labelled $\langle u_i \rangle$, and defined as:

$$\langle u_i(t) \rangle = \frac{1}{A \times B \times C}\sum_{a=1}^{A}\sum_{b=1}^{B}\sum_{c=1}^{C} u_i(x_a, y_b, z_c, t_n) \tag{3.11}$$

where the specific elements within the sample volume (or data arrays) are indexed with a, b and c for x_1 (i.e. x), x_2 (i.e. y) and x_3 (i.e. z).

The run mean velocity consists of a spatial average of $\overline{u}_i$ or, conversely, a temporal average of $\langle u_i \rangle$, and defined as:

$$\langle \overline{u}_i \rangle = \frac{1}{A \times B \times C \times N}\sum_{n=1}^{N}\sum_{a=1}^{A}\sum_{b=1}^{B}\sum_{c=1}^{C} u_i(x_a, y_b, z_c, t_n) \tag{3.12}$$

Figure 3.21 presents the time-series of $\langle u_i \rangle$. Here, it is apparent that $\langle u_i \rangle$ represent the joint effect of the mean tidal flow and waves or scales larger than that of the 3D-PTV sample volume (however the amplitude of this is weak when compared to $\langle \overline{u}_i \rangle$). Larger-amplitude, longer-period oscillations are also seen. The effect of waves or scales larger than the size of the sample volume are characterised by the rms velocity, defined as:

$$[u_i]_{rms} = \left[\frac{1}{N}\sum_{n=1}^{N}(\langle u_i(t_n) \rangle - \langle \overline{u_i} \rangle)^2\right]^{\frac{1}{2}} \tag{3.13}$$

The $\langle \overline{u}_i \rangle$ and $[u_i]_{rms}$ data for the velocity time-series are presented in Table 3.2. As expected, the rms values exceed the global average values.

To ensure that appropriate conclusions are yielded in data analysis, other sample volume mean flow parameters must be considered.

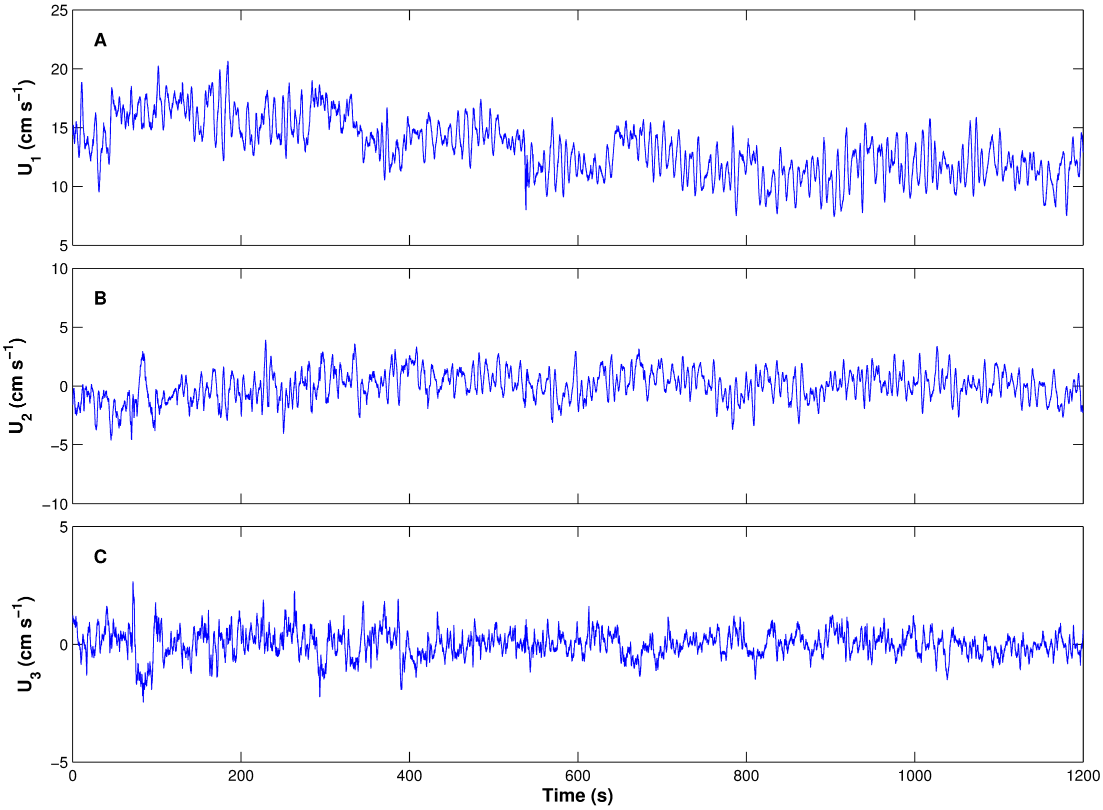

Figure (3.21). Time series of sample volume mean velocity components.

	$\langle\overline{u}\rangle$	$\langle\overline{u}_{rms}\rangle$
u_1	13.2971	13.3096
u_2	0.0034	1.1217
u_3	0.0168	0.5950

Table (3.2). Mean and rms statistics for the data used.

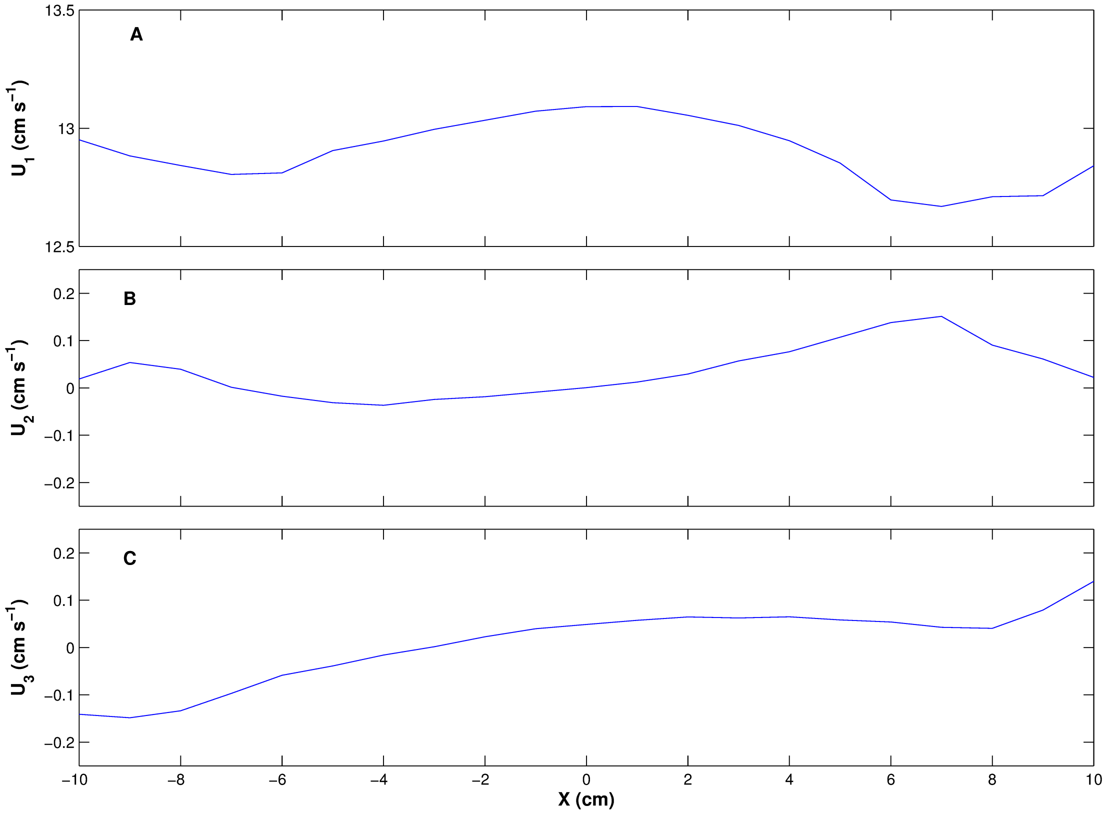

Figure (3.22). Sample volume mean velocity profile aligned with the x-axis.

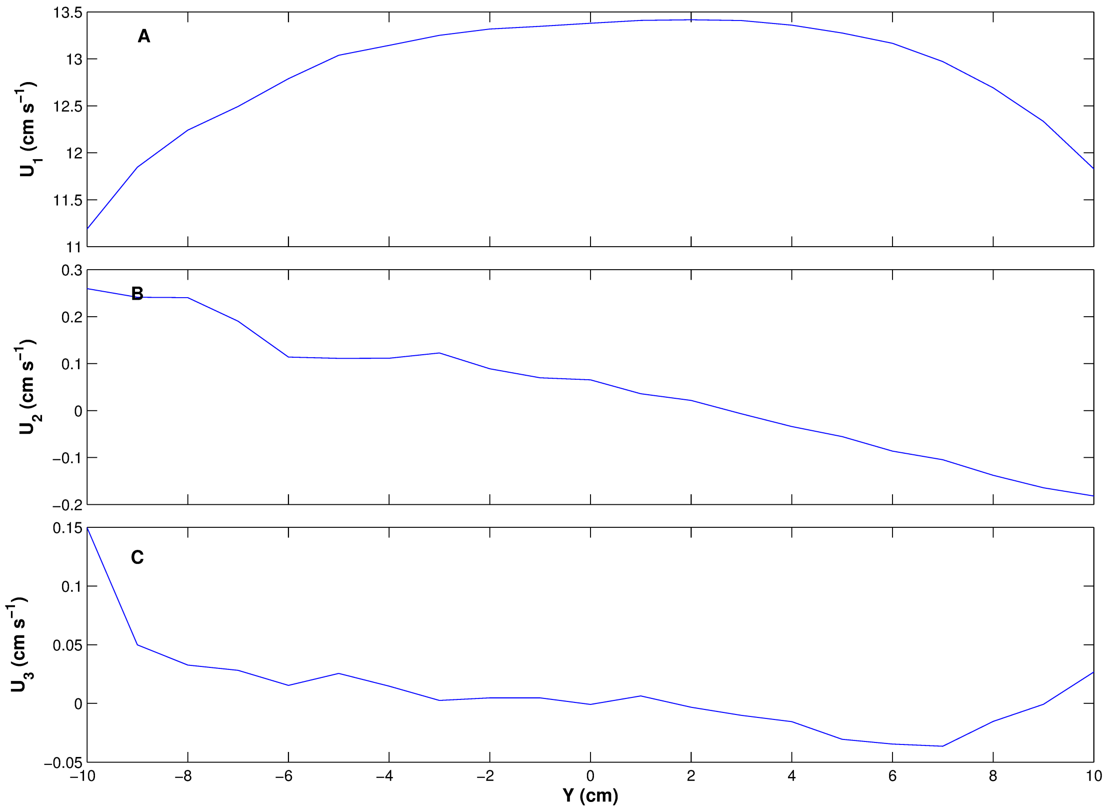

Figure (3.23). Sample volume mean velocity profile aligned with the y-axis.

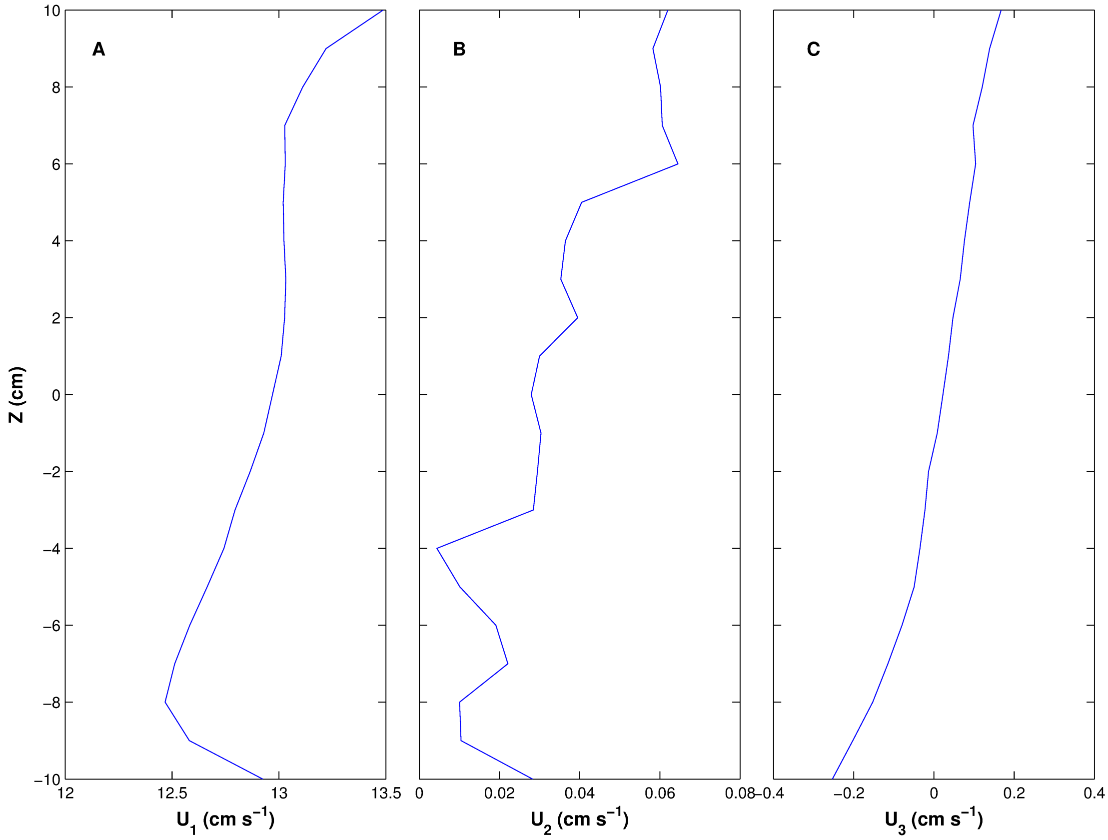

Figure (3.24). Sample volume mean velocity profile aligned with the z-axis.

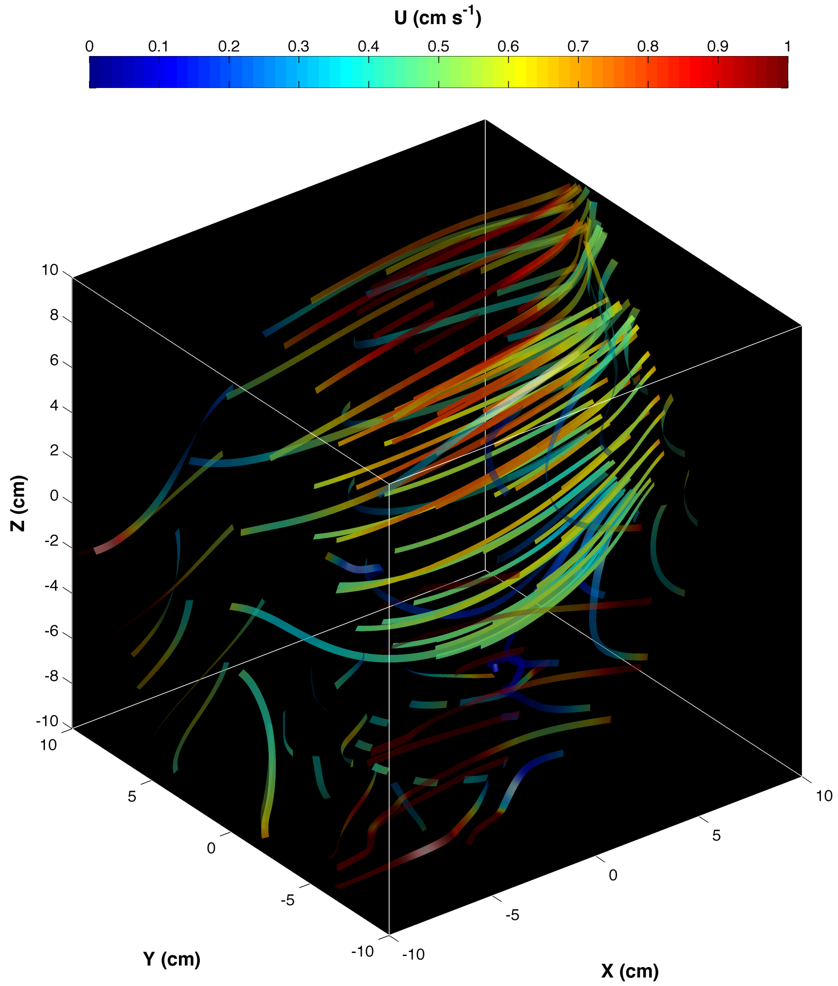

Figure (3.25). Sample volume time-averaged flow conditions (zero-mean). The small-scale coherent structures are only present around the periphery of the sample volume, contributing to a low SnR ratio.

The sample volume mean velocity profile $(\overline{u}_i(x_j))$ is defined:

$$(\overline{u}_i(x_j)) = \frac{1}{A \times B \times N} \sum_{n=1}^{N} \sum_{a=1}^{A} \sum_{b=1}^{B} u_i(x_j, a, b, t_n) \tag{3.14}$$

Figure 3.22, Figure 3.23 and Figure 3.24 present the sample volume mean velocity profile aligned with the x_1, x_2 and x_3 components. Most importantly, these exhibit spatial variation across the sample volume, that will bias velocity gradient statistics. Likely to be an artefact of poor illumination, this effect is limited by confining averaging to within the middle part of the sample volume.

Similarly, to confirm the absence of coherent structures within the (averaged) zero-mean conditions, a Reynolds Decomposition was applied to $\overline{u}_i$, i.e.

$$\overline{u}_i' = \overline{u}_i - \langle \overline{u}_i \rangle \tag{3.15}$$

Figure 3.25 illustrates small-scale velocity gradients are only present around the periphery of the sample volume, meaning that any coherent structures recorded within the 3D-PTV sample volume are not an artefact of the mean flow.

3.5.4 Convergence

Turbulence statistics are dependant on the sampling rate, f_s, and the sampling duration, t_s (Graham, 2010). While a high f_s and t_s are highly desirable, in reality these parameters represent a compromise between necessary resolution and instrumentation constraints. Typically, the sampling rate and duration for existing 2D-PIV measurements in the coastal ocean is up to 4000 frames at a rate of 3.33 Hz (Nimmo-Smith et al., 2005). While this is likely to be a reflection of sampling limits and set up, a higher sample rate is used in 3D-PTV due to the need to follow individual particles as this is easier of very small distances and longer trajectories (Nimmo-Smith, 2008). Here, the optimum sampling rate is bounded by the minimum distance over which particles may be resolved and the velocity of the flow. In the present thesis $f_s = 25$ Hz. The optimum t_s may be estimated from the long term data of the convergence to temporal stability, with this being defined as the shortest duration to obtain stable statistics, e.g. 10,% of the long-term mean (Graham, 2010). Figure 3.26 presents the convergence to stability, yielding $t_s \approx 600$ s (red lines). Since the data reported within the

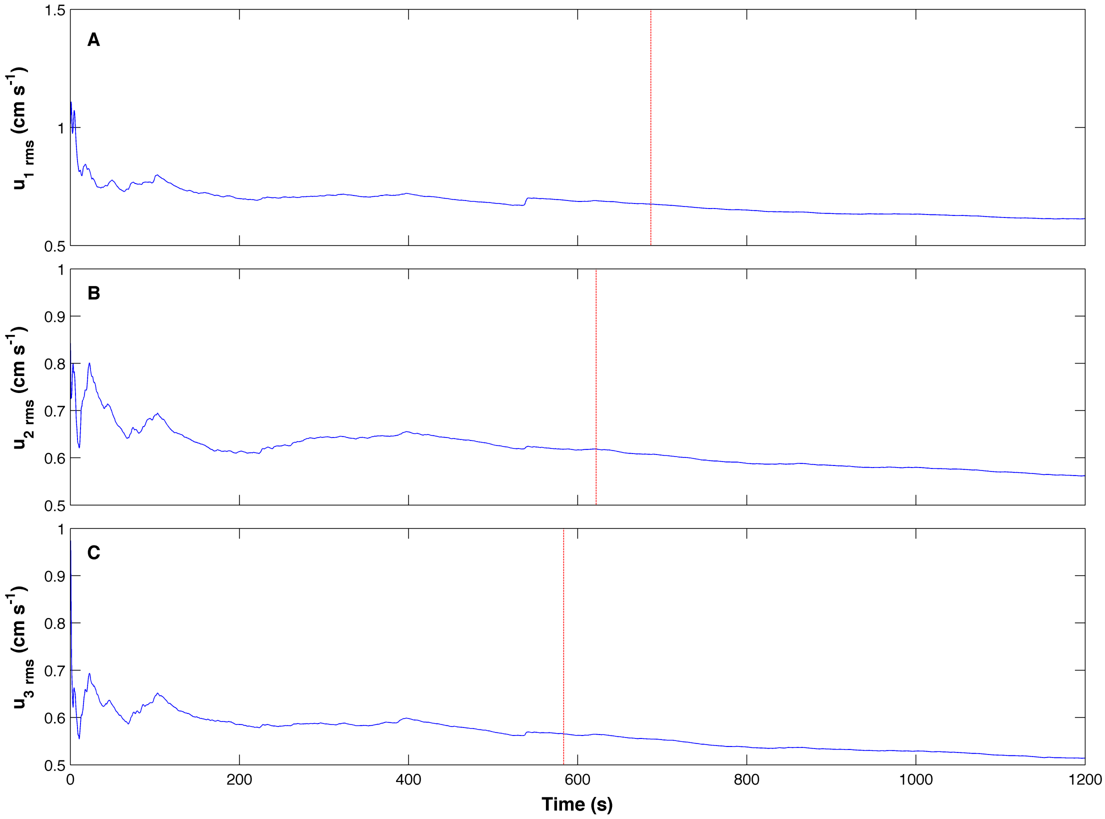

Figure (3.26). Time-series of convergence to long term rms value for the sample volume mean velocity components.

present study comprises a 1200 s period, this is approximately twice the minimum t_s and therefore these statistics are deemed to be representative.

3.6 Conclusions

In this chapter, the instrumentation that will be used for turbulence measurements of a tidal flow have been discussed. These consist of a vessel-mounted 600 kHz Acoustic Döppler Current Profiler (ADCP) used in obtaining background flow conditions, a 1200 kHz Acoustic Döppler Current Profiler, Acoustic Doppler Velocimeter and submersible three-dimensional particle tracking velocimetry system (3D-PTV).

The methods of processing the raw data from each of these have been established. For the Döppler instrumentation, this involves the removal of Döppler noise contamination and spurious spiking. In the case of the ADCP this is achieved using manufacturer supplied ADCP processing software, whereas in the case of the ADV a combination of Gaussian low-pass filtering and phase space despiking have been shown to be robust and consequently are used for the post processing of ADV data. The 3D-PTV data processing involves an initial calibration, that is used to relate the exposure from the four cameras, such that the 3D-position of particles is yielded. Tracking of particles is done in both image and object space, running the linkages between adjacent fames, contained by dynamic tracking parameters updated using a time-series from the ADV. The position of the particles at each time-step is then determined by low-pass filtering the position signal with a moving cubic spline from which the velocity is obtained by differentiation.

A complexity associated with submersible 3D-PTV in the coastal ocean is that gaps and noise affect the accuracy of the data collected. To accommodate this, a new Physics-Enabled Flow Restoration Algorithm has been tested for the restoration of gappy and noisy velocity measurements where a standard PTV or PIV laboratory set-up (e.g. concentration / size of the particles tracked) is not possible and the boundary and initial conditions are not known *a priori*. Implemented as a black-box approach, where no user-background in fluid dynamics is necessary, this is able to restore the physical structure of the flow from gappy and noisy data, in accordance with its hydrodynamical basis. In addition to the restoration of the velocity flow field, PEFRA also estimates the maximum possible deviation of the output from the true flow. When applied to submersible 3D-PTV measurements from the bottom boundary layer of the coastal ocean, it is apparent that using PEFRA is beneficial in processing data collected under difficult conditions, such as where the number (and reliability) of tracer-particles is very sparse.

An excellent agreement exists between the restored sample volume mean velocity measurements recorded by the 3D-PTV system and the mean ADCP and ADV data, confirming the potential of the system for the study of three-dimensional turbulence characteristics of the bottom boundary layer of the coastal ocean.

Chapter 4

Three-dimensional coherent structures

4.1 Introduction

Turbulence in shelf-seas has a strong influence on the large-scale distribution of biological production (Tett et al., 1993) and suspended sediments (Jago and Jones, 1998). Tidally-generated turbulence limits the areas of thermal stratification (Simpson and Hunter, 1974), which in turn affects the shelf-sea "pumping" of carbon dioxide and is an important process for the global carbon cycles (Thomas et al., 2004). Modelling work has also shown that small changes in the vertical distribution of the stress associated with turbulence can have a strong effect on the patterns of circulation at much larger scales (Lentz, 1995). In tidal flows, turbulence is generated near the seabed (Heathershaw, 1974). However, while its one-dimensional characteristics have been well-studied, little is known of its three-dimesional structure and subsequent development throughout the water column.

On reaching the surface of well-mixed waters, bottom-generated "boils" – areas of local upwelling and associated eddies – have a marked impact on the dispersion of pollution and the contributes to the replacement of surface waters from depth (Nimmo-Smith et al., 1999, Thorpe et al., 2008).

Laboratory measurements (Adrian et al., 2000b, Ganapathisubramani et al., 2006, Dennis and Nickels, 2011a) and numerical modelling (Zhou et al., 1999, Adrian and Liu, 2002, Wu and Moin, 2009) indicate the energy-containing turbulence of boundary layer flows comprises coherent packets of "hairpin" vortices (Robinson, 1991). These have a specific – but rarely, if ever, perfectly symmetrical – form that, in an ideal case, consists of a cross-stream arch (comprising both head and neck components) with two counter-rotating along-stream legs (Figure 4.1A). The induction of the flow surrounding the eddy causes an upward "burst" inboard of the head and legs. It is here that vorticity elements are focused and, in turn, cause an area of low-momentum fluid below and upstream of the arch. Outboard of the head and legs, fluid flows down and forward, forming a sweep. The induction of the flow here is unfocused and so the strength of the burst exceeds that of the sweep. The opposing burst / sweep motion causes a shear layer, inclined at 25-45° from the boundary (Adrian, 2007). Two-dimensional flow visualisation methods have shown that these coherent structures (i.e. elementary organised motions that exhibit both spatial and temporal persistence) also exist in the bottom boundary layer of tidal flows (Figure 4.1B). Conditional sampling based on vorticity revealed that these coherent structures contribute most to the Reynolds stress and, as such, are the key areas where energy is extracted from the mean flow and into turbulence (Nimmo-Smith et al., 2005). However, questions remain as to the full three-dimensional form of such coherent structures, that may eventually grow into the depth-scale boils seen at the sea surface.

Here, for the first time, we present an analysis of the instantaneous three-dimensional form of turbulence in the bottom boundary layer of a tidal flow. The measurements shed light on the dynamical phenomena responsible for the statistical properties that are traditionally recorded by standard instrumentation or obtained through numerical modelling, providing in situ evidence to support an interpretation of the bottom boundary layer of the coastal ocean as comprising coherent structures consistent with laboratory and numerical experiments presented in the scientific literature. The impact on the Reynolds shear stress and spatial energy spectra is also examined.

4.1.1 Vortex identification

A vortex can be identified using the characteristic roots of the velocity gradient tensor, $\nabla \mathbf{u}$ (Chong et al., 1990, Dallman et al., 1991) and the streamlines containing the core said to be spiralling where two of these roots form a complex-conjugate pair (Zhou et al., 1999). The swirling strength of this core (i.e. the magnitude of the imaginary part of these complex roots, λ_{ci}) is both quantitatively and qualitatively similar to the vorticity, however it is only associated with the asymmetric part of $\nabla \mathbf{u}$ corresponding to rotation and discriminates against the symmetric part of $\nabla \mathbf{u}$ corresponding to shear. It is frame-independent, with a firm mathematical basis and unambiguous physical interpretation (Adrian et al., 2000a, Chakraborty et al., 2005).

Vortices are extracted by $\lambda_{ci} > t$, where T is an arbitrary threshold; typically

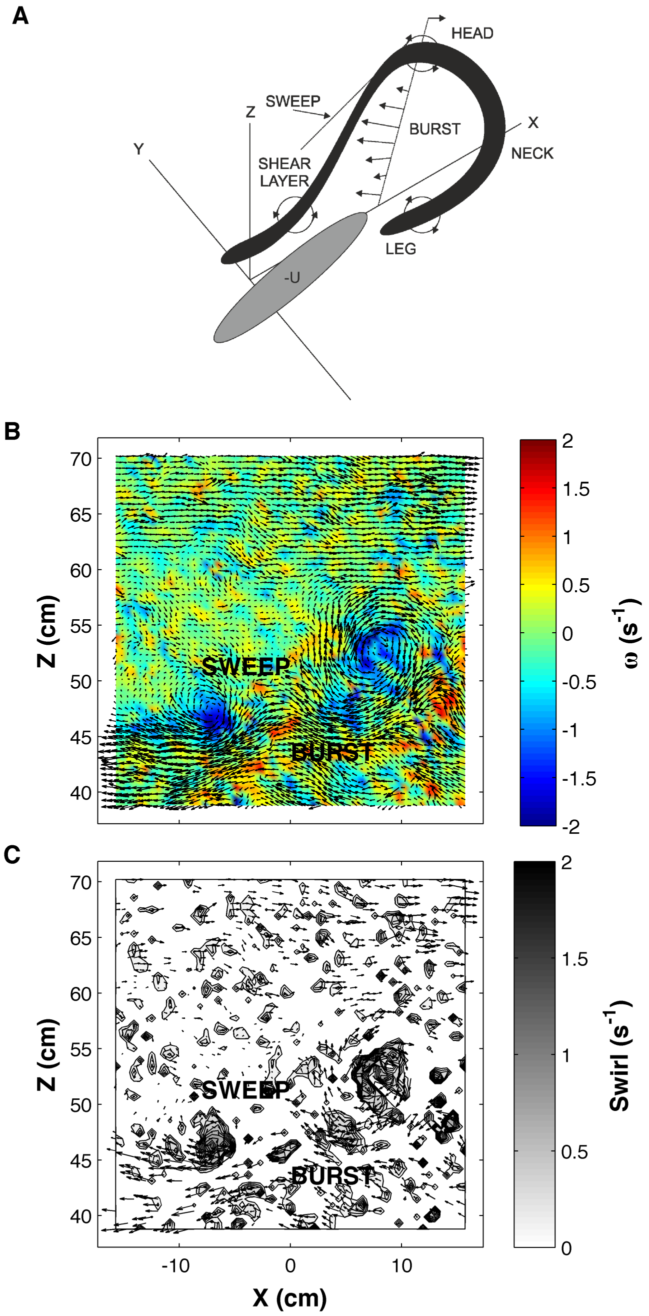

Figure (4.1). (A) Sketch of the form of a hairpin vortex in a boundary layer at a moderate Reynolds number (after Adrian, 2007). (B) Sample instantaneous zero-mean velocity and vorticity distribution and (C) corresponding swirling strength distribution (and the zero-mean velocity associated with these peaks), obtained from 2D in-situ flow visualisation measurements in the bottom boundary layer of the coastal ocean (after Nimmo-Smith et al, 2005).

a few percent of the data maximum. While theoretically setting $T = 0$ is sufficient to enable vortex identification, a higher threshold of λ_{ci} yields a smoother output, facilitating visualisation. Zhou et al. (1999) established that the general topology of a vortex is independent of the magnitude of the λ_{ci} threshold used, with characteristics such as the tilt angle of the vortex heads, the tilt angle of the vortex legs, the along-stream distance between successive vortex heads and the cross-stream distance between the vortex legs all remaining unaffected. However, as both the diameter and the length of the vortex decreases as the magnitude of the λ_{ci} threshold used increases, reliable statistics are not available for the scale of these eddies.

To limit the effect of noise, a $3 \times 3 \times 3$ box filter is applied to the data and a $\lambda_{ci} = 0.25\,\mathrm{s}^{-1}$ threshold is used. This is consistent with the approach employed in existing in-situ two-dimensional flow visualisation measurements by Hackett et al. (2011). To show the effectiveness of the method, the data presented in Figure 4.1B is replotted using the swirling strength in Figure 4.1C. To prevent erroneous inferences based on vortices consisting of only a few points (e.g. isolated velocity vectors in Figure 4.1C), only the statistics from those occupying at least $n \geq 1.0\%$ of the sample volume are counted.

4.2 Results and discussion

4.2.1 Flow structures

Figure 4.2A presents a time series of the sample volume mean turbulence intensity over the 20 minute period, revealing the patchiness within the flow. Importantly, the peaks do not occur randomly, nor exist in isolation, but exhibit the temporal persistence typical of the passage of a packet of hairpin vortices through the sample volume (Adrian, 2007). This is highlighted in Figure 4.2B for a 10 sec subset of the data where a section of high turbulence intensity is seen to be surrounded by sections of low turbulence intensity. Over the full 20 min duration, each of the individual velocity flow fields where a vortex was detected is marked, comprising a total of 1452 eddies in 1426 instantaneous realisations of the sample volume. It is this complete data set that is analysed. To account for the same eddies being tracked over multiple instantaneous realisations, an uninterrupted sequence of vortices is used to compute a mean period between occurrences of 4.3 sec.

The interpretation of this is that for most (96.5 %) of the time, the flow is quiescent, with little apparent structure, or with scales that are too small for the instrument to resolve clearly. Figure 4.2C presents an example velocity flow field where the sample volume mean velocity has been subtracted from each individual velocity vector to reveal the weak motion of the turbulence. Here, the flow is mostly laminar but small (diameter $<$ 5 cm) vortices, such as seen on the left hand side of the volume, may also occur. In contrast to the moderately quiescent conditions are the example eddies presented in Figure 4.2D and Figure 4.2E. These large vortices with a diameter of 5-15 cm occur intermittently, either singly or in groups, and remain coherent for at least the time that they are advected through the sample volume by the mean flow ($\sim$2 sec). Of the many of different orientations present, some vortices exhibit cores aligned approximately cross-stream (Figure 4.2D), or "arced" cores comprising an along-stream section in their

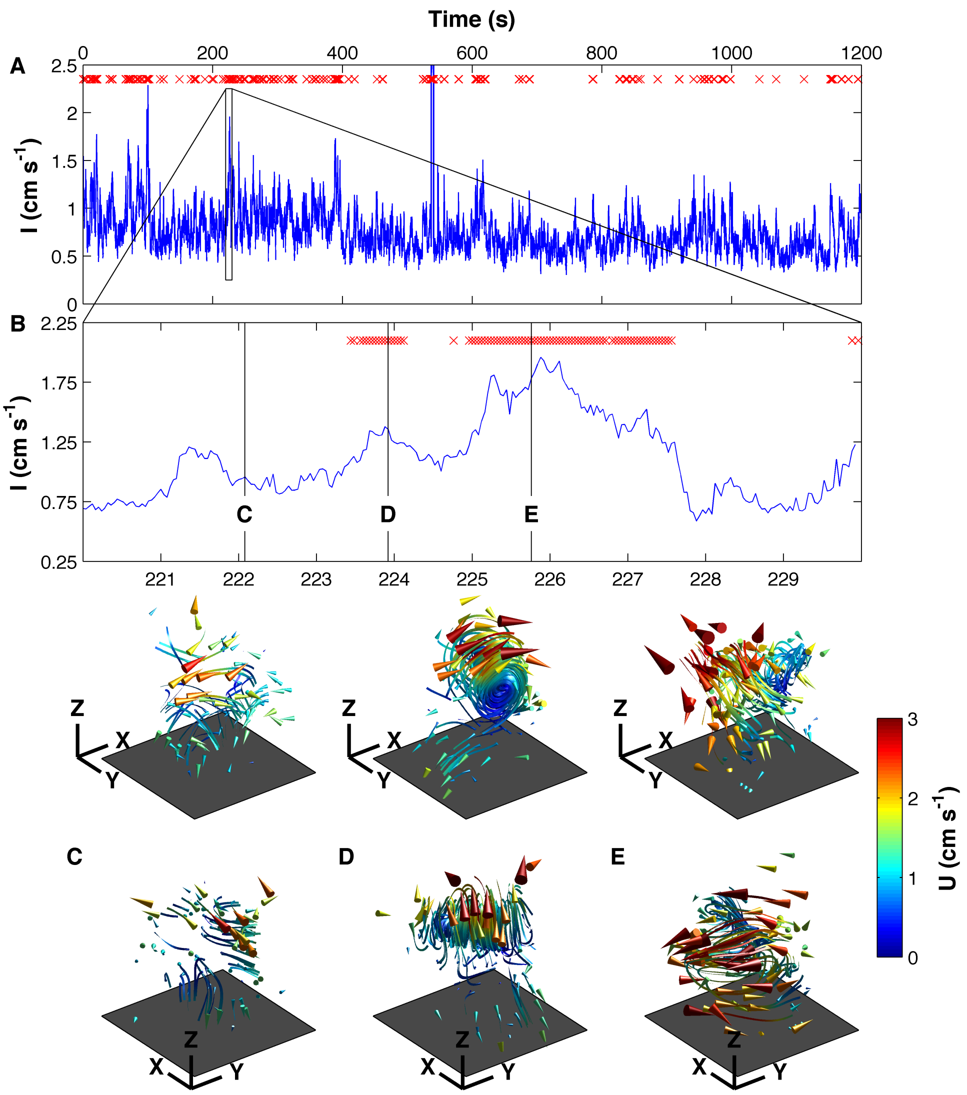

Figure (4.2). (A) Time-series of the sample volume mean turbulence intensity over a 20 min sampling period. The magnified area (B) shows the temporal persistence associated with the passage of coherent structures (marked by red crosses). (C-E) Pairs of simultaneous views of instantaneous sample coherent structures. To reveal the turbulence structures, the sample volume mean velocity components (U, V and W) have been subtracted from each individual vector. Streamlines, starting at the position of each vector and coloured by the local velocity, illustrate the pattern of the flow. The axes are 5 cm in length, with the x-axis aligned with the mean flow.

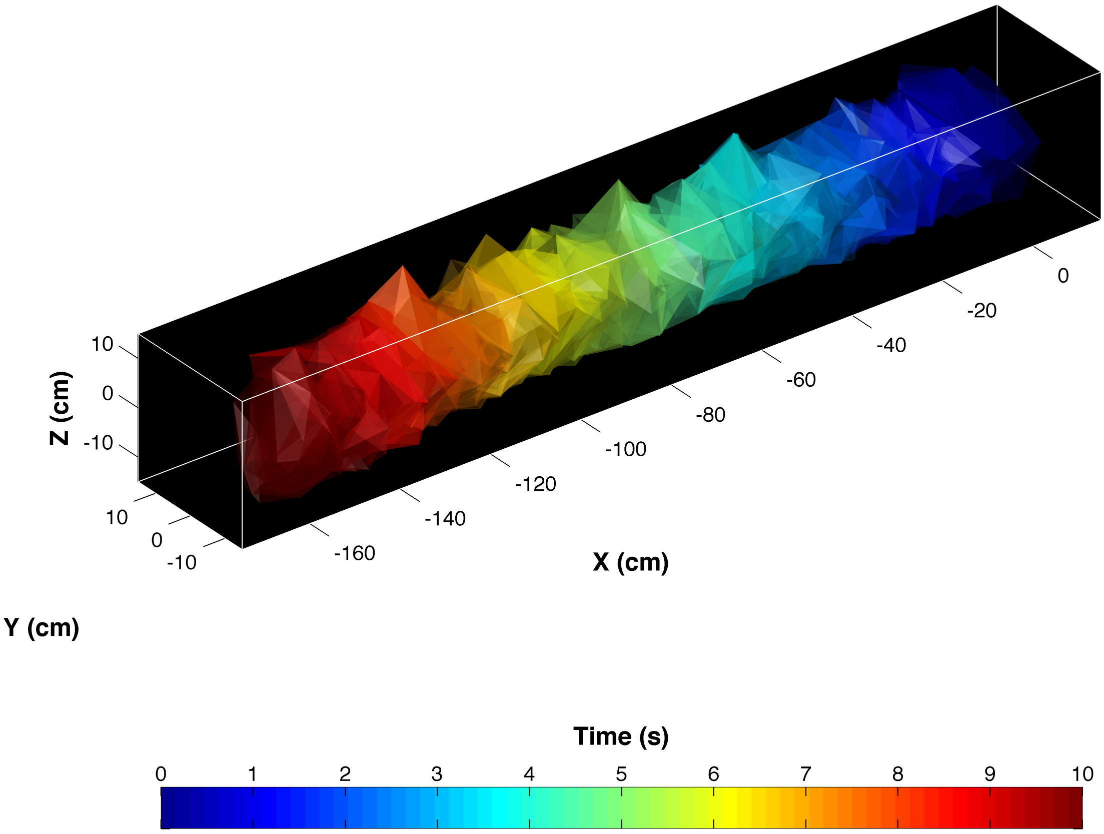

Figure (4.3). Illustration of the spatial projection of temporal data, created using a "frozen-field" approximation and offsetting the convex hull of the individual sample volumes (coloured) by the product of the sample rate and the instantaneous mean velocity.

lower parts, that are similar to the head and neck component of hairpin vortices, respectively. Additionally, others are aligned as along-stream legs (Figure 4.2E), usually inclined from the seabed. This visualisation is, however, limited by the size of the 3D-PTV sample volume, meaning that an extended volume of flow must be considered to be able to see the eddies in context.

The larger scales of the turbulence can be revealed using a "frozen-field" approximation (Taylor's Hypothesis) and offsetting the data within the instantaneous realisations of the sample volume according to the sampling rate and the instantaneous mean velocity. Taylor's Hypothesis ($x_i = U_i t$) allows the spatial projection of temporal data (illustrated in Figure 4.3), assuming the characteristics of the eddies remain unchanged with advection past the sensor and $u^2/U^2 \ll 1$ where, here, $u^2/U^2 = 0.04$ is the ratio of the zero-mean velocity to the mean velocity (Taylor, 1938). Dennis and Nickels (2008) established that this method is accurate over a projection distance of more than 6δ where, here, $\delta = 11.8\,\mathrm{m}$ is the boundary layer thickness.

The velocity flow field associated with each vortex over the 20 min period was reviewed and the hairpin-like structures found to be consistent, within the parameters of a natural environment. As an example, the results of applying this method to the 10 second interval around the structure presented in Figure 4.2D, giving a volume of flow measuring $190 \times 20 \times 20\,\mathrm{cm}^3$, are presented in Figure 4.4A. The large cross-stream vortex is readily visible (II), with a second large inclined along-stream vortex (III) seen upstream and lower down than the first (seen in the side view). The first vortex appears to be curling around from along-stream to cross-stream with distance downstream (seen in the plan view). The two vortices appear intertwined and together have an along-stream length in excess of 50 cm. This coherent structure is surrounded by more quiescent flow conditions (I and IV), although these again contain evidence of small scale vortical motion.

The vorticity characteristics of the extended volume are presented in Figure 4.5. This is the three-dimensional equivalent of the planar evidence provided by Nimmo-Smith et al. (2002, 2005) and Hackett et al. (2011) that have shown the counter-clockwise and clockwise rotation of cross-stream vortices within the bottom boundary layer of the coastal ocean. The large cross-stream vortex (II) exhibits clockwise rotation (negative vorticity) consistent with a “head”.

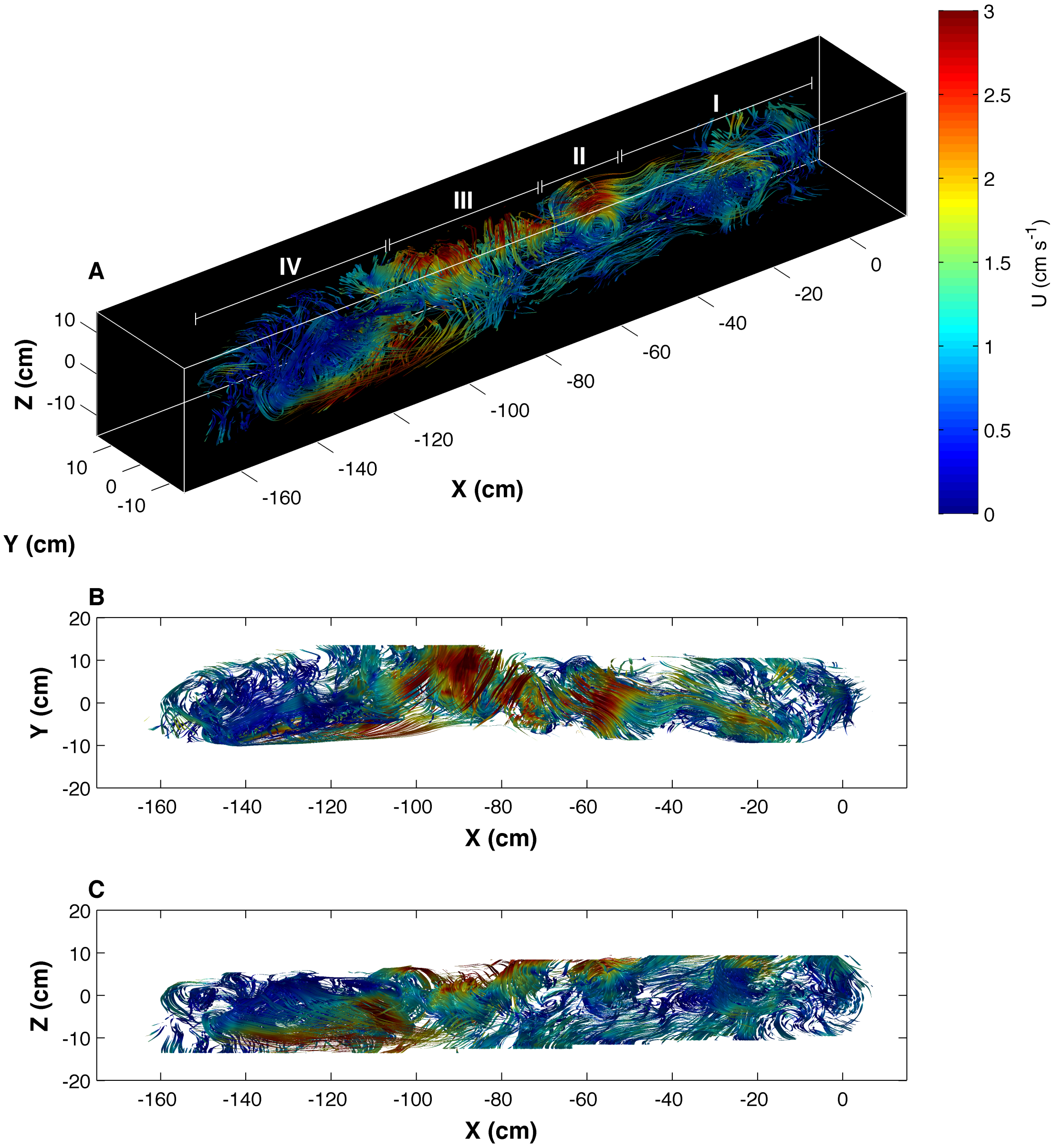

Figure (4.4). Visualisation of velocity of coherent structures within an extended volume created using a frozen field approximation. The velocity is viewed in (A) 3D view; (B) plan view; and (C) side view, respectively. Coherent structures consistent with the head, neck and legs of hairpin vortices occur within sections labelled II and III, surrounded by more quiescent flow (sections labelled I and IV).

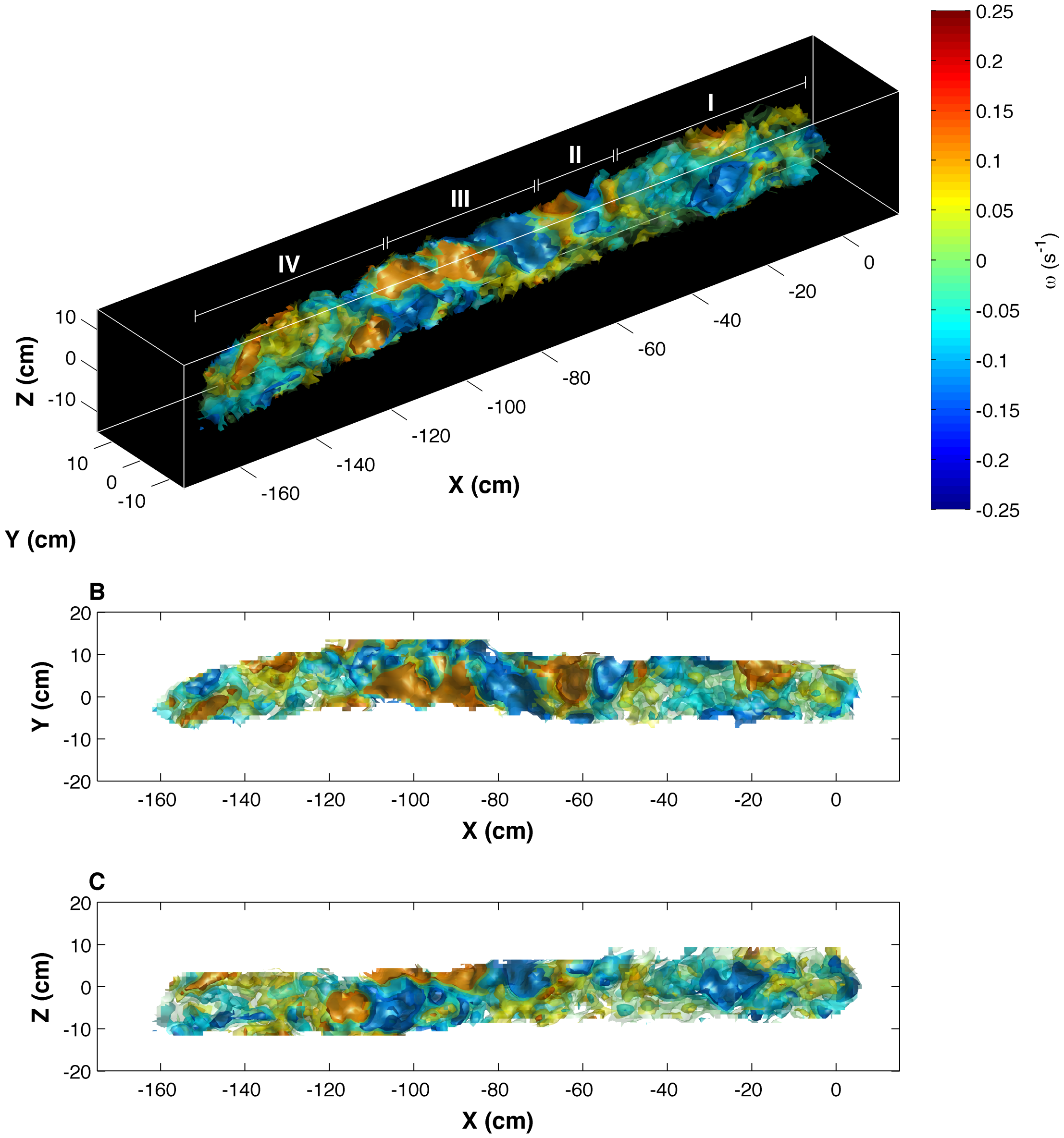

Figure (4.5). Visualisation of vorticity of coherent structures within an extended volume created using a frozen field approximation. The vorticity is viewed in (A) 3D view; (B) plan view; and (C) side view, respectively. Coherent structures consistent with the head, neck and legs of hairpin vortices occur within sections labelled II and III, surrounded by more quiescent flow (sections labelled I and IV).

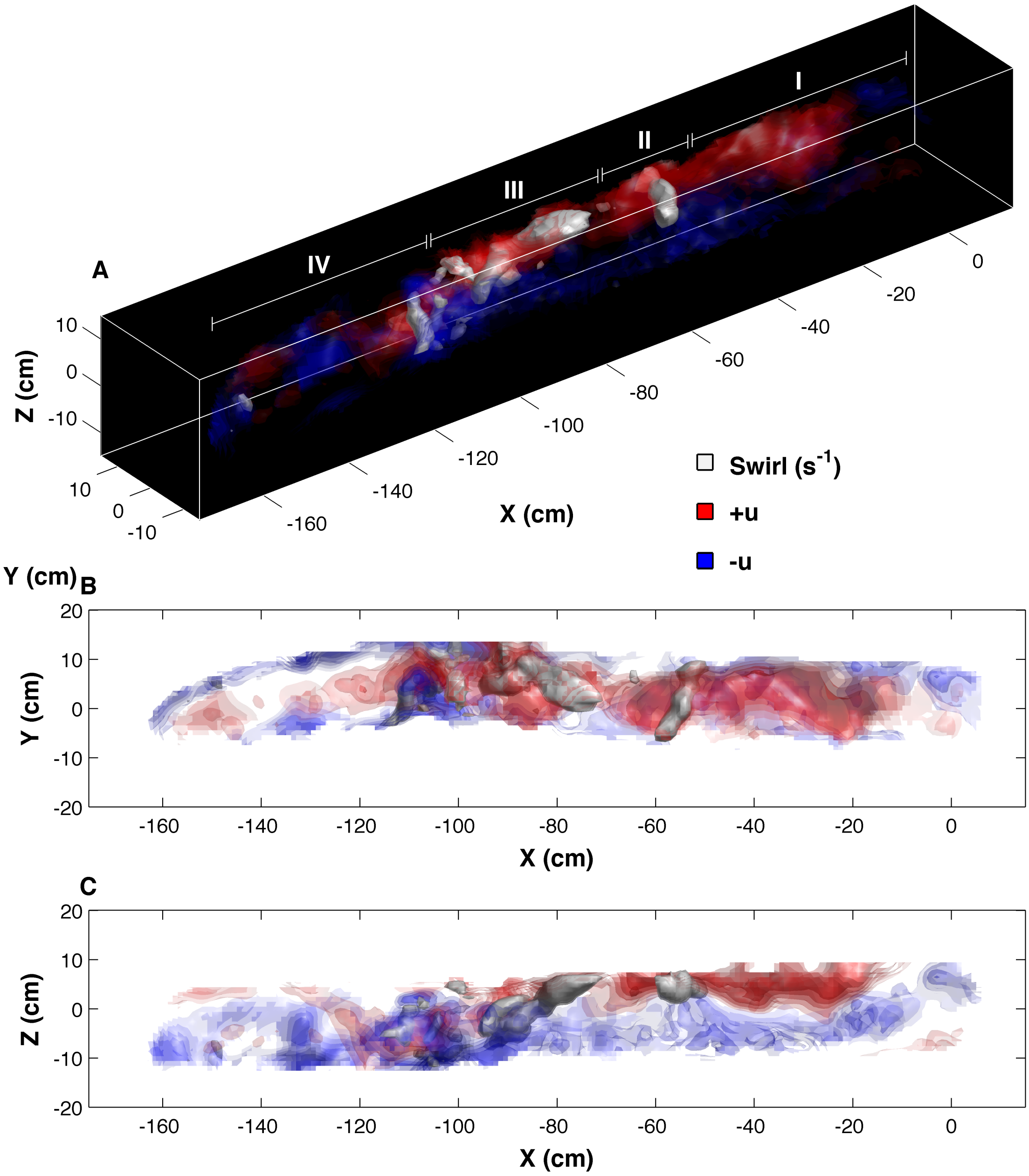

Figure (4.6). Visualisation of swirling strength of coherent structures within an extended volume created using a frozen field approximation. The swirling strength is viewed in (A) 3D view; (B) plan view; and (C) side view, respectively. Coherent structures consistent with the head, neck and legs of hairpin vortices occur within sections labelled II and III, surrounded by more quiescent flow (sections labelled I and IV).

To complement the visualisation of the velocity and vorticity characteristics of these flows, the spatial measurements recorded by the 3D-PTV are used to determine λ_{ci} of the fluid. Figure 4.6 presents the three-dimensional iso-surface of λ_{ci}, as well as the iso-surface of the negative and positive zero-mean along-stream velocity ($u' = \pm 1\ \mathrm{cm\,s^{-1}}$). The agreement between the loci of the vortices and the negative along-stream velocity are completely consistent with the pattern of the velocity flow field expected of a packet of hairpin vortices (Adrian, 2007). These straddle sections of negative zero-mean along-stream velocity, the part of the flow inboard of the head and legs, while the part of the flow outboard of the head and legs has a positive zero-mean along-stream velocity. Examination of the 3D-PTV data suggests that vortices often appear to be asymmetric, i.e. having one leg stronger than the other, giving an appearance similar to a"walking-cane". This cane-like topology is, in fact, the most probable condition (Robinson, 1991), since individual eddies are affected by other large scale motions within the velocity flow field. Similar results have been presented in data collected by Dennis and Nickels (2011a), with an "ideal" hairpin only revealed through conditional sampling.

Statistical evidence of hairpin vortices (or, more accurately, "hairpin-like" vortices - a term encompassing canes, heads, necks, legs and three-quarter-hairpin vortices) in situ, is yielded from an assessment of their alignment and elevation angles from the mean flow direction and the seabed, respectively. To establish the link with laboratory measurements and numerical modelling, it is apparent (on average) that one vortex must be aligned as a cross-stream head for every two aligned as along-stream legs, and that these are inclined from the seabed at an angle of 25-45° (Adrian, 2007). To compute the alignment (α_{xy}) and elevation

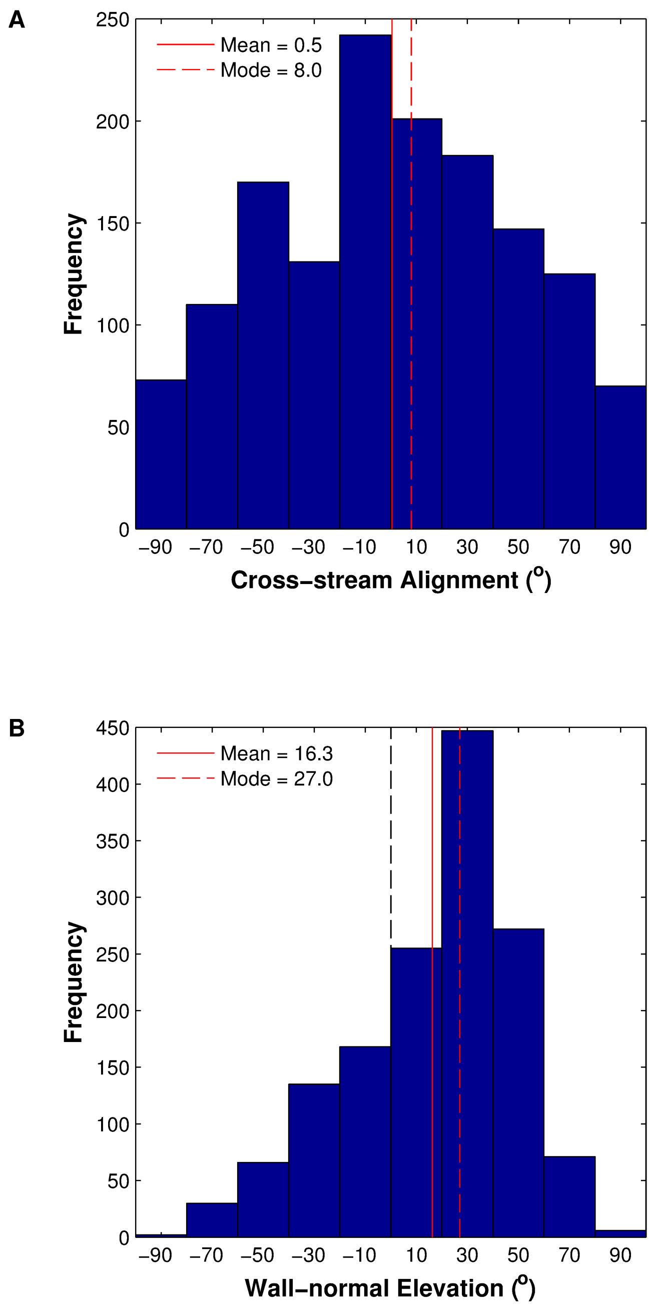

Figure (4.7). (A) Alignment angle (α_{xy}) of vortices relative to the mean flow direction (mean: 0.5 °, mode: 8.0 °, standard deviation: 47.8°). (B) Elevation (or tilt) angle (α_{xz}) of vortices relative to the seabed (mean: 16.3 °, mode: 27.0 °, standard deviation: 32.6°). Sample size = 1452 vortex components (recorded in 1426 instantaneous velocity flow fields).

(α_{xz}) angle, all connected points within the iso-surface of $\lambda_{ci} > 0.25\,\mathrm{s}^{-1}$ are identified. A three-dimensional least-squares line (1st order polynomial) is fitted to each set of connected points and the minimum and maximum along-stream coordinates are used to compute α_{xy} and α_{xy} trigonometrically. Note that data are yielded from an analysis of each set of points from each of the instantaneous realisations of the sample volume to account for the multiple component angles within the vortex (e.g. its head, neck and legs). This is conducted using the 20 min time-series to ensure that statistics are representative. Figure 4.7A presents a histogram of vortex alignment, binned according to their angle (α_{xy}) from the mean flow. The ratio of cross-stream components ($|\alpha_{xy}| > 45$) to along-stream components ($|\alpha_{xy}| < 45$) is 596:856, with a most common alignment of $\alpha_{xy} = 8.0\,°$. Figure 4.7B presents a histogram of vortex elevation, binned according to their angle (α_{xz}) from the seabed. Most of the vortices (72.4 %) are inclined at positive angles, with a most common elevation of $\alpha_{xz} = 27.0\,°$. Setting a higher threshold of λ_{ci} or n suggests that stronger vortices are inclined slightly more steeply. The shapes of the two histograms, as well as the α_{xy} and the α_{xz} angles obtained are in agreement with laboratory measurements. Like here, in data presented by Ganapathisubramani et al. (2006) from a wind tunnel at $Re_\theta = 2,800$ and Dennis and Nickels (2011a) from a water tunnel at $Re_\theta = 4,700$, vortices are seen to be typically aligned in an along-stream direction with a most common elevation angle of $\alpha_{xz} = 38.0\,°$ and $\alpha_{xz} = 26.5\,°$, respectively. These angles fall within the nominal range of 25-45 ° expected of a packet of hairpin vortices, with the exact differences between the two associated with differences in the experimental set-up and, therefore, the way the elevation angles are computed. Similarly, these vortices are predominantly inclined at positive angles from the wall (87.5 %, in data presented by Dennis and Nickels (2011a)), supporting the idea of these boundary layer flows being made up of forward leaning cores.

These results offer the first three-dimensional evidence of hairpin-like vortices in the bottom boundary layer of the coastal ocean. From both the qualitative and quantitative analysis of the characteristics of these vortices recorded in situ, it is clear that data collected through both laboratory and numerical experiments presented in the scientific literature are directly applicable to geophysical scales.

Coherent structures have been identified as important to the resuspension of sediment (Jackson, 1976, Cellino and Lemmin, 2004) and the vortices presented here may act as a transport and trapping mechanism for non-neutrally buoyant material, e.g. oil (Stommel, 1949). The cores of the vortices appear helical (e.g. Figure 4.2D), that may lead to the separation of different-size suspended particles, with smaller particles retained within and transported along the inner cores. It is suggested that this will affect the characteristics of aggregates near the seabed, since a settling floc trapped within a vortex may experience a higher number of collisions with other particles and therefore grow in size – at least up until the point it is sheared across the edge of the vortex.

The Reynolds numbers based on the momentum thickness (and estimated from the ADCP) are of the order of $Re_\theta = 267,970$ (two orders of magnitude higher than reported by Ganapathisubramani et al. (2006) and Dennis and Nickels (2011a) in the laboratory). These moderate levels of turbulence are typical of other flat, coastal sites, under calm conditions, which may be encountered over large areas of the continental shelf. However, further measurements are necessary to extend our understanding of the three-dimensional turbulence characteristics of tidal flows to more extreme conditions, such as those with larger currents and oscillatory flow over bed forms. It is clear the submersible 3D-PTV system offers a viable method to collect this data, although upgrading the hardware to use high-speed cameras will be necessary to allow a faster flow-rate to be sampled. Similarly, it is anticipated that adapting the setup to allow mid-water column measurements will complement the present study by eliciting the three-dimensional turbulence characteristics associated with stratified conditions.

4.2.2 Impact on the Reynolds shear stress

The turbulence associated with coherent structures in boundary layer flows comprises an internal shear stress, whose components are summarised by the tensor:

$$\tau_{ij} = \rho\overline{u_i'u_j'} = \rho\begin{pmatrix} \overline{u_1'u_1'} & \overline{u_1'u_2'} & \overline{u_1'u_3'} \\ \overline{u_2'u_1'} & \overline{u_2'u_2'} & \overline{u_2'u_3'} \\ \overline{u_3'u_1'} & \overline{u_3'u_2'} & \overline{u_3'u_3'} \end{pmatrix} \tag{4.1}$$

where, i is the direction normal to the stress, while j is the direction of the stress (Simpson and Sharples, 2012). Note that $\tau_{ij} = \tau_{ji}$ giving six independent terms. The three terms where $i = j$ are normal stresses, whereas the three terms where $i \neq j$ are tangential stresses.

In ocean flows, turbulence statistics (such as τ_{ij}) are contaminated by surface wave motion that contain much more energy that the turbulence (Trowbridge, 1998). As the tangential stresses are a correlation of two orthogonal components, this is compounded by the unknown alignment of the system to the mean flow.

In recent years, several methods have been developed for the separation of surface wave motion and turbulence from such data, exploiting the statistical characteristics of the velocity flow field (Trowbridge, 1998, Shaw and Trowbridge, 2001, Feddersen and Williams III, 2007). Used for its efficiency, the methods developed by Trowbridge (1998) assumes that the spatial separation between two sensors is larger than the correlation scale of the turbulence but smaller than the inverse wavenumber of the surface wave motion, and that there exists zero-correlation between the surface wave motion and the turbulence. Doing so allows the Reynolds shear stress to be computed from the covariance of the velocity difference between two points, as long as this separation (r_i) is sufficiently large. Under these assuptions, issues arising from the misalignment of these instrumentation to the mean wave flow are eliminated, as long as this angle-error is small ($< 2°$).

Following the implementation by Nimmo-Smith et al. (2002) the velocity is decomposed into $u = \bar{u}_i + \tilde{u}_i + u_i'$, where $\bar{u}_i$ is the mean of the time-series, $\tilde{u}_i$ is the surface wave motion and u_i' is the turbulence. Defining $\Delta u_i = u_i(x_i + r_i) - u_i(x_i)$, the covariance of the difference between the two points, or second-order structure function, $D_{ij}(r_i, x_i)$ is equal to:

$$D_{ij}(r_i, x_i) = \overline{\Delta u_i \Delta u_j} = \overline{[u_i(x_i + r_i) - u_i(x_i)][u_j(x_i + r_i) - u_j(x_i)]} \tag{4.2}$$

Assuming homogeneity,

$$\overline{[u_i(x_i)u_j(x_i)]} = \overline{[u_i(x_i + r_i)u_j(x_i + r_i)]} \tag{4.3}$$

and

$$\overline{[u_i(x_i)u_j(x_i + r_i)]} = \overline{[u_i(x_i + r_i)u_j(x_i)]} \tag{4.4}$$

then

$$D_{ij}(r_i, x_i) = 2\overline{[u_i(x_i)u_j(x_i)]} - 2\overline{[u_i(x_i + r_i)u_j(x_i)]} \tag{4.5}$$

Assuming $\overline{\tilde{u}_i u_i'} \approx 0$ (i.e. zero-corrleation between wave motion and turbulence), this is then decomposed as:

$$D_{ij}(r_i, x_i) = 2\left[\overline{\tilde{u}_i\tilde{u}_j} + \overline{u_i'u_j'}\right] - 2\left[\overline{\tilde{u}_i(x_i + r_i)\tilde{u}_j(x_i)} + \overline{u_i'(x_i + r_i)u_j'(x_i)}\right] \tag{4.6}$$

If the wavelength, λ, of the surface wave motion exceeds the characteristic scale of the turbulence, l, and as long as $r_i \ll \lambda$, then:

$$D_{ij}(r_i, x_i) = \underbrace{2\left[\overline{u_i'u_j'}\right]}_{1} - \underbrace{2\left[\overline{u_i'(x_i + r_i)u_j'(x_i)}\right]}_{2} \tag{4.7}$$

where term 1 (in under-brackets) is the mean stress between the two points, i.e. the quantity of interest, and term 2 (in under-brackets) is the spatial covariance tensor, $R_{ij}(r_i)$, which decreases as r_i increases (and disappears when r_i exceeds the characteristic scale of the turbulence). Therefore, this stress is equal to minus the density multiplied by half the velocity difference (Trowbridge, 1998). Trowbridge (1998) established that this method successfully reduces any wave bias present in the velocity measurements to an acceptably low level under conditions of low surface wave motion, as found at this site.

Using the 3D-PTV data from within the middle part of the sample volume to overcome edge-effects (see Chapter 3), as well as data from the ADV (mounted adjacent to, but 0.45 m downstream of, the 3D-PTV system) $D_{ij}(r_i)$ is computed. Unlike point-measurements, the spatial extent of the 3D-PTV data means that characteristic scale of the turbulence does not have to be known *a priori*, since a separation of up to $r_1 = 48$ cm may be established by multiplying the velocity difference of the two corresponding vectors. At $r_1 \leq 6$ cm, the vectors are located within the 3D-PTV sample volume alone, while at $r_1 \geq 6\,\text{cm}$, the vectors are located between the two sensors. Data from multiple points (but from the same height) are used to increase the number of samples, giving estimates of the six independent terms at the same time.

Figure 4.8 presents the mean spatial profile of $-0.5D_{13}(r_1)$ (Figure 4.8A), $-0.5D_{23}(r_1)$ (Figure 4.8B) and $0.5D_{12}(r_1)$ (Figure 4.8C). Initially, $D_{ij}(r_1)$ increases linearly with r_1, but asymptotes as the separation becomes more comparable to the height of the sample volume above the seabed. As r_1 jumps between the 3D-PTV and the ADV, a difference in $D_{ij}(r_1)$ occurs, but the sign remains constant. Note that at $6\,\text{cm} < r_1 < 42\,\text{cm}$ reliable data are not available and the approximate shape of each profile is represented using a spline.

Interestingly, it is seen that each profile exhibits a maximum at $r_1 \approx 42\,\text{cm}$, whereafter $D_{ij}(r_1)$ decreases. The exact causes of the downturn are unknown, but it is likely that this is amplified as a consequence of the spatial inhomogeneity of the flow (e.g. associated with the alignment of the 3D-PTV system to the mean flow and variability within the upstream topography), as supported by the low correlation ($r^2 = 0.44$) between the instantaneous turbulence intensity between the middle of the 3D-PTV sample volume and the ADV. Although not specifically identified, this downturn is also seen in data collected by Nimmo-Smith et al. (2002) and Nimmo-Smith et al. (2005) under low to moderate flow, albeit to a lesser degree consistent with the 2D-PIV system being aligned to the mean flow. A bias will also be present in point-measurements but, without an array of sensors, this is impossible to detect. However, using the position of the maximum, the Reynolds shear stress may be determined as: $-0.5D_{13} =$

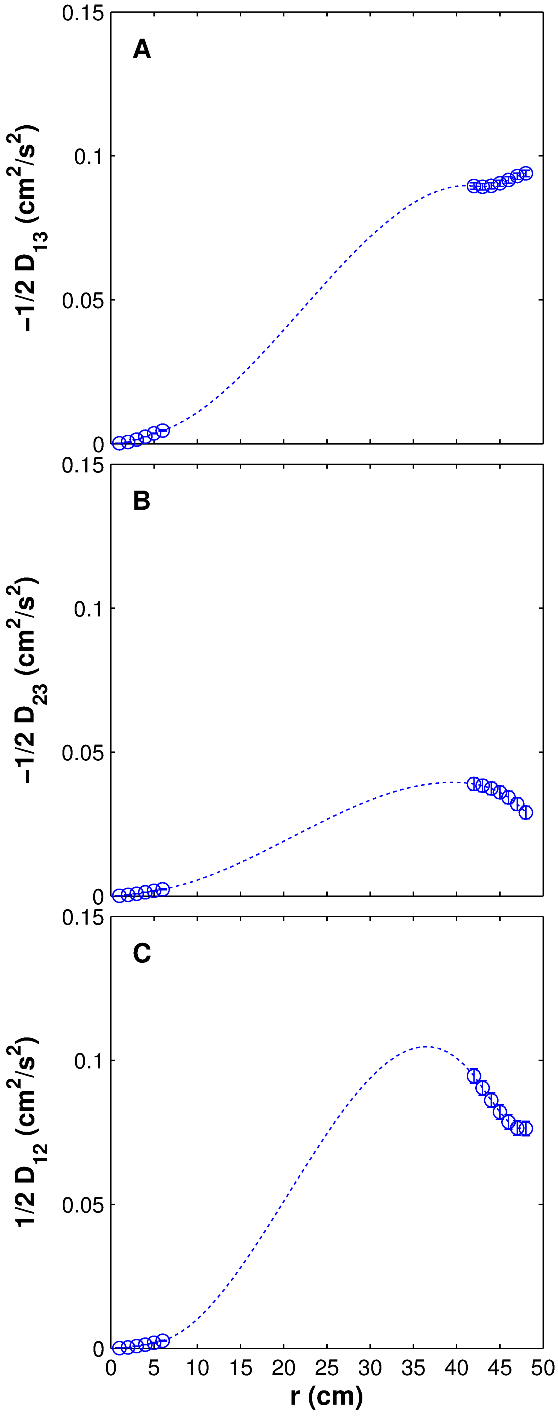

Figure (4.8). Spatial profile of (A) D_{13}, (B) D_{23}, and (C) D_{12} as a function of horizontal separation (r_1) using data from within the middle ($7 \times 7 \times 7\,\mathrm{cm}^3$) part of the 3D-PTV sample volume ($r < 6$), as well as that from an adjacent ADV ($r > 42$). The approximate shape of the profiles between $6 < r_1 < 42$ are represented using a spline.

$0.10\,\mathrm{cm\,s^{-2}}$, $-0.5D_{23} = 0.04\,\mathrm{cm\,s^{-2}}$ and $0.5D_{12} = 0.08\,\mathrm{cm\,s^{-2}}$.

Statistical evidence for the impact of coherent structures on the Reynolds shear stress is yielded from conditional sampling. Here, vortex identification methods are used to classify each of the individual velocity flow fields into groups of low, intermediate and high λ_{ci} using an arbitrary threshold, with each of the groups containing a corresponding third of the data (9997 frames), sorted into ascending order. This is conducted using the 20 min time-series to ensure that statistics are representative. However, as these groups contain 9,997 instantaneous snapshots of the sample volume, this is close to the minimum sampling duration necessary for temporal stability (Chapter 3).

Figure 4.9 presents the mean spatial profile of $-0.5D_{13}(r_1)$ (Figure 4.8A), $-0.5D_{23}(r_1)$ (Figure 4.9B) and $0.5D_{12}(r_1)$ (Figure 4.9C) classified by λ_{ci}. Adrian (2007) highlighted that coherent structures may be responsible for the vertical exchange of momentum via bursts and sweeps that are represented in the Reynolds shear stress. Bursts occur when negative along-stream momentum lifts away from the wall and sweeps occur when positive along-stream momentum moves towards the wall. This motion is associated with the anti-correlation of the u and w components, such that (as here) $0.5D_{13}(r_1)$ is negative. However, as these vortices are not aligned completely along-stream, this motion is also associated with the anti-correlation of the v and w components, such that $0.5D_{13}(r_1)$ is also negative. While conditional sampling reveals that coherent structures contribute most to these Reynolds shear stress components, the difference between the groups of low, intermediate and high λ_{ci} are much less for $0.5D_{13}(r_1)$ than for $0.5D_{23}(r_1)$. This is associated with the shape of the corresponding probability density function

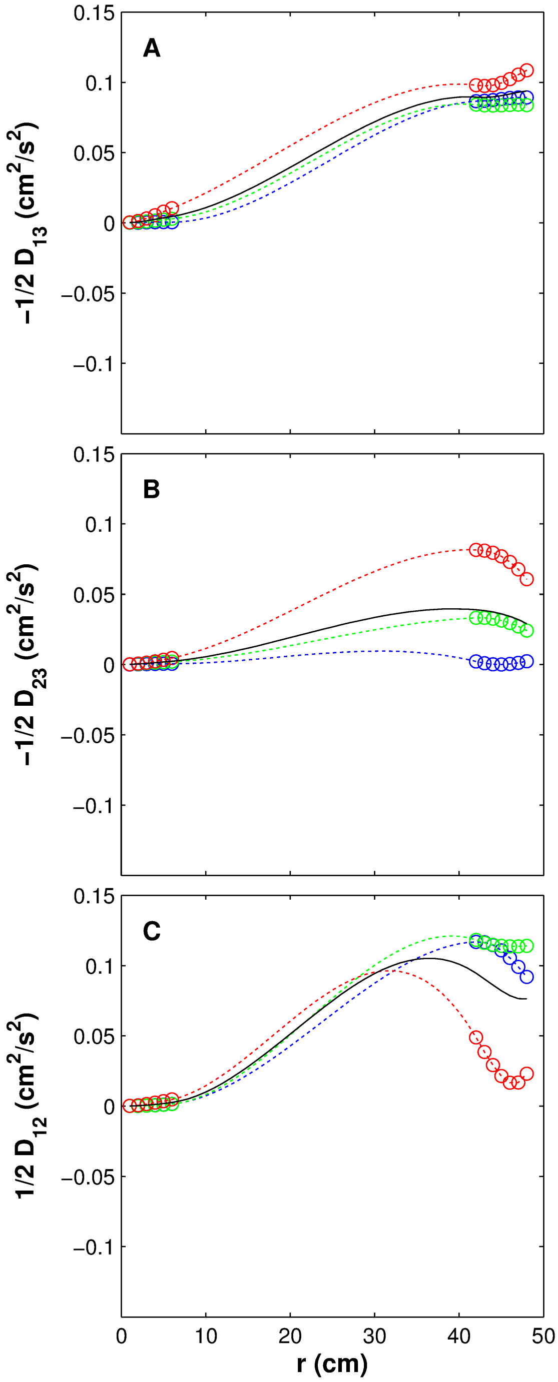

Figure (4.9). Mean spatial profile of (A) $-0.5D_{13}(r_1)$, (B) $-0.5D_{23}(r_1)$, and (C) $0.5D_{12}(r_1)$, classified into groups of low (blue), intermediate (green) and high (red) λ_{ci}. In each plot, the mean spatial profile using all data (irrespective of λ_{ci}) is illustrated in black.

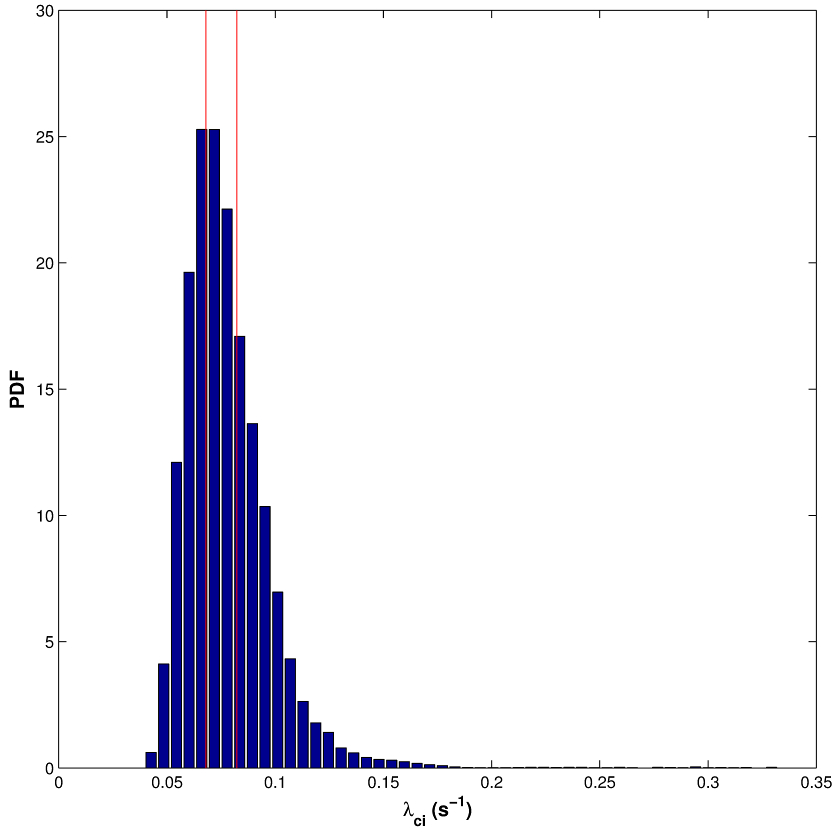

Figure (4.10). Probability Density Function of λ_{ci}, used to classify the flow into groups of low, intermediate and high λ_{ci}. The threshold boundaries are marked by red lines.

(Figure 4.10) as the sample volume mean λ_{ci} of most of the velocity flow fields are close to these threshold boundaries. Conversely, coherent structures seem to have a lesser impact on $0.5D_{12}(r_1)$, however it is likely that this is biased by the alignment of the 3D-PTV system to the mean flow (as a consequence of the spatial inhomogeneity).

The results offer the first three-dimensional view of the impact of coherent structures on the Reynolds shear stress, complementary to data presented by Nimmo-Smith et al. (2005). To definitively unravel the impact of large coherent structures on the Reynolds shear stress, it is necessary to use each of the individual velocity flow fields where a vortex was detected as the criteria for the conditional sampling. However, as this flow is mostly (96.5 %) quiescent, it suggested that this analysis is conducted using a larger database of 3D-PTV measurements to be collected in the future.

4.2.3 Impact on the spatial energy spectra

The turbulence associated with coherent structures in boundary layer flows comprises a continuum of wavenumber scales, whose components are summarised by an energy spectra.

Following the implementation by Nimmo-Smith et al. (2005), this is achieved by mean subtraction, linear detrending and Fourier transformation:

$$F_i(k_1, z) = \sum_n u_i(x_{n,z}) \exp(-ik_1 x_n) \tag{4.8}$$

where k_i is the wavenumber and, unlike Doron et al. (2001), no window function is used. Accordingly, the spectral energy density is:

$$E_{ii}(k_1) = \frac{L}{2\pi N^2} \sum_n F_i(k_1, z) F_i^*(k_1, z) \tag{4.9}$$

where L is the domain length, N is the number of points and F_i^* is the complex conjugate of F_i. Note that these spectra are determined from each instantaneous velocity flow field recorded by the 3D-PTV system prior to averaging over the 20 min period and do not rely on Taylor's Hypothesis (Taylor, 1938).

Using the data from the middle part of the 3D-PTV sample volume, to overcome edge-effects (see Chapter 3), the spatial energy spectra of u_1 (E_{11}), u_2 (E_{22}) and u_1 (E_{33}) in the along-stream (k_1), cross-stream (k_2) and vertical (k_3) direction are determined (Figure 4.11). Where appropriate a 3/4 coefficient is used as (assuming isotropy) the ratios are 4:3 between $E_{ii}(k_1)$ and $E_{ii}(k_j)$, where $i \neq j$.

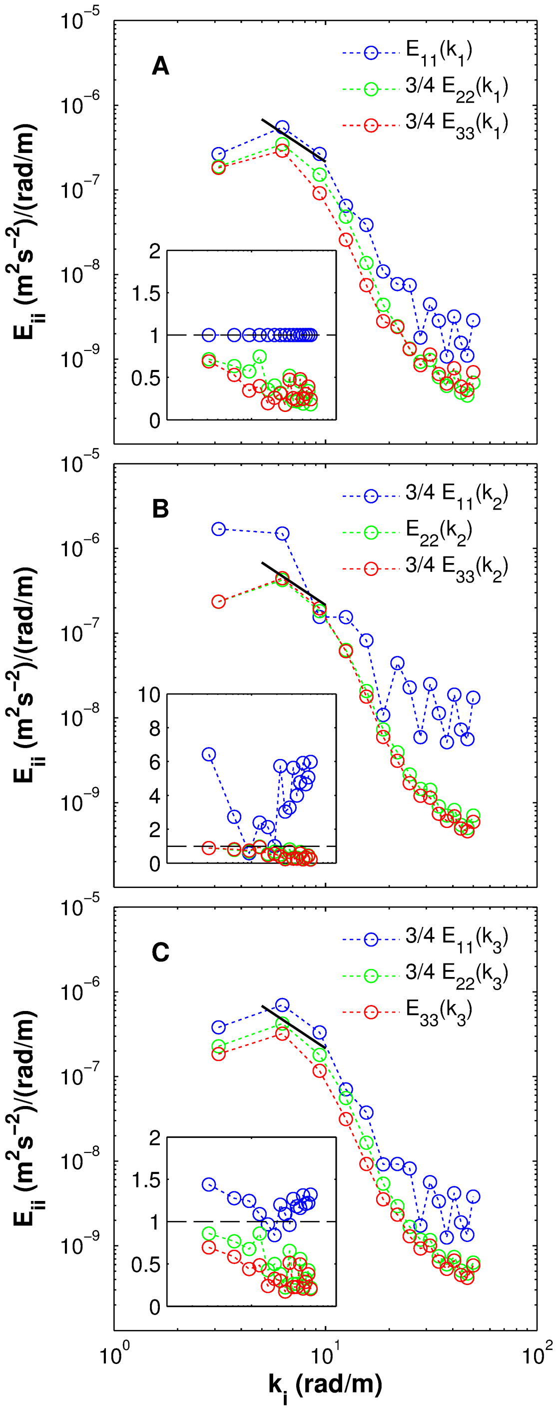

Figure (4.11). Mean spatial energy spectra with direction of integration in the (A) along-stream, (B) cross-stream and (C) wall-normal directions. ***Inset*:** Spectral ratios determined by dividing each component by $E_{11}(k_1)$. Under conditions of isotropy, these ratios should be equal to 1 (dashed line). The solid line with a gradient of -5/3 has been included at the same position in each plot to assist in making comparisons.

Note that both the use of low-pass filtering (to limit the jitter arising from imaging errors) and the use of PEFRA (to account for the increases in noise level associated with tracking unevenly-shaped, naturally-occurring tracers scattered inhomogeneously within the sample volume) have been identified as important stages in 3D-PTV data processing (Chapter 3), however such spatial smoothing causes attenuation at high wavenumber scales and modification of the slope of the spatial energy spectra (Hackett et al., 2009, Vlasenko, 2010). Therefore, these spatial energy spectra are only used to demonstrate the (substantial) anisotropy between the velocity components.

Consistent with past in situ 2D-PIV measurements (Nimmo-Smith et al., 2005, Luznik et al., 2006) the spatial energy spectra of the along-stream velocity component (E_{11}) are higher than the cross-stream (E_{22}) and vertical velocity component (E_{33}), irrespective of wavenumber (Figure 4.11), as highlighted by the spectral ratios determined by dividing each component by $E_{11}(k_1)$ (inset). In general, it is seen that the effect of direction of integration on these spectra are small for the k_1 and k_3 component, with the large difference for the k_3 component associated with the out-of-plane motion being the most difficult of the velocity components to resolve.

Statistical evidence for the impact of coherent structures on the spatial energy spectra is yielded from conditional sampling using the same protocols presented in §4.2.2. Figure 4.12 presents the spatial energy spectra classified by λ_{ci}. In all cases, anisotropy remains at all wavenumber scales and increases as λ_{ci} decreases, suggesting that conditions of anisotropy become more prevalent under more quiescent conditions, while vortices appear to have a regularising effect on

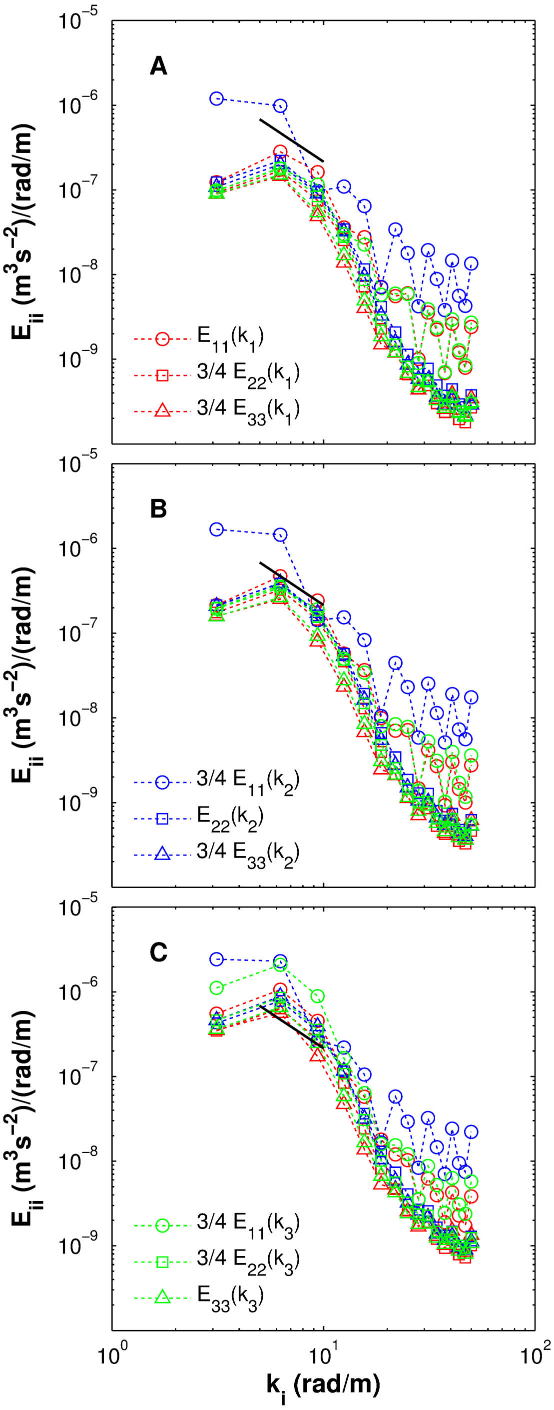

Figure (4.12). Mean spatial energy spectra, classified into groups of low (A), intermediate (B) and high (C) λ_{ci}. The solid line (with a gradient of -5/3) has been included at the same position in each plot to assist in making comparisons. Note that the format of these panels are different to Figure 4.11.

the flow.

As isotropy is a fundamental assumption in most turbulence measurements (e.g. airfoil-type shear sensors), conditions of anisotropy will have significant implications for the sampling of these types of flows in-situ (Smyth and Moum, 2000, Nimmo-Smith et al., 2005). The full consequences of anisotropy on turbulence measurements are considered in detail in Chapter 5.

4.3 Conclusions

3D-PTV measurements have been performed in the bottom boundary layer of the coastal ocean at moderate Reynolds number. The results show that coherent structures, consistent with the hairpin-like vortices highlighted in laboratory measurements and numerical modelling, were frequently present within the logarithmic layer at a height of 0.64 m ($z^+ = 0.35$) above the seabed. These exhibit a modal alignment of $\alpha_{xz} = 8.0\,^\circ$ and a modal elevation of $\alpha_{xz} = 27.0\,^\circ$, with a mean period of occurrence of 4.3 sec, and appear to straddle sections of negative zero-mean along-stream velocity, consistent with an interpretation as "packets". From these direct measurements, it is clear that data collected through both laboratory and numerical experiments are directly applicable to geophysical scales – a finding that will enable the fine-scale details of particle transport and pollutant dispersion to be studied in future.

Conditional sampling of the Reynolds shear stress (without using Taylor's Hypothesis) reveals that coherent structures are responsible for the vertical exchange of momentum via bursts and sweeps (τ_{13} and τ_{23}) and, as such, are the key areas where energy is extracted from the mean flow and into turbulence.

However, these vortices seem to have a lesser impact on τ_{12}, although it is likely that this is biased by the alignment of the 3D-PTV system to the mean flow (as a consequence of the spatial inhomogeneity).

Conditional sampling of the spatial energy spectra (without using Taylor's Hypothesis) reveals that coherent structures appear to have a regularising effect on the flow, although it is clear that (substantial) anisotropy remains at all wavenumber scales. As isotropy is a fundamental assumption in most turbulence measurements (e.g. airfoil-type shear sensors), conditions of anisotropy will have significant implications for the sampling of these types of flows in-situ. The full consequences of anisotropy on turbulence measurements are considered in detail in Chapter 5.

Chapter 5

Implications for turbulence measurements

5.1 Introduction

Measurements of the turbulence kinetic-energy (TKE) dissipation rate are often made to quantify the mixing processes that are essential to explaining the large-scale distribution of biological production, suspended sediments and ocean pollutants. Similarly, on this basis, vertical diffusion coefficients, friction velocities and other important parameters, such as the Kolmogorov microscale, are determined (Osborn, 1980, Dewey and Crawford, 1988).

The TKE dissipation rate, as defined in the Reynolds-averaged TKE equation, is:

$$\epsilon = \nu \overline{\frac{\partial u_i}{x_j}\left(\frac{\partial u_i}{x_j} + \frac{\partial u_j}{x_i}\right)} \tag{5.1}$$

where ν is the kinematic viscosity of the water, u is the velocity component and x is the spatial (cartesian) co-ordinate (Moum et al., 1995). Tensor notation

$(i, j = 1, 2, 3)$ denotes summation over three components, giving nine independent terms (i.e. 12 terms in total) that are almost always impossible to obtain simultaneously using standard instrumentation (Stips, 2005). However, under conditions of isotropy (i.e. the turbulence has no preferred orientation) these terms are simply related by:

$$\epsilon = \underbrace{\frac{15}{1}\nu\left(\overline{\frac{\partial u_1}{\partial x_1}}\right)^2}_{1} = \underbrace{\frac{15}{2}\nu\left(\overline{\frac{\partial u_1}{\partial x_3}}\right)^2}_{2} \tag{5.2}$$

where formula 1 (in under-braces) applies equally to the other two components of strain (i.e. $\partial u_2/\partial x_2$ and $\partial u_3/\partial x_3$) while formula 2 (in under-braces) applies equally to the other five components of shear (i.e. $\partial u_1/\partial x_2$, $\partial u_2/\partial x_1$, $\partial u_2/\partial x_3$, $\partial u_3/\partial x_1$ and $\partial u_3/\partial x_2$). The overbars seen in Equation 5.1 and Equation 5.2 denote that data are averaged over many samples. Typically, these measurements of the individual components of shear, assuming isotropy, are made using airfoil-type sensors (Prandke, 2005), but the possible consequences of using such an assumption under stratified conditions and in boundary layer flows, where the turbulence dynamics are modified, are often neglected.

Numerical modelling (Itsweire et al., 1993, Smyth and Moum, 2000) indicates that turbulence in a stratified shear layer comprises significant anisotropy at all scales, arising from the straining of the flow by the mean shear and the suppression of the vertical motions by the buoyancy forces. Such anisotropy causes a difference in the TKE dissipation rate estimates depending on the shear terms used, with the best shear-based approximations using the $\partial u_1/\partial x_2$ component and the $\partial u_2/\partial x_3$component. Two-dimensional flow visualisation methods (Doron et al., 2001, Nimmo-Smith et al., 2005) have shown that significant anisotropy also exists within the bottom boundary layer of tidal flows, arising from the background shear associated with the proximity of the seabed. Comparisons of TKE dissipation estimates, assuming isotropy and using one component of shear, with estimates based on available in-plane data revealed that, while the instantaneous realisations vary, the averaged estimates for the $\partial u_1/\partial x_3$ component and the in-plane estimates agree and follow the same pattern. At the same time, the averaged estimates for the $\partial u_3/\partial x_1$ component were typically 50% less than that of the in-plane estimates, but also follow the same pattern. However, questions remain as to the magnitude of the errors associated with other components of shear and how these relate to the full three-dimensional form of the turbulence.

The resurgence of measurements utilising airfoil-type shear sensors mounted on Autonomous Underwater Vehicles (AUVs, e.g. Goodman et al. 2006 and moored platforms (Fer and Paskyabi, 2014), renews the need to make certain these systems are used most effectively. Here, we present an analysis of the effect of anisotropy on measurements of the TKE dissipation rate using three-dimensional data collected in the bottom boundary layer of the coastal ocean and consider the consequences for higher-order quantities, such as the Kolmogorov microscale. These measurements shed light on the statistical properties of data traditionally recorded by standard instrumentation, providing crucial in situ evidence to inform the deployment of airfoil-type shear sensors as well as the subsequent interpretation of velocity microstructure data.

5.1.1 Implementation with 3D-PTV

Unlike standard instrumentation, 3D-PTV measurements yield an instantaneous three-dimensional velocity distribution within a sample volume. A sequence of

3D-PTV measurements yield a time-series of the spatial distribution. With such data, it is possible to compute the nine independent terms of the TKE dissipation rate, as well as the isotropic formulae that use one term, directly from the spatial derivatives of velocity without assuming Taylor's Hypothesis. The turbulence statistics are yielded through spatial and / or temporal averaging of these measurements.

In total, nine different estimates for the TKE dissipation rate, assuming isotropy, are compared against that presented in Equation 1 (ϵ_{3D}). These estimates encompass the six components of shear (e.g. $\partial u_1/\partial x_3$) presented in Equation 2 (formula 2), as well as the results of combining two opposing components of shear to represent data obtained from two orthogonally-mounted sensors profiling in the same direction:

$$\epsilon_{\partial x_1} = \frac{15}{4}\nu \left[\overline{\left(\frac{\partial u_2}{\partial x_1}\right)^2 + \left(\frac{\partial u_3}{\partial x_1}\right)^2} \right] \tag{5.3}$$

$$\epsilon_{\partial x_2} = \frac{15}{4}\nu \left[\overline{\left(\frac{\partial u_1}{\partial x_2}\right)^2 + \left(\frac{\partial u_3}{\partial x_2}\right)^2} \right] \tag{5.4}$$

$$\epsilon_{\partial x_3} = \frac{15}{4}\nu \left[\overline{\left(\frac{\partial u_1}{\partial x_3}\right)^2 + \left(\frac{\partial u_2}{\partial x_3}\right)^2} \right] \tag{5.5}$$

Similarly, following Luznik et al. (2006) and assuming the missing cross-stream components are equal to the in-plane components, the equivalent wall-normal two-dimensional Particle Image Velocimetry (2D-PIV) data are estimated using:

$$\begin{aligned} \epsilon_{2D} = 4\nu \Bigg[& \overline{\left(\frac{\partial u_1}{\partial x_1}\right)^2 + \left(\frac{\partial u_3}{\partial x_3}\right)^2 + \frac{3}{4}\left(\frac{\partial u_1}{\partial x_3}\right)^2 + \frac{3}{4}\left(\frac{\partial u_3}{\partial x_1}\right)^2} \\ & \overline{+\left(\frac{\partial u_1}{\partial x_1}.\frac{\partial u_3}{\partial x_3}\right) + \frac{3}{4}\left(\frac{\partial u_1}{\partial x_3}.\frac{\partial u_3}{\partial x_1}\right)} \Bigg] \end{aligned} \tag{5.6}$$

The results are presented on both an instantaneous and a spatially-averaged basis using only the data within the central half ($11 \times 11 \times 11\,\mathrm{cm}^3$, 1331 points) of the sample volume to limit the effect of spatial variation at its edges (Nimmo-Smith, 2008) and ensure that measurements are averaged over a similar number of points (typically $1025 - 2050$ points) as used in processing velocity microstructure data. Note that the mean vector separation ($d = 1$ cm) in these 3D-PTV data are larger than the mean Kolmogorov microscale of $\eta = (\nu^3/\epsilon)^{1/4} = 0.31$ cm by 3.23η. Consequently, the TKE dissipation rate is underestimated. Due to the limited size of the 3D-PTV sample volume, and therefore the resolution of the spatial energy spectra to which comparisons can be made with no assumption of Taylor's Hypothesis (Chapter 4), the magnitude the TKE dissipation rate is underestimated cannot be established. However, past in situ 2D-PIV measurements (Nimmo-Smith et al., 2005), with a larger sample volume (and therefore resolution of the spatial energy spectra), but similar grid resolution and flow conditions, suggest that this difference is likely to be between 26% and 45%. For the present study, this impacts on the exact quantities calculated, however the relationship between TKE dissipation rate, SGS dissipation rate and Kolmogorov microscale estimates (considered in Chapter 5 and Chapter 6) will be unaffected.

5.2 Results and discussion

5.2.1 Dissipation rate estimates

Figure 5.1A presents a time-series of the spatially-averaged TKE dissipation rate over the 20 min period, revealing moderate levels of turbulence ($\langle\epsilon_{3D}\rangle = 1.4855e^7\,m^2\,s^{-3}$). Chapter 4 established the patchiness within this flow is linked to the presence of persistent motions, called eddies or coherent structures, as highlighted in Figure 5.1B for a 10 sec subset of the data. In each plot, every individual velocity flow field where a vortex was detected in Chapter 4 is marked. These large coherent structures occur singly or in groups, consistent with a packet of hairpin-like vortices (Robinson, 1991). The three-dimensional dissipation characteristics of this packet is revealed using a frozen-field approximation (Taylor's Hypothesis) and offsetting the data within individual velocity flow fields according to the sampling rate and the instantaneous mean velocity (Figure 5.1C). Here, a section of high TKE dissipation, associated with the position of the vortices, is readily visible. This is surrounded by sections of lower TKE dissipation, although these again contain small patches of enhanced turbulence associated with simple shear layers arising from the proximity of the seabed or the passage of vortices that are much larger than the limited size of the 3D-PTV sample volume. It is in this context that the ten different estimates of the TKE dissipation rate for two different flow conditions (S1 and S2) are discussed.

Figure 5.2 compares the ten different estimates of the TKE dissipation rate against ϵ_{3D} (Equation 5.1), where $\langle \epsilon_{3D} \rangle = 0.1452e^{-6}\, m^2\, s^{-1}$. These represent the data that are typically obtained from airfoil-type shear sensors profiled in the along-stream direction (Figures 5.2A-C), the cross-stream direction (Figures 5.2D-F) and the vertical direction (Figures5.2G-I), with the wall-normal 2D-PIV view presented in Figure 5.2J and the reference 3D-PTV view presented in Figure 5.2K. Clearly, the panels are not identical (as must be the case were the assumption of isotropy to hold). Under these moderately quiescent conditions, the difference in the TKE dissipation rate varies from a mean underestimate of 83.7% ($\partial u_3/\partial x_1$) to a mean overestimate of 150.1% ($\partial u_1/\partial x_3$). The best horizontal

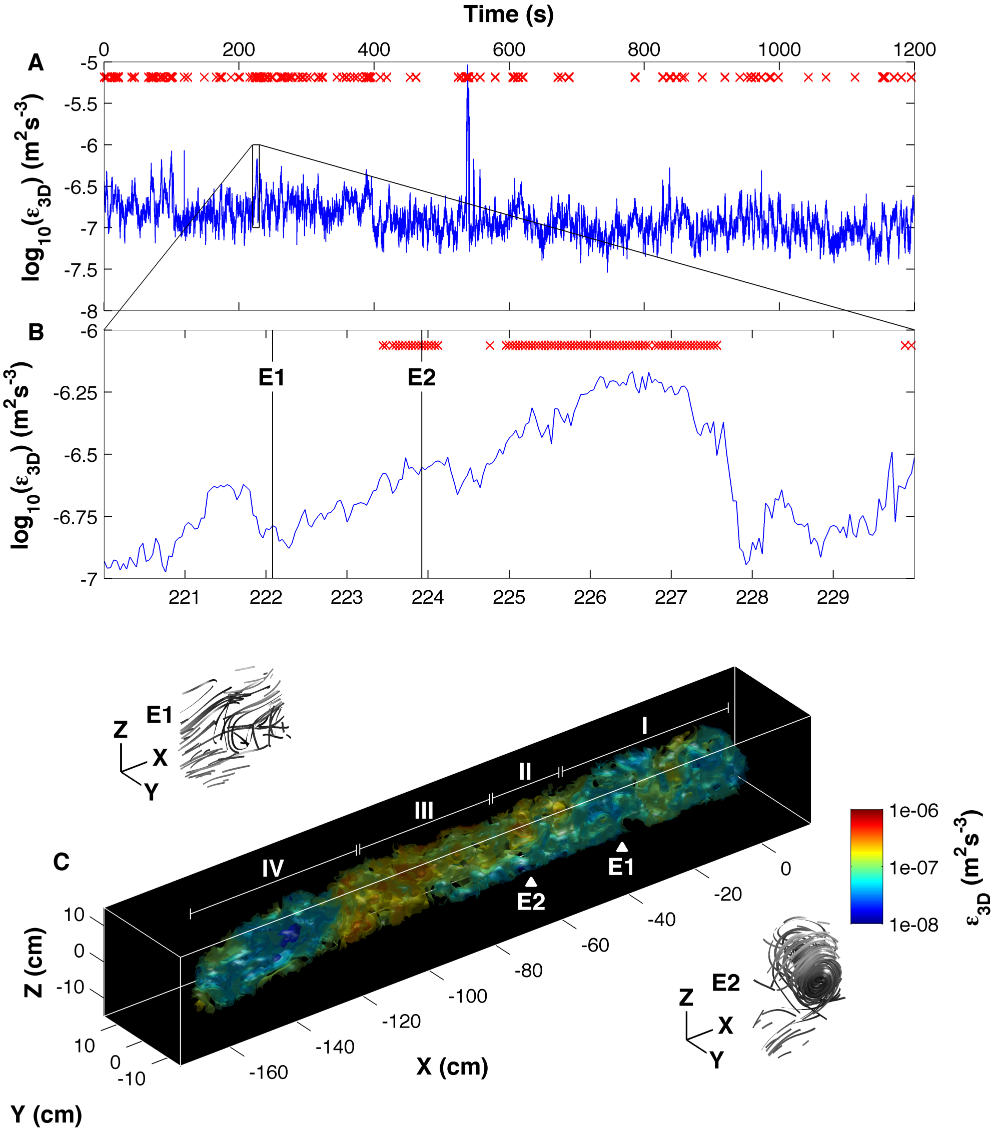

Figure (5.1). (A) Time-series of the sample volume mean TKE dissipation rate over a 20 min sampling period. The magnified area (B) shows the TKE dissipation rate associated with the passage of coherent vortical structures (marked by crosses). (C) Visualisation of the spatial distribution of the TKE dissipation rate within the magnified area, created using a frozen field approximation. An example snapshot of the velocity flow field associated with typical quiescent conditions (S1) and a large cross-stream vortex (S2) is also presented. Streamlines, starting at the position of each particle tracked and coloured by the local velocity (0=black; 2=white) illustrate the pattern of the flow. The axes are 5 cm in length with the x-axis aligned with the mean flow.

and vertical shear-based approximations are by the $\partial u_1/\partial x_2$ ($0.0618e^{-6}\, m^2\, s^{-1}$) and the $\partial u_2/\partial x_3$ ($0.1018e^{-6}\, m^2\, s^{-1}$), while $\partial u_3/\partial x_1$ ($0.0239e^{-6}\, m^2\, s^{-1}$) offers the poorest of these estimates. Therefore, the results of combining two orthogonal components of shear indicate that using $\epsilon_{\partial x}$ will underestimate ϵ_{3D} by 76.1%, $\epsilon_{\partial y}$ will underestimate ϵ_{3D} by 63.8% and $\epsilon_{\partial z}$ will overestimate ϵ_{3D} by 60.1%. As the mean TKE dissipation rate computed for the 2D-PIV view is constructed using the four terms that also appears in $\epsilon_{\partial x}$ and $\epsilon_{\partial z}$, $\langle \epsilon_{2D} \rangle = 0.2390e^{-6}\, m^2\, s^{-1}$. This overestimate of ϵ_{3D} by 64.6% is inflated by a high $\partial u_1/\partial_3$ in particular (as is highlighted in Figure5.2G).

Figure 5.3 compares the ten different estimates of the TKE dissipation rate against ϵ_{3D} (Equation 5.1), where $\langle \epsilon_{3D} \rangle = 0.2301e^{-6}\, m^2\, s^{-1}$. The format of the panels are the same as for the last figure. In contrast to the moderately quiescent conditions, the presence of the large cross-stream vortex appears to have a regularising effect on the flow and, consequently, the TKE dissipation rate varies from a mean underestimate of 77.5% ($\partial u_1/\partial x_2$) to a mean overestimate of 71.5% (ϵ_{2D}). The best horizontal and vertical shear-based approximations are the $\partial u_1/\partial x_2$ ($0.1953e^{-6}\, m^2\, s^{-1}$) and $\partial u_2/\partial_3$ ($0.2774e^{-6}\, m^2\, s^{-1}$), while $\partial u_3/\partial x_2$ ($0.0518e^{-6}\, m^2\, s^{-1}$) offers the poorest of these estimates. However, the results of combining two orthogonal components of shear indicate that $\epsilon_{\partial x}$ will only fractionally underestimate ϵ_{3D} by 1.5% as the low $\partial u_2/\partial x_1$ term ($0.1953e^{-6}\, m^2\, s^{-1}$) is balanced by the high $\partial u_3/\partial x_1$ term ($0.1953e^{-6}\, m^2\, s^{-1}$). At the same time, $\epsilon_{\partial y}$ will underestimate ϵ_{3D} by 46.3% and $\epsilon_{\partial z}$ will overestimate ϵ_{3D} by 43.7%. This is in agreement with the magnitude of the error of these two components presented in Figure 5.3 . Similarly, ϵ_{2D} ($0.3947e^{-6}\, m^2\, s^{-1}$) will also overestimate ϵ_{3D} due to the

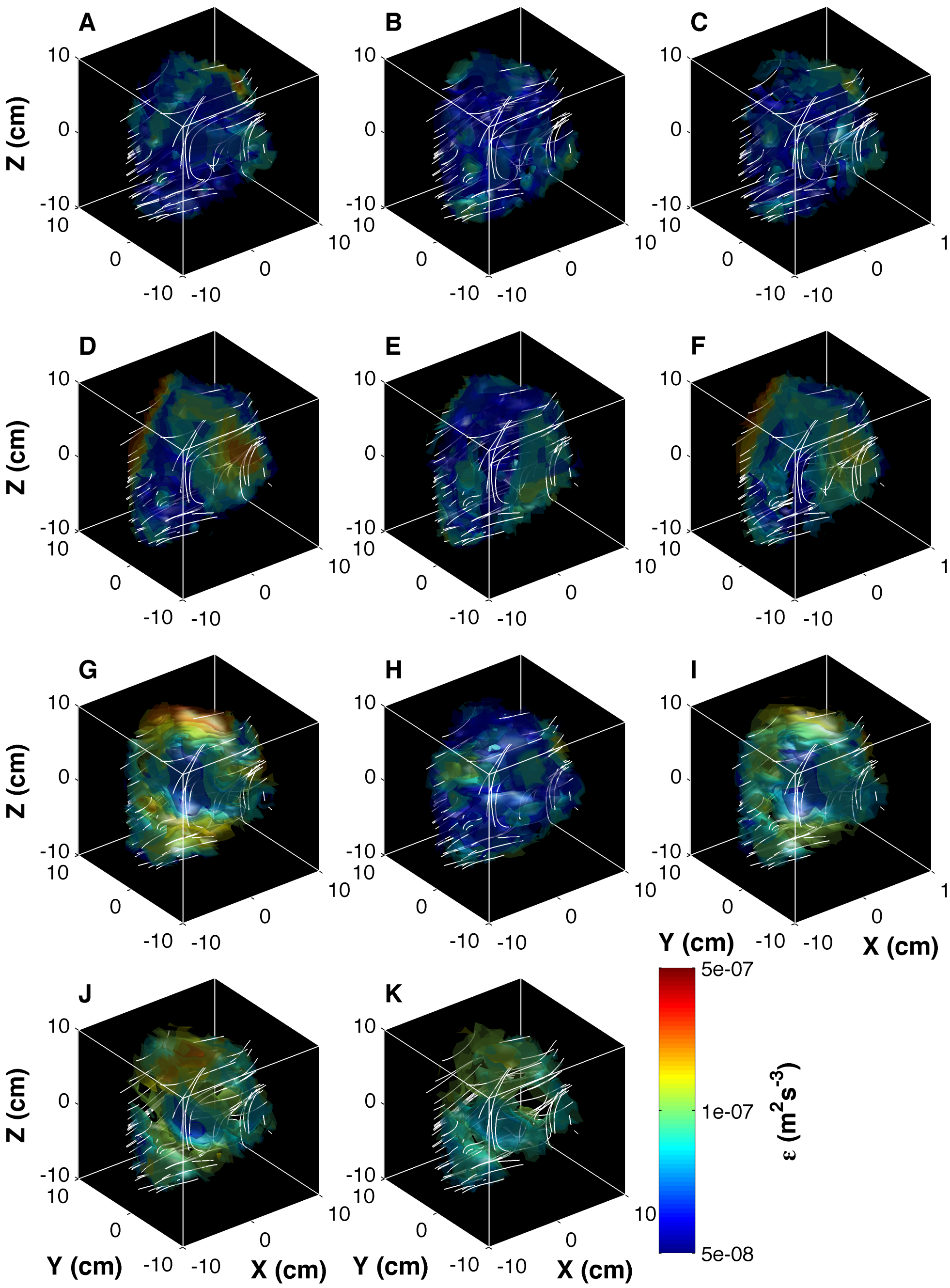

Figure (5.2). Instantaneous dissipation rate within the sample volume at $\langle\epsilon_{3D} >= X\,\mathrm{m}^2\,\mathrm{s}^{-1}1$ obtained using the ten different estimates tested: (A) $\partial u_2/\partial x_1$, (B) $\partial u_3/\partial x_1$ (C) ∂x_1, (D) $\partial u_1/\partial x_2$, (E) $\partial u_3/\partial x_2$, (F) ∂x_2, (G) $\partial u_1/\partial x_2$, (H) $\partial u_2/\partial x_3$, (I) ∂x_3, (J) ϵ_{2D}, the wall-normal 2D-PIV view, and (K) ϵ_{2D}, the reference 3D-PTV view.

three high estimates it comprises. To reconcile the difference in these estimates, the spatial pattern of the TKE dissipation rate within the sample volume must be considered in reference to the three-dimensional form of turbulence. Here, the large cross-stream vortex exhibits a clockwise rotation (negative vorticity), bordered at its upper surface by a section of positive along-stream velocity and at its lower surface by a section of negative along-stream velocity. Therefore, the TKE dissipation rate (ϵ_{3D}) will be higher within the upper half of the vortex, where it is associated with the elevated shear. By rotating around the three-dimensional sample volume, it is seen that this area of slightly higher dissipation extends slightly upstream and lower down than the core, which arises from the opposing burst / sweep motions arising from the induction of the flow surrounding the eddy (Adrian, 2007). The effect of the shear at the upper surface of the vortex is emphasised within the individual terms that make up Equation 5.1 and in $\partial u_3/\partial x_1$ (Figure 5.3B) and $\partial u_1/\partial x_3$ (Figure 5.3G) in particular. As the orientation of this vortex is not completely cross-stream, but at an angle of 77^o from the mean flow direction, the cross-stream vector is non-zero, so an area of higher dissipation is also seen in $\partial u_2/\partial x_1$ (Figure 5.3 A) and $\partial u_2/\partial x_3$ (Figure 5.3H). Note that the small peaks seen in $\partial u_1/\partial x_2$ (Figure 5.3D) and $\partial u_3/\partial x_2$ (Figure 5.3E) occur at the lateral edges of the sample volume and are an artefact of imaging deficiencies associated with the limits of the camera focal range (Nimmo-Smith, 2008).

To complement the assessment of the individual velocity flow fields presented above, Figure 5.4A compares the spatially-averaged time-series of the ten different estimates of the TKE dissipation rate against ϵ_{3D} (Equation 5.1) for the 10 sec subset of the data. Examination of the time-series reveals that ϵ_{2D} and ϵ_{3D}

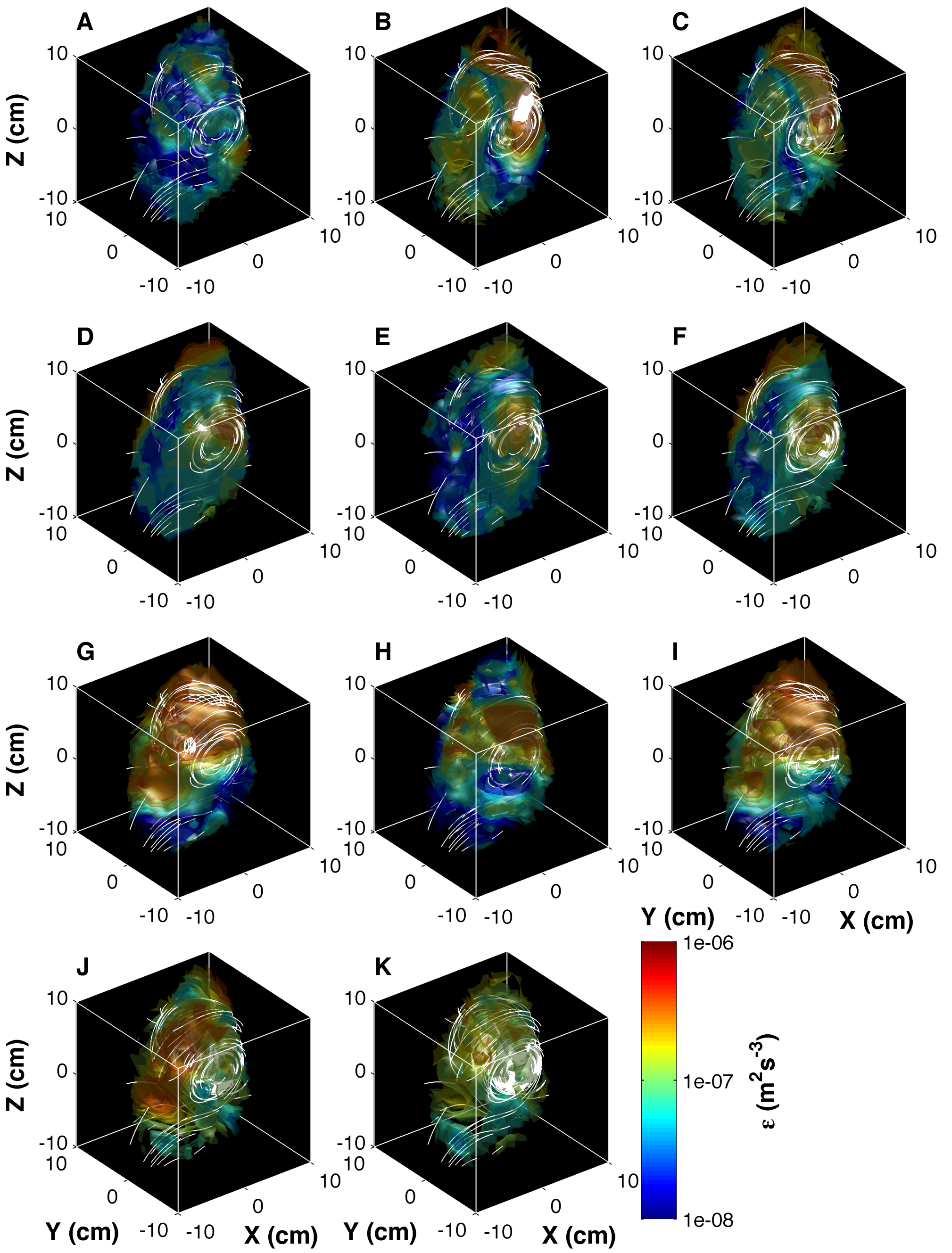

Figure (5.3). Instantaneous dissipation rate within the sample volume at ¡E3D¿=Xm$^2 s^{-1}$ obtained using the ten different estimates tested: (A) $\partial u_2/\partial x_1$, (B) $\partial u_3/\partial x_1$ (C) ∂x_1, (D) $\partial u_1/\partial x_2$, (E) $\partial u_3/\partial x_2$, (F) ∂x_2, (G) $\partial u_1/\partial x_2$, (H) $\partial u_2/\partial x_3$, (I) ∂x_3, (J) ϵ_{2D}, the wall-normal 2D-PIV view, and (K) ϵ_{2D}, the reference 3D-PTV view.

typically are more comparable than an arbitrary selection of one of the terms from each pair of orthogonal components, however this is less significant when the individual components are combined together (i.e. $\epsilon_{\partial x}$, $\epsilon_{\partial y}$ and $\epsilon_{\partial z}$). In agreement with the instantaneous realisations presented in Figure 5.2 and Figure 5.3, $\epsilon_{\partial x}$ indicate a tendency to most significantly underestimate ϵ_{3D}, while $\epsilon_{\partial y}$, $\epsilon_{\partial z}$ and ϵ_{2D} all indicate a (generally) higher level of turbulence, more consistent with ϵ_{3D}.

Statistical evidence of this is yielded from the analysis of the joint probability density functions (Figure 5.4B-5.4K) and frequency histogram (Figure 5.4L) of the spatially-averaged TKE dissipation rate over the 20 min period. As for most (96.5%) of the time the flow has little apparent structure or with scales that are too small for the instrument to resolve clearly (Chapter 4), it is unsurprising that the magnitude of the error in the TKE dissipation rate from assuming isotropy follows the same (mean) patterns as have been identified in Figure 5.4A, where $\langle \epsilon_{\partial x} \rangle = 7.1391^{-8}\, m^2\, s^{-1}$, $\langle \epsilon_{\partial y} \rangle = 1.0088e^{-7}\, m^2\, s^{-1}$, $\langle \epsilon_{\partial z} \rangle = 1.1516e^{-7}\, m^2\, s^{-1}$, $\langle \epsilon_{2D} \rangle = 1.5464e^{-7}\, m^2\, s^{-1}$ and $\langle \epsilon_{3D} \rangle = 1.2253e^{-7}\, m^2\, s^{-1}$. The three estimates using two components of shear all slightly underestimate ϵ_{3D} in an average sense, however these data show $\epsilon_{\partial z}$ will overestimate the turbulence at $\epsilon_{3D} > 5e^{-7}\, m^2\, s^{-1}$. Increasing the number of points within each individual realisation suggests that this pattern is robust. Similarly, in data presented by Nimmo-Smith et al. (2005), $\epsilon_{\partial z}$ offers the best shear-based approximation of the TKE dissipation rate, whereas $\epsilon_{\partial x}$ is consistently 55-64% smaller than ϵ_{3D}. These results are also consistent with data from numerical modelling of turbulence in a stratified shear layer (Itsweire et al., 1993, Smyth and Moum, 2000), where the along-stream derivatives offers the poorest of these estimates.

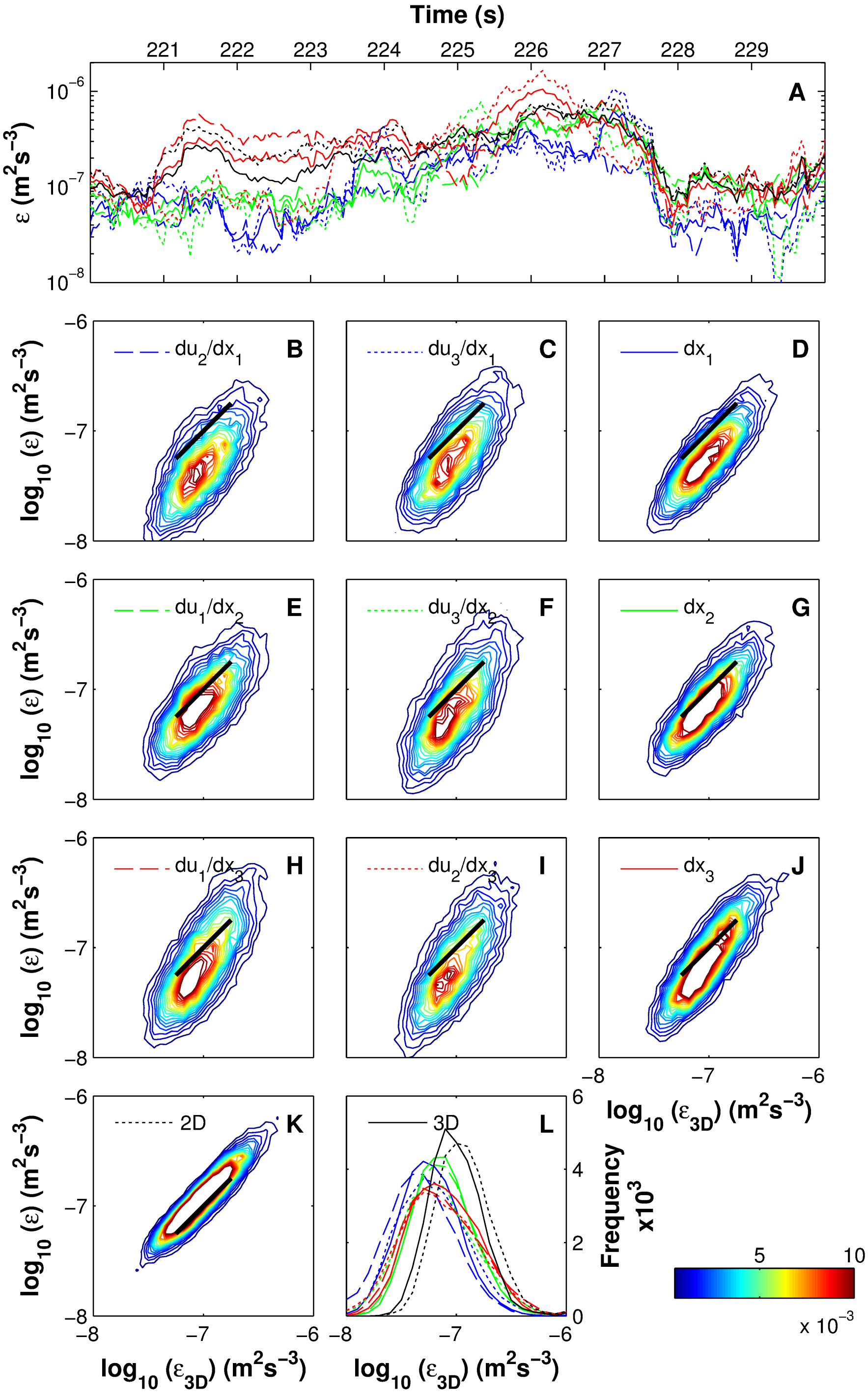

Figure (5.4). (A) Time-series of the sample volume mean of ten different TKE dissipation rate estimates over a 10 sec period. (B-J) JPDF of the sample volume mean of ten different TKE dissipation rate estimates over a 20 min period, as a function of E3D. (K) Histogram of the ten different TKE dissipation rate estimates presented in (B-J). Solid line: 1:1 relationship.

These results show the first assessment of the magnitude of the errors associated with assuming isotropy on shear-based approximations of the TKE dissipation rate using three-dimensional data recorded in situ in the bottom boundary layer of the coastal ocean.

From both the qualitative and quantitative analysis of these estimates, it is clear that they support the validity of measurements using airfoil-type shear sensors mounted on Autonomous Underwater Vehicles (AUVs) and on vertical free-fall platforms. Where data from two airfoil-type shear sensors are available, it is recommended that these are mounted orthogonally to each other and the results averaged to yield a more reliable estimate of the TKE dissipation rate than an arbitrary selection of one of the terms from each pair of orthogonal components. In addition, it is preferable that profiling in the direction of the mean flow be avoided when planning an AUV deployment. As this is also the recommended best practice when sampling turbulence in a stratified shear layer (Itsweire et al., 1993, Smyth and Moum, 2000), the same sampling protocol may be used throughout the water column.

The TKE dissipation rate has been identified as an important quantity used in scaling parameterisations such as the Kolmogorov microscale, η, defined as the ratio between the Kinematic viscosity and the TKE dissipation rate, and represents the size of the smallest eddies within the velocity flow field.. Among other things, the Kolmogorov microscale is thought to impose an upper limit on the mean size of cohesive sediment by eddies which have length scales with similar dimensions to the particles themselves(van Leussen, 1997) – a relationship based on empirical evidence and typically used in modelling flocculation processes

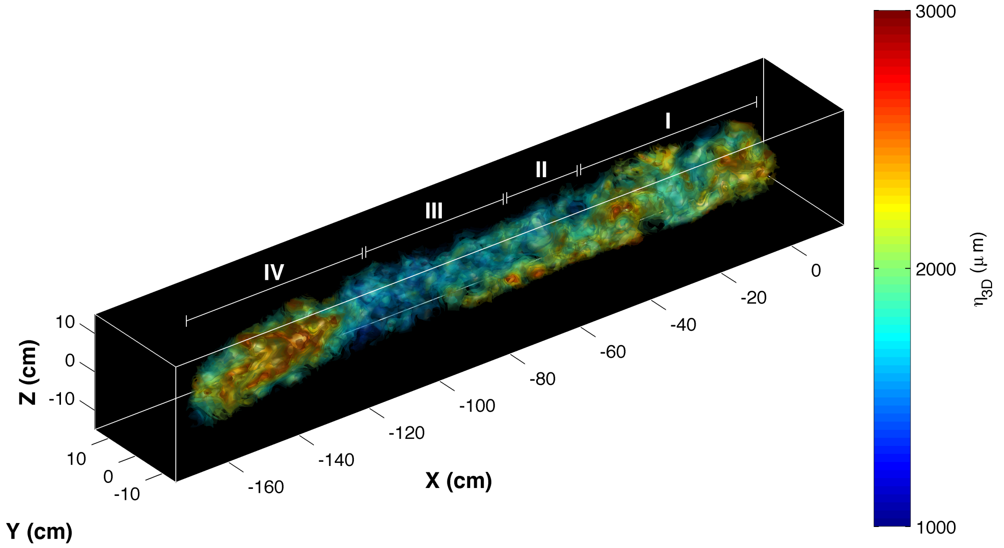

Figure (5.5). Visualisation of the spatial distribution of the Kolmogorov microscale within the magnified area, created using a frozen field approximation.

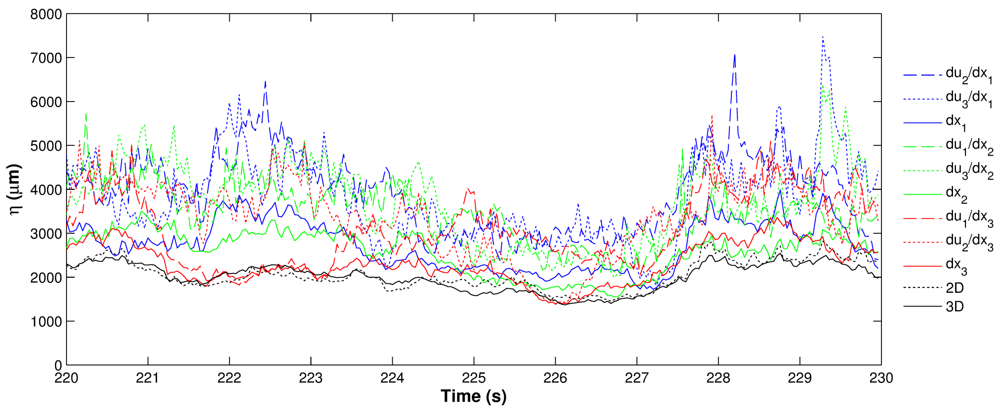

Figure (5.6). Time-series of the sample volume mean of ten different Kolmogorov microscale estimates over a 10 sec period.

(Soulsby et al., 2013).

Figure 5.5 demonstrates the inversion of the TKE dissipation rate into the Kolmogorov microscale for the 10 sec subset of the data presented in Figure 5.1. As expected from this inversion, the Kolmogorov microscale is smallest during the passage of coherent structures, and largest during the quiescent periods, since the smallest length scales occur under conditions of most shear. Examination of the spatial distribution of the Kolmogorov microscale reveals that a difference of

40.5% from the mean typically occur over distances <10 cm. As a consequence, a small offset in the sample volumes measurement instrumentation used to establish the empirical evidence between particles and turbulence (e.g. Cross 2012) will have significant implications for the validity of the results.

To complement the assessment of the extended velocity flow fields presented above, Figure 5.6 compares the spatially-averaged time series of the ten different estimates of the Kolmogorov microscale (using the ten different estimates of the TKE dissipation rate, assuming isotropy) against η_{3D}. As a linear scale is used, the effect of the difference between the Kolmogorov microscale estimates is amplified. The three estimates using two components of shear all substantially overestimate the length scales, while a good agreement exists between η_{2D} and η_{3D}. Over the 20 min period, assuming isotropy in the TKE dissipation rate term used in the computation of η, a difference in results ranging from $2.3e^3\,\mu m$ (η_{3D}) to $3.1e^3\,\mu m$ ($\eta_{\partial x}$) highlights the care that is necessary in interpreting velocity microstructure data under conditions of anisotropy.

The data presented here are typical of moderate levels of turbulence ($Re_\theta = 267,970$) within the logarithmic part of the bottom boundary layer of the coastal ocean that may be encountered over large areas of the continental shelf. The boundary layer thickness based on the momentum thickness (estimated from the ADCP) is $\delta^\theta = 1.9\,m$, and therefore 17% of the water column is also likely to be affected by anisotropy. However, further measurements are necessary to extend our understanding of the severity of these impacts to higher in the water column. It is clear that the submersible 3D-PTV system offers a viable method to achieve this, and adapting the setup to allow mid-water column measurements will complement the present study by eliciting the errors in the TKE dissipation rates associated with stratified conditions.

5.2.2 Sampling decisions

Turbulence statistics are affected by sampling decisions, such as the number and siting of samples recorded and the size of the sample volume (Figure 5.7).

Using an example 10 sec subset of the data recorded by the 3D-PTV system, Figure 5.8A presents the TKE dissipation rate from five individual grid-points and Figure 5.9A presents the TKE dissipation rate within an increasing size of sample volume, over the same period. Figure 5.8B and Figure 5.9B show the impact of these on the Kolmogorov microscale estimates.

As seen from the instantaneous velocity flow fields (e.g. Figure 5.2 and Figure 5.2) presented in §5.2.1, and immediately apparent here, is the high degree of spatial variability associated with turbulence. These discrepancies are most pronounced in one-dimensional measurements (where the difference within the sample volume often exceeds a factor of three) compared to higher dimensional

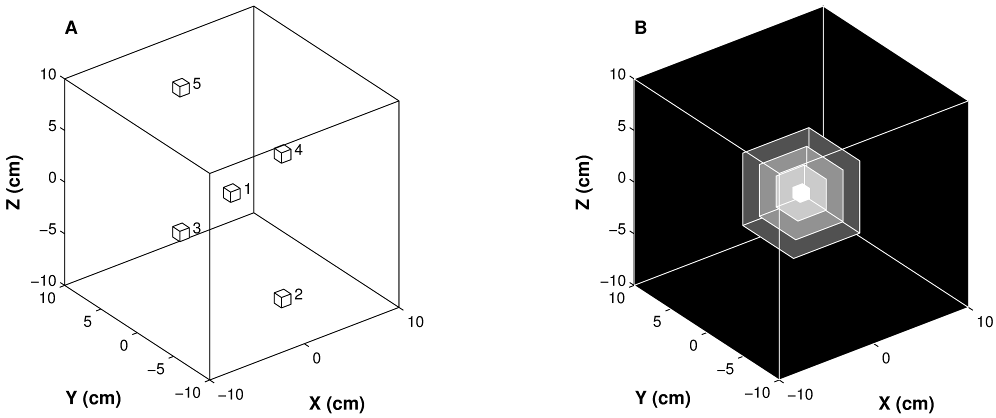

Figure (5.7). The sample volume where the data used in Figure 5.8 and Figure 5.9 were extracted (A) sample volume sites. (B) Sample volume sizes.

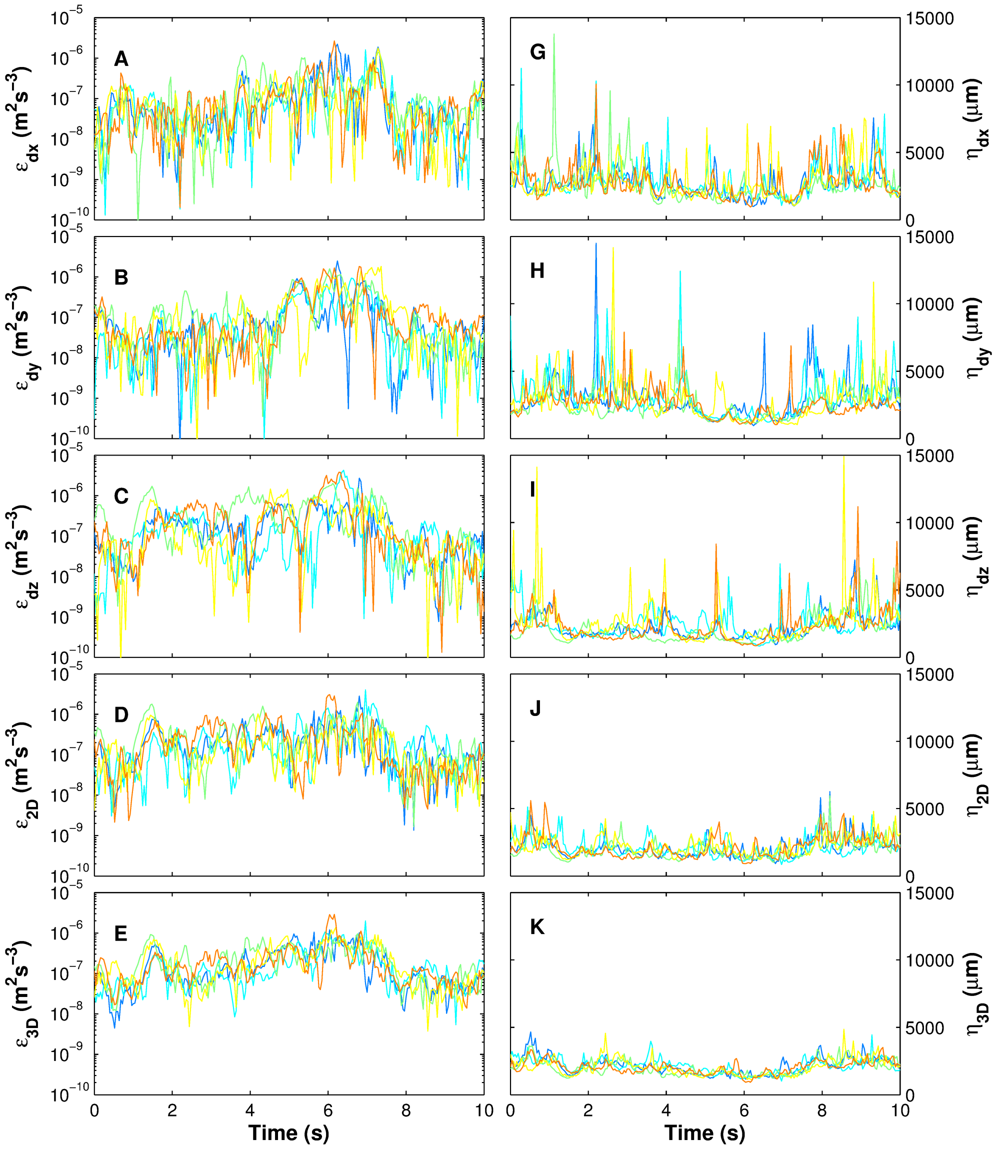

Figure (5.8). (A-E) TKE dissipation rate estimates, and (F-J) Kolmogorov microscale estimates, associated with different sample volume sites (Figure 5.7) determined using five different shear-based formulae.

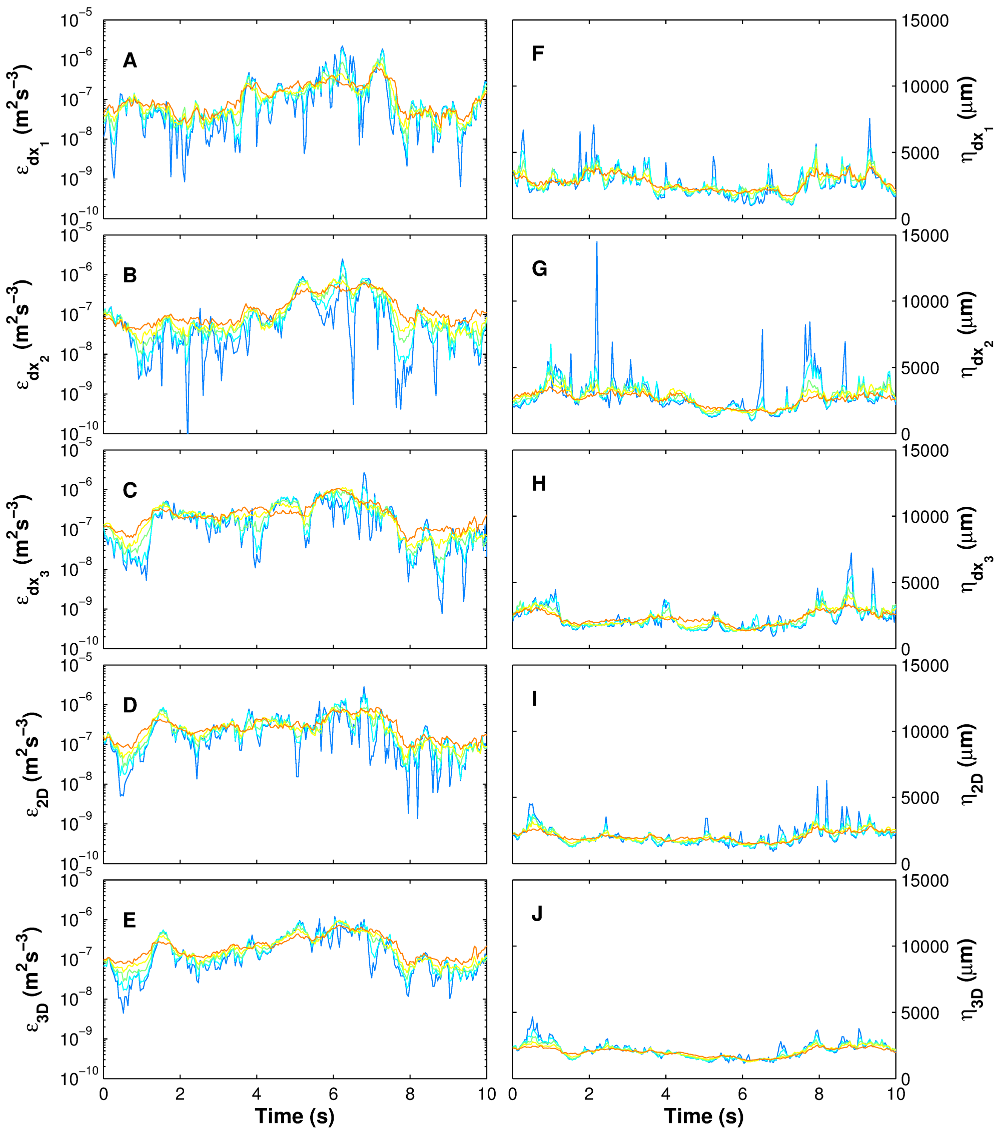

Figure (5.9). (A-E) TKE dissipation rate estimates, and (F-J) Kolmogorov microscale estimates, associated with different sample volume sizes (Figure 5.7) determined using five different shear-based formulae.

estimates, such as data that are typically obtained from 2D-PIV or 3D-PTV. Consequently, the difference also causes spiking in Kolmogorov microscale estimates. In these cases, spatial and / or temporal filtering of one-dimensional measurements is highly beneficial in overcoming siting issues to achieve reliable TKE dissipation rate and Kolmogorov microscale estimates. Applied to airfoil-type shear sensors, this is why a large bin size (typically >0.5 m-1.0 m or 1024-2050 points) is used.

The impact of an increasing size of sample volume was tested between 1 cm^3 (size 1), 27 cm^3 (size 2), 125 cm^3 (size 3), 343 cm^3 (size 4) and 1000 cm^3 (size 5). Here, the largest difference occurs between the two smallest sizes, meaning that using a small amount of averaging to these peaks within a larger volume achieves more representative results. This is important when two sensors with a different size of sample volume (e.g. ADV and ADCP) are used. It is interesting to postulate that, as a consequence of the increased averaging, the comparatively large sample volume size of the ADCP would be of benefit in obtaining reliable TKE dissipation estimates from that instrument. However, to achieve this will need further development of the 3D-PTV system since, in its present configuration, it is limited by the size of the sample volume.

5.3 Conclusions

3D-PTV measurements have been performed in the bottom boundary layer of the coastal ocean at moderate Reynolds number. These data are processed to represent the data that are typically obtained from airfoil-type shear sensors profiled in the along-stream, cross-stream direction and vertical direction. The results indicate a high degree of spatial variability associated with the flow conditions, meaning that it is recommended that pairs of sensors are mounted orthogonally and the measurements averaged. The averaged data supports the validity of measurements obtained by horizontal and vertical profilers, however the along-stream velocity derivatives underestimate the TKE dissipation rate by more than 40% – a factor of two higher than for the equivalent cross-stream and vertical estimates. This has important implications for the deployment of these sensors and the subsequent interpretation of higher-order statistics.

The benefit of increased data in overcoming issues of the siting of samples and the size of the sample volume have been well documented. This is shown using the in situ 3D-PTV data and emphasises the need to be aware of sampling decisions at the outset.

Chapter 6

Implications for numerical modelling

6.1 Introduction

In Large Eddy Simulations (LES), the Navier-Stokes equations are spatially filtered such that the small-scale turbulence characteristics are modelled, while the large-scale turbulence characteristics are resolved, giving:

$$\frac{\partial \tilde{u}_i}{\partial t} + \tilde{u}_j \frac{\partial \tilde{u}_i}{\partial x_j} = \nu \frac{\partial^2 \tilde{u}_i}{\partial x_j \partial x_j} - \frac{\partial \tau_{ij}^{SGS}}{\partial x_j} - \frac{1}{\rho}\frac{\partial \tilde{p}}{\partial x_i} + \tilde{f}_i \tag{6.1}$$

where $\tilde{...}$ indicates that data are spatially filtered over a filter scale of $\triangle$, $\tilde{f}_i$ is a body force and τ_{ij}^{SGS} is a subgrid-scale (SGS) stress used to close Equation 6.1:

$$\tau_{ij}^{SGS} = \widetilde{u_i u_j} - \tilde{u}_i \tilde{u}_j \tag{6.2}$$

This SGS stress is modelled using the parameters from the filtered (resolved) velocity flow field, according to the energy continuity equation, yielded by multiplying Equation 6.1 by u_i, i.e.:

$$\frac{\partial \frac{1}{2}\tilde{u}_i\tilde{u}_j}{\partial t} + \tilde{u}_j \frac{\partial \frac{1}{2}\tilde{u}_i\tilde{u}_j}{\partial x_j} = \frac{\partial}{\partial x_i}\left[\tilde{u}_j\left(2\nu\tilde{S}_{ij} - \tau_{ij}^{SGS} - \frac{\tilde{p}}{\rho}\delta_{ij}\right)\right] - 2\nu\langle\tilde{S}_{ij}\tilde{S}_{ij}\rangle - \epsilon^{SGS} + \tilde{f}_i\tilde{u}_i \tag{6.3}$$

where $\tilde{S}_{ij} = 0.5(\partial\tilde{u}_i/\partial x_j + \partial\tilde{u}_j/\partial x_i)$ is the filtered strain rate, δ_{ij} is the Kronecker delta and ϵ^{SGS} is the SGS dissipation rate that represents the transferral of energy from the filtered (resolved) velocity flow field, or the production of SGS energy:

$$\epsilon^{SGS} = -\tau_{ij}^{SGS}\tilde{S}_{ij} \tag{6.4}$$

Therefore, SGS stress models aim to achieve the correct levels of SGS dissipation that, on average, will be approximately equal to the levels of TKE dissipation, $\epsilon^{TKE} = 2\nu\langle\tilde{S}_{ij}\tilde{S}_{ij}\rangle$, when the filter scale falls within the inertial subrange of the turbulence (Pope, 2000). Note that unlike TKE dissipation, SGS dissipation arises from inviscid processes and can be negative (interpreted as the backscatter of energy from the modelled scale).

As LES is becoming an increasingly important tool in ocean modelling (e.g. Skyllingstad et al. (1999), Skyllingstad and Wijesekera (2004), Noh et al. (2004), Min and Noh (2004), Li et al. (2005)), it is necessary to test the SGS stress and SGS dissipation estimates from these models using experimental data (e.g. Liu et al. 1994, 1999, Tao et al. 2002, Chen et al. 2005, 2006). Two dimensional flow visualisation methods (Nimmo-Smith et al., 2005, 2007) have shown that the difference between the SGS dissipation rate and TKE dissipation rate in the bottom boundary layer is small for strong tidal flows but large for weak to moderate tidal flows. Conditional sampling based on vorticity reveals that this difference is associated with the lack of coherent structures. However, questions remain as to the impact of the missing out-of-plane component on these results.

Here, an analysis of the SGS stress and SGS dissipation rate using three-dimensional data collected in the bottom boundary layer of the coastal ocean are presented for the four most popular models used (i.e. the Smagorinsky model with static coefficients, the Smagorinsky model with dynamic coefficients, the Structure Function model and the Nonlinear model). An outline of each of the models is presented below.

6.1.0.1 Smagorinsky model with static parameters

The Smagorinsky model (Smagorinsky, 1963) for the deviatoric part of the SGS stress $(\tau_{ij} - (1/3)\tau_{kk}^{SGS}\delta_{ij})$ is:

$$\tau^S = -2\underbrace{(C_s\Delta)^2|\tilde{S}|}_{\nu}\tilde{S}_{ij} \tag{6.5}$$

where term ν (in underbraces) is the scalar eddy viscosity, $|S| = \sqrt{(2\tilde{S}_{ij}\tilde{S}_{ij})}$ is the strain rate magnitude, and C_s is the (static) Smagorinsky coefficent defined, such that $\epsilon^S = -\tau_{ij}^S\tau S_{ij}$, i.e.:

$$C_s^2 = \frac{\langle\epsilon^{SGS}\rangle}{\Delta^2\langle|S|^3\rangle} \tag{6.6}$$

where $\langle...\rangle$ represents ensemble averaging. Typically, $C_s = 0.16$ (Lilly, 1967). As C_s is, by definition, inherently positive, this Smagorinsky model is absolutely dissipative and energy only transferred from the filtered (resolved) scale to the modelled scale.

6.1.0.2 Smagorinsky model with dynamic parameters

While the Smagorinsky model is often used for its simplicity, robustness and lack of numerical instabilities, phenomena such as shear and stratification affect the SGS dissipation rate such that a constant coefficient is not appropriate. To overcome these limitations, Germano et al. (1991) proposed a dynamic coefficient, determined from the filtered (resolved) scale:

$$C_d^2 = \frac{\langle L_{ij} M_{ij} \rangle}{\langle M_{ij} M_{ij} \rangle} \tag{6.7}$$

where, $L_{ij} = \overline{\tilde{u}_i \tilde{u}_j} - \bar{\tilde{u}}_i \bar{\tilde{u}}_j$ and $M_{ij} = -2\Delta^2(\alpha^2 |\bar{\tilde{S}}| \bar{\tilde{S}}_{ij} - \overline{|\tilde{S}| \tilde{S}_{ij}})$ and the overbar denotes test filtering at a scale $(\alpha\Delta)$, yielded from the assumption of scale invariance, i.e. $C_d^{\Delta} = C_d^{\alpha\Delta}$ (Meneveau and Katz, 2000, Porte-Agel et al., 2000). This is associated with a highly variable viscosity field, where the SGS dissipation can be negative, causing numerical instabilities and increasing the SGS dissipation in the positive and negative ranges. The solution to this is the use of averaging, with the remaining (negative) SGS dissipation quantities clipped to zero.

6.1.0.3 Structure function model

Assuming a cut-off wavenumber in the inertial subrange of the energy spectra, Metais and Lesieur (1992) expressed the energy at the cutoff using a second order structure function at the filtered (resolved) scale, with the SGS stress determined by:

$$\tau_{ij}^{SF} = -2K_m \tilde{S}_{ij} \tag{6.8}$$

where $K_m = 0.063\Delta[F(x)]^{0.5}$ and $F(x)$ is the second order structure function:

$$F(x) = \langle |u_i(x_i) - u_i(x_i + r_i)| \rangle^2 \tag{6.9}$$

Piomelli (1999) established that, on an even grid, the structure function model is equal to the Smagorinsky eddy-viscosity model with the strain rate replaced by the velocity gradient tensor, i.e. $F = |S|^2 + |\omega|^2$. However, comparisons suggest that this Structure Function model is less dissipative under conditions of isotropy but more dissipative under conditions of shear, where typically $C_s = 0.18 - 0.23$.

6.1.0.4 Nonlinear model

The nonlinear model is known to perform significantly better in predicting the SGS stresses that the Smagorinsky eddy-viscosity model, while overcoming the computational cost of the secondary filtering needed for the dynamic model:

$$\tau_{ij}^{NL} = C_{NL}\Delta^2 \frac{\partial \tilde{u}_i}{\partial x_k} \frac{\partial \tilde{u}_j}{\partial x_k} \tag{6.10}$$

where C_{NL} in the Nonlinear coefficient defined such that $\epsilon_{NL} = -\tau_{ij}^{NL}\tilde{S}_{ij}$. In this model the SGS dissipation can be negative, causing numerical instabilities and increasing the SGS dissipation in the positive and negative ranges. The solution to this is the use of a mixed model, by combining the Nonlinear model and the Smagorinsky eddy-viscosity model. The eddy-viscosity term increases the SGS dissipation (as, by definition, this is inherently positive) and therefore decreases the backscatter of energy from the modelled scale.

6.1.1 Implementation with 3D-PTV

Unlike standard instrumentation, 3D-PTV yields an instantaneous realisation of the three-dimensional velocity flow field within the sample volume. A sequence of measurements yields a time-series of these spatial velocity data. With such data, it is possible to test each SGS stress model and SGS dissipation rate estimates for LES.

Following the implementation by Nimmo-Smith et al. (2007), the velocity is filtered using a box (top hat) filter, i.e.:

$$\tilde{u}_i(x) = \int_{-\infty}^{\infty}\int_{-\infty}^{\infty}\int_{-\infty}^{\infty} u_i(x - x')F_{\Delta}d^3x \tag{6.11}$$

$$F_{\Delta}(x) = \begin{cases} K_1 & \text{if } |x| < \Delta/2 \\ 0 & \text{otherwise} \end{cases} \tag{6.12}$$

where $i = 1, 2, 3$ and K_1 is a constant to ensure that the integral of the filter equals unity.

To represent data that are typically obtained from LES, center-differencing of $\triangle$= 3, 5 and 7 grid-points ($d = 1$) are used, based on the data available. Note that while center-differencing of 2$\triangle$ is more appropriate, Nimmo-Smith et al. (2007) established that the impact of the discrepancies are small and do not justify the loss of data that arises from the edge effects of the coarser differencing.

6.2 Results and discussion

6.2.1 Dissipation rate estimates

Figure 6.1A presents a time-series of the spatially-averaged SGS dissipation over the 20 min period, using a filter scale of $\triangle/d = 5$. Chapter 4 established that the

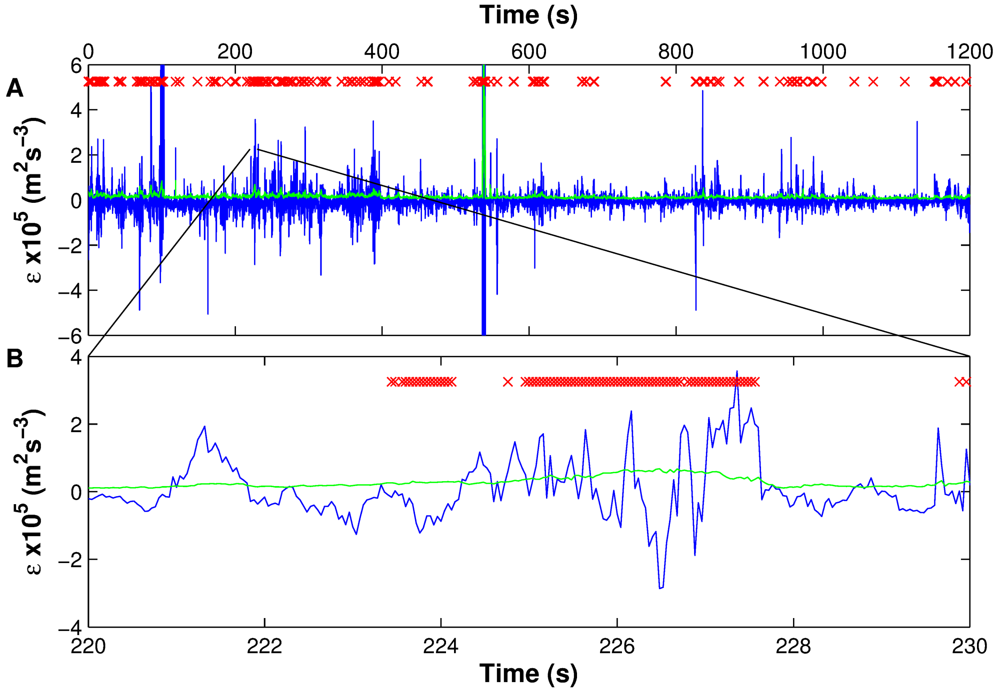

Figure (6.1). (A) Time-series of the sample volume mean SGS dissipation rate (blue) and the sample volume mean TKE dissipation rate (green) over a 20 min sampling period. The magnified area (B) shows the temporal persistence associated with the passage of coherent structures (marked by red crosses).

patchiness within this flow is linked to the presence of persistent motions, called eddies or coherent structures, as highlighted in Figure 6.1B for a 10 sec subset of the data. In each plot, each individual velocity flow field where a vortex was detected in Chapter 4 is marked. These large coherent structures occur singly or in groups, consistent with a packet of hairpin vortices (Robinson, 1991). As for the TKE dissipation (also included on each plot), a section of high amplitude SGS dissipation fluctuation, associated with the position of the vortices, is readily visible. This is surrounded by sections of lower SGS dissipation, although these again contain small patches of enhanced turbulence associated with simple shear layers arising from the proximity of the seabed or the passage of vortices that are much larger than the limited size of the 3D-PTV sample volume.

The agreement between the loci of the vortices and the high amplitude positive and negative SGS dissipation signal indicates that the presence of these large coherent structures are accompanied by both a forwardscatter and a backscatter of energy. However, the impact of spatial filtering on the limited resolution of the 3D-PTV grid ($1 \times 1 \times 1\,\mathrm{cm}^3$) make it impossible to be more specific as to where the peaks in positive and negative SGS dissipation occur within these vortices.

Consistent with past in situ 2D-PIV measurements (Nimmo-Smith et al., 2007), the time average of the SGS dissipation rate ($\epsilon^{SGS} = 6.1130e^{-8}$) is an order of magnitude less than the TKE dissipation rate ($\epsilon^{SGS} = 1.4855e^{-7}$) over the same 20 min period. Note that substantial discrepancies between ϵ^{SGS} and ϵ^{TKE} have also been observed in Direct Numerical Simulations of boundary layer flows (Piomelli et al., 1991). Since SGS models aim to achieve the correct level of SGS dissipation (assuming $\epsilon^{SGS} \approx \epsilon^{TKE}$), the difference between these two quantities will have significant implications for the numerical modelling of these types of flows in LES.

Figure 6.2 presents the results of conditional sampling using the same protocols as presented in §4.2.2. Here, both the positive and negative SGS dissipation rate (normalised by ϵ^{TKE}) increases as λ_{ci} increases. At low λ_{ci}, backscatter exceeds forwardscatter such that $\epsilon^{SGS} < \epsilon^{TKE}$, while at high λ_{ci} forwardscatter exceeds backscatter such that $\epsilon^{SGS} > \epsilon^{TKE}$. The interpretation of this is that moderately quiescent conditions are associated with a large number of negative points, while coherent structures are associated with a large number of positive points and therefore are necessary for $\epsilon^{SGS} \approx \epsilon^{TKE}$. This is consistent with the assumptions of homogeneity and isotropy, as well as data presented by Nimmo-

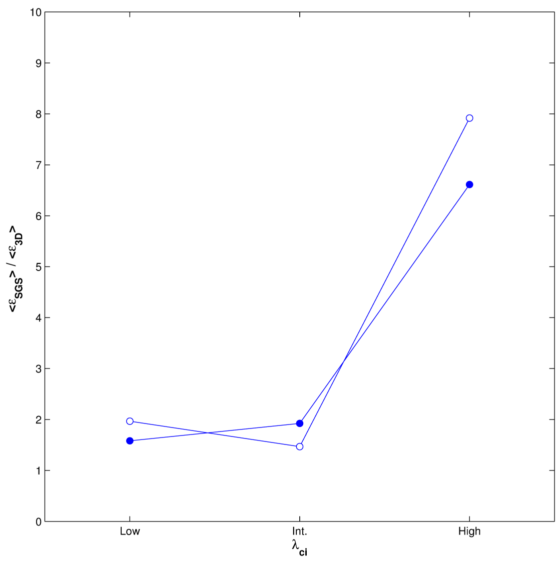

Figure (6.2). Positive and negative SGS energy fluxes at $\Delta/\delta = 5$ classified by λ_{ci}. Open symbols: positive SGS energy flux; Closed symbols: negative SGS energy flux.

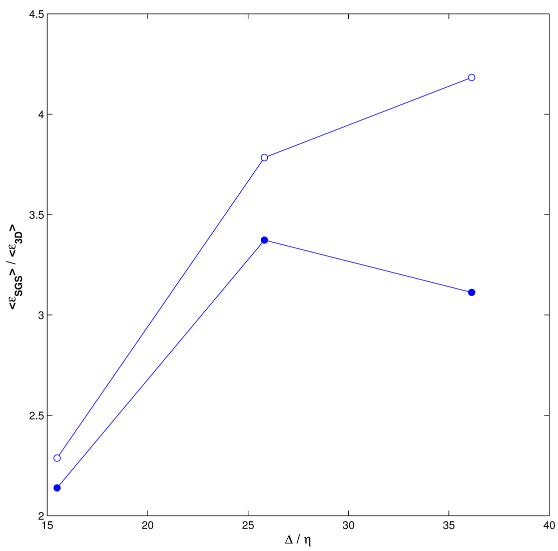

Figure (6.3). Positive and negative SGS energy fluxes, classified by filter scale. Open symbols: positive SGS energy flux; Closed symbols: negative SGS energy flux.

Smith et al. (2007), where only flows containing a substantial number of vortices will appear to have a mean SGS dissipation rate comparable to the mean TKE dissipation rate. Clearly, this is not the case for the present data as, here, vortices were only detected in 3.5% of the velocity flow fields.

Figure 6.3 presents the effect of filter size on the positive and negative SGS dissipation rate. In all cases both forwardscatter and backscatter increases with the filter size. The magnitude of this increase is higher between $\triangle/d = 3$ to 5 than between $\triangle/d = 5$ to 7. However, for the three filter sizes, backscatter constitutes a substantial part of the forwardscatter – a finding consistent with data collected under laboratory / idealised flows (Liu et al., 1994, 1999, Tao et al., 2002) and past in situ 2D-PIV measurements (Nimmo-Smith et al., 2007).

6.2.2 *A priori* tests

The performance of SGS models can be assessed using a series of comparisons of the measured τ_{ij}^{SGS} and the modelled τ_{ij}^{M} (termed *a priori* analysis), allowing more insight into their fundamental physics, and the reasons they do or do not work, than comparisons that use the results of Direct Numerical Simulations (termed *a posteriori* analysis) (Piomelli et al., 1988, Meneveau and Katz, 2000).

6.2.2.1 Correlation coefficients

Following the implementation by Nimmo-Smith et al. (2007), the correlation coefficient between the measured τ_{ij}^{SGS} and the modelled τ_{ij}^{M} is defined as:

$$\rho(\tau_{ij}^{M}, \tau_{ij}^{SGS}) = \frac{\langle \tau_{ij}^{M} \tau_{ij}^{SGS} \rangle - \langle \tau_{ij}^{M} \rangle \langle \tau_{ij}^{SGS} \rangle}{[(\langle (\tau_{ij}^{M})^2 \rangle - \langle \tau_{ij}^{M} \rangle)^2 \langle (\tau_{ij}^{SGS})^2 \rangle - \langle \tau_{ij}^{SGS} \rangle^2)]^{0.5}} \tag{6.13}$$

where τ_{ij}^M is τ_{ij}^S, τ_{ij}^D, τ_{ij}^{SF} or τ_{ij}^{NL} and $i = 1, 2, 3$.

The correlation coefficient for each of the four SGS stress models tested are presented for the three tangential SGS stress terms (τ_{12}, τ_{13} and τ_{23}) in Table 6.1.

	$\rho(\tau_{ij}^M, \tau_{ij}^{SGS})$	$\rho(\tau_{ik}^M, \tau_{ik}^{SGS})$	$\rho(\tau_{jk}^M, \tau_{jk}^{SGS})$
$M = \tau^S(\Delta/\delta = 3)$	-0.06	-0.48	-0.14
$M = \tau^S(\Delta/\delta = 5)$	-0.03	-0.51	-0.09
$M = \tau^S(\Delta/\delta = 7)$	0.12	-0.32	0.05
$M = \tau^D(\Delta/\delta = 5)$	-0.00	0.01	0.00
Threshold x10^5	1.39		
% data above threshold	24.10		
$M = \tau^D(\Delta/\delta = 5)$ above threshold	0.08	0.44	0.15
% data above 2×threshold	20.9298		
$M = \tau^D(\Delta/\delta = 5)$ above 2×threshold	0.08	0.44	0.15
$M = \tau^{SF}(\Delta/\delta = 5)$	-0.02	-0.52	-0.10
$M = \tau^{NL}(\Delta/\delta = 5)$	0.94	0.96	0.92

Table (6.1). Correlation coefficients between measured (τ_{jk}^M) and modelled (τ_{jk}^{SGS}) tangential SGS stress models.

The data indicate that τ_{ij}^{NL} exhibits the best correlation with τ_{ij}^{SGS}, while τ_{ij}^{SF} exhibits the poorest correlation with τ_{ij}^{SGS} .

While the Smagorisky model exhibits a low correlation with the τ_{ij}^{SGS}, this is a popular selection as it is not susceptible to numerical instabilities, while providing appropriate levels of SGS dissipation. However, this model is enhanced by replacing the static model coefficient (represented by τ_{ij}^S) with the dynamic model coefficient (represented by τ_{ij}^D) interpreted using an appropriate threshold to account for the highly variable viscosity field associated with small $M_{ij}M_{ij}$ quantities. These small $M_{ij}M_{ij}$ quantities are an artefact of the experimental error of individual velocity measurements and bias the correlation (Liu et al., 1994). To overcome these limitations, this threshold is typically set at 20%-24% of the data.

The difference between the Smagorinsky model and the Structure function model is considered in Figure 6.4, where the joint probability density function of the SGS dissipation rate and the strain rate magnitude are presented. Here, the probability lines spread in a positive and a negative direction with increasing $|S|$ that can be represented by cubic polynomial. This is consistent with the implied proportionality between ϵ^{SGS} and $|S|^3$ for the Smagorinsky model, but not the implied proportionality between ϵ^{SGS} and $|S|^3$ for the Structure Function model.

Consistent with past in situ 2D-PIV data (Nimmo-Smith et al., 2007), these results suggest that the Nonlinear model represents the best SGS stress model to use for the present data. This is unsurprising in light of the complexities of turbulence near the seabed as these changing dynamics are not easily incorporated into more simplistic models. However, it is important that the performance of SGS models have been verified using three-dimensional in situ data. The consequence of the alignment between two-dimensional and three-dimensional data analysis allows more simplistic data sets to be collected and used with greater confidence.

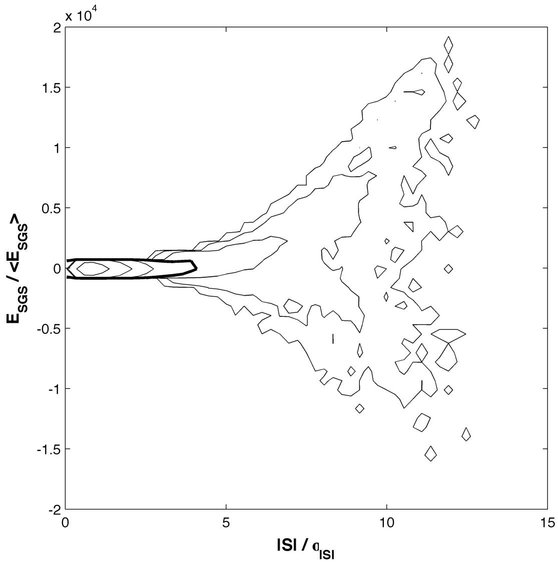

Figure (6.4). Joint Probability Density Function of the SGS dissipation rate and the strain-rate magnitude (normalised by its standard deviation) at $\Delta/\delta = 5$. The contours are at 10^{-7}, 10^{-6}, 10^{-5}, 10^{-4}, 10^{-3}, 10^{-2}, 10^{-1}, with the level at $10^{-}4$ emphasised.

6.2.3 Model coefficients

The model coefficient for each of the four SGS stress models tested are presented in Table 6.2.

While all model coefficients for the static Smagorisky model presented in Table 6.2 are less than the standard parameter of $C_s = 0.16$ established by Lilly (1967), assuming isotropy, it is seen the magnitude of the coefficient increases as the filter scale increases. At the largest filter scale, the magnitude of this coefficient ($C_s = 0.0599$) is approximately equal to that used in Direct Numerical Simulations of boundary layer flows ($C_s = 0.0650$) by Moin and Kim (1982). Similarly, this is consistent with data presented by Porte-Agel et al. (2000) which indicates C_s decreases as mean shear increases.

The model coefficients for the dynamic Smagorinsky model, the Structure

	C_M
$C_s(\Delta/\delta = 3)$	0.0246
$C_s(\Delta/\delta = 5)$	0.0360
$C_s(\Delta/\delta = 7)$	0.0599
$C_d(\Delta/\delta = 5)$	0.9998
$C_{sf}(\Delta/\delta = 5)$	-0.3004
Km $x10^6$	9.7808
$C_{nl}(\Delta/\delta = 5)$	0.3817

Table (6.2). Model coefficients.

Function model and the Nonlinear model are determined using global ensemble averaging of the form: $C_m = \langle \epsilon^{SGS} \rangle / \langle \epsilon^m \rangle$, where $\epsilon^m = -\tau_{ij}^m S_{ij}$ is the SGS dissipation from the SGS stress.

Consistent with past in situ 2D-PTV measurements (Nimmo-Smith et al., 2007), the dynamic Smagorinsky model coefficient (C_d) determined at $\Delta/d = 5$ exceeds the static Smagorinsky model coefficient (C_s) determined at $\Delta/d = 7$, with a likely convergence at $\alpha\Delta$ (the scale of the larger filter scale used to obtain them). The negative Structure Function model coefficient (C_{sf}) determined at $\Delta/d = 5$ is associated with the low K_m and is unreliable. The high Nonlinear model coefficient (C_{NL}) is associated with the high mean shear that exists within the bottom boundary layer of the coastal ocean.

Statistical evidence for the impact of coherent structures on the model coefficients is yielded from conditional sampling using the same protocols presented in §4.2.2. Figure 6.5 presents the model coefficients classified by λ_{ci}. Here, the

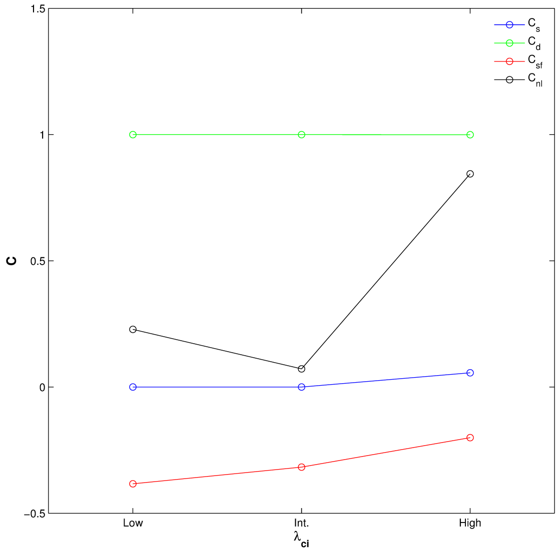

Figure (6.5). Model coefficients classified by λ_{ci}.

static Smagorinsky model coefficient increases as λ_{ci} increases, while the dynamic Smagorinsky model coefficient is unaffected. The Structure Function model coefficient increases as λ_{ci} increases, however these are negative and so are meaningless. The most substantial difference is seen for the Nonlinear model coefficient that decreases with transition from low to intermediate λ_{ci}, then increases with transition from intermediate to high λ_{ci}. The exact causes of this pattern are unknown, however it is likely that this is associated with the shape of the corresponding probability density function (Figure 6.5) as the sample volume mean λ_{ci} of most of the velocity flow fields are close to the threshold boundaries.

The results offer the first three-dimensional view of the impact of coherent structures on the SGS model coefficients, complementary to data presented by Nimmo-Smith et al. (2007).

6.3 Conclusions

3D-PTV measurements have been performed in the bottom boundary layer of the coastal ocean at moderate Reynolds number. These data are processed to test four popular stress models and SGS dissipation estimates for LES using experimental data. Consistent with past in situ 2D-PIV measurements (Nimmo-Smith et al., 2007), the time average of the SGS dissipation rate ($\epsilon^{SGS} = 6.1130e^{-8}$) is an order of magnitude less than the TKE dissipation rate ($\epsilon^{SGS} = 1.4855e^{-7}$) over the same 20 min period. Since SGS models aim to achieve the correct level of SGS dissipation (assuming $\epsilon^{SGS} \approx \epsilon^{TKE}$), the difference between these two quantities will have significant implications for the numerical modelling of these types of flows in LES, arising from the assumptions of homogeneity and isotropy. Consequently, coherent structures, such as hairpin vortices, are predominantly associated with the forwardscatter of energy from filtered (resolved) scale to the modelled scale, while quiescent conditions are associated with backscatter of energy from the modelled scale to the filtered (resolved) scale. Therefore, only flows containing a substantial number of vortices have a mean SGS dissipation rate comparable to the TKE dissipation rate.

A priori analysis of the correlation coefficients and SGS model coefficients for the Smagorinsky model (with both static and dynamic coefficients), the Structure Function model and the Nonlinear model has been conducted. These follow the general patterns inferred from lower-dimensional data. Here, the Nonlinear model represents the best SGS stress model to use for the present data.

The Smagorinsky model with dynamic coefficients is an improvement over the Smagorinsky with static coefficients and the Structure Function model. The latter are therefore not recommended for modelling the present data.

Model coefficients are consistent with that used in existing Direct Numerical Simulations of boundary layer flows. The static Smagorinsky model coefficients are less than that from laboratory / idealised flows, and increases as λ_{ci} increases, while the dynamic Smagorinsky model coefficients are unaffected. The dynamic Smagorinsky model coefficients exceed the static Smagorinsky model coefficients and appear to be more comparable to the results from a larger filter scale. The Nonlinear model coefficients are higher than in laboratory / idealised flows, consistent with the high mean shear that exists within the bottom boundary layer of the coastal ocean.

Chapter 7

Summary and conclusions

This thesis offers a qualitative and quantitative insight into small-scale turbulence in the ocean. Measurements have been made in the bottom boundary layer of a tidally-dominated shelf-sea using recently-developed Particle Tracking Velocimetry methods. The data and analysis documented in this work are in line with that reported within the scientific literature, but examines, for the first time, the three-dimensional form of the coherent structures within the bottom boundary layer of the coastal ocean, relating these to existing experiments conducted under laboratory / idealised flows. The eventual goal would be to aid the interpretation of experimental in situ measurements and the accuracy and reliability of numerical models of all kinds.

Ocean flows have traditionally been sampled using a multiplicity of methods, spanning a one, two and three-dimensional domain in space / time (Burchard et al., 2008). However, these each miss at least one spatial dimension, requiring assumptions to be made to quantify the turbulence statistics. In contrast, time-resolved submersible 3D-PTV is capable of providing an instantaneous snapshot of the velocity flow field in a $20 \times 20 \times 20\,\mathrm{cm}^3$ sample volume and therefore represents an important tool for the in situ study of mixing processes, although such methods demand a significantly higher computational cost (both in data collection and processing) than ADV, MSS or ADCP-based methods.

The 3D-PTV system was found to operate well in conditions typical of coastal waters. The use of optical flow visualisation methods are limited to conditions containing sufficient particles to reveal the turbulence characteristics but not so many as to overload the Particle Tracking Velocimetry software. Tracking of particles is possible in flows of up to 20 $\mathrm{cm\,s^{-1}}$, becoming more difficult as the mean displacement between images exceeds the mean separation of the particles. As with other methods that use the scattering of light and sound to compute velocity, 3D-PTV assumes that particles act as neutrally-buoyant tracers of the velocity flow field. Individual tracer characteristics (e.g. bubbles, large or heavy particles) will, therefore, bias the results. However, in these cases, these characteristics can be verified by checking the original camera images of each of the particles when unexpected results are encountered.

A complexity associated with submersible 3D-PTV in the coastal ocean is that gaps and noise affect the accuracy of the data collected. To accommodate this, a new Physics-Enabled Flow Restoration Algorithm has been tested for the restoration of gappy and noisy velocity measurements where a standard PTV or PIV laboratory set-up (e.g. concentration / size of the particles tracked) is not possible and the boundary and initial conditions are not known *a priori*. Implemented as a black-box approach, where no user-background in fluid dynamics is necessary, this is able to restore the physical structure of the flow from gappy and noisy data, in accordance with its hydrodynamical basis. In addition to the restoration of the velocity flow field, PEFRA also estimates the maximum possible deviation of the output from the true flow. When applied to submersible 3D-PTV measurements from the bottom boundary layer of the coastal ocean, it is apparent that using PEFRA is beneficial in processing data collected under difficult conditions, for example, where the number (and reliability) of tracer-particles is very sparse.

Laboratory measurements (Adrian et al., 2000b, Ganapathisubramani et al., 2006, Dennis and Nickels, 2011a) and numerical modelling (Zhou et al., 1999, Adrian and Liu, 2002, Wu and Moin, 2009) at low Reynolds number ($Re_\theta < 4,700$) indicate the energy containing turbulence of boundary layer flows comprises coherent packets of hairpin vortices. This thesis confirms tidal flows also contain gusts of large vortices separated by periods of more quiescent conditions at higher Reynolds numbers ($Re_\theta = 267,970$). The 1,452 vortices recorded over the 20 min period are typically aligned along-stream (modal angle: 8°) and inclined to the seabed (modal angle: 27°), with a mean frequency of occurrence of 4.3 sec. Therefore, the results lend three-dimensional, in situ, evidence for the existence of coherent packets of hairpin vortices in the bottom boundary layer of the coastal ocean. This demonstrates a direct linkage from low Reynolds number experiments to these higher Reynolds number flows that, importantly, will enable the fine-scale details of particle transport and pollution dispersion to be studied in future.

Conditional sampling of the Reynolds shear stress suggests that coherent structures are responsible for the vertical exchange of momentum via bursts and sweeps (τ_{13} and τ_{23}) and, as such, are the key areas where energy is extracted from the mean flow and into turbulence. However, these vortices seem to have a lesser impact on τ_{12}, although it is likely that this is biased by the alignment of the 3D-PTV system to the mean flow (as a consequence of the spatial inhomogeneity). At the same time, conditional sampling of the spatial energy spectra suggests that coherent structures appear to have a regularising effect on the flow, although it is clear that (substantial) anisotropy remains at all wavenumber scales as the local turbulence dynamics are modified by the proximity to the seabed. Note that although the mean turbulence statistics computed from all mean velocity flow fields over the 20 min period are reliable (i.e. over twice the necessary duration to achieve statistical convergence to within 10% of the long term mean), the process of classifying these data into groups of low, intermediate and high swirling strength magnitude reduces the confidence in the results of the conditional sampling. However, this trend is consistent with past in situ 2D-PIV measurements (Nimmo-Smith et al., 2005). To definitively unravel the impact of large coherent structures on the Reynolds shear stress and the spatial energy spectra it would be insightful to use each of the instantaneous velocity flow fields where a vortex was detected as the criterial for the conditional sampling but, as this flow is mostly (96.5%) quiescent, it is suggested that this analysis is conducted using a larger database of 3D-PTV measurements.

Consistent with previously published spatial energy spectra (Luznik et al., 2006), and without exception here, all along-stream velocity components are higher than the cross-stream and wall-normal components. The impact of this anisotropy is to bias estimates of the TKE dissipation rate inferred from one- and two- dimensional data. As isotropy is a fundamental assumption in most turbulence measurements (e.g. airfoil-type shear sensors), conditions of anisotropy will have significant implications for the sampling of these types of flows in situ. Here, direct measurements of the Turbulence Kinetic energy dissipation rate within the bottom boundary layer of the coastal ocean are used to compare estimates based on horizontal and vertical velocity derivatives. These represent the data that are typically obtained from airfoil-type shear sensors profiled in the along-stream, cross-stream and vertical direction. As the grid size exceeds the Kolmogorov microscale, the exact magnitude of the dissipation rate will be underestimated. However, as this is constant between quantities compared, this does not impact on the overall trends reported. Note that this is not unique to the present thesis, as this is also seen in direct estimates of the TKE dissipation rate obtained in past in situ 2D-PIV measurements (Nimmo-Smith et al., 2005, Luznik et al., 2006, Hackett et al., 2011). The results indicate a high degree of spatial variability associated with the flow conditions, meaning it is recommended that pairs of airfoil-type shear sensors are installed orthogonally and the measurements averaged. The averaged data supports the validity of measurements obtained by horizontal and vertical profilers, however along-stream velocity derivatives underestimate the TKE dissipation rate by more than 40 % – a factor of two higher than for the equivalent cross-stream and vertical estimates. As a consequence, it is recommended that horizontal (AUV) transects are made across the direction of the mean flow but, as the trend identified from the present study are in agreement with that identified from numerical modelling of a stratified shear layer (Itsweire et al., 1993, Smyth and Moum, 2000), a constant sampling pattern can be followed throughout the water column. The anisotropy of ocean flows has important implications for the subsequent interpretation of higher-order statistics. For example, the present study reveals that an (erroneous) assumption of isotropy in the TKE dissipation rate term used in the computation of the Kolmogorov microscale causes a difference in results of 40.5 % from the mean within individual vortices or 800 μm. As this parameter is used to relate the flow dynamics to particle characteristics in models of flocculation processes (Soulsby et al., 2013), care is necessary in interpreting lower-dimensional data collected under conditions of anisotropy.

The data have been processed to test four popular SGS stress models and SGS dissipation rate estimates for LES using experimental data. Consistent with past in situ 2D-PIV measurements (Nimmo-Smith et al., 2007), the time average of the SGS dissipation rate ($\epsilon^{SGS} = 6.1130e^{-8}$) is an order of magnitude less than the TKE dissipation rate ($\epsilon^{SGS} = 1.4855e^{-7}$) over the same 20 min period. Since SGS models aim to achieve the correct level of SGS dissipation (assuming $\epsilon^{SGS} \approx \epsilon^{TKE}$), the difference between these two quantities will have significant implications for the numerical modelling of these types of flows in LES, arising from the assumptions of homogeneity and isotropy. Consequently, coherent structures, such as hairpin vortices, are predominantly associated with the forwardscatter of energy from filtered (resolved) scale to the modelled scale, while quiescent conditions are associated with backscatter of energy from the modelled scale to the filtered (resolved) scale. Therefore, only flows containing a substantial number of vortices have a mean SGS dissipation rate comparable to the TKE dissipation rate. Furthermore, when the correlation and SGS model coefficients are compared, the Nonlinear model represents the best SGS stress to use for the present data.

While the data presented in this thesis relate to calm weather conditions on the accelerating phase of the ebb-tide, the agreement with two-dimensional measurements by Nimmo-Smith et al. (2005) suggests that these are typical of coastal waters with weak to moderate currents. Further observations are therefore necessary to extend our understanding of three-dimensional turbulence structure to different conditions, such as under stratified flows and waves, as well as other sites with stronger currents and different topography. To achieve this will require further development of the 3D-PTV system since, in its present configuration, the 3D-PTV is limited by the resolution of the cameras, sampling rate and the seeding density of the particles. Upgrading the system to use high-speed cameras would allow faster flow rates to be sampled at higher resolution, although these would also require changes to the data storage.

The significance of the measurement and analysis of turbulence in the coastal ocean is important in its wider context. It has been stated at the outset that the rotational, eddying and dynamic motions implied by the term turbulence are the dominant state of fluid movement on Earth. As such, turbulence is effective in the transferral of heat and momentum in the sea, as well as dispersing, stressing and straining both particles and living matter in the water column, while diluting and stirring its chemical constituents (Thorpe, 2004). Detailed measurement and analysis of coherent structures in the coastal ocean is therefore critical for the development of numerical models and for the further study of all marine processes, offering new ways of looking at in situ phenomena.

Appendices

Appendix A

Swirling Strength

Following Ganapathisubramani (2004), the velocity gradient tensor is defined as:

$$D = \nabla u = \begin{pmatrix} \frac{\partial U_1}{\partial X_1} & \frac{\partial U_1}{\partial X_2} & \frac{\partial U_1}{\partial X_3} \\ \frac{\partial U_2}{\partial X_1} & \frac{\partial U_2}{\partial X_2} & \frac{\partial U_2}{\partial X_3} \\ \frac{\partial U_3}{\partial X_1} & \frac{\partial U_3}{\partial X_2} & \frac{\partial U_3}{\partial X_3} \end{pmatrix} \tag{A.1}$$

The characteristic eigen-value equation of this tensor is:

$$\lambda^3 + P\lambda^2 + Q\lambda + R = 0 \tag{A.2}$$

where P, Q and R are the invarients of D, i.e.:

$$P = trace(D) \tag{A.3}$$

$$Q = \frac{1}{2}[P^2 - trace(DD)] \tag{A.4}$$

$$R = \frac{1}{3}[-P^3 + 3PQ - trace(DDD)] \tag{A.5}$$

This characteristic equation is a cubic polynomial, whose discriminant is defined as:

$$\Delta = \tilde{R}^2 + \tilde{Q}^3 \tag{A.6}$$

where,

$$\tilde{R} = \frac{1}{6}(PQ - 3R) - \frac{1}{27}P^3 \tag{A.7}$$

$$\tilde{Q} = \frac{1}{3}(Q) - \frac{1}{9}P^2 \tag{A.8}$$

This polynomial will have three real roots or one real root and a pair of complex-conjugate roots, as identified by the discriminant. If $\Delta < 0$, all roots are real and if $\Delta > 0$ one root is real and a pair of complex-conjugate roots exist. The roots of the characteristic equation where $\Delta > 0$ are determined as follows: Let,

$$s1 = \left[\tilde{r} + \sqrt{\Delta}\right]^{1/3} \tag{A.9}$$

$$s2 = \left[\tilde{r} - \sqrt{\Delta}\right]^{1/3} \tag{A.10}$$

Then, the roots $z1$, $z2$ and $z3$ are defined as:

$$z1 = (s1 + s2) - \frac{P}{3} \tag{A.11}$$

$$z2 = -\frac{1}{2}(s1 + s2) - P3 + \frac{i\sqrt{3}}{2}(s1 - s2) \tag{A.12}$$

$$z2 = -\frac{1}{2}(s1 + s2) - P3 - \frac{i\sqrt{3}}{2}(s1 - s2) \tag{A.13}$$

Therefore, the complex roots are of the form:

$$z = \lambda_{cr} + i\lambda_{ci} \tag{A.14}$$

$$\lambda_{cr} = -\frac{1}{2}(s1 + s2) - \frac{P}{3} \tag{A.15}$$

$$\lambda_{ci} = -\frac{\sqrt{3}}{2}(s1 - s2) \tag{A.16}$$

The swirling strength is defined as the imaginary part of the complex root, λ_{ci}.

Appendix B

Publications

Andrey Vlasenko, **Edward C. C. Steele**, and W. Alex M. Nimmo-Smith (2015), A physics-enabled flow restoration algorithm for sparse PIV and PTV measurements, *Measurement Science & Technology*, 26, 065301 (23pp).

This is an author-created, un-copyedited version of an article accepted for publication in Measurement Science & Technology. The publisher is not responsible for any errors or omissions in this version of the manuscript or any version derived from it. The Version of Record is available online at:

http://www.dx.doi.org/10.1088/0957-0233/26/6/065301

Abstract

The gaps and noise present in Particle Image Velocimetry (PIV) and Particle Tracking Velocimetry (PTV) measurements affect the accuracy of the data collected. Existing algorithms developed for the restoration of such data are only applicable to experimental measurements collected under well-prepared laboratory conditions (i.e. where the pattern of the velocity flow field is known), and the distribution, size and type of gaps and noise may be controlled by the laboratory set-up. However, in many cases, such as PIV and PTV measurements of arbitrarily turbid coastal waters, the arrangement of such conditions is not possible. When the size of gaps or the level of noise in these experimental measurements become too large, their successful restoration with existing algorithms becomes questionable. Here, we outline a new Physics-Enabled Flow Restoration Algorithm (PEFRA), specially designed for the restoration of such velocity data. Implemented as a "black box" algorithm, where no user-background in fluid dynamics is necessary, the physical structure of the flow in gappy or noisy data is able to be restored in accordance with its hydrodynamical basis. The use of this is not dependent on types of flow, types of gaps or noise in measurements. The algorithm will operate on any data time-series containing a sequence of velocity flow fields recorded by PIV or PTV. Tests with numerical flow fields established that this method is able to successfully restore corrupted PIV and PTV measurements with different levels of sparsity and noise. This assessment of the algorithm performance is extended with an example application to *in situ* submersible 3D-PTV measurements collected in the bottom boundary layer of the coastal ocean, where the naturally-occurring plankton and suspended sediments

used as tracers causes an increase in the noise level that, without such denoising, will contaminate the measurements.

A Introduction

Particle Image Velocimetry (PIV) and Particle Tracking Velocimetry (PTV) are two established methods for the measurement of instantaneous distributions of velocity components within an illuminated 2D sample area or 3D sample volume. In both cases, digital cameras are commonly used to record traces of particles suspended in the flow field. A pair of traces are yielded by two successive laser-sheet pulses or two successive camera frames in PIV and PTV, respectively. The displacements in all the particles (on an ensemble-averaged or an individual basis) are then divided by the fixed time delay between the two exposures, thus obtaining the corresponding velocity distributions.

While the idea of the PIV and PTV methods is simple, the noise and gaps present in experimental measurements typically affects the accuracy of the data collected (Westerweel, 1994, Raffel et al., 2007). The noise arises from errors connected with the characteristics of the particles and their representation in the images (Hart, 2000). A low seeding density complicates these issues, as well as any subsequent analysis (Cenedese and Querzoli, 1997, 2000, Stanislas et al., 2004).

In recent years, several methods have been developed for the denoising and restoration of such data; exploiting the statistical or the physical characteristics of the velocity flow field.

In statistical methods, individual vectors that depart from the ensemble of the recorded velocity flow field are identified and subsequently eliminated. Such data post-processing commonly consists of using global-mean, local-mean or local-median tests or using global histogram operators (Westerweel and Scarano, 2005, Raffel et al., 2007, Duncan et al., 2010). Here, it is assumed that locally-occurring errors are randomly scattered within the sample volume, and that a sufficient quantity of tracers are present for the outliers to be detected. These methods are used for their convenience, computational cost and ease of implementation. However, only individual vectors are eliminated and not the noise that exists homogeneously within the sample volume.

Concomitant issues relate to infilling gaps in experimental measurements, and are tackled after statistical denoising. The restoration of 'gappy' data commonly consists of using different types of interpolation, e.g. kriging, nearest neighbour or polynomial interpolation from linear to nth order (cf. Stuer and Blaser 2000). Similarly, methods that employ Proper Orthogonal Decomposition have gained popularity, remaining cost efficient while still being applicable to any type of flow (Venturi and Karniadakis, 2004, Gunes and Rist, 2008). These exhibit good restoration capabilities where the sparsity of these data are 50 %, but the performance decreases as the sparsity of the data approaches 20 %.

In physical methods, hydrodynamical equations, e.g. Navier-Stokes (NSE) or Vorticity Transport Equations (VTE), are used for the restoration of noisy *and* gappy data. Typically, this is achieved by fitting numerical pre-estimates of the (same) velocity flow field to data collected from experimental measurements using Kalman filtering (Suzuki, 2012) or variational methods (Okuno et al., 2000, Suzuki et al., 2009a,b), such that they are similar. Since the velocity data from these schemes are determined from the results of the numerical hydrodynamical model, the results of the restoration are physically-plausible yet are not limited by the occurrence of noise or the sparsity of the data. However, this is only feasible where numerical pre-estimates of the velocity flow field are possible (i.e. where boundary and initial conditions are known *a priori*).

Contrary to methods using numerical pre-estimates, Sciacchitano et al. (2012) suggested deriving boundary conditions directly from experimental measurements, that then are used to infill gappy data in a physically-plausible way. However, this is very sensitive to noise (Sciacchitano et al., 2012).

All these methods are able to be used for the denoising and restoration of experimental measurements within the context of a well-prepared laboratory set-up, where no unsuitable particles are present and tracers with known light scattering characteristics are selected and seeded in the velocity flow field. Tuning laboratory settings (e.g. by optimising the concentration / size of the particles tracked) results in the permissible level of gaps and noise that allows successful restoration using existing methods. Even if gaps and noise cannot be sufficiently reduced, the laboratory set-up offers enough details that numerical pre-estimates are possible, as the boundary conditions or the pattern of the velocity flow field are known *a priori*. However, in several cases, it is not possible for these gaps and noise to be sufficiently reduced nor any pre-estimates to be made. An example of this is seen in PIV and PTV measurements in ocean flows (Nimmo-Smith et al., 2002, 2005, Nimmo-Smith, 2008) where the arrangement of usual experimental conditions using ideal tracers is not possible and naturally-occurring suspended particles are used instead. The uneven shape of these particles, scattered inhomogeneously within the velocity flow field, causes an increase in the occurrence of gaps and noise that, in turn, complicates any later analysis. In addition, as only the part of the ocean advected through the sample volume are recorded, the boundary conditions are unknown and numerical pre-estimates are not feasible. Therefore, restoration of such data with existing methods is debatable; requiring the development of a new Physics-Enabled Flow Restoration Algorithm (PEFRA) for these velocity measurements. This is founded on a hydrodynamical basis, as represented by the Vorticity Transport Equation (VTE), however it is independent of specified boundary conditions and the algorithm exhibits a weak sensitivity to noise, as confirmed by tests using both artificial/numerical and in-situ experimental data.

PEFRA is from the same pedigree as the Physically-Consistent and Efficient Variational Denoising (PCEVD) algorithm developed by Vlasenko and Schnorr (2010), but with a significant improvement that allows restoration of gappy and noisy data. Both methods conform to a black box philosophy, requiring no specific user-background in fluid dynamics (except in special cases) and may be applied to any velocity time-series, formed from any type of flow and corrupted by any type of noise. However, PCEVD is limited in the sparsity permitted, especially under turbulence. This failing is corrected in PEFRA, and confirmed by the restoration of a velocity flow field with only 10% of data available.

Here, PCEVD is outlined in §B, with the development of PCEVD into PEFRA outlined in §C. In §D, the algorithm sensitivity to noise and sparsity is discussed, with an assessment of the algorithm performance using artificial/numerical data modelling different flow conditions presented in §E. This assessment is extended to submersible 3D-PTV measurements in ocean flows, in §F, where naturally-occurring suspended particles are used as tracers. The pseudo-code outline of PEFRA is presented in Appendix B.

B PCEVD algorithm

A detailed discussion of the mathematical background to PCEVD containing the complete proofs may be found in Vlasenko (2010) (or in compact form in Vlasenko and Schnorr 2010), and only a summary (without theoretical substantiation) is provided here as the context for the solution of the problem. To do so, $\vec{a}(\vec{x})$ and $\vec{b}(\vec{x})$ are defined as two vector functions in a volume, V, where $\vec{x} \in V$ is a three-dimensional coordinate vector. Then, assuming that $\vec{a}(\vec{x})$ and $\vec{b}(\vec{x})$ are differentiable, the L2 norm is defined as: $\|\vec{a}\|_2 = \sqrt{\int_V \vec{a}(\vec{x})^2 d\vec{x}}$, the inner product is defined as $\langle(\vec{a}, \vec{b})\rangle = \int_V (\vec{a} \cdot \vec{b}) d\vec{x}$ and the convolution of these is defined as: $\vec{a}(\vec{x}) \star \vec{b}(\vec{x}) = \int_{-\infty}^{+\infty} \vec{a}(\vec{x})\vec{b}(\vec{t} - \vec{x})d\vec{t}$.

The curl, finally, is defined as: $\nabla \times \vec{a} = [\frac{\partial a_z}{\partial y} - \frac{\partial a_y}{\partial z}; \frac{\partial a_x}{\partial z} - \frac{\partial a_z}{\partial x}; \frac{\partial a_x}{\partial y} - \frac{\partial a_y}{\partial x}]$. Importantly, the VTE is yielded when this operator is applied to both the LHS and the RHS of the NSE:

$$\frac{\partial \vec{\omega}}{\partial t} + (\vec{\omega} \cdot \nabla)\vec{v} + (\vec{v}\nabla)\omega = \nu \triangle \vec{\omega} \qquad \text{(B.1)}$$

where, $\omega = \nabla \times \vec{v}$, $\triangle = \nabla^2$ is the Laplace operator and ν is the viscosity.

The benefit in using the VTE over the NSE is that it does not contain pressure as an additional variable. For the sake of simplicity, the LHS of the VTE is denoted by an $\vec{e}$, i.e. $\vec{e}(\vec{v}) = \frac{\partial \vec{\omega}}{\partial t} + (\vec{\omega} \cdot \nabla)\vec{v} + (\vec{v}\nabla)\vec{\omega}$. This shorthand is especially useful when the VTE is presented in weak form, i.e. $J(\vec{\omega}) = \nu\|\nabla \times \vec{\omega}\|_2^2 +$

$2\langle \vec{e}(\vec{v}_s), \vec{\omega} \rangle$. The weak form of the VTE reverts to the normal form of the VTE by differentiation by $\vec{\omega}$.

PCEVD is an iterative algorithm that was developed for the denoising and restoration of three-dimensional velocity time-series data recorded in PIV, PTV or other velocity measurements. This is implemented in four stages: Gaussian filtering, solenoidal projection (i.e. divergence removal, demanded by the continuity equation), vorticity restoration and velocity restoration. On each loop, the quality of this output is checked by a termination criteria. If this is not achieved, the process repeats using the results generated in the last output. The idea of this sequence is that high-frequency noise, as well as any divergence, is eliminated by Gaussian filtering and solenoidal projection, respectively. Any remaining noise is then eliminated by vorticity restoration, where the pattern of the vorticity flow field is also recovered (– if it is corrupted). Finally, the last part of the algorithm, velocity restoration, links the pattern of the vorticity flow field and the filtered pattern of the velocity flow field, providing an additional connection to the PIV or PTV data. These stages are detailed below, via the restoration of a gappy and noisy velocity flow field, v_m, recorded in an incompressible fluid.

B.1 Stage 1: Gaussian filtering

The restoration of the velocity flow field, $\vec{v}_m$, is initiated by Gaussian filtering:

$$\vec{v}_d = g \star \vec{v}_m, \qquad g = \frac{1}{(2\pi\sigma^2)^{3/2}} \exp\left(-\frac{\sigma^2}{2}|\vec{x}|^2\right) \tag{B.2}$$

where, $\vec{v}_m$ is the recorded velocity flow field, $\star$ is the convolution and σ is the variance governing the strength of the Gaussian filtering (discussed in Section

D) that removes high frequency noise. The filtered velocity flow field $\vec{v}_d$ is then passed to Stage 2 where the divergence is eliminated.

B.2 Stage 2: solenoidal projection

As it is assumed that this fluid is incompressible, divergence within the velocity flow field constitutes noise and must be eliminated. Therefore, $\vec{v}_d$ is the sum of the divergence (∇p) and the solenoidal ($\vec{v}_s$) velocity components, i.e. $\vec{v}_d = \nabla p + v_s$, to which the divergence operator may be applied giving:

$$\nabla \vec{v}_d = \triangle p \tag{B.3}$$

Solving Equation B.3 with zero boundary conditions results in the divergence part, $\triangle p$. This is subtracted from $\vec{v}_d$, giving the divergence-free velocity flow field v_s (consistent with the continuity equation) passed to Stage 3.

B.3 Stage 3: vorticity restoration

The physical plausibility of the flow that was filtered in Stage 1 and Stage 2 is enforced by the VTE. This is done by minimising the functional:

$$J(\omega) = \|\vec{\omega} - \vec{\omega}_s\|_2^2 + \alpha\Big(\nu\|\nabla \times \vec{\omega}\|_2^2 + 2\big\langle \vec{e}(\vec{v}_s), \vec{\omega}\big\rangle_{\vec{\omega}}\Big) \tag{B.4}$$

where, $\vec{\omega}_s = \nabla \times \vec{v}_s$ is the vorticity computed from the velocity flow field in Stage 2, and $\vec{\omega}$ is the vorticity to be found.

Minimization of Equation B.4 with respect to $\vec{\omega}_s$ means that both terms must remain as small as possible with respect to the L2 norm. The minimized sum (in brackets) represents the weak form of the VTE and enforces the physical flow structures in $\vec{\omega}_s$, while the term outside the brackets (i.e. $\|\vec{\omega} - \vec{\omega}_s\|_2^2$) links $\vec{\omega}$ and $\vec{\omega}_s$ such that the difference in the L2 norm between these two vector fields is minimal. The balance between the two components dictates the strength of the restoration and this, in turn, is controlled by a control parameter, α that has the dimensions of time (discussed in Section D). The weak form of the VTE reverts to the normal form of the VTE, after the first variation in $\vec{\omega}$ is computed.

The first variation of this functional is:

$$\vec{\omega} - \alpha\nu\triangle\vec{\omega} = \vec{\omega}_s - \alpha\vec{e}(\vec{v}_s) \tag{B.5}$$

Note that if $\vec{\omega}_s$ satisfies the VTE, $\vec{\omega} = \vec{\omega}_s$.

In cases where the exact boundary conditions are known, solving Equation B.5 is easily done analytically or numerically. In all other cases, it is assumed that volume V freely allows in-/out-flow (i.e. it is open), requiring that constant-flux boundary conditions must be used:

$$\left.\frac{\partial\vec{\omega}}{\partial n^-}\right|_{\partial V_l} = \left.\frac{\partial\vec{\omega}}{\partial n^+}\right|_{\partial V_l} \tag{B.6}$$

where, n^- is the inner normal to V and n^+ is the outer normal to V.

Such boundary conditions are sufficient in solving Equation B.5 and do not rely on fixed vorticity or velocity fluxes. The filtered vorticity flow field $\vec{\omega}$ is then passed to Stage 4.

B.4 Stage 4: velocity restoration

The velocity restoration is done by minimising the functional:

$$\min_{\vec{u}} \left\{ \|\vec{u} - \vec{v}_s\|_\Omega^2 + \|\nabla \times \vec{u} - \vec{\omega}\|_\Omega^2 \right\}. \tag{B.7}$$

This is implemented similarly to Equation B.4, and the output is an optimum velocity flow field, u, determined from Stage 2 and Stage 3. Here, term $\|\vec{u} - \vec{v}_s\|_\Omega^2$ links the output u and velocity field v_s from Stage 2 such that the L2 norm difference between them is minimal (and therefore also the experimental measurements), while the term $\|\nabla \times \vec{u} - \vec{\omega}\|_\Omega^2$ links the output pattern of the velocity flow field in u and the restored pattern of the vorticity flow field in $\vec{\omega}$ from Stage 3. Dimensional consistency is achieved using a constant that equals one, but has the dimensions of length squared. For the sake of simplicity, this constant is omitted in later derivations.

The first variation of this functional is:

$$\vec{u} - \triangle\vec{u} = \vec{v}_s - \nabla \times \vec{\omega} \tag{B.8}$$

The boundary conditions to Equation B.8 are the same as in Stage 3, and solving results in the rectified velocity flow field, $\vec{u}$.

Note that Equation B.2, Equation B.5 and Equation B.8 each represent a low-pass filter that causes a suppression of energy that must be recovered. Although this suppression is negligible for a single iteration, it becomes considerable if the algorithm executes more than 10 iterations. Here, it is assumed that the main fraction of the noise energy present in the data collected is concentrated in the middle and high frequency part of the spectrum (e.g. white noise). Therefore, low-pass filtering causes the large decay of that fraction after the first iteration, while the decay of the true signal is insignificant. The implication of this is that, after the first iteration, the energy of the remaining low frequency part is negligible compared to the true energy of the flow, such that the energy of the noisy flow approximately equals the true energy of the flow. The energy of this flow is recovered starting from the second iteration when the output $\vec{u}$ is multiplied by the ratio between the energy of the first iteration and that of the rectified data.

B.5 Algorithm termination

Algorithm termination occurs after a user-predefined maximum number of iterations or when the mean angle deviation between u and v_m is less than user specified tolerance. If this is not met, the velocity flow field, u, is defined as if it were v_m and the process repeats using the results generated in the last output.

C Algorithm development

Vlasenko and Schnorr (2010) established that PCEVD offers good restoration capabilities for any type of flow, corrupted by any type of noise. It is also able to accommodate gappy data, however the quality of this output is detrimentally affected by the sparsity. The large gaps within the velocity flow field are not considered as noise, as they meet the divergence-free criteria (Stage 2) and the trivial solution of the VTE (Stage 3 and Stage 4). Therefore, PCEVD merges the large gaps with the PIV or PTV data, changing the complete pattern of the velocity flow field. It is this failing especially, rather than the hydrodynamical theory applied, that prompted the development of a new algorithm, PEFRA. This new algorithm is applicable to any type of (incompressible) flow, and offers similar restoration capabilities to its PCEVD predecessor, but with less sensitivity to the sparsity of the data.

PEFRA consists of three blocks: interpolation, linear approximation and restoration. Here, weighted-average interpolation methods are used to infill gappy data in the first block. This is then smoothed by linearization, using a modified PCEVD algorithm (with Stage 2 omitted and $\vec{e}(\vec{v})$ in Stage 3 set to zero), such that it fits the pattern of the laminar vorticity flow field. Finally, restoration is done using a differently modified PCVED algorithm (with Stage 2 omitted) and the output velocity flow field established iteratively, as in §B. The omission of Stage 2 from PEFRA may be justified by its small effect on the reconstruction of gappy elements within the velocity flow field. The reason for this is that both Block 2 and Block 3 decrease the vorticity (proof in Appendix) on each loop, such that the output vectors are almost divergence-free. The scheme and pseudo-code of PEFRA for its numerical implementation are given in Appendix B.

C.1 PEFRA volume and boundary conditions

In cases where the boundary conditions are not known, continuity flux boundary conditions are used in both PEFRA and PCEVD. In PCEVD, these are applied to the same volume as that where the data were collected but, in PEFRA, a larger volume is needed. This is apparent when Equation B.5 is considered, with respect of the normal vorticity component, at the boundary of V. These continuity flux boundary conditions convert Equation B.5 to:

$$\vec{\omega}^n = \vec{\omega}^n_s - \alpha \vec{e}^n(\vec{v}_s). \tag{B.9}$$

where, n is the normal component of the vector.

Therefore, the unknown vorticity component, $\vec{\omega}$, is unambiguously defined by the difference between $\vec{\omega}_s$ and $\alpha\vec{e}(\vec{v}_s)$, where the noisy $\vec{\omega}_s$ is corrected by $\alpha\vec{e}(\vec{v}_s)$. However, when experimental measurements are highly sparse, Equation B.9 is not appropriate as the lack of velocity data at the boundary means the fluxes in Equation B.9 are computed incorrectly. Note that after interpolation and linearization, $\vec{v}_s$ is a linear function, as is $\vec{\omega}$ and $\alpha\vec{e}(\vec{v}_s)$. Consequently, ω is also linear – irrespective of the dynamics within the sample volume – requiring enlargement of this volume in PEFRA.

To understand these, a volume, V, containing the fluid motion, surrounded by a larger volume V_l of the same shape, is considered. The walls of V and V_l are invisible to fluid movement and freely allow in-/out-flow. Critically, the center of these volumes are co-positioned, meaning the distance, d, that offset the walls of V from the walls of V_l are the same to each face. Therefore, if V_l is sufficiently large, any turbulence present in V diminishes at the boundary of V_l due to viscosity effects. Here, flows near the boundary are linear, so constant-flux boundary conditions (Equation B.6) are appropriate.

To explain the computation of d, the analogy of fractal turbulence may be considered. Here, it is suggested that a velocity flow field may be represented as an overlapping set of vortices with different characteristic length scales (Giacomazzi et al., 1999). Let L be the characteristic length of the largest vortices in the set. Following Kolmogorov theory (Landau and Lifshitz, 2000), an individual eddy is divided into several vortices twice as small as the original after a distance of twice its characteristic length. Therefore, the largest vortices in the set are divided into several smaller vortices with a characteristic length of $L/2$ after a distance of $2L$. These smaller vortices are then sub-divided after a distance of L and the process repeats until the minimum eddy length scales are met. In discrete cases, this is set by the number of grid-points that are needed for the resolution of the smallest vortices (i.e. three grid-points). The equation for the minimum length of d is, therefore:

$$d = \sum_{i=0}^{N} \frac{L}{2^{i-1}}, \qquad N = \log_2 \left(\frac{L}{3} \right) \tag{B.10}$$

The enlargement of V to V_l by d means that flow near the boundary are constant and linear, so constant-flux boundary conditions (Equation B.6) are appropriate. To emphasize that constant flux boundary conditions are applied to a larger volume where the pattern of the vorticity flow field is linear, these are termed open boundary conditions. If L is unknown, and estimation of d using Equation B.10 is impossible, then this is able to be obtained iteratively. The algorithm to do so is as follows: initially, all control parameters are set as default (§D.3.1) and $d = 1$. PEFRA runs with this set of control parameters until the termination criterion is satisfied, and the root-mean-difference between the input and output velocity flow field is saved for further reference. Then d is incremented by one and the procedure repeated, whereupon the root-mean-square differences between the experimental measurements and the restored data from the present and the preceding iterations are compared. If the relative difference between these two values is sufficiently small (e.g. smaller than 1%) the algorithm terminates and V_l is estimated. Otherwise, d is incremented by one and the sequence repeated again. Note that if this tolerance is set close to zero, the estimated d will be the same as in Equation B.10.

C.2 Interpolation

After the enlargement of V to V_l, all empty grid-points in V are filled by interpolation of the experimental measurements, prior to the velocity flow field from V being extrapolated into V_l. Tests using different types of interpolation (i.e. nearest neighbour, splines and weighted-average) reveal that weighted-average schemes are most appropriate, since they achieve the best convergence rate of PEFRA. Consequently, these schemes are used in this algorithm. Here, it is assumed that all the available PIV or PTV data are presented on a regular grid (or projected from an irregular grid onto a regular grid), with a grid-step h. Each empty node is surrounded by a sphere of $2h$. If there are two or more measured velocity vectors in that sphere, a weighted average interpolation can be applied and the node is filled with the interpolated data. If not, the radius of the sphere is increased by h and the availability of measured velocity vectors is re-checked. If, again, there are less than two recorded velocity vectors the radius of the sphere increased until the amount of measured vectors within the sphere becomes greater than or equal to two. The weights for interpolation are set as the inverse distance from the node to the center of the sphere.

C.3 Linearization

In several cases, ramps are present at junctions between the infilled data and the recorded velocity flow field, however the smoothing of these ramps by Gaussian Filtering (Stage 1) may be insufficient at avoiding large non-linear $\vec{e}(\vec{v})$ terms at these junctions. Increasing the filter variance will strengthen the severity of the smoothing of these ramps but this, in turn, risks over-smoothing the pattern of the velocity flow field such that two adjacent vortices may be amalgamated into one and so must be avoided. This over- or under-smoothing is prevented by fitting the interpolated velocity flow field to the linear VTE, since the linear VTE does not have problematic non-linear terms and can filter-out the junctions as discussed below. Helpfully, this solution of the linear VTE is also the first-order (linear) approximation of the non-linear VTE. This solution is obtained by performing a single Gaussian filtering operation, prior to executing step 3 and step 4, sequentially, with the linear VTE, until the termination criterion is satisfied. Therefore, the algorithm establishes linear flow such that, among all the possible linear solutions, the difference in the L2 norm of the velocity and vorticity, with the corresponding $\vec{\omega}_s$ and $\vec{v}_s$, is minimal. The energy of the flow is subsequently recovered, as in PCEVD. After each iteration, the obtained linear velocity field fills the gaps in the measurements. The resultant field is used then as an input field for the next iteration.

Note that PEFRA is an iterative method, and therefore its computational speed performance may be significantly improved if the correct initial estimate (known also as initial guess) is found. Since the linear flow is traditionally used as the first approximation of any type of flow (Pedlosky, 1990), the construction of linear flow is the preparation of this estimate. It decreases the time needed for the restoration in the final block – irrespective of the dynamics within the sample volume.

C.4 Restoration

The final block, restoration, consists of two stages. Initially, it is the same as linearization but with the full form of $\vec{e}(\vec{v})$ used for the vorticity restoration. Here, on each iteration, the grid-points containing the restored data are substituted with the non-zero data from the sparse experimental measurements. After the algorithm termination criteria is met, this last stage is again repeated only without the input of the PIV or PTV data into the output velocity flow field such that noise injected with the experimental measurements is filtered out. The energy of the flow is subsequently recovered, as in PCEVD.

D Algorithm sensitivity

The sensitivity of PEFRA to noise, sparsity and control parameters is discussed analytically here, with an experimental verification provided in §E.

For the purposes of analysis, the restoration is considered to be successful if the L2 difference between the true flow and the restored flow decreases on each iteration, ultimately becoming less than a user-defined criterion. Although the true flow in experimental measurements is unknown, it is possible to anticipate the cases where restoration will be successful from only the characteristics of the PIV or PTV data. This is examined using an extreme example. Here, a velocity flow field only consisting of two vectors is considered. If the two vectors are far apart, then they may be connected to one large vortex or two smaller separate vortices (or, indeed, any other type of flow) and any later restoration will be ambiguous. Consequently, a necessary criterion for the successful restoration specifies that a velocity flow field fitting the PIV or PTV data must be unique. If this correct restoration is not still possible when any part of the velocity flow field is omitted then this flow is labelled as critically sparse. Therefore, this necessary criterion for the successful restoration is met if the sparsity of these data are above critical.

The necessary sparsity criterion for the successful restoration may be checked using homogeneously sparse velocity measurements, presented on a regular grid. Here, S is the sparsity of the data, i.e. the number of grid-points containing data, divided by the total number of grid-points (expressed in percent), while L_s is the characteristic length scale (expressed in grid-points) of the **smallest resolved**[1] entities within the measured, discrete, velocity flow field. According to §C, an approximation of the velocity flow field within the sample volume is yielded by an initial interpolation and subsequently improved and specified iteratively. The interpolation of the smallest entities of this flow is possible where at least two vectors are present at a distance of L_s, i.e. if the sparsity of the data satisfies a *critical sparsity condition*:

$$S \geq \frac{8}{L_s^3} \times 100\% \tag{B.11}$$

In cases of turbulence, the number of grid-points that are needed for the resolution of the smallest vortices is four grid-points, meaning that for the correct restoration $S \geq 12.5\%$. It is suggested that 12.5% is considered to be the default value for critical sparsity, since all types of flows with $S \geq 12.5\%$ may be successfully reconstructed, providing the noise level in the experimental measurements is below its critical value (discussed below).

[1]The flow feature is resolved on the grid if all its velocity maxima and minima can be projected on the corresponding grid nodes

D.1 Algorithm sensitivity to noise (critically-sparse velocity flow field)

The sensitivity of PEFRA to a critically sparse velocity flow field containing noise, $\vec{\delta^o}$, is considered in reference to Equation B.4. If the restoration of the pattern of the vorticity flow field is unaffected by noise, the only solution to this expression is the true vorticity, $\vec{\omega^T}$. The substitution of $\vec{\omega^T}$ into Equation B.4 reduces term 1 to $\|\vec{\delta^o}\|$ and term 2 disappears. If this is affected by noise, the restoration results in a new vorticity flow field, $\vec{\omega^T} + \vec{\theta}$, where $\vec{\theta}$ is the difference between $\vec{\omega^T}$ and the new output. Since the output satisfies the VTE, the substitution of $\vec{\omega^T} + \vec{\theta}$ into Equation B.4 reduces term 1 to $\|\vec{\delta^o} - \vec{\theta}\|$ and term 2 disappears. If this is minimized by $\vec{\omega^T} + \vec{\theta}$ it must be true that:

$$\frac{J(\vec{\omega^T})}{J(\vec{\omega^T} + \vec{\theta})} = \frac{\|\vec{\delta^o}\|_\Omega^2}{\|\vec{\delta^o} - \vec{\theta}\|_\Omega^2} > 1 \tag{B.12}$$

The inequality on the RHS of Equation B.12 is true if $|\vec{\theta}| < 2|\vec{\delta^o}|$, meaning that if the extremely sparse velocity measurements contain 5% noise, the difference between the true vorticity and the post-restoration vorticity is less than 10%. Therefore, the critically sparse velocity flow field will be successfully reconstructed, with data containing much less than 50 % of the noise, i.e.:

$$\frac{\|\vec{\delta^o}\|_\Omega^2}{\|\vec{\omega^T}\|_\Omega^2} \ll 0.5 \tag{B.13}$$

Note that Equation B.13 considerably underestimates the upper limit of the noise level in the input data permissible for successful restoration to still be achieved. In reality, successful restoration is possible even when $\|\vec{\delta^o}\|_\Omega^2 / \|\vec{\omega^T}\|_\Omega^2 \simeq 0.5.$, however as Equation B.13 unambiguously ensures successful restoration, it is this that is used for the noise level condition.

D.2 Algorithm sensitivity to noise (non critically-sparse velocity flow field)

The sensitivity of PEFRA to a non-critically sparse velocity flow field is identical to that completed for the PCEVD algorithm (cf. Vlasenko 2010, where a detailed study of the effect of noise in the data at each restoration stage of the algorithm is presented). Since PCEVD and PEFRA are from the same pedigree, these conclusions will remain the same for the present algorithm, so only a summary is provided here.

According to Vlasenko (2010), the noise in the experimental measurements contains a fraction that satisfies the VTE and, consequently, will be referred to here as the hydrodynamical component of the noise. Therefore, the velocity estimates generated from noisy PIV or PTV data, f, may be considered as consisting of the sum of three components: $f = \vec{v}^T + (\vec{h} + \vec{\vec{\delta}})$, where $\vec{v}^T$ is the true velocity, and the expression in brackets is noise consisting of a hydrodynamical component ($\vec{h}$) and a non-hydrodynamical component ($\vec{\delta}$), that does not satisfy VTE. The algorithm sensitivity to each of these is considered separately below.

D.2.1 The hydrodynamical component of the noise

The hydrodynamical component of the noise is a systematic error of both PCEVD and PEFRA that cannot be eliminated. The results will therefore be identical to that established for the earlier algorithm. Vlasenko (2010) applied PCEVD to two sets of data, each of 1000 vector fields, consisting of pure identically-distributed white noise with zero-mean and pure Gaussian-distributed white noise with zero-mean, respectively. These data suggest that if the noise contain such a component, it will pass the PCEVD filtering. Therefore, the application of PCEVD to these data revealed that each of the 1000 vector fields in the two sets contain a pattern suggestive of a turbulent motion, whose substitution into the discrete VTE results in equality. Figure G.1 is an example of one of these vector fields, obtained from one of the 1000 samples of white noise. It was established that in the two sets, the fraction of the hydrodynamical component of the noise obeys the same bell-shaped distribution. Its mean, variance and maximum (normalized by the noise level) equals 0.115, 0.510 and 13, respectively. These experiments with both types of noise revealed that the hydrodynamical component of the noise always results in an arbitrary isotropic turbulent-like pattern (e.g. Figure G.1) if the noise level in each component is identical. However, if the noise level in one component is significantly greater than for the others, it results in a flow field, satisfying the VTE, with anisotropy in that component. In cases of zero-mean distributed noise, the anisotropy causes a pattern similar to Kelvin-Helmholz instabilities. In cases of nonzero-mean distributed noise, the noise-pattern appears embedded within the constant background flow, whose components are proportional to the mean of the noise in the corresponding velocity components. Due to nonlinear terms, the VTE does not possess the property of linear additivity, meaning that if noise is present in measurements it will affect the form of the hydrodynamical component. These statistical experiments with artificial measurements revealed a weak anti-correlation, which is not smaller than -0.1. The subtraction of the corresponding artificial true velocity field from the restored output shows that, with the exception of differences in small details, the hydrodynamical component remains the same as the hydrodynamical component filtered from the pure noise. On the results of these experiments Vlasenko (2010) concluded that noise contains a hydrodynamical component that cannot be removed by PCEVD (nor by PEFRA) as it is merged with the output data. Defining n as the inverse of the signal-to-noise ratio (i.e. the ratio between the L2 norms of the noisy and true velocity flow field), the fraction of this component in the output is greater than $0.9n$ but less than $13n$ for zero mean noise. If the noise has nonzero mean, the hydrodynamical fraction is estimated as the sum of the mean noise level and $0.13n$.

D.2.2 The non-hydrodynamical component of the noise

If it is assumed that noise exists homogeneously within the sample volume and that this is able to be expanded spectrally, where a_i is the amplitude of these harmonics at a spatial frequency of $\phi = L/i$ $(i = 1, 2, ..., N)$ and U is defined as twice the characteristic velocity. According to Vlasenko (2010) an approximation of the non-hydrodynamical component of the noise is yielded by:

$$\epsilon_i \leq \underbrace{\exp^{-(\sigma i)^2/2}}_{1} \underbrace{\frac{a_i}{1+i^2}}_{2} \left(\sqrt{1 + \left(\underbrace{\frac{U}{(\phi^2\alpha)^{-1} + \nu}}_{3} \right)} \right) \tag{B.14}$$

where, ϵ_i is the harmonics remaining after one iteration of the restoration in the final block. Term 1, term 2 and term 3 (in under-brackets) represent the eigen-reduction factors of the noise of the Gaussian filtering, vorticity and velocity restoration steps, as if these are applied independently. The upper bounds for the non-hydrodynamical component of the noise remaining in the data at each step (separately) are provided in Vlasenko (2010). Equation B.14 is an approximation of the upper bound of the joint impact of these errors (from all stages) in the restoration block. This expression is, however, difficult to apply practically. A more convenient expression is achieved through correct selection of control parameters ν and α (§D.3). If this is done, the product of term 2 and the expression under the square-root in Equation B.14 is less than or equal to one, and ϵ_i may be expressed as: $\epsilon_i \leq \exp^{-(\sigma)^2/2} a_i$. When the L2 norm is subtracted from the LHS and RHS and both, in turn, are divided by the L2 norm of the true velocity flow field, a new inequality (in terms of the signal-to-noise ratio) is yielded: $n_r \leq \exp^{-(\sigma)^2/2} n_n$, where n_n and n_r are the inverse of the signal-to-noise ratio of the non-hydrodynamical component of the noise before and after the restoration in turn. Since the non-hydrodynamical component of the noise is a fraction of the noise quantified by the inverse of the signal-to-noise ratio, n, i.e. $n_n \leq n$, then it must be true that: $n_r \leq \exp^{-(\sigma)^2/2} n$. Using this inequality and the estimates for the hydrodynamical component of the noise, the total error remaining after the restoration may be expressed as:

$$n_{total} \leq n(0.13 + \exp^{-(\sigma)^2/2}) \tag{B.15}$$

As an example, if $\sigma = 1.34$, then according to the inequality, $n_{total} \leq 1$, when $n = 2.2$. Similarly as in Equation B.12, the inequality underestimates the upper limit of the noise level in the input data permissible for successful restoration to still be achieved.

D.3 Sensitivity to control parameters

The sensitivity of PEFRA to control parameters, σ, α and ν, is considered in reference to Equation B.14. Term 1 is the error reduction from Gaussian filtering and is always less than one and, therefore, never causes an increase in the noise-level. In fact, the opposite is true as an increase (linearly) in parameter σ (§B) decreases the noise-level exponentially, as well as smoothing the pattern of the velocity flow field. However, to prevent over-smoothing, Vlasenko (2010) established that σ must be less than 1.34. Similarly, term 2 is the error reduction from velocity restoration and this is always less than one. This is affected by term 3, that characterizes the upper limit of the impact of the vorticity restoration on the velocity restoration. Since the term under the square root is always more than one, it is possible that $\epsilon_i > a_i$ and this, in turn, causes an increase in the noise-level. To ensure that this upper limit is not achieved $\epsilon_i/a_i < 1$ and the control parameters selected accordingly. When the left hand side and the right hand side of Equation B.14 are divided by a_i, the right hand side is less than one. Simple mathematical operations show that this right hand side is always less than one if:

$$0 < \frac{U}{\alpha^{-1} - 3\nu} < 1 \tag{B.16}$$

Therefore, the permissible values of α and ν are unambiguously defined by Equation B.16 (referred to as *nu-alpha condition*). Note that the spatial frequency in front of α^{-1} is set to one and omitted here. However, it is important to remember its dimensions ($\mathrm{m\,s^{-1}}$) remain and these balance the denominator.

D.3.1 Optimum selection of control parameters

If the nu-alpha condition is satisfied, the sparsity and quantity of noise in the data allow successful restoration, and the noise in the experimental measurements has a zero-mean, then the noisy velocity flow field and the reconstructed velocity fields may be expressed as: $\vec{v}_{noisy} = \vec{v}_{true} + \vec{N}$ and $\vec{v}_{PEFRA} = \vec{v}_{true} + \vec{A} + \vec{N}_h$. Here, $\vec{v}_{true}$ is the true velocity flow field, $\vec{N}$ is noise in the experimental measurements, $\vec{N}_h$ is the hydrodynamical component of $\vec{N}$ and $\vec{A}$ represents the artefacts caused by poor selection of control parameters. The residual between the noisy velocity vectors and the reconstructed velocity vectors at the grid node k is $\vec{v}^k_{noisy} - \vec{v}^k_{PEFRA} = \vec{N}^k - \vec{N}^k_h - \vec{A}^k$. According to §D.2.1, if $\vec{N}$ has a zero-mean, $\vec{N}_h$ has an arbitrary isotropic noise-pattern (and therefore the difference $\vec{N}' = \vec{N} - \vec{N}_h$ also has zero-mean), and $\vec{v}^k_{noisy} - \vec{v}^k_{PEFRA} = \vec{N}'^k - \vec{A}^k$, the root-mean-square difference between the true velocity flow field and the reconstructed flow field may be estimated as:

$$\Delta = \sqrt{\frac{1}{K}\sum_k^K (\vec{v}^k_{noisy} - \vec{v}^k_{PEFRA})^2} = \sqrt{\overline{A^2} - 2\overline{A \cdot N'} + \overline{\vec{N}'^2}} \qquad \text{(B.17)}$$

where the overline denotes averaging. Note that $\vec{N}'$ has no hydrodynamical component, which means that that $\vec{A}$ and $\vec{N}'$ are independent. Moreover, $\vec{N}'$ has zero mean, hence $\overline{\vec{A} \cdot N'} = \overline{\vec{A}} \cdot \overline{\vec{N}} = 0$. Equation B.17 therefore may be simplified to:

$$\Delta = \sqrt{\frac{1}{K}\sum_k^K (\vec{v}^k_{noisy} - \vec{v}^k_{PEFRA})^2} = \sqrt{\overline{A^2} + (1-C)^2\overline{N^2}} \qquad \text{(B.18)}$$

where $C \in [0.09, 0.13]$ is the fraction of hydrodynamical component in $\vec{N}$. If the noise in the experimental measurements has a nonzero mean, the reasoning and intermediate conclusions remain the same – only the data $\vec{A}$, $\vec{N}$ and $\vec{N}_h$, are expressed as the sum of the corresponding zero mean variables $\vec{A}_0$, $\vec{N}_0$, $\vec{N}_{0h}$ and their corresponding means. The root of the mean-square-difference may then be computed by repeating the reasoning above. Since the arithmetic for this is cumbersome, it is omitted here and the final expression is provided instead:

$$\Delta = \sqrt{\frac{1}{K}\sum_{k}^{K}(\vec{v}^{k}_{noisy} - \vec{v}^{k}_{PEFRA})^2} = \sqrt{\overline{A_0^2} + (1-C)^2\overline{N_0^2} + \mu^2} \tag{B.19}$$

where μ is the sum of means of $\vec{A}$ and $\vec{N}$. Note that Δ in Equation B.18 and Equation B.19 is minimal when $\overline{A^2}$ and $\overline{A_0^2}$ are minimal. The artefacts are, in turn, minimal only when the optimum set of parameters are selected. Therefore, the problem of finding of optimum set of parameters is equivalent to the problem of finding the set of parameters that minimize Δ.

The search of parameters that minimize Δ may be achieved, for example, using the gradient descent method (cf. Talagrand and Courtier 1987), with the following control parameters used by default for the computation of the first gradient step: $\sigma = 1.34$ (see Vlasenko and Schnorr (2010)), ν can be set to its physical value and $\alpha = (U^{-1} + 3\nu)^{-1}$, starting at the boundary of nu-alpha condition (Equation B.16), where twice the maximum velocity of the noisy flow can be used as U. Note that if the noise in the experimental measurements is homogeneously distributed in both time and space, the control parameters may be considered the same for all frames. The simplest version of this algorithm is presented in the pseudo-code outline of PEFRA (Table G.4 in Appendix B.

D.3.2 Estimation of maximum discrepancy between true and restored flows

An important corollary of §D.3.1 will occur under ideal conditions, where $\vec{v}^k_{PEFRA} = \vec{v}_{true}$, or where the experimental measurements are noise free, and $\vec{v}^k_{noisy} = \vec{v}_{true}$. In these cases, Equation B.19 is never equal to zero. Note that in noise free measurements $\Delta = \sqrt{\vec{A}_0^2 + \mu^2}$ measures only the fraction of artefacts in the restored data, while the occurrence of noise in data only causes an increase in Δ. Therefore, the root-mean-square difference between the **true** velocity flow field and **restored** velocity flow field never exceeds Δ. If the mean and the variance of $\vec{N}$ are known (e.g. from a reference experiment with constant flow), Equation B.19 is an exact estimate of the root-mean-square difference between the true and restored velocity flow field.

D.4 Algorithm sensitivity to flow parameters: time, length, velocity.

D.4.1 Velocity

Due to the assumption of incompressibility PEFFRA may only be applied to a flow where the Mach number is much smaller than one.

D.4.2 Length

The quality of restoration for any individual flow entities depends on its grid-representative characteristic scale (expressed in grid-points) but not on its actual size. According to Vlasenko (2010), the energy spectrum of the rectified velocity flow field is proportional to $1/(1+\nu\phi^2)$, where ϕ is a discrete frequency, inversely proportional to the characteristic length (expressed in grid-points). Following Kolmogorov theory, the high band part of the energy spectrum will obey the $-5/3$ law. Therefore, in cases of turbulent flow, the high-band part of the energy spectrum of the rectified velocity flow field is steeper than expected. As a consequence, the small-scaled (in terms of grid-scales) flow entities associated with high frequencies present in the rectified velocity flow field are always smoother than the same entities in the true velocity flow field. However, tests using the artificial data containing zero-sparsity, obtained from direct numerical simulations, revealed that this smoothing error – defined as mean-square-difference between the input and output velocity flow field – is of the order of 0.1%.

D.4.3 Time

PEFRA uses the full VTE and therefore its accuracy in time depends only on how accurately the selected numerical scheme approximates the time derivative in the VTE. If τ is a time interval between two measurements, and O is big O notation, then for the first-order directed difference this error equals $O(\tau)$.

D.4.4 Summary of algorithm sensitivity to noise, sparsity and control parameters

In summary, successful restoration is possible for a critically sparse velocity flow field when Equation B.13 is satisfied and for a non-critically sparse velocity flow field when Equation B.15 is satisfied, and both the critical sparsity condition (Equation B.11) and the nu-alpha condition (Equation B.16) are met. If the critical sparsity of the experimental measurements is not known, then 12.5% may be used by default. Equation B.18 and Equation B.19 estimate the maximum discrepancy between the true flow and the restored flow for the zero-mean and the non-zero mean noise respectively, while the minimization of Δ with respect to α, ν and σ yields the optimum set of parameters.

E Algorithm performance

The performance of PEFRA is assessed using a series of twin-experiments, where the true velocity flow field is provided by Direct Numerical Simulation. From this artificial/numerical data, vectors are removed and noise added, such that a gappy and noisy sample is generated. After restoration, the results are compared to the true flow to establish if the two are similar (i.e. like"twins").

For these tests, direct numerical simulation data modelling turbulence in the wake of a cylinder (computed on a three-dimensional grid that consists of $128 \times 256 \times 128$ grid-points) and that of the development of a convection cell within a tank (that consists of $32 \times 32 \times 132$ grid-points) were used. The quality of the subsequent restoration is assessed normalized using the root-mean-square error, Δ_n, and the mean angle deviation, θ.

The Δ is defined as:

$$\Delta_n = \frac{\|\vec{v}_{true} - \vec{v}_{PEFRA}\|_2}{\|\vec{v}_{true}\|_2} \tag{B.20}$$

and measures the total difference between the true flow, $\vec{v}_{true}$, and the PEFRA output, $\vec{v}_{PEFRA}$. Note that Δ_n is the same as Δ discussed in §D.3.2, and $\vec{v}_{noisy} = \vec{v}_{true}$, but normalized using the root-mean-square of the true flow. For the twin experiments Δ_n is more convenient than Δ, since it measures the relative deviation of the restored flow from the true flow.

The θ is defined as:

$$\theta = \frac{\int_V |\arccos(\vec{v}_{true} - \vec{v}_{PEFRA})| d\mathbf{x}}{\int_V d\mathbf{x}} \tag{B.21}$$

and measures the mean angle difference between the true flow, $\vec{v}_{true}$, and the PEFRA output, $\vec{v}_{PEFRA}$. Therefore, if all the vectors in $\vec{v}_{PEFRA}$ have the same direction (i.e. the same pattern of the velocity flow field) as $\vec{v}_{true}$, then $\theta = 0$. Similar measures with $curl(\vec{v}_{true})$ and $curl(\vec{v}_{PEFRA})$ are used to qualify the vorticity reconstruction. They are denoted as Δ^{curl} and θ^{curl}

E.1 Sensitivity to sparsity, control parameters and type of flow

E.1.1 Experiment 1: Sensitivity to sparsity.

The sensitivity of PEFRA to sparse, noise-free velocity measurements is assessed using artificial/numerical data modelling turbulence in the wake of a cylinder. Here, two conditions are considered, where the sparsity of the data, S (Equation B.11), is 30% (i.e. $> 2.5\times$ critical sparsity) and 12.5% (i.e. = critical sparsity), respectively. A horizontal cross-section (HXS) of this flow is presented in Figure G.2A, while the sparse (input) conditions are presented in Figure G.2B and Figure G.2C. The black dots represent empty grid-points. To facilitate a visual post-restoration assessment, the HXS of the true flow is repeated in Figure G.3A, and the PEFRA output is presented in Figure G.3B ($S = 30\%$) and Figure G.3C ($S = 12.5\%$). Despite the sparsity of the PEFRA input, the restoration of the pattern of the velocity flow field is almost completely achieved in both cases, as confirmed by the quality statistics, where $\Delta_n = 0.1180$, and $\theta = 7.8860$, when $S = 30\%$ and $\Delta_n = 0.2260$, and $\theta = 11.2600$ when $S = 12.5\%$. A small difference between these two may be seen in fine details of the vorticity flow field, however the three-dimensional iso-surfaces of these both resemble the true flow. The iso-surfaces of vorticity absolute (further referred to as vorticity iso-surfaces) are used here for the visualisation of the reconstruction capabilites of PEFRA vorticism. The iso-surfaces in all experiments correspond to the mean of the true vorticity absolute. The vorticity iso-surface of the true flow is presented in Figure G.4A, and the PEFRA output is presented in Figure G.4B ($S = 30\%$) and Figure G.4C ($S = 12.5\%$). The vorticity iso-surface of $S = 30\%$ is similar to the true flow, except in fine details such as the artificial tongue seen in the lower-left corner of Figure G.4B. The artificial tongue also occurs in the vorticity iso-surface of $S = 12.5\%$, with it apparent the quality of the restoration decreases with the sparsity of the data (such that only large-scale components in Figure G.4C resemble the true iso-surface in Figure G.4A). The quality statistics show that when $S = 30\%$, $\Delta^{curl} = 0.2120$ and $\theta^{curl} = 12.43$ but when $S = 12.5\%$, $\Delta^{curl} = 0.4112$, and $\theta^{curl} = 20.680$.

E.1.2 Experiment 2: Sensitivity to sparsity and type of flow.

To extend the analysis, the algorithm performance is assessed under different flow conditions (such as adjacent to a rigid boundary) using artificial/numerical data modelling the development of a convection cell in a tank. The sinking of the cold, dense fluid generates two vortices, each with a characteristic length equalling half the length of the tank (i.e. 16 grid-points). Therefore, the critical sparsity (Equation B.11) of this flow is 98%. A vertical cross-section of this flow is presented in Figure G.5A, while the sparse (input) conditions are presented in Figure G.5B.

The black dots again represent empty grid-points. To facilitate a visual post-restoration assessment, the vertical cross-section of the true flow is repeated in Figure G.6A and the PEFRA output is presented in Figure G.6B. Note that the tank has rigid walls, meaning that exact boundary conditions may be defined. However, these exact boundary conditions were not used in place of the constant flux conditions specified in §C, enabling their application to a velocity flow field bounded by rigid walls to be assessed. Again, the restoration of the velocity flow field is almost completely achieved, even at its edges, as confirmed by θ (11.9000°) being similar to that for the wake of the cylinder. Under these conditions, Δ_n (0.4200) for the convection cell is larger. Such a large difference in Δ_n and small difference in θ indicates that, in cases of critical sparsity, the restoration of the direction (pattern) of the vectors is independent of the type of flow, while their magnitude (length) is flow dependent. The reason for this dependency is that the mean lengths of these vectors are proportional to the square-root of the mean energy of the flow. Due to the filtering attributes of PEFRA (§B), the average energy of the PEFRA output decreases after every iteration. This is compensated by setting it to the average energy of the sparse velocity flow field as it is assumed these (sparse) non-zero vectors are a representative sample of the true flow, and therefore their average energy is also representative (§B). However, in cases of a small volume containing highly sparse velocity measurements, this sampling is not representative and PEFRA cannot correctly recover the energy. Increasing the sparsity of the data beyond the critical level causes the algorithm to fail completely. An example of this failure is seen in Figure G.6C, where the sparsity is 99%. Therefore, Equation B.11 permits a correct estimate of the sparsity bounds where successful restoration is possible.

E.1.3 Experiment 3: Sensitivity to control parameters.

In Figure G.2 and Figure G.5, the optimum set of parameters were used to facilitate the restoration. For the example of the wake of the cylinder (Figure G.2), $\nu = 0.0025$, $\sigma = 0.1000$ and $\alpha = 0.0025$. If σ and ν are too large, over-filtering results (§D.3). The effects of this over-filtering is presented in Figure G.7, where the same flow as in Figure G.2A ($S = 30\%$) is used where $\nu = 2$ (Figure G.7A) and $\sigma = 2$ (Figure G.7B). These parameters cause the small-scale velocity components to be amalgamated or over-smoothed. If, however, α is too large, the nu-alpha condition is violated and this, in turn, causes the redundant small-scale velocity components that are seen in Figure G.7C (where $\alpha = 2$, i.e. 6.5× higher than that permitted in Equation B.16).

E.2 Sensitivity to sparsity and noise and comparison with other methods

E.2.1 Experiment 4: Sensitivity to noise (critically-sparse velocity flow field).

The restoration capabilities of PEFRA under extreme conditions (i.e. both critical sparsity and high noise level) are assessed using numerical data of the wake of a cylinder, but from a different time-step to that considered earlier, where the sparsity of the data, S, is 12.5%. In addition, white Gaussian noise (signal-to-noise ratio = 2) is added such that the quality statistics for the resultant gappy and noisy velocity flow field are $\Delta_n = 1.0260$ and $\theta = 52.4800°$. The sparse conditions are illustrated by the vectors within a HXS (Figure G.8A). The HXS of the true flow is presented in Figure G.8B and its three-dimensional vorticity iso-surface presented in Figure G.8C, such that they may be compared to the PEFRA outputs in Figure G.9A and Figure G.10A, respectively. Again, the difference in the quality statistics ($\Delta_n = 0.3230$ and $\theta = 20.9390°$, and $\Delta^{curl} = 0.5429$ and $\theta^{curl} = 26.9390°$) is seen in fine details, while the large-scale features still resemble the true flow. Note that from Equation B.12, it is possible that $\Delta_n \sim 2$ however, after restoration, the remaining error in this flow is almost a factor of 2 less than in the gappy and noisy velocity flow field. This fact warrants a comment on Equation B.12 that this noise reduction is possible even when the critically sparse velocity flow field is highly contaminated by noise. At the same time, θ decreases by almost a factor of 2.5. In the equivalent tests without noise ($S = 12.5\%$), Δ_n decreases by a factor of 2, while θ decreases by a factor of 1.5. Therefore, the error of the restoration of gappy and noisy data (with signal-to-noise ratio = 2) causes an increase in the error of the restoration by a factor of 2. Consequently, it is concluded this restoration is successful even if the velocity flow field is critically sparse and contaminated by noise.

E.2.2 Experiment 5: Comparison with other methods.

To complement the assessment of the algorithm performance, PEFRA is compared to PCEVD and Weighed Average Interpolation (WAI). The connection to PCEVD is made to show the benefit of the new algorithm over its predecessor. The connection to WAI is made to facilitate benchmarking against other methods as using specialist restoration method (e.g. PCEVD) is only meaningful to those familiar with that method. WAI, however, is both commonly used and easy to implement, and therefore can be a reference restoration method with which PEFRA or any other restoration method are compared. Here, the same gappy and noisy velocity flow field presented in Figure G.8A is processed using PCEVD (Figure G.9B and Figure G.10B) and WAI (Figure G.9C and Figure G.10C), respectively. It was established above that the same data was mostly recovered by PEFRA, as confirmed by the quality statistics, where $\Delta_n = 0.3230$ and $\theta = 20.9390°$. In contrast, the PCEVD output has little in common with the true flow and, consequently, $\Delta_n = 99.0000$ and $\theta = 87.0000°$, $\Delta^{curl} = 346.12$ and $\theta^{curl} = 102.03°$. The implication of this is that vectors are orientated randomly with respect to the true solution and the restoration failed completely. The WAI output is an improvement over PCEVD ($\Delta_n = 0.9130$ and $\theta = 43.969°$,$\Delta^{curl} = 1.132$ and $\theta = 56.7°$), however these input vectors are too gappy and too noisy for the pattern of the resultant velocity flow field to be easily identified.

E.2.3 Dependency of restoration performance on inhomogeneity

The restoration performance is inversely proportional to the quantity of the hydrodynamical component of the noise and PEFRA artefacts remaining in the data. The difference between the true flow and restored flow yields a vector field which is a merger of the hydrodynamical error and PEFRA artefacts remaining in the restored data. Such a difference, presented as a vector field in Figure G.11, is obtained for the flow represented in Figure G.8A (experiment 4). The length of the vectors at each grid-point represents the magnitude of the error at that point, while its direction does not have any particular sense. Note that although the true flow and restored flow (see Figures G.8B and G.9A) exhibit an isotropic pattern in their center and an anisotropic pattern at their edges, the error still remains isotropic. The relative root-mean-square of this vector field equals $\Delta_n = 0.3230$. For the similar field, with $S = 12.5\%$ but in the absence of noise, Experiment 1 revealed that the quantity of PEFRA artefacts, A, in the restored velocity flow field equals 0.22. According to §D.2.1, the mean quantity of hydrodynamical components may be estimated as $0.11n = 0.22$, where $n = 2$ is the noise level in the experiment. If the PEFRA artefacts and the hydrodynamical component of the noise are independent, the root of the sum of the squares of these two will be approximately equal to Δ_n in this experiment, which is confirmed. Therefore, the affects of sparsity and noise on PEFRA restoration are independent.

F Implementation with 3D-PTV

PEFRA was developed for the restoration of gappy and noisy velocity measurements where the arrangement of a standard laboratory PIV or PTV set-up is not possible. Here, the assessment of the algorithm performance is extended to submersible 3D-PTV measurements in ocean flows, i.e. using data collected in-situ under extreme conditions.

Presently, our employment of 3D-PTV is for the study of the three-dimensional turbulence characteristics of the bottom boundary layer of the coastal ocean (Nimmo-Smith, 2008). Unlike laboratory measurements, where small neutrally-buoyant particles are seeded within the flow, plankton and suspended sediments are used as tracers. The use of these arises from the impracticality of seeding the ocean with tracers, meaning that a reliance on naturally available seed material is essential (Bertuccioli et al., 1999). The uneven shape of these particles especially, scattered inhomogeneously within the sample volume, causes an increase in the noise level since it cannot always be assumed that they act as passive tracers of the velocity flow field. In these cases, using PEFRA is highly beneficial, and this application is discussed below.

As in §E, the quality of the subsequent restoration is assessed using the normalized root-mean square error, Δ_n, and the mean angle deviation, θ. The only difference is in normalization – selected to be the root-mean-square of the noisy velocity flow field. Since the in-situ velocity flow field has an arbitrary turbulent pattern and the PIV or PTV instrumentation is directionally independent, it is assumed that the noise has zero-mean and its level in these experimental measurements is at least twice as small as the level of the signal. In these cases, the variation between the root-mean-square difference of the noisy and the true flow is not greater than 12% and may be considered as approximately equal. Therefore, as before, Δ_n estimates the approximate relative maximum deviation from the true flow, permitting estimation of the optimum set of parameters, as discussed in §D.3.1 and §D.3.2.

If it is assumed that the plankton and sediments used as tracers are equally distributed within the small, arbitrarily turbulent sample volume, the experimental measurements have approximately constant level of noise and sparsity throughout the time series with small biases around this constant. Similarly, as sampling was conducted over periods of less than half an hour, and the site itself was sheltered from surface effects, the background flow conditions were also approximately constant throughout data collection. This means that restored velocity flow fields will have the same quality with the same level of artefacts. According to §D.3.1 and §D.3.2 Δ_n equals the sum of the root-mean-square of the noise in the data and artefacts produced by PEFRA during restoration. Any bias in noise or artefacts causes the corresponding bias in Δ_n, that over a sufficiently long time series will exhibit a random bell shaped distribution with a narrow variance. Following the random value distribution theory, it is expected that most of Δ_n biases will not exceed the variance, while the probability that Δ_n biases considerably exceed this value is close to zero. Therefore, an anomalous increase of Δ_n may be interpreted as an inconsistency in PEFRA or an incorrect assumption of homogeneous noise distribution for the instantaneous flow field. To arbitrate in such cases, the additional data available from 3D-PTV becomes important, as these contain an image of each of the particles and may be checked when unexpected results are encountered (Nimmo-Smith, 2008). Following Adrian and Westerweel (2010), it is expected that a small, regular particle will behave more like an ideal tracer – and, therefore, contaminate the velocity flow field less – than a large, more irregular particle. In addition, in the ocean, a minority of these large tracers may also be mobile plankton capable of independent movement. Consequently, the vectors established from tracking a small particle will need less adjustment by PEFRA, while the vectors established from tracking a large particle will need more adjustment by PEFRA. Therefore, if an instantaneous flow field is associated with an anomalous velocity arising from the presence of extremely large particles (or a high total number of large particles), it will be concluded that it is as a result of these tracers that the velocity flow field will contain more noise that results in an increase in Δ_n and θ. Moreover, it will be concluded that this is the only reason for the increase, and there is no inconsistency in PEFRA if the corrections of velocity vectors corresponding to small particles are much smaller than the corrections of velocity vectors corresponding to large particles.

F.1 Instrumentation

The submersible 3D-PTV system is detailed fully by Nimmo-Smith (2008). It consists of four 1002×1004 pixel 8-bit digital cameras that view a $20 \times 20 \times 20\,\mathrm{cm}^3$ sample volume illuminated by four 500 W underwater lights. Electrical power is supplied from a surface support vessel using an umbilical cable. The cable also enables communication with the 3D-PTV master computer, that synchronises the triggering of the cameras at the rate of 25 Hz. Data from each of these cameras is recorded by its own computer, each with $2 \times 400\,\mathrm{GB}$ of hard disk storage (3.2 TB total). All underwater components are mounted on a rigid frame. A vane attached to the frame aligns it at an angle to the mean flow to prevent the contamination of the sample volume by the wake of the system. This alignment is monitored by an Acoustic Döppler Velocimeter (ADV) that also offers auxiliary turbulence statistics at the same height as the sample volume.

F.2 Data processing and use of PEFRA

After the calibration of the system (Svoboda et al., 2005), data processing is completed in three stages using the specialist 'Particle Tracking Velocimetry' software developed by Maas et al. (1993) and Willneff (2003). Here, particles are identified within the exposures from the four cameras by high-pass filtering, segmentation and weighted-centroid methods. In addition, maximum and minimum size criteria are used to limit contamination by noise or large objects. The calibration parameters are then used to relate the exposures from the four independent cameras, such that the three-dimensional position of the particles is yielded. Finally, tracking is done in image- and object-space, running the sequence in both directions so that linkages between adjacent frames are maximised, and the velocity of each of the particles at each time-step established by low-pass filtering their trajectories using a moving cubic spline (Luthi et al., 2005).

The experimental measurements are projected from an irregular grid onto a regular grid, where only the nearest neighbour of each of the detected particles are filled by interpolation (and all others set to zero) to minimise noise that arises from gridding. Similarly, if the distance, D, between each of the particles and the nearest grid node exceeds $0.5\sqrt{h_x^2 + h_y^2 + h_z^2}$ (where, h_x, h_y and h_z are the spatial discretization in X, Y and Z, respectively), these grid-points are set to zero also. Note that this algorithm is therefore adaptable to processor speed and memory such that, in theory, at an infinite resolution, all the particles will fall on the grid exactly.

F.3 *In situ* 3D-PTV experiments

The submersible 3D-PTV system was deployed on the east side of Plymouth Sound, Plymouth, UK, on 9 June 2005 in 12 m deep water on an ebb tide over a period of about 4 hours. The centre of the sample volume was set at the height of 0.64 m above the seabed. Data was recorded in 20 minute runs directly to hard disk storage.

For the following discussion, a right-handed Cartesian co-ordinate system is used, where X is aligned with the along-stream velocity component (U), Y is aligned with the cross-stream velocity component (V), and Z is aligned (upwards) with the wall-normal velocity component (W). Within this frame of reference, the zero-mean velocity is established using Reynold's Decomposition, i.e.:

$$u \equiv U - \langle U \rangle, \qquad v \equiv V - \langle V \rangle, \qquad \text{and} \qquad w \equiv W - \langle W \rangle, \tag{B.22}$$

where, $\langle\rangle$ is the mean of that velocity component.

Consistent with past in situ 2D-PIV measurements (Nimmo-Smith et al., 2002, 2005), a variety of different conditions were recorded, as characterised by different turbulence strengths ($I = \sqrt{u^2 + v^2 + w^2}$). Here, the restoration of two different conditions – corresponding to the 5th ($I = 0.6065$) and the 85th ($I = 1.0929$) percentile of the turbulence strengths during an example 10 minute time-series – are discussed. The sparsity of these flows are 2.14 % and 1.95 % while their characteristic lengths are 9 and 8 grid-points, in turn. Therefore, following Equation B.11, the critical sparsity equals 1.09 % where $I = 0.6065$ and 1.56 % where $I = 1.0929$. Since the sparsity of these data exceeds the critical sparsity condition, it is expected that a successful restoration is possible.

Three orthogonal cross-sections of these flows are presented in Figure G.12A to Figure G.12C and Figure G.12D to Figure G.12F. The vectors corresponding to the PEFRA input (red) and the PEFRA output (black) are overlapped to illustrate the adjustment made. The projection of the convex hull of the tracked particles, representing the area where data were recorded, is shaded white. The subsequent restoration of these data culminates in the vorticity iso-surfaces presented in Figure G.13A and Figure G.13B. Qualitatively, Figure G.13A exhibits small velocity gradients typical of a low turbulence level and Figure G.13B is consistent with that expected of a higher turbulence level. While these cannot themselves confirm a correct restoration, the excellent agreement between the PEFRA input and the PEFRA output for the two different conditions, as well as that of the coherent structures and the turbulence level (Adrian, 2007), implies the physics of these flows have been successfully restored. Specific details of the restoration of Figure G.13A and Figure G.13B are quantified below.

Figure G.14 presents an instantaneous velocity flow field where $I = 0.6065$. Here, 79 particles output by the tracking software survived filtering by moving cubic spline (Figure G.14A). For the grid used ($h_x = h_y = h_z = 1\,\text{cm}$), $D > 0.87\,\text{cm}$ at one of these grid-points (red '+' markers). The interpolation of the velocity components onto the remaining grid-points results in a usable number of seed-points for the new algorithm of 78 (green '+' markers). After the application of PEFRA Δ_n and θ are quantified on a particle-by-particle basis (Figure G.14B). The corresponding velocity flow field that has been modified by PEFRA is presented in Figure G.14C, where the instantaneous sample volume mean velocity components have been subtracted from each of the vectors to reveal the three-dimensional turbulence structures. This is similar to the pattern of the velocity flow field presented in Figure G.14D, where PEFRA was not applied. The cause of this similarity is that the sparsity of the data exceeds the critical sparsity condition by a factor of two and therefore will not affect the quality of the restoration. This, in turn, is aided by the small velocity gradients within the sample volume meaning that both large particles and small particles will follow the streamlines alike. Consequently, neither particles increase the noise level substantially.

Figure G.15 presents an instantaneous velocity flow field where $I = 1.0929$. The format of these panels are the same as for the last figure, with 75 unique seed points used (Figure G.15A). An increase in Δ_n and θ on a particle-by-particle basis (Figure G.15B) is visible and more adjustment seen in the velocity flow field that was modified by PEFRA (Figure G.15C) over that where PEFRA was not applied (Figure G.15D). The cause of this adjustment is that the sparsity of the data is nearer the critical sparsity condition and therefore a very small part of this modification is likely to be an error (that increases as the sparsity of the data approaches the critical sparsity). This, in turn, is compounded by the large velocity gradients within the sample volume, as large particles cannot react to these as quickly as small particles and are affected by differential shear along their length.

As a verification of the adjustment made by PEFRA, the image containing a record of each of the particles must be examined to establish whether individual tracer characteristics (e.g. bubbles, large or heavy particles) are responsible for these differences. Figure G.16 presents three sections of the image, viewed from each of the four different camera angles. The particles corresponding to the frame minimum Δ_n (0.6798) and frame minimum θ (0.0461) are highlighted in Figure G.16A and Figure G.16B. Although exhibiting the differences in shape expected of natural particles, these appear to be small in size and therefore the lack of adjustment is in agreement with the reasoning that they will not affect the noise level as much as a larger, more irregular particle. Accordingly, the particle corresponding to the frame maximum Δ_n (29.2589) and θ (15.9934) is revealed in Figure G.16C to be a larger, irregular aggregate typical of a sediment floc. Such particles increase the noise level, and therefore need adjustment by PEFRA. Note that this connection to individual tracer characteristics is appropriate as there are a sufficient number of particles within the sample volume for the algorithm not to fail, while the small distance that separates these from their nearest grid-points (i.e. $D < 0.87\,\mathrm{cm}$) ensures that errors linked with interpolation will also be small.

This approach also provides a secondary method of validation. In 3D-PTV, individual particles are tracked as they are advected through the three-dimensional sample volume. If a time-series of the instantaneous velocity flow field is examined (Figure G.17A, Figure G.17B and Figure G.17C), it may be seen from the stream ribbons that depict the gridded PEFRA output that the same coherent vortical structure is spatially and temporally coherent, and from the cones that depict the gridded particle positions that these progress through the sample volume. If the PEFRA output were incorrect, then there would be no coherence in the structure over the sequence of snapshots. Additionally, for any single particle moving through the sample volume, a similar correction (related to the individual tracer characteristics, as discussed with Figure G.16) may be expected. Figure G.17D and Figure G.17E present a time-series the correction of a total of 12 different particles associated with the maximum and minimum adjustments that were made in Figure G.17B to the total difference and angle deviation, respectively, over a sequence of 7 frames. These are seen to be both spatially and temporally invariant, giving confidence that it is the physical characteristics of the particles that causes the errors that are successfully corrected by PEFRA.

To complement the assessment of the instantaneous velocity flow fields presented above, Figure G.18 shows a time-series of the particle and turbulence strength and total particle count (Figure G.18A and Figure G.18B), as well as the corresponding Δ_n and θ quantities (Figure G.18C and Figure G.18D). An increase in the sample volume mean turbulence intensities are generally connected to the passage of large coherent motions. This, in turn, is associated with the corresponding increase in Δ_n and θ that arises from tracking difficulties when the flow structures are more complex. In extreme instances of swimming particles not advected through the flow field, however, a single tracer can bias both restoration and turbulence statistics. An example of this is presented in Figure G.19, where one particle is seen to move very differently to that of the pattern of the velocity flow field and necessitates a large adjustment by PEFRA (Figure G.19A). The examination of the original image (Figure G.19B) reveals that this 'particle' has a distinct body and tail, is 4.0 mm in length, and swims at a speed of $5.68\,\mathrm{cm\,s^{-1}}$, or 14.2 body lengths per second. These quantities are consistent with laboratory measurements of the swimming speed of fish larvae (Bellwood and Fisher, 2001). This contamination is easily eliminated by removing single outliers using local Δ_n and θ anomalies and reprocessing the affected frame, but the example also confirms that PEFRA correctly identifies erroneous biological particles in situ.

G Conclusions

A new Physics-Enabled Flow Restoration Algorithm (PEFRA) has been developed for the restoration of gappy and noisy velocity measurements where a standard PTV or PIV laboratory set-up (e.g. concentration/size of the particles tracked) is not possible, and the boundary and initial conditions are not known *a priori*. Implemented as a black box approach, where no user-background in fluid dynamics is necessary, this is able to restore the physical structure of the flow from gappy and noisy data, in accordance with its hydrodynamical basis. In addition to the restoration of the velocity flow field, PEFRA also estimates the maximum possible deviation of the output from the true flow. A theoretical and numerical assessment of the algorithm sensitivity demonstrates its successful employment under different flow conditions. When applied to submersible 3D-PTV measurements from the bottom boundary layer of the coastal ocean, it is apparent that using PEFRA is beneficial in processing data collected under difficult conditions, such as where the number (and reliability) of tracer-particles is very sparse.

Acknowledgements

E. C. C. Steele was funded by the School of Marine Science and Engineering, Plymouth University, Plymouth, UK. The method for the denoising of fluid flows was adapted under a visiting fellowship award from the Marine Institute (Plymouth University), Plymouth, UK. Development of the 3D-PTV system was funded by the Royal Society, the Nuffield Foundation and the UK Natural Environment Research Council. We are grateful to C. Bunney, E. Davies and D. Uren for assistance with the deployment of the 3D-PTV system.

Appendix A

Let $\mathbf{p}$ be a divergence-free vector function. Following Vlasenko (2010),

$$\mathbf{q} - \mathbf{a\Delta q} = \mathbf{p} \tag{B.23}$$

(with constant flux boundary conditions applied) will only have a divergence-free solution. Therefore, the vorticity restoration in PCEVD and PEFRA will only have a divergence-free output. The equation for the velocity restoration is similar, however, in PEFRA, $\mathbf{p}$ is divergent, since this is not eliminated in $\vec{v}_s$ by solenoidal projection. To estimate the divergence remaining in the reconstructed velocity flow field after one iteration, the *div* operator is applied to both the LHS and the RHS of Equation B.8. In doing so, the divergence-free term $\nabla \times \vec{\omega}$ on the RHS of Equation B.8 disappears and the equation transforms to:

$$u - \triangle u = f \tag{B.24}$$

where, $u = div(\vec{u})$ and $f = div(\vec{v}_s)$.

Expanding u and f in a trigonometrical Fourier series, and substituting them into Equation B.24, achieves:

$$u_n + 4(\pi n/L)^2 u_n = f_n, \qquad n = 1, 2, ..., N \tag{B.25}$$

where, u_n and f_n is the amplitude of harmonic n and L is the horizontal scale of the sample volume, V, where the data were recorded. Simple arithmetical manipulation achieves:

$$u_n = \frac{f_n}{1 + 4(\pi n/L)^2} \tag{B.26}$$

After each iteration, the divergence in $\vec{u}$ reduces by at least a factor of $1/(1 + 4(\pi n/L)^2)$, such that, after iteration i, this is by a factor of $1/(1 + 4(\pi n/L)^2)^i$. Therefore, with an increase in i, the divergence in $\vec{u}$ decreases, becoming negligible after several iterations.

Appendix B

The three tables comprising Appendix G are a pseudo-code representation of PEFRA, that follows the form of the MATLAB code written by the authors. Table 1 is a wrapper to PEFRA, and referred to as the PEFRA software. It sets the boundary conditions, finds the optimum set of parameters and launches the PEFRA function. The only user input needed in this software is to set the desirable tolerance and the viscosity of the fluid. The software then loads the time series of N velocity measurements (line 4), calibrates the size of V_l (lines 5-12) and determines the optimum set of control parameters (line 14), initialising the restoration of the measurements in the time series (lines 15-17). Table 2 outlines the PEFRA function, responsible for the interpolation of the data to the empty grid-points in V and extrapolation of the data into V_l (line 5), obtaining the linear flow field (lines 6-13) and performing the final restoration (lines 14-21). Table 3 outlines the PCEVD function, used by the software as external function. The stages of this algorithm are the same as discussed in §B with the only difference being that Step 2 (Solenoidal projection) is not applied. The 'cgs' function and 'speye' operator used are the Conjugate Gradients Squared Method and Sparse identity matrix operator, respectively, as included with a core MATLAB distribution. The algorithm for obtaining the optimum set of control parameters is presented in Table G.4.

% **- - - !!!! PROGRAM PEFRA !!!! - - -**

% *values* ν*, tol(desirable tolerance) and* τ *must be specified by user*

$[\vec{U}^{t=1:N}]$ = get_time_series % *read velocity measurements*

$(\vec{U}) = (\vec{U}^{t=1,2})$ % *first pair of vector fields*

$[\nu, \alpha, \sigma, d]$ = Set_default_values($\vec{U}$)

% *Initialization with* $\sigma = 1.34$, $d = 1$, $\alpha = (U^{-1} + 3\nu)^{-1}$

do

$[\vec{V}_1]$ = function_PEFRA($\vec{U}, \nu, \alpha, \sigma, \tau, d$)

d = d+1

$[\vec{V}_2]$ = function_PEFRA($\vec{U}, \nu, \alpha, \sigma, \tau, d$)

$[term]$ = termination_criterion($\vec{V}_1, \vec{V}_2$) % *term = true, when* $\|\vec{V}_1 - \vec{V}_2\|_2 < tol$

While (term_criterion = false)

% *search of optimal* (ν, α, σ)

$[\nu, \alpha, \sigma]$ = gradient_descent($\nu, \alpha, \sigma, \vec{U}, d$)

for t = 1: N % go through the whole time series

$[\vec{V}]$ = function_PEFRA($\vec{U}^t, \nu, \alpha, \sigma, \tau, d$)

end - - - !!!! END OF PROGRAM PEFRA !!!! - - -

Table (G.1). A wrapper to PEFRA, which computes boundary conditions, optimal set of parameters and starts PEFRA for the given time series.

function $[\vec{V}]$ = function_PEFRA($\vec{U}, \nu, \alpha, \sigma, \tau, d$)

V_l = Set_Vl(d,size($\vec{U}$)) % *Enlarge $\vec{U}$ by given d, Set volume V_l*

Interpolate values into empty nodes

$[\vec{V_l}]$ = Interpolation_and_Extrapolation($\vec{V_l}$)

do % *Get linear flow*

$[\vec{V_l^k}]$ = function_Linear_PCEVD($\vec{V_l}, \nu, \alpha, \sigma, \tau$)

% *In function_Linear_PCEVD, function Vector_E is substituted with $\partial \vec{\omega}_s / \partial t$,*

$[term]$ =termination_criterion($\vec{V_l^k}, \vec{V_l^{k-1}}$) % *term = true, when* $\|\vec{V_l^k} - \vec{V_l^{k-1}}\|_2 < tol$

$k = k + 1$

$\vec{V_l} = \vec{V_l^k}$

$[\vec{V_l}]$ = inserter($\vec{V_l}, \vec{U}$) % *Inserts nonempty values $\vec{U}$ into $\vec{V_l}$*

While (term_criterion = false)

do

$[\vec{V^k}]$ = function_PCEVD($\vec{V_l}, \nu, \alpha, \sigma, \tau$)

$[term]$ =termination_criterion($\vec{V_l^k}, \vec{V_l^{k-1}}$)

$k = k + 1$

$\vec{V_l} = \vec{V_l^k}$

$[\vec{V_l}]$ = inserter($\vec{V_l}, \vec{U}$) % *Inserts nonempty values $\vec{U}$ into $\vec{V_l}$*

While (term_criterion = false)

$[\vec{V_l}]$ = function_PCEVD($\vec{V_l}, \nu, \alpha, \sigma, \tau$) % *Final filtering*

Table (G.2). Function PEFRA.

function $[\vec{V}]$ = function_PCEVD($\vec{U}, \nu, \alpha, \sigma, \tau$) % *Without* **Step 2**

$\vec{U}_s$ = Gaussian_filter($\vec{U}, \sigma$) % - - - - - - **Step 1**

$\vec{\omega}_s$ = curl($\vec{U}_s$)

$\vec{e}$ = Vector_E($\vec{U}_s, \vec{\omega}_s, \tau$) % *vector_E computes LHS of VTE*

$\vec{F} = \vec{\omega}_s - \alpha\vec{e}$

A = speye(V_{lg}, V_{lg})-$\alpha * \nu$*Lap

% *Lap = Laplace operator in matrix form,* V_{lg} *= number of grid nodes in* V_l

$\vec{\omega}$ = cgs(A,$\vec{F}$) % - - - - - - **Step 3**

% it cgs = Conjugate Gradients Squared Method

B = speye(V_{lg}, V_{lg})-Lap

$\vec{F}_2$ = curl($\vec{\omega}$)+$\vec{U}_s$

$\vec{V}$= cgs(B,$\vec{F}_2$) % - - - - - - **Step 4**

$\vec{V}$= Energy($\vec{U}, \vec{V}$)% *Energy recovery*

Table (G.3). Function PCEVD.

1	function $[\vec{V}]$ = gradient_decent$(\vec{U}, \vec{V}, \nu, \alpha, \sigma, \tau, d)$
2	step = 0.05*σ; k = 1; $\Delta^1 = \infty$
3	**do**
4	$\Delta^{old} = \Delta^k$
5	$[\vec{V}]$ = function_PEFRA$(\vec{U}, \nu, \alpha, \sigma, \tau, d)$
6	Δ^k = delta_est$(\vec{U}, \vec{V})$ *compute* Δ *using Equation* (B.19)
7	k = k+1
9	**while(**$\Delta^{old} > \Delta^k + tol^{gr}$ **or** $k \leq 5$ **)** % *by default* $tol^{gr} = 0.001\Delta^{old}$
10	*repeat lines 2-9 for* ν *and* α
11	*if* $(,\nu, \alpha, \sigma, \tau)$ *is optimal, do all again until* $\Delta^{old} - \Delta^k < tol$

Table (G.4). The search of optimal set of parameters for PEFRA based on gradient descent method.

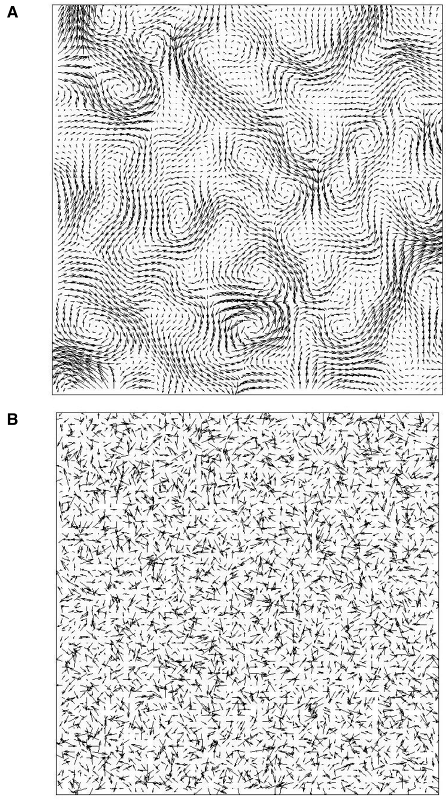

Figure (G.1). (A) The hydrodynamical component of noise, extracted from (B) the distribution of white Gaussian noise.

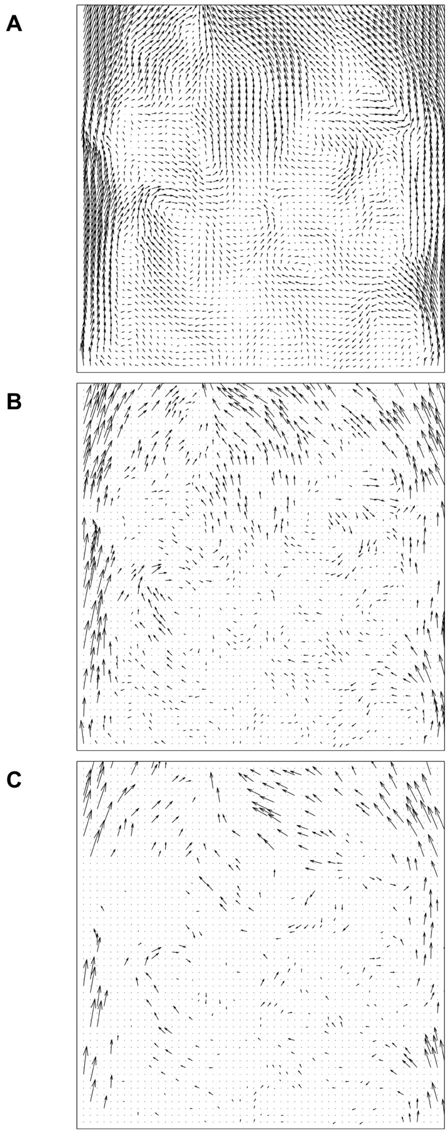

Figure (G.2). The horizontal cross-section of a velocity flow field modelling turbulence in the wake of a cylinder. (A) True flow, (B) with $S = 30\%$, and (C) with $S = 12.5\%$. Black dots represent empty-grid points.

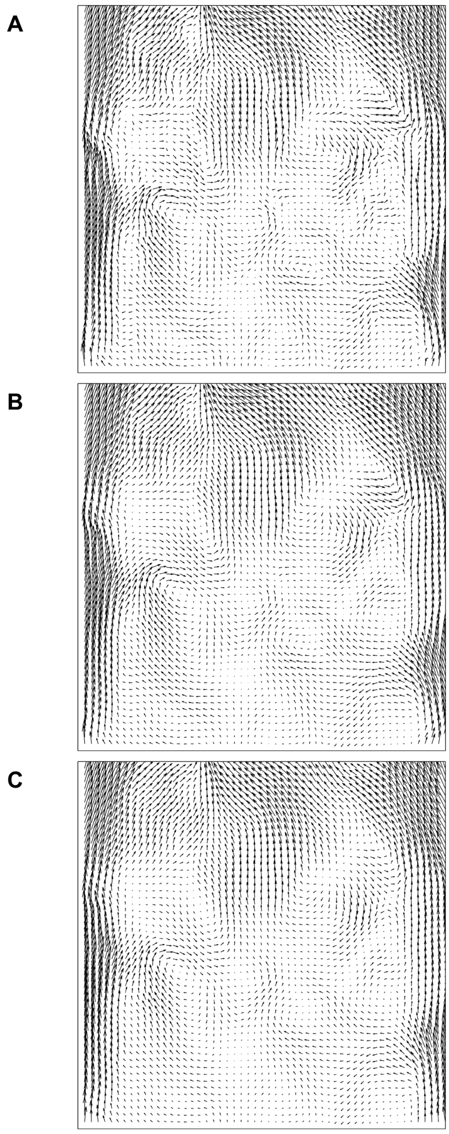

Figure (G.3). The horizontal cross-section of a velocity flow field modelling turbulence in the wake of a cylinder. (A) True flow, (B) PEFRA output from the restoration of Figure G.2B, and (C) PEFRA output from the restoration of Figure G.2C.

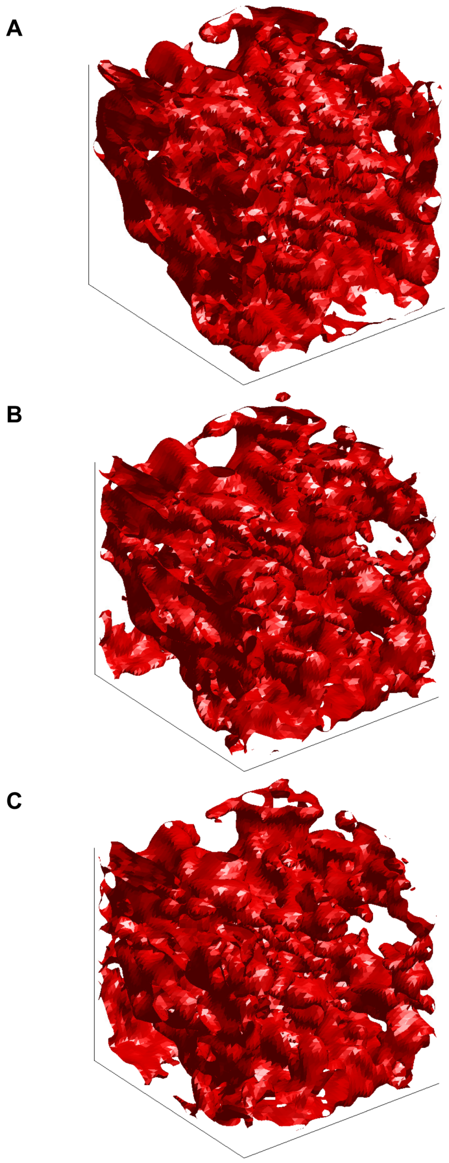

Figure (G.4). The three-dimensional vorticity iso-surface, corresponding to Figure G.3. (A) True flow, (B) PEFRA output from the restoration of Figure G.2B, and (C) PEFRA output from the restoration of Figure G.2C.

A

B

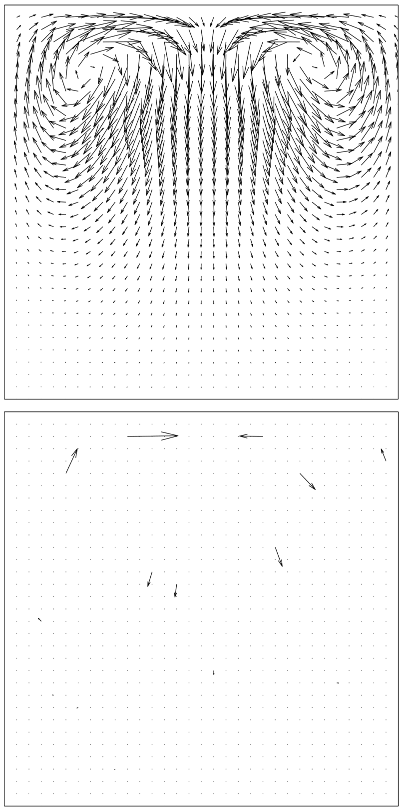

Figure (G.5). A vertical cross-section of the velocity flow field modelling a convection cell. (A) True flow, and (B) sparse velocity flow field where $S = 98\%$. The black dots represent empty grid-points.

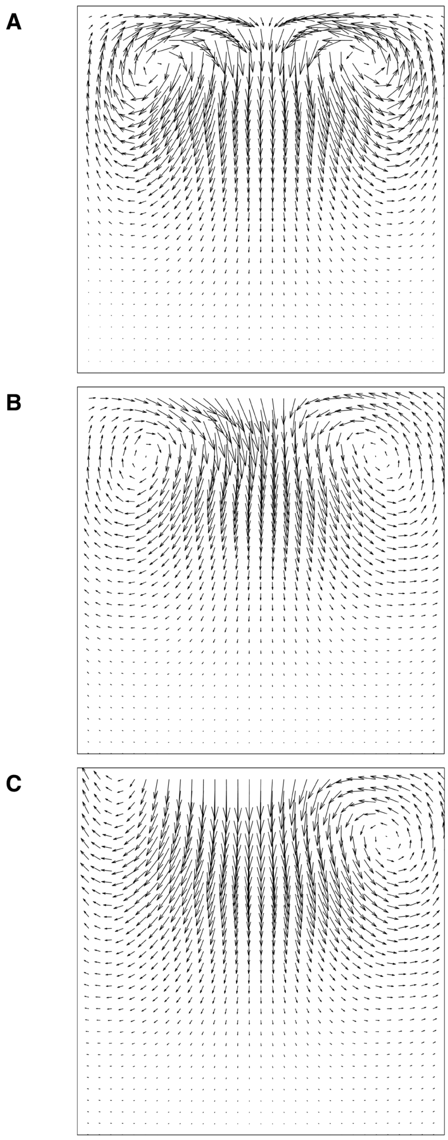

Figure (G.6). A vertical cross-section of the velocity flow field modelling a convection cell. (A) True flow, (B) PEFRA output from the restoration of Figure G.5B. $S = 98\%$, (C) PEFRA output from the restoration of the same flow which sparsity $S = 99\%$ is below critical value ($S_{critical} = 98\%$).

A
B
C

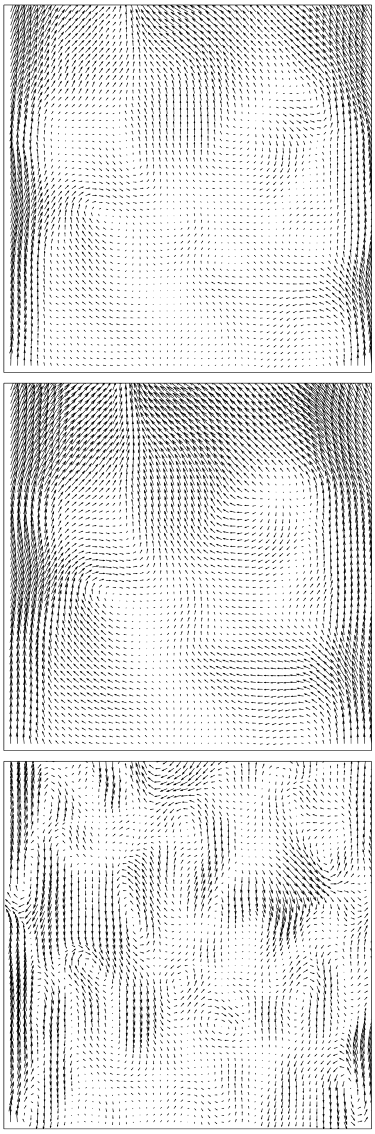

Figure (G.7). The horizontal cross-section of a velocity flow field modelling turbulence in the wake of a cylinder (Figure G.2), reconstructed by PEFRA with (A) $\nu = 2$, (B) $\sigma = 2$ and (C)$\alpha = 3$.

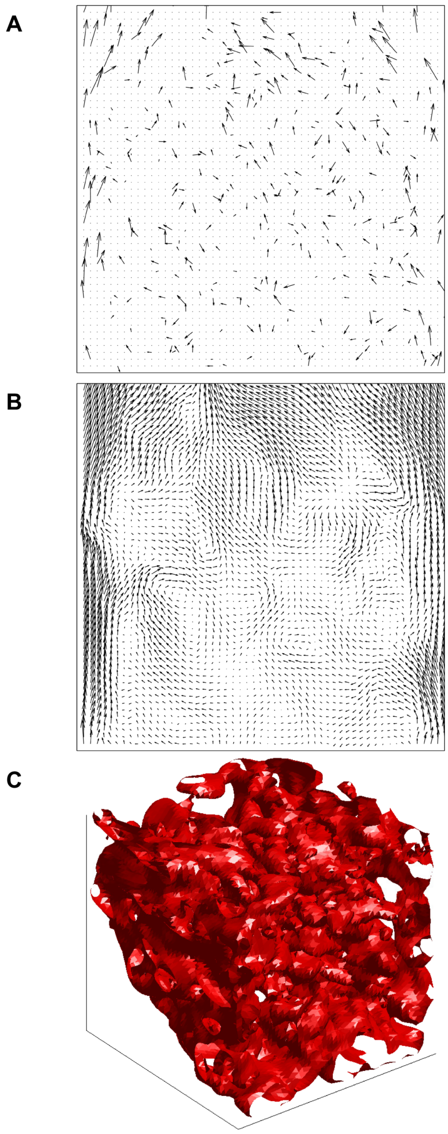

Figure (G.8). (A) The horizontal cross-section of a gappy and noisy velocity flow field modelling turbulence in the wake of a cylinder, and the corresponding (B) true flow and (C) vorticity iso-surface.

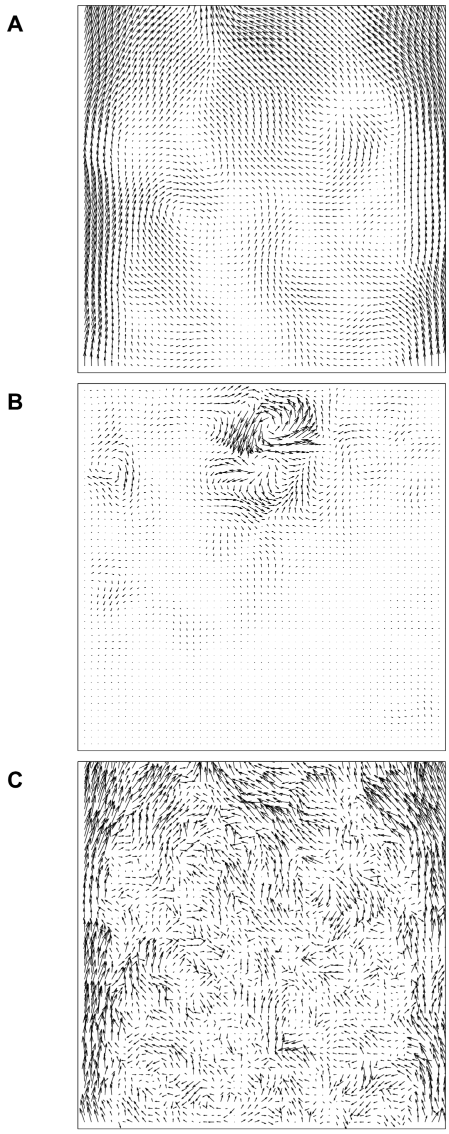

Figure (G.9). The horizontal cross-section of a velocity flow field modelling turbulence in the wake of a cylinder (Figure G.8), reconstructed by (A) PEFRA, (B) PCEVD and (C) AWI.

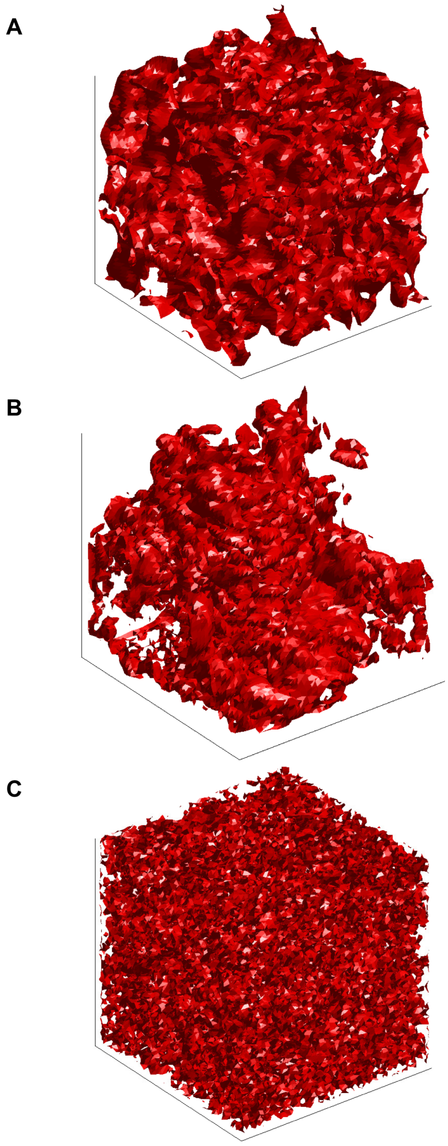

Figure (G.10). The three dimensional vorticity iso-surface corresponding to Figure G.9, reconstructed by (A) PEFRA, (B) PCEVD and (C) AWI.

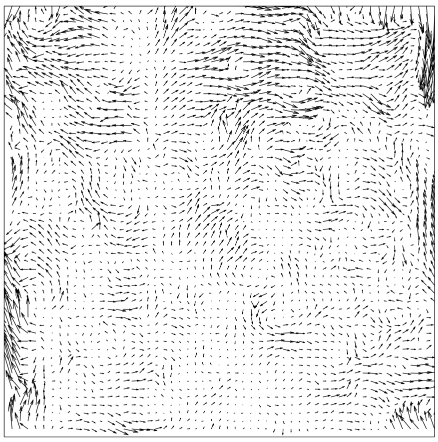

Figure (G.11). The difference between the true and restored field yields the vector field shown, obtained from data presented in Figure G.8B and Figure G.9A.

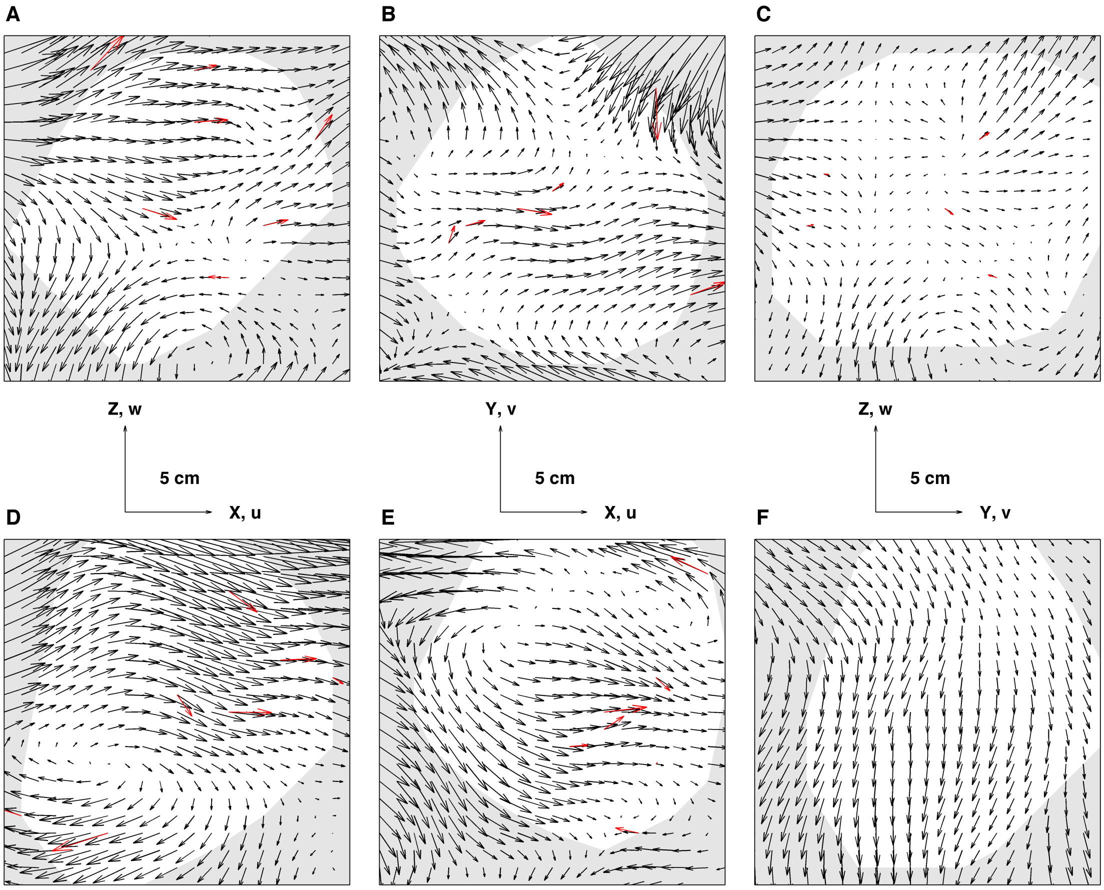

Figure (G.12). Row 1: cross-section of the velocity flow field corresponding to the minimum turbulence intensities recorded. Row 2: cross-section of the velocity flow field corresponding to the maximum turbulence intensities recorded. In each case, the orientation of the slices are indicated by the axes. The 3D-PTV measurements (red) and post-restoration velocity distribution (black) are overlapped. The projection of the convex hull of the tracked particles is shaded white.

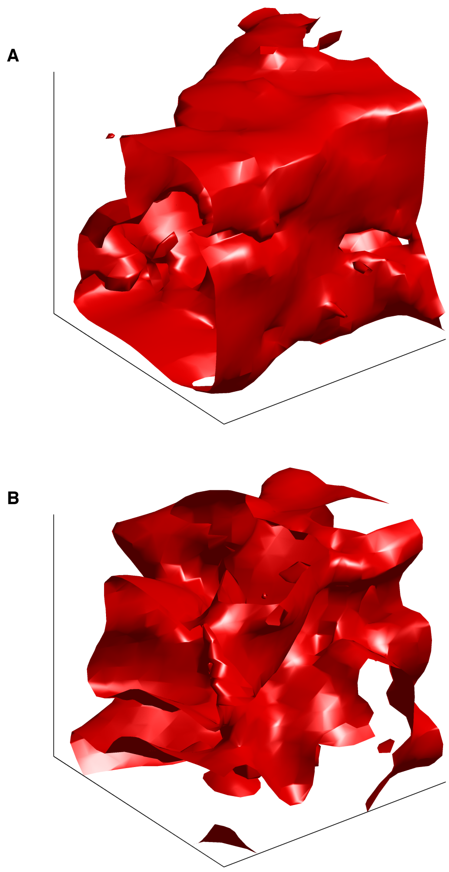

Figure (G.13). Vorticity iso-surfaces of the PEFRA output for the two conditions presented in Figure G.12.

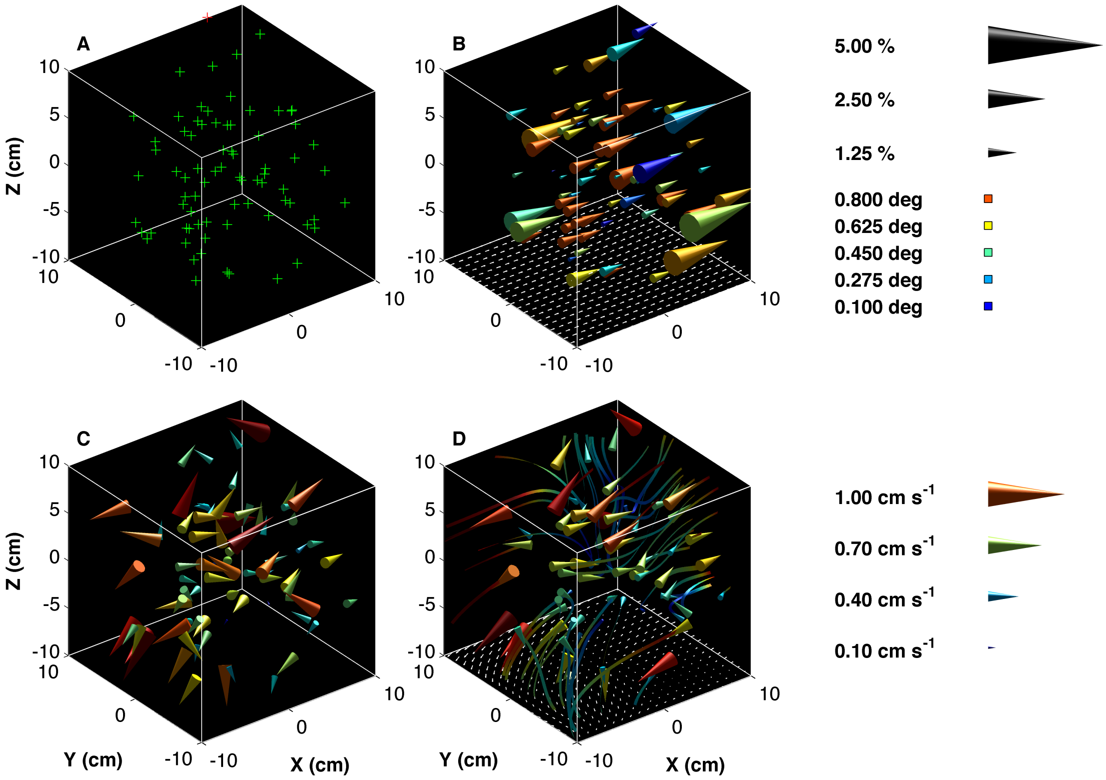

Figure (G.14). An instantaneous velocity flow field with a low turbulence strength: (A) output from the tracking software and gridding process; (B) The Δ_n (vector scale) and θ (vector colour) between the input and output velocity flow field at each of the seed-points; (C) Velocity distribution (coloured and scaled by the velocity magnitude) corrected by PEFRA; (D) Velocity distribution (coloured and scaled by the velocity magnitude) not corrected by PEFRA

.

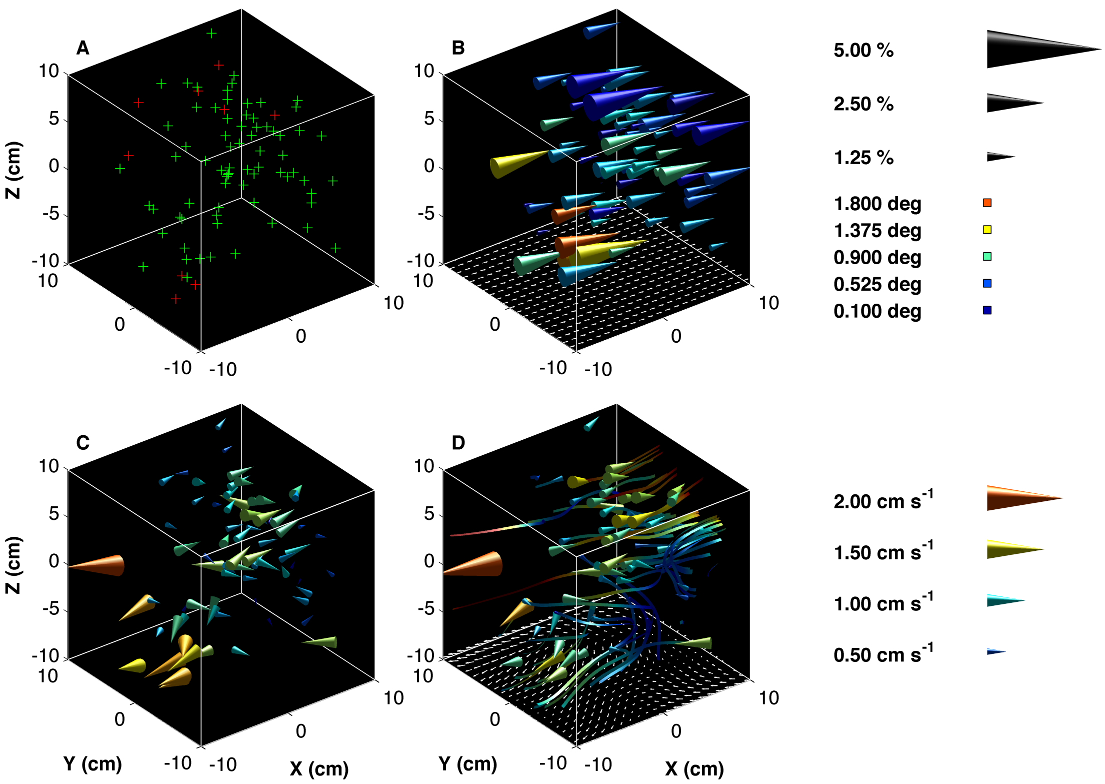

Figure (G.15). An instantaneous velocity flow field with a higher turbulence strength. The visualisation process is as per Figure G.14.

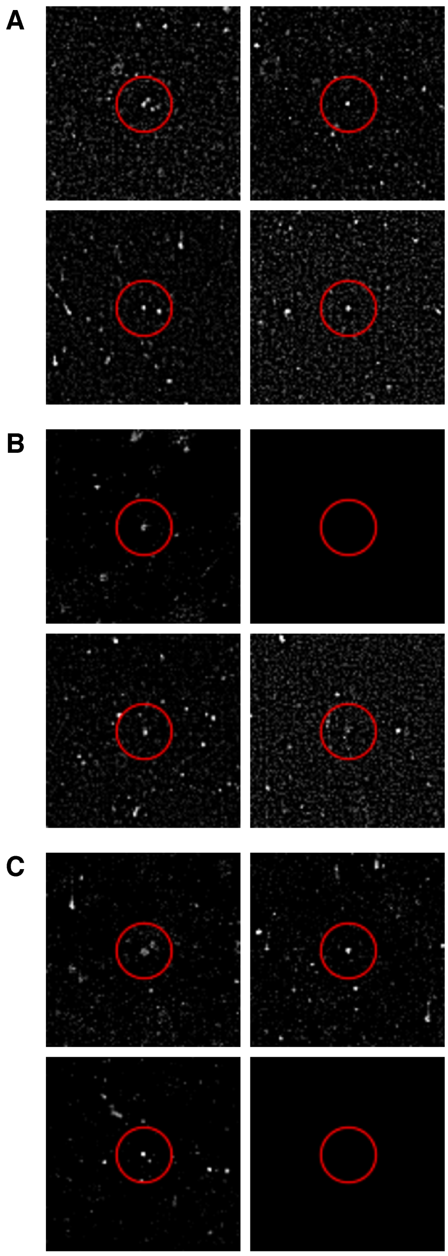

Figure (G.16). Three sections from the 3D-PTV image (A to C), viewed from each of the four different camera angles. The particles nearest the grid-points corresponding to: (A) the frame-minimum Δ_n; (B) the frame-minimum θ; (C) the frame-maximum Δ_n and frame-maximum θ are highlighted.

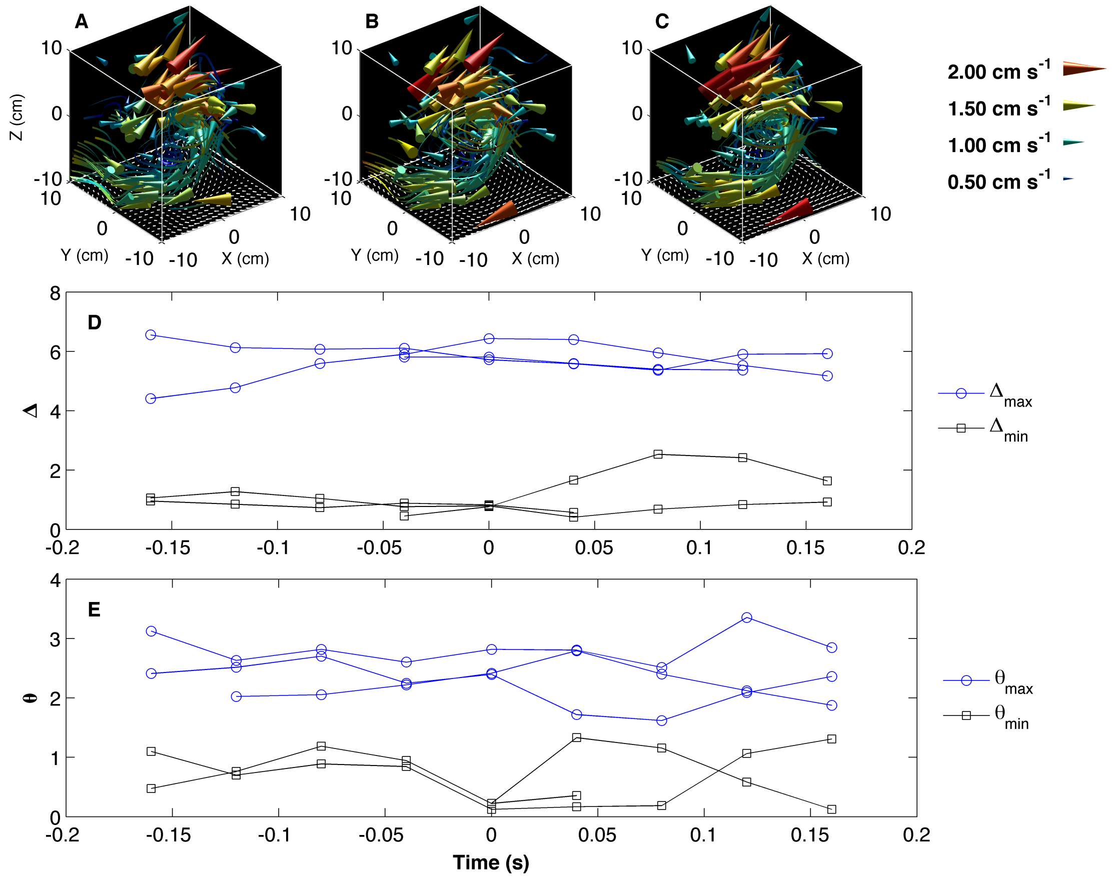

Figure (G.17). (A to C) Time-series of the instantaneous velocity flow field of a three-dimensional coherent structure at intervals of 1/25 s. Visualisation procedures are as in Figure and Figure. (D) Time-series of the adjustment made by PEFRA to 6 particles that represent the 3 maximum and 3 minimum Δ corrections made in (B) over a sequence of 7 frames. (E) Time-series of the adjustment made by PEFRA to 6 particles that represent the 3 maximum and 3 minimum θ corrections made in (B) over a sequence of 7 frames.

.

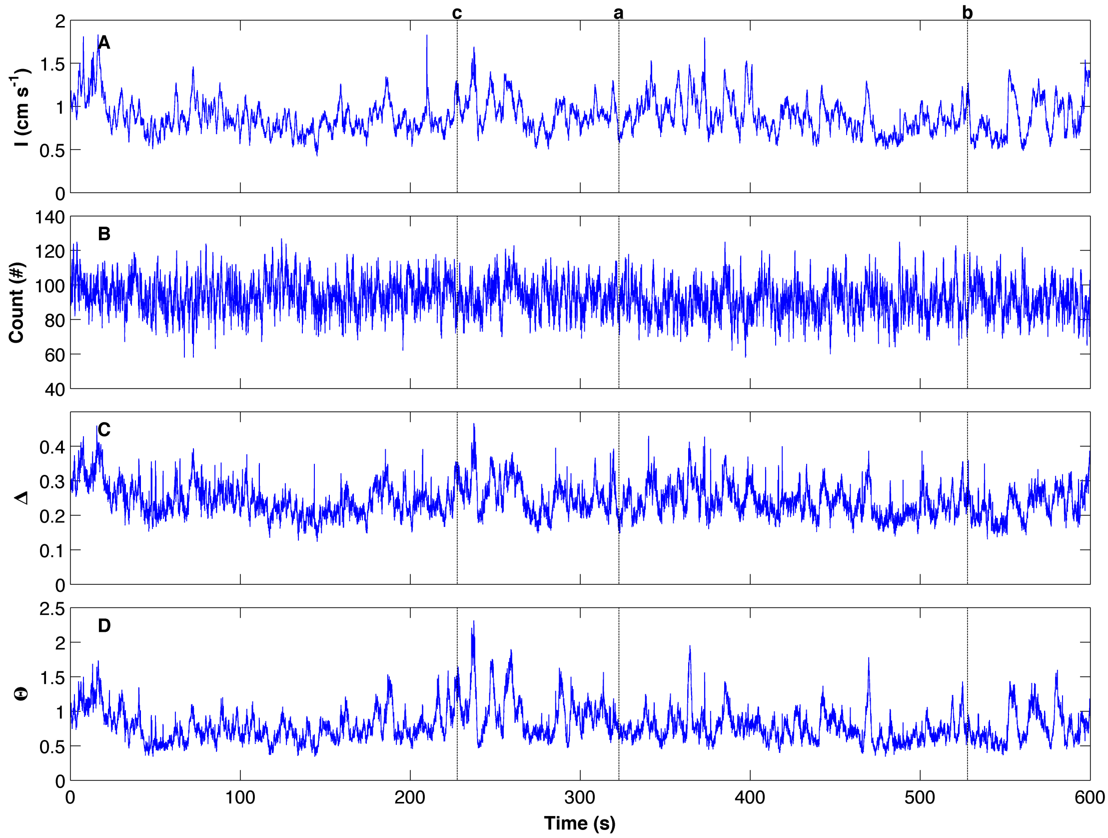

Figure (G.18). Time-series of the sample volume (A) mean turbulence strength, (B) total particle count, (C) frame-averaged Δ_n and (D) frame-averaged θ. The black lines represent where the velocity distributions shown in (a) Figure G.14, (b) Figure G.15 and (c) Figure G.19 occurs in the sequence.

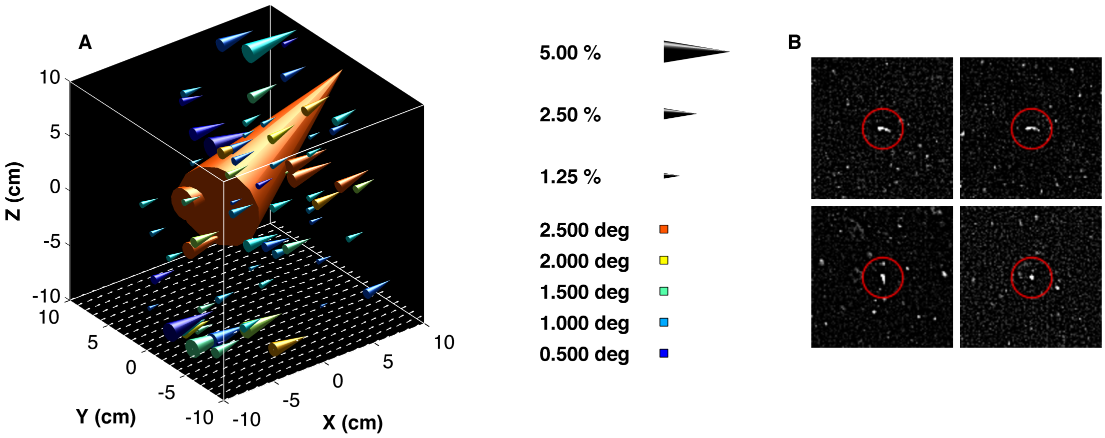

Figure (G.19). (A) The Δ_n and θ between the input and output velocity flow field at each of the seed-points. (B) Section from the 3D-PTV image, viewed from each of the four different camera angles, with the particle responsible for the single large vector in (A) highlighted.

Bibliography

R. J. Adrian. Hairpin vortex organisation in wall turbulence. *Physics of Fluids*, 19:041301, 2007.

R. J. Adrian and Z.-C. Liu. Observation of vortex packets in direct numerical simulation of fully turbulent channel flow. *Journal of Visualisation*, 5:9–19, 2002.

R. J. Adrian and J. Westerweel. *Particle image velocimetry*. Cambridge University Press, 2010.

R. J. Adrian, K. T. Christensen, and Z.-C. Liu. Analysis and interpretation of instantaneous turbulent velcocity fields. *Experiments in Fluids*, 29:275–290, 2000a.

R. J. Adrian, C. D Meinhart, and C. Tomkins. Vortex organisation in the outer region of the turbulent boundary layer. *Journal of Fluid Mechanics*, 2000b.

P. Bandyopadhyay. Large structure with a characteristic upstream interface in turbulent boundary layers. *Physics of Fluids*, 23:2326–2327, 1980.

D. R. Bellwood and R. Fisher. Relative swimming speed in reef fish larvae. *Marine Ecology Progress Series*, 2001.

L. Bertuccioli, G. I. Roth, J. Katz, and T. R. Osborn. A submersible particle image velocimetry system for turbulence measurements in the bottom boundary layer. *Journal of Atmospheric and Oceanic Technology*, 1999.

P. M. Biron, A. G. Roy, and J. L. Best. A scheme for resampling, filtering and subsampling unevenly spaced laser doppler anemometer data. *Mathematical Geology*, 27:731–748, 1995.

P. M. Biron, C. Robson, M. F. Lapointe, and S. J. Gaskin. Comparing different methods of bed shear stress estimates in simple and complex flow fields. *Earth Surface Processes and Landforms*, 29:1403–1415, 2004.

K. F. Bowden and L. A. Fairbairn. Measurements of turbulent fluctuations and reynolds stresses in tidal currents. *Proceedings of the Royal Society of London, Series A*, 237:422–438, 1956.

H. Burchard, P. D. Craig, J. R. Gemmrich, H. van Haren, P.-P. Mathieu, H. E. M Meier, W. A. M. Nimmo-Smith, H. Prandke, T. P. Rippeth, E. D Skyllingstad, W. D. Smyth, D. J. S. Welsh, and H. W. Wijesekera. Observational and numerical modeling methods for quantifying coastal and ocean turbulence and mixing. *Progress in Oceanography*, 76:399–442, 2008.

D. R. Caldwell and T. M. Chriss. The viscous boundary layer at the sea floor. *Science*, 205:1131–1132, 1979.

M. Cellino and U. Lemmin. In flows of coherent flow structures on the dynnamics of suspended sediment transport in open-channel flow. *Journal of Hydraulic Engineering*, 130:1077–1088, 2004.

A. Cenedese and G. Querzoli. Lagrangian statistics and transilient matrix measurements by PTV in a convective boundary layer. *Meas. Sci. Technol.*, 8: 057002, 1997.

A. Cenedese and G. Querzoli. Particle tracking velocimetry with new algorithms. *Meas. Sci. Technol.*, 11:603–613, 2000.

P. Chakraborty, S. Balachandar, and R. J. Adrian. On the relationships between local vortex identification schemes. *Journal of Fluid Mechanics*, 535:189–214, 2005.

J. Chen, J. Katz, and C. Meneveau. Implication of mismatch between stress and strain rate in turbulence subjected to rapid straining and destraining on dynamic LES models. *Transactions of ASME: Journal of Fluids Engineering*, 127:840–850, 2005.

J. Chen, C. Meneveau, and J. Katz. Scale interactions of turbuelnce subjected to a straining-relaxation-destraining cycle. *Journal of Fluid Mechanics*, 562 (123-150), 2006.

S. I. Chernyshenko and M. F. Baig. Streaks and vortices in near-wall turbulence. *Philosophical Transactions of the Royal Society of London, Series A*, 363:1097–1107, 2005.

M. S. Chong, A. E. Perry, and B. J. Cantwell. A general classification of three-dimensional flow fields. *Physics of Fluids*, 2:765–777, 1990.

T. M. Chriss and D. R. Caldwell. Evidence for the influence of form drag on bottom boundary layer flow. *Journal of Geophysical Research*, 87:4148–4154, 1982.

D. Coles. The law of the wake in the turbulent boundary layer. *Journal of Fluid Mechanics*, 1:191–226, 1956.

D. Conley and D. Inman. Ventilated oscillatory boundary-layers. *Journal of Fluid Mechanics*, 273:261–284, 1994.

E. R. Corino and R. S. Brodkey. A visual investigation of the wall region in turbulent flow. *Journal of Fluid Mechanics*, 37:1–30, 1969.

J. Cross. *Dynamics of suspended particles in a seasonally stratified coastal sea*. PhD thesis, University of Plymouth, 2012.

U. Dallman, A. Hilgenstock, B. Schulte-Werning, and H. Vollmers. On the footprints of three-dimensional separated vortex flows around blunt bodies. *Proceedings of the AGARD Conference*, 1991.

E. J. Davies. *Scattering properties of suspended particles*. PhD thesis, University of Plymouth, 2013.

D. J. Dennis. *The structural building blocks of turbulent wall-bounded flow*. PhD thesis, University of Cambridge, 2009.

D. J. Dennis and T. B. Nickels. On the limitations of taylor's hypothesis in constructing long structures in a turbulent boundary layer. *Journal of Fluid Mechanics*, 614:197–206, 2008.

D. J. Dennis and T. B. Nickels. Experimental measurement of large-scale three-dimensional structures in a turbulent boundary layer; part 1: vortex packets. *Journal of Fluid Mechanics*, 673:180–217, 2011a.

D. J. Dennis and T. B. Nickels. Experimental measurement of large-scale three-dimensional structures in a turbulent boundary layer; part 2: long structures. *Journal of Fluid Mechanics*, 673:218–244, 2011b.

R. K. Dewey and W. R. Crawford. Bottom stress estimates from vertical dissipation rate profiles on the continental shelf. *Journal of Physical Oceanography*, 18:1167–1177, 1988.

D. L. Donoho and I. M. Johnstone. Ideal spatial adaptation by wavelet shrinkage. *Biometrika*, 81:425–455, 1994.

P. Doron, L. Bertuccioli, J. Katz, and T. R. Osborn. Turbulence characteristics and dissipaiton estimates in the coastal ocean bottom boundary layer from PIV data. *Journal of Physical Oceanography*, 31:2108–2134, 2001.

J. Duncan, D. Dabiri, J. Hove, and M. Gharib. Universal outlier detection for particle image velocimetry (piv) & particle tracking velocimetry (ptv) data. *Measurement Science and Technology*, 21:1553–1561, 2010.

F. Feddersen and A. J. Williams III. Direct estimation of the reynols stress vertical structure in the nearshore. *Journal of Atmospheric and Oceanic Technology*, 24:102–116, 2007.

I. Fer and M. B. Paskyabi. Autonomous ocean turbulence measurements using shear probes on a moored instrument. *Journal of Atmospheric and Oceanic Technology*, 31:474–490, 2014.

B. Ganapathisubramani. *Investigation of turbulent boundary layer structure using stereoscopic particle image velocimetry.* PhD thesis, University of Minnesota, 2004.

B. Ganapathisubramani, E. K. Longmire, and I. Marusic. Experimental investigation of vortex properties in a turbulent boundary layer. *Physics of Fluids*, 18(055105), 2006.

M. Germano, U. Piomelli, P. Moin, and W. H. Cabot. A dynamic subgrid-scale eddy viscosity model. *Physics of Fluids*, 3:1760, 1991.

E. Giacomazzi, C. Bruno, and B. Favini. Fractal modelling of turbulent mixing. *Combustion Theory Modelling*, 3:637–655, 1999.

L. Goodman, E. R. Levine, and R. G. Lueck. On measuring the terms of the turbulent kinetic energy budget from an auv. *Journal of Atmospheric and Oceanic Technology*, 23:977–990, 2006.

C. M. Gordon. Intermittent momentum transport in a geophiscal boundary layer. *Nature*, 248:392–394, 1974.

D. G. Goring and V. I. Nikora. Despiking acoustic döppler velocimeter data. *Journal of Hydraulic Engineering*, 128:117–126, 2002.

G. W. Graham. *Biomediation of turbulence and suspended sediment characteristics in marsh surface flows - the influence of Spartina Anglica.* PhD thesis, University of Plymouth, 2010.

A. J. Grass, R. J. Stuart, and M. Mansour-Tehrani. Votrical structures and coherent motions in turbulent flow over smooth and rough boundaries. *Philosophical Transactions of the Royal Society of London, Series A*, 336:35–65, 1991.

H. Gunes and U. Rist. On the use of kriging for enhanced data reconstruction in a separated transitional flat-plate boundary layer. *Physics of Fluids*, 20: 104–109, 2008.

E. Hackett, L. Luznik, J. Katz, and T. Osborn. Effect of finite spatial resolution on the turbulent energy spectrum measured in the coastal ocean bottom boundary layer. *Journal of Atmospheric and Oceanic Technology*, 26:2610–2625, 2009.

E. Hackett, L. Luznik, A. R. Nayak, J. Katz, and T. R. Osborn. Field measurements of turbulence at an unstable interface between current and wave bottom boundary layers. *Journal of Geophysical Research*, 116(C02022), 2011.

A. H. Haidari and C. R. Smith. The generation and regeneration of single hairpin vortices. *Journal of Fluid Mechanics*, 277:135–162, 1994.

D. P. Hart. PIV error correction. *Experiments in Fluids*, 29:13–22, 2000.

M. R. Head and P. Bandyopadhyay. New aspects of turbulent boundary layer structure. *Journal of Fluid Mechanics*, 107:297–338, 1981.

A. D. Heathershaw. Bursting phenomena in the sea. *Nature*, 248:394–395, 1974.

E. C. Itsweire, J.R. Koseff, D. A. Briggs, and J. H. Ferziger. Turbulence in stratified shear flows: inplications for interpreting shear-induced mixing n the ocean. *Journal of Physical Oceanography*, 23:1508–1522, 1993.

R. G. Jackson. Sedimentological and fluid-dynamic implications of the turbulent bursting phenomenon in geophysical flows. *Journal of Fluid Mechanics*, 77: 531–560, 1976.

C. F. Jago and S. E. Jones. Observation and modelling of the dynamics of benthic fluff resuspended from a sandy beach in the southern north sea. *Continental Shelf Research*, 18:1255–1283, 1998.

J. Kim and P. Moin. The structure of the vorticity field in turbulent channel flow; part 2: study of ensemble-averaged fields. *Journal of Fluid Mechanics*, 162:339–363, 1986.

S.-C. Kim, C. T. Friedrichs, J. P.-Y. Maa, and L. D. Wright. Estimating bottom stress in tidal boundary layer from acoustic doppler velocimeter data. *Journal of Hydraulic Engineering*, 6:399–406, 2000.

J. C. Klewicki. Reynolds number dependence, scaling and dynamics of turbulent boundary layers. *Journal of Fluids Engineering*, 132(094001), 2010.

S. J. Kline, W. C. Reynolds, R. A. Schraub, and P. W. Runstadler. The structure of turbulent boundary layers. *Journal of Fluid Mechanics*, 30:741–733, 1967.

L. D. Landau and E. M. Lifshitz. *Fluid mechanics*. Butterworth-Heinemann, 2000.

S. Lentz. Sensitivity of the inner-shelf circulation to the form of the eddy viscosity profile. *Journal of Physical Oceanography*, 25:19–28, 1995.

M. Li, L. Sanford, and S. Y. Chao. Effects of time dependence in ustratified tidal boundary layers: results from large eddy simulations. *Estuarine, Coastal and Shelf Science*, 62:193–204, 2005.

R.-C. Lien and T. B. Sanford. Spectral characteristics of velocity and vorticity fluxes in an unstratified turbulent boundary layer. *Journal of Geophysical Research*, 105:8659–8672, 2000.

D. K. Lilly. The representation of small-scale turbulence in numerical simulations. In *Proceedings IBM Scientific Computing Symposium on Environmental Sciences*, 1967.

S. Liu, C. Meneveau, and J. Katz. On the properties of similarity subgrid-scale models as deduced from measurement in a turbulent jet. *Journal of Fluid Mechanics*, 275:83–119, 1994.

S. Liu, J. Katz, and C. Meneveau. Evolution and modeling of subgrid scales during rapid straining of turbulence. *Journal of Fluid Mechanics*, 387:281–320, 1999.

R. G. Lueck and Y. Lu. The logarithmic layer in a tidal channel. *Continental Shelf Research*, 17:1785–1861, 1997.

B. Luthi, A. Tsinober, and W. Kinzelbach. Lagrangian measurement of vorticity dynamics in turbulent flow. *Journal of Fluid Mechanics*, 528:87–118, 2005.

L. Luznik. *Turbulence characteristics of a tidally driven bottom boundary layer of the coastal ocean.* PhD thesis, The Johns Hopkins University, 2006.

L. Luznik, R. Gurka, W. A. M. Nimmo-Smith, J. Katz, and T. R. Osborn. Distribution of energy spectra, reynolds stresses, turbulence production and dissipation in a tidally driven bottom boundary layer. *Journal of Physical Oceanography*, 37:1527–1550, 2006.

H. G. Maas, A. Grun, and D. Papantoniou. Particle tracking in three dimensional turbulent flows. part 1: Photogrammetric determination of particle coordinates. *Experiments in Fluids*, 15:133–146, 1993.

C. Meneveau and J. Katz. Scale-invariance and turbuelnce models for large-eddy simulation. *Annual Review of Fluid Mechanics*, 32:1–32, 2000.

O. Metais and M. Lesieur. Spectral large-eddy simulation of isotropic and stably stratified turbulence. *Journal of Fluid Mechanics*, 239:157–194, 1992.

H. S. Min and Y. Noh. Influence of the surface heating on langmuir circulation. *Journal of Physical Oceanography*, 34:2630–2641, 2004.

P. Moin and J. Kim. Numerical investigation of turbulent channel flow. *Journal of Fluid Mechanics*, 118:341–377, 1982.

P. Moin and J. Kim. The structure of the vorticity field in turbulent channel flow; part 1: analysis of instantaneous and statistical correlation. *Journal of Fluid Mechanics*, 155:441–464, 1985.

N. Mori, T. Suzuki, and S. Kakuno. Noise of acoustic doppler velocimeter data in bubbly flows. *Journal of Engineering Mechanics*, 133:122–125, 2007.

J. N. Moum, M. C. Gregg, R. C. Lien, and M. E. Carr. Comparision of turbulence kinetic energy dissipation rate estimates from two ocean microstructure profilers. *Journal of Atmospheric and Oceanic Technology*, 12:346–366, 1995.

W. A. M. Nimmo-Smith. 3d flow visualisation in the bottom boundary layer of the coastal ocean. *OCEANS 2007*, pages 1–7, 2007.

W. A. M. Nimmo-Smith. A submersible three-dimensional particle tracking velocimetry system for flow visualization in the coastal ocean. *Limnology and Oceanography: Methods*, 6:96–104, 2008.

W. A. M. Nimmo-Smith, S. A. Thorpe, and A. Graham. Surface effects of bottom-generated turbulence in a shallow tidal sea. *Nature*, 400:251–254, 1999.

W. A. M. Nimmo-Smith, P. Atsavapranee, J. Katz, and T. R. Osborn. PIV measurements in the bottom boundary layer of the coastal ocean. *Experiments in Fluids*, 33:962–971, 2002.

W. A. M. Nimmo-Smith, J. Katz, and T. R. Osborn. On the structure of turbulence in the bottom boundary layer of the coastal ocean. *Journal of Physical Oceanography*, 35:72–93, 2005.

W. A. M. Nimmo-Smith, J. Katz, and T. R. Osborn. The effect of waves on subgrid-scale stresses, dissipation and model coefficients in the coastal ocean of the bottom boundary layer. *Journal of Fluid Mechanics*, 583:133–160, 2007.

Y. Noh, H. S. Min, and S. Raasch. Large eddy simulation of the ocean mexed layer: the effects of wave breaking and langmuir circulation. *Journal of Physical Oceanography*, 34:720–735, 2004.

T. Okuno, Y. Sugii, and S. Nishio. Image measurement of flow flow field using physics-based dynamic model. *Measurement Science and Technology*, 11:667–676, 2000.

T. R. Osborn. Estimates of the local rate of vertical diffusion from dissipation measurements. *Journal of Physical Oceanography*, 10:83–89, 1980.

S. Ott and J. Mann. An experimental investigation of the relative diffusion of particle pairs in three-dimensional turbulent flow. *Journal of Fluid Mechanics*, 422:207–233, 2000.

R. L. Panton. Oberview of the self-sustaining mechanisms of wall turbulence. *Progress in Aeronautical Sciences*, 37:341–383, 2001.

J. Pedlosky. *Geophysical fluid dynamics*. Springer-Verlag, 1990.

A. E. Perry and M. S. Chong. The mechanism of wall turbulence. *Journal of Fluid Mechanics*, 119:173–217, 1982.

U. Piomelli. Large-eddy simulation: achievements and challenges. *Progress in Aerospace Sciences*, 35:335–362, 1999.

U. Piomelli, P. Moin, and J. H. Ferziger. Model consistency in large eddy simulation of turbulent channel flows. *Physics of Fluids*, 31:1884–1891, 1988.

U. Piomelli, W. H. Cabot, P. Moin, and S. Lee. Subgrid-scale backscatter in turbulent and transition flows. *Physics of Fluids*, 3:1766–1771, 1991.

S. B. Pope. *Turbulent flows*. Cambridge University Press, Cambridge, Massachusetts, 2000.

F. Porte-Agel, C. Meneveau, and M. B. Parlange. A scale-dependent dynamic model for large-eddy simulation: application to a neutral atmospheric boundary layer. *Journal of Fluid Mechanics*, 415:261–284, 2000.

H. Prandke. Microstructure sensors. In H. Z. Baumert, J. Simpson, and J. Sundermann, editors, *Marine turbulence: theories, observations and models*, chapter Microstructure sensors. Cambridge University Press, Cambridge, United Kingdom, 2005.

M. Raffel, C. E. Willert, S. T. Wereley, and J. Kompenhans. *Particle image velocimetry: a practical guide*. Springer, 2007.

T. P. Rippeth, J. H. Simpson, E. Williams, and M. E. Inall. Measurement of the rates of production and dissipation of turbulent kinetic energy in energetic tidal flow: red wharf bay revisited. *Journal of Physical Oceanography*, 33:1889–1901, 2003.

S. K. Robinson. A review of vortex structures and associated coherent motions in turbulent boundary layers. In *Proceedings of the 2nd IUTAM symposium on structures, turbulence and drag reduction*, Zurich, Switzerland, 1989.

S. K. Robinson. Coherent motions in the turbulent boudnary layer. *Annual Review of Fluid Mechanics*, 23:601–639, 1991.

T. B. Sanford and R.-C. Lien. Turbulent properies in a homogeneous tidal bottom boundary layer. *Journal of Geophysical Research*, 104:1245–1257, 1999.

H. Schlichting. *Boundary layer theory.* McGraw-Hill Book Company, New York City, New York, 1960.

A. Sciacchitano, R. P. Dwight, and F. Scarano. Navier–stokes simulations in gappy piv data. *Experiments in Fluids*, 29:1421–1435, 2012.

W. Shaw and J. Trowbridge. The direct estimation of near-bottom turbulent fluxes in the presence of energetic wave motions. *Journal of Atmospheric and Oceanic Technology*, 18:1540–1557, 2001.

J. H. Simpson and J. Hunter. Fronts in the irish sea. *Nature*, 250:404–406, 1974.

J. H. Simpson and J. Sharples. *Introduction to the physical and biological oceanography of shelf seas.* Cambridge University Press, New York City, New York, 2012.

B. A. Singer and R. D. Joslin. Metamorphosis of a hairpin vortex into a young turbulent spot. *Physics of Fluids*, 6:3724–3736, 1994.

E. D. Skyllingstad and H. W. Wijesekera. Large-eddy simulation of flow over two-dimensional obstacles: high drag states and mixing. *Journal of Physical Oceanography*, 34:94–112, 2004.

E. D. Skyllingstad, W. D. Smyth, J. N. Moum, and H. W. Wijesekera. Upper-ocean turbulence during a westerly wind burst: a comparison of large-eddy simulation results and microstructure measurements. *Journal of Physical Oceanography*, 29:5–28, 1999.

J. Smagorinsky. General circulation experiments with primitive equations. *Monthly Weather Review*, 91:99–164, 1963.

C. R. Smith. A synthesized model fo the near-wall behaviour in turbulent boundary layers. In *Proceedings of the 8th Symposium on Turbulence*, Rolla, United States of America, 1984.

C. R. Smith and S. P. Metzler. The characteristics of low-speed streaks in the near wall region of a turbulent boundary layer. *Journal of Fluid Mechanics*, 129:27–54, 1983.

C. R. Smith, J. D. A. Walker, A. H. Haidari, and U. Sobrun. On the dynamics of near-wall turbulence. *Philosophical Transactions of the Royal Society of London, Series A*, 336:131–175, 1991.

W. D. Smyth and J. N. Moum. Anisotropy of turbulence in stably stratified mixing layers. *Physics of Fluids*, 12, 2000.

R. L. Soulsby, A. J. Manning, J. Spearman, and R. J. S. Whitehouse. Settling velocity and mass settling flux of flocculated estuarine sediments. *Marine Geology*, 339:1–12, 2013.

M. Stanislas, J. Westerweel, and J. Kompenhans, editors. *Particle image velocimetry: recent improvements*. Springer, 2004.

A. Stips. Dissipation measurement: theory. In H. Z. Baumert, J. Simpson, and J. Sundermann, editors, *Marine turbulence: theories, observations and models*. Cambridge University Press, Cambridge, United Kingdom, 2005.

H. Stommel. Trajectories of small bodies sinking slowly through convection cells. *Journal of Marine Research*, 8:24–29, 1949.

H. Stuer and S. Blaser. Interpolation of scattered 3d ptv data to a regular grid. *Flow, Turbulence and Combustion*, 64:215–232, 2000.

T. Suzuki. Reduced-order kalman-filtered hybrid simulation combining particle tracking velocimetry and direct numerical simulation. *Journal of Fluid Mechanics*, 709:249–288, 2012.

T. Suzuki, J. Hui, and F. Yamamoto. Unsteady ptv velocity field past an airfoil solved with dns: Part 2. validation and application at reynolds numbers up to re 104. *Experiments in Fluids*, 47:977–994, 2009a.

T. Suzuki, H. Ji, and F. Yamamoto. Unsteady ptv velocity field past an airfoil solved with dns: Part 1. algorithm of hybrid simulation and hybrid velocity field at re 103. *Experiments in Fluids*, 47:957–976, 2009b.

T. Svoboda, D. Martinec, and T. Pajdla. A convenient multi-camera self-calibration for virtual environments. *PRESENCE: teleoperators and virtual environments*, 14:407–422, 2005.

O. Talagrand and P. Courtier. Variational assimilation of meteorological observations with adjoint vorticity equation. i: Theory. *Quarterly Journal of the Royal Meteorological Society*, 113:1311–1328, 1987.

B. Tao, J. Katz, and C. Meneveau. Statistical geometry of subgrid-scale stresses determined from holographic particle image velocimetry measurements. *Journal of Fluid Mechanics*, 457:35–78, 2002.

G. I. Taylor. The spectrum of turbulence. *Proceedings of the Royal Society of London, Series A*, 164:476–490, 1938.

P. B. Tett, I. R. Joint, D. A. Purdie, ¡. Baars, S. Oosterhuis, G. Daneri, F. Hannah, D. K. Mills, D. Plummer, A. J Pomroy, A. W. Walne, H. J Witte, M. J. Howarth, and R. Lankeste. Biological consequences of tidal stirring gradients in the north sea. *Philosophical Transactions of the Royal Society of London, Series A*, 343:493–508, 1993.

T. Theodorsden. Mechanism of turbulence. In *Proceedings of the mid-western conference on fluid mechanics*, Ohio, United States of America, 1952.

H. Thomas, Y. Bozec, K. Elkalay, and H. J. W de Baar. Enhanced open ocean storage of c02 from shelf sea pumping. *Science*, 304:1005–1008, 2004.

S. A. Thorpe. *The turbulent ocean*. Cambridge University Press, Cambridge, Massachusetts, 2004.

S. A. Thorpe. *An introduction to ocean turbulence*. Cambridge University Press, Cambridge, Massachusetts, 2007.

S. A. Thorpe, J. A. M Green, J. H. Simpson, T. R. Osborn, and W. A. M. Nimmo-Smith. Boils and turbulence in a weakly stratified shallow tidal sea. *Journal of Physical Oceanography*, 38:1711–1730, 2008.

A. A. Townsend. *The structure of turbulent shear flow*. Cambridge University Press, Cambridge, Massachusetts, 1956.

J. Trowbridge. On a technique for measurement of turbulent shear stress in the presence of surface waves. *Journal of Atmospheric and Oceanic Technology*, 15:290–298, 1998.

W. van Leussen. The kolmogorov microscale as a limiting value for the floc sizes of suspended fine-grained sediments in estuaries. In N. Burt, R. Parker, and J. Watts, editors, *Cohesive Sediments: Proceedings of INTERCOH '94*, pages 45–62. John Wiley and Sons, 1997.

D. Venturi and G. Karniadakis. Gappy data and reconstruction procedures for flow past a cylinder. *Journal of Fluid Mechanics*, 509:315–336, 2004.

M. Virant and T. Dracos. 3d-ptv and its application on lagrangian motion. *Measurement Science and Technology*, 8:1539, 1997.

A. Vlasenko. *Physics-based fluid flow restoration method*. PhD thesis, University of Heidelberg, 2010.

A. Vlasenko and C. Schnorr. Physically consistent and efficient variational denoising of image fluid flow estimates. *IEEE Transactions on Image Processing*, 19:586–595, 2010.

A. Vlasenko, E. C. C. Steele, and W. A. M. Nimmo-Smith. A physics-enabled flow restoration algorithm for sparse PIV and PTV measurements. *Measurement Science and Technology*, 26:065301, 2015.

G. Volguaris and J. H. Trowbridge. Evaluation of the acoustic Doppler velocimeter ADV for turbulence measurements. *Journal of Atmospheric and Oceanic Technology*, 15:272–289, 1998.

T. L. Wahl. Discussion of 'despiking acoustic doppler velocimeter data'. *Journal of Hydraulic Engineering*, 129:484–488, 2003.

J. Westerweel. Efficient detection of spurious vectors in particle image velocimetry data. *Experiments in Fluids*, 12:236–247, 1994.

J. Westerweel and F. Scarano. Universal outlier detection for PIV data. *Experiments in Fluids*, 39:1096–1100, 2005.

J. Willneff. *A spatio-temporal matching algorithm for 3D particle tracking velocimetry*. PhD thesis, ETH Zurich, 2003.

X. Wu and P. Moin. Direct numerical simulation of turbulence in a nominally zero-pressure-gradient flat-plate boundary layer. *Journal of Fluid Mechanics*, 630:5–41, 2009.

J. Zhou, R. J. Adrian, and S. Balachandar. Autogeneration of near-wall vortical structures in channel flow. *Physics of Fluids*, 8:288–290, 1996.

J. Zhou, R. J. Adrian, S. Balachandar, and T. M. Kendall. Mechanisms for generating coherent packets of hairpin vortices in channel flow. *Journal of Fluid Mechanics*, 387:353–396, 1999.